

Copyright

by

Yawen He

2017

**The Dissertation Committee for Yawen He Certifies that this is the approved
version of the following dissertation:**

**Seismic Chronostratigraphy for Reservoir Characterization:
Modeling and Applications**

Committee:

Charles Kerans, Supervisor

Hongliu Zeng, Co-Supervisor

William Fisher

Sergey Fomel

Xavier Janson

**Seismic Chronostratigraphy for Reservoir Characterization:
Modeling and Applications**

by

Yawen He, B.E.; B.A.

Dissertation

Presented to the Faculty of the Graduate School of

The University of Texas at Austin

in Partial Fulfillment

of the Requirements

for the Degree of

Doctor of Philosophy

The University of Texas at Austin

May 2017

Dedication

To my grandfather

Yunsheng Li

To my parents

Fangbo He and Yingchuan Li

Acknowledgements

My Ph.D. journey would not have been possible without tremendous supports and guidance from my academic advisors, Dr. Charles Kerans and Dr. Hongliu Zeng, who have jointly helped me design a fascinating dissertation project, encouraged me to achieve my academic goals and frequently provided feedbacks on my progress. I would like to thank Prof. Kerans for being a charismatic leader, who has always optimistically helped me to confront and resolve research problems, granted me opportunities to present and communicate this dissertation project with industrial sponsors, and patiently introduced me to carbonate geology, Permian Basin geology, sequence stratigraphy, and reservoir characterization. Meanwhile, I would also like to appreciate Dr. Zeng for letting me fulfill my dream of being a graduate student at UT Austin, for always welcoming me for casual discussions on technical details in this dissertation, and for supporting me during my most difficult times to adjust from exploration geophysics background to this reservoir-focused modeling and interpretation research topic.

I would also like to address my special gratitude to my committee members for their valuable time, insightful feedback and hands-on helps on my dissertation projects. I first met Dr. Fisher during the sequence stratigraphy class, and I appreciate him for insightful lectures and for helping me improve a proper usage of sequence stratigraphic concept in this dissertation and referring me to insightful references. I thank Dr. Fomel for his seismic imaging and multi-dimensional data analysis courses, his advice on the petrophysical calibration and geophysical application aspects on this dissertation, and also for supporting my application of dissertation writing fellowship and career seeking so that I could efficiently and peacefully complete this May. I am grateful for Dr. Janson for his

collaborations and many pieces of advice on the modeling part of this dissertation, and also for helping me improve my skills in scientific writing. Dr. Janson also introduced me to Dr. Jereon Kenter, who kindly shared with us his laboratory measurements of outcrop plugs from LCC to accomplish this study.

I would like to address my thanks to consortium and institutions providing financial supports to my education, as well as related project experiences to enhance my understanding of the dissertation projects. Special thanks go to RCRL (Reservoir Characterization Research Laboratory) and Project STARR (State of Texas Advanced Oil and Gas Recovery) at the Bureau of Economic Geology for offering me Graduate Research Assistantship. Special thanks go to RCRL sponsors especially Occidental Petroleum for sponsoring subsurface data used in this study and advice from Bill Fitchen and Kate Pollard, RCRL sponsors and former students sharing their previous works on LCC and CBP, including M. Sonnenfeld, J. Kenter, S. Z. Scott, R. Phelps, and J. Sitgreaves, and Dr. Michele Claps for sharing his experience on geocellular modeling. I also appreciate the Department of Geological Sciences for offering my Teaching Assistantship, where I introduced the beauty of geosciences to undeclared aspirant students, and fortunately witnessed some of them finally chosen geosciences as their major. Besides, I appreciate Landmark Software & Service of Halliburton and GoM Reservoir Development of BP America for offering internship opportunities to work on projects closely-related to the application aspect of my dissertation, with mentorship from Dr. Jesse Lomask, Felix Segovia, and Fran Rollins.

Gratitude is also extended to UT faculties and Jackson School of Geosciences staff for providing interesting courses and for sharing their opinions on my dissertation, including but not limited to Drs. Bob Hardage, Malik Krishan, David Mohrig, Lorena Moscardelli, Allison Roberts, Mrinal Sen, Kyle Spike, Ron Steel, Carlos Torres-Verdin,

Sanjay Srinivasan, and Chris Zahm. I also appreciate Poe Chen, Dallas Dunlap, Reuben Reyes, Joseph Yeh at the Bureau of Economic Geology for their IT supports and professional advice on data managements, as well as thank Philip Guerrero, Stephaine Lane, Mellisa Garcia and Jacobo Anselmo for their administrative assistances and for addressing my handful of questions in graduate school, and to Maurine Riess for providing career advice.

I appreciate my graduate lab mates and colleagues for their supports and friendship during my 5.8 years' stay at Austin, including but not limited to Yaser Alzayer, Taylor Canada, Nick Danger, Nick Ettinger, Marina C Frederik, Reynaldy Fifariz, Baiyuan Gao, Sam Hiebert, Greg Hurd, Siwei Li, Han Liu, Kyle M McKenzie, Andrea Nolting, Alex Parker, Yang Peng, Kelly Regimbal, Qi Ren, Ben Smith, Junzhe Sun, Lucy Ko-Tingwei, Kris Voorhees, Zhiguang Xue, Jie Xu and Jinyu Zhang.

Finally, I would like to appreciate my grandfather, Yunsheng Li, for inspiring me to study geosciences, my parents Fangbo He and Yingchuan Li for their love, encouragements, and supports for my choice to study away from home, and my boyfriend, Tianhao Zheng for the adventures we took together.

Seismic Chronostratigraphy for Reservoir Characterization: Modeling and Applications

Yawen He, Ph.D.

The University of Texas at Austin, 2017

Supervisors: Charles Kerans and Hongliu Zeng

The assumption of the chronostratigraphic significance of seismic reflections serves as a fundamental premise in interpreting stratigraphy from seismic images. This hypothesis proposed in 1977 was initially applied to delineate depositional sequences as the basic interpretive unit, and then to reconstruct Wheeler Diagram and regional sea level curves. After a further comparison against with global eustatic events, these regional curves can further facilitate predicting the age, distribution, and facies of depositional sequence before drilling in a seismic-covered area during petroleum exploration. With a boom in reservoir-level seismic applications, for obtaining significant high frequency sequence (HFS) surfaces as the bounding surfaces in static reservoir model construction, this fundamental assumption was inevitably extended to characterize HFS and even high-frequency cycles (HFC) during seismic reservoir characterization.

For an ultimate improvement in constructing reservoir-bounding surfaces, the author targeted at evaluating the validity of this fundamental assumption as applied to high-order seismic stratigraphy. The author conducted the entire project via the forward seismic modeling upon geologic models with known chronostratigraphic relationship. Besides, these input models carefully honor the reservoir geology for meaningful discussions on (1) shallow marine siliciclastic reservoirs in Starfak Field, GoM, (2) shallow-water mixed

carbonate/clastic Upper San Andres-Grayburg reservoirs in Permian Basin, and (3) shallow-water carbonate Abo shelf margin-Clear Fork platform in Permian Basin.

This study has achieved three-fold contributions. On the aspect of realistic geocellular, property and seismic modeling at the reservoir scale, the author integrated high-resolution sequence stratigraphic framework, published 3D depositional model, intra-facies heterogeneity in 3D modeling to selectively apply advanced geostatistical methods to model hierarchical heterogeneity. Subsequently, the author proposed an evaluation scheme with a defined parameter ('time-correlation error/TCE') to assess HFS-scale reservoir-bounding surfaces. These assessments revealed an interactive influence from (1) stratal geometry, (2) lateral lithofacies variation, (3) lithofacies-sonic velocity relationship in pure- versus mixed-lithology successions, (4) intra-facies heterogeneity, and (5) seismic frequency. Finally, based on these forward modeling results, the author proposed a decision tree to determine valid interpretation strategy in seismic chronostratigraphic correlation in scenarios with geoscientists' expert knowledge and recommended an attribute-driven volumetric picking scheme to improve published algorithms for scenarios without prior knowledge.

Table of Contents

List of Tables	xiv
List of Figures	xvi
Chapter 1: Introduction	1
1.1 RESEARCH TOPIC AND SIGNIFICANCE IN PETROLEUM GEOSCIENCES	1
1.1.1 Chronostratigraphic significance of seismic reflections – the fundamental assumption for seismic stratigraphy.....	1
1.1.2 Scale of applications of this fundamental assumption: original versus present	2
1.1.3 Significances of the research topic	4
1.2 MOTIVATIONS AND RESEARCH QUESTIONS	6
1.2.1 Motivations	6
1.2.2 Research questions	7
1.3 EXPERIMENTAL DESIGN AND CONTROLLABLE VARIABLES ..	8
1.3.1 Five variables to test at the reservoir scale	8
1.3.2 An overview of experimental design	11
1.4 STRUCTURE OF THIS DISSERTATION.....	13
Chapter 2: An introductory example – conceptual siliciclastic reservoirs with flat- lying stratal geometry	18
2.1 INTRODUCTION	19
2.2 METHODS	22
2.3 MODEL DESIGN: IMPEDANCE AND SEISMIC MODELS	24
2.3.1 Impedance models	24
2.3.2 Seismic models	29
2.4 QUANTIFY THE QUALITY OF RELATIVE GEOLOGIC TIME CORRELATION	33
2.4.1 The time-correlation error for a manually tracked seismic event	33
2.4.2 The time-correlation error for a manually tracked seismic event	34
2.5 RESULTS AND INTERPRETATIONS	37

2.5.1 The time-correlation error distribution related to lateral impedance variation	37
2.5.2 The time-correlation error distribution related varying seismic frequencies	41
2.6 POTENTIAL APPLICATIONS TO SEISMIC CHRONOSTRATIGRAPHY	45
2.6.1 Looking for a useful attribute	46
2.6.2 Integrating autotracking and phantom slicing (stratal slicing) ...	48
2.7 CONCLUSIONS AND FUTURE WORKS	50
2.7.1 Conclusions.....	50
2.7.2 Future Works	51
Chapter 3: Improving 3D seismic horizon interpretation for reservoir model construction: an example of 3D geocellular and seismic model of Permian San Andres shelf-Grayburg platform mixed carbonate/elastic strata	
3.1 INTRODUCTION	54
3.2 STUDY TARGET AND CHALLENGES.....	58
3.2.1 Seismic stratigraphic interpretation challenges for uSA shelf reservoirs.....	58
3.2.2 An opportunity to investigate seismic stratigraphy through forward modeling	60
3.3 STUDY AREAS, GEOLOGIC SETTING AND DEPOSITIONAL MODELS	60
3.3.1 Study areas and datasets.....	60
3.3.2 Geologic setting	64
3.3.3 Depositional models for San Andres-Grayburg strata	65
3.4 MODELING WORKFLOW AND METHODOLOGY OVERVIEW...68	
3.4.1 Workflow	68
3.4.2 Methodology overview	69
3.5. STRATIGRAPHIC CORRELATION, MODELING AND GRIDDING (STEP 2~3)	72
3.5.1 An overview of hard constraints and modeling methods.....	72
3.5.2 Outcrop-constrained upper PCS-10 flattened to HSS (Model I-b)	73
3.5.3 Outcrop-constrained lower PCS-10 (Model I-a).....	76

3.5.4	Cropped subsurface-constrained PCS-11 (Model II).....	78
3.5.5	Integration for a single stratigraphic model.....	80
3.6	FACIES MODELING (STEP 4)	81
3.6.1	PCS-10 facies modeling overview and method selection per zone.....	81
3.6.2	PCS-10 along-strike facies variability and dimensionality from outcrop photos.....	84
3.6.3	Modeling highly-ordered facies transition using TGS with trend – an example of Scenario 3.....	89
3.6.4	Modeling localized objects using SOM – an example of Scenario 2	94
3.6.5	Modeling both large- and small-scale heterogeneity – an example of Scenario 4.....	96
3.6.6	Modeling complex facies distribution using PGS – an subsurface example.....	99
3.7.	PROPERTY AND SEISMIC MODELING (STEP 5~6)	102
3.7.1	Data sources for acoustic properties (outcrop and subsurface)	102
3.7.2	Relationship between acoustic velocity and impedance	103
3.7.3	Acoustic velocity analytic results and adjustments	104
3.7.4	Seismic modeling parameters	108
3.8.	RESULTS AND DISCUSSIONS ON CHRONOSTRATIGRAPHIC SIGNIFICANCE FOR A RESERVOIR TOP AND BASE	109
3.8.1	2D and 3D evaluation methods and examples.....	110
3.8.2	Discussion and recommendations.....	115
3.8.2.1	Interpreted G9 HFS bottom and interpretation strategy.....	116
3.8.2.2	Interpreted G9 HFS top and alternative interpretation strategy	118
3.9	CONCLUSIONS AND FUTURE WORK	120
Chapter 4:	Improving 3D seismic stratigraphic correlation for reservoir model construction: evaluation and discussions	122
4.1	INTRODUCTION	123
4.2	MODELING AREAS AND DATASETS	124
4.2.1	Modeling areas.....	124

4.2.2 Datasets for Case 1 and Case 2	125
4.3 MODEL DESIGN: WORKFLOW AND RESULTS	129
4.3.1 An overview of modeling workflow	129
4.3.2 Results: Case 2 model construction	131
4.3.3 Results: velocity variogram analysis and models	137
4.3.4 Results: seismic models	143
4.4 EVALUATION METHODS AND EXAMPLES	147
4.4.1 An example on evaluating one horizon from one seismic model	147
4.4.2 An example of cross-comparison among multi-frequency seismic models	150
4.5 EVALUATION RESULTS AT HFS AND HFC SCALE	153
4.5.1 Evaluation results of flat-lying G12 HFS top	153
4.5.2 Evaluation results of clinoformal G9 HFS bottom	158
4.5.3 Evaluation results of diachronous HFC-scale seismic reflections	164
4.6 DISCUSSIONS ON POTENTIAL FIELD APPLICATIONS	172
4.6.1 A decision tree based on forward models in Chapter 3 and 4 ..	172
4.6.2 A hybrid volumetric-picking scheme based on Chapter 2.....	175
4.7 CONCLUSIONS AND FUTURE WORK	177
Chapter 5: Conclusions and Future Work.....	179
5.1 CONCLUSIONS.....	179
5.2 FUTURE WORK.....	182
Appendix.....	184
Glossary	188
References.....	189
Vita	203

List of Tables

Table 1.1:	Five variables to be tested in this study for a reservoir-scale evaluation, compared with Vail et al. (1977c)'s original experiment design targeted at exploration scale.	9
Table 2.1:	Engineering description of geologic complexity (Weber and van Geuns, 1990). The reservoir heterogeneity is characterized by different extents of lateral lithofacies discontinuity/variation.	29
Table 3.1:	Surface modeling methodology overview and integration of three sub-models.	72
Table 3.2:	Facies modeling overview, with zonation information, as well as number of measured sections, layering and modeling method per zone.	83
Table 3.3:	The decision tree to select and combine facies modeling methods, and four scenarios.	84
Table 3.4:	Three types of facies transition, modeled by TGS with Trend in this study, for Scenario 3 or Scenario 4.	90
Table 3.5:	Raw analytic results of P-wave velocity before adjusting systematic differences, which was originated from different acoustic property data sources.	106
Table 4.1:	Velocity variograms for selected zones used in this study, with (a) good, (b) intermediate/experimentally-fitted, and (c) poor velocity continuity.	140
Table 4.2:	General conclusions for influencing factors on the ‘chronostratigraphic significance of seismic reflections at the HFS scale.	178
Table G.1:	Abbreviations used in this dissertation.	188

List of Figures

- Figure 1.1: Seismic chronostratigraphic correlation applied to conventional seismic stratigraphy and modern computational seismic chronostratigraphy. Modified from Vail et al. (1977a), (a) and (b) show applications of seismic stratigraphy to interpret stratigraphic cross-section in (a), as well as Wheeler Diagram and then regional relative sea-level curve in (b). Modified from Fomel (2010), (c) and (d) present an advanced automated picking algorithm of predicative painting in computational seismic chronostratigraphy, which is capable of densely picking all seismic reflections in (c) and then reconstruct a seismic Wheeler Diagram in (d).
.....4
- Figure 1.2: An overview of experiment design, containing a forward modeling and evaluation workflow, and five predefined controllable variables.....13
- Figure 1.3: Focus of three dissertation projects. Chapter 2 to 4 presents these projects as stand-alone elements. Note their interrelations as stated in objectives.17
- Figure 2.1: Correlation between seed wells. (a) Original correlation in subsea true vertical depth. Interpreted chronostratigraphic surfaces (cs1–4) defined three chronostratigraphic units (zones 1–3) and (b) adjusted correlation in TWT. Flattened chronostratigraphic surfaces (cs1–4) bounded three slightly compressed/ stretched chronostratigraphic units (zones 1'–3'). The AI for sandstone is lower in this study.26

Figure 2.2: A 2D illustration of the interpolation scheme used in this study. (a) Conversion from the original scheme (left) to the correlation scheme (right), where all chronostratigraphic layering (gray solid lines) is horizontal. (b) Little wireline-log distortion resulted during the conversion (average of 2% for each zone). The original and adjusted chronostratigraphic surfaces (cs1–4 and cs1–4) are marked with dashed orange lines, and (c) the adjusted scheme facilitates easier observation of seismic time transgression. Time transgression Δt is proportional to dip α (compare I and II).27

Figure 2.3: Impedance models with increasing lateral lithofacies variation. (a) Variograms to simulate impedance models via GRFS. Given the same seed wells (A, B, C, and D), the decreased lateral range in the input variogram produces increased lateral impedance complexity. (b) Layer-cake model I, generated with a lateral correlative distance/range of 50,000 m, 50 times its model size (1000 m). (c) Intermediate model II, generated with a lateral range of 1000 m. (d) Complex model III, produced with a lateral range of 200 m.28

Figure 2.4: Comparison of seismic models: convolution versus exploding-reflector. (a and b) In layer-cake cases, both models work well. In more complex cases, the exploding-reflector model provided more realistic synthetics, with enhanced horizon continuity, than did the convolution model. Thus, the exploding-reflector model was used in this study.....31

Figure 2.5: Most of the impedance/lithofacies units in this study are below seismic resolution. More than 70% of high-impedance shaly units (blue curve) and low-impedance sandstone units (red curve) were irresolvable at multiple frequencies.32

Figure 2.6: Comparison between 90°- and zero-phase seismic models. (a) Impedance section, (b) 90° seismic model, in which the top and bottom of a high-impedance unit (black lines) are, respectively, expressed as a $-t$ zero crossing and a t zero crossing (yellow lines), and (c) zero-phase seismic model, in which the top and bottom of the unit are, respectively, represented as a peak and a trough (yellow lines). Panel (b) was used in this study for its straightforward correlation to the impedance model (panel [a]).32

Figure 2.7: The TCE of a horizon, measuring the time difference between a seismic event hk and the nearest chronostratigraphic surface Csk . (a) In a general case, a shift of the seismic event is needed to measure only the minimum time difference. (b) In this specific scheme, a seismic event hk is compared with an arbitrary flat geologic timeline, e.g., the median value for the seismic event hk34

Figure 2.8: An RGT volume estimated from a seismic time-amplitude volume (from Stark, 2003). (a) Seismic cube and (b) estimated RGT volume, in which the constant-value surface is equal to a seismic horizon. Therefore, the RGT volume could be viewed as a densely interpreted cube.36

Figure 2.9: TCE for a seismic RGT cube. (a) RGT volume from the seismic model, with curved RGT lines and (b) RGT volume from the impedance model, with flat RGT lines. Contours = 10 ms in panels (a,b). (c) The difference between panels (a,b) is an estimation of TCE. Where reflections follow geologic timelines, the TCE is small (box I). Boxes II and III show positive (overestimated) and negative (underestimated) TCE, respectively. Note that higher TCE offset values around the margins result from a seed reference trace emplaced in the center.36

Figure 2.10: Visual comparison for geologic time correlation of seismic events, among models with increasing lateral impedance variation. From models I to III, there is an increase in dipping and chaotic reflections, indicating increased TCE. The front, side, and top frames of a cube, respectively, show the center crossline (crossline = 500 m), inline (inline = 500 m), and time slice (time = 120 ms). The same visualization cube also applies to Figure 2.12.38

Figure 2.11: TCEs for selected horizons (h1, h2, and h3) at 40 Hz, showing an increasing trend with increasing lateral impedance variation. Event width = 12.5 ms. Units for the maximum time transgression (delta) and standard deviation (std. dev.) are milliseconds (ms).....39

Figure 2.12: TCEs for the same intersection extracted from 40-Hz seismic volumes. Panel (a-c) are the TCEs for models I to III. The same inline was visualized in the same color scheme. (d) Overlaying TCE histograms of three models. The visual comparison among (a-c) and histograms in panel (d) show increasing TCEs with increasing lateral lithofacies variation.40

Figure 2.13: Visual comparison for geologic time correlation of seismic events at multiple frequencies. The TCE tends to decrease with increasing seismic frequency for the (b) intermediate and (c) complex models. It is difficult to visually identify a trend for the layer-cake model (a).....42

Figure 2.14: TCEs for seismic event h2 (see Figure 2.10 for position) at different seismic frequencies. The accuracy of the chronostratigraphic correlation tends to improve with the increasing seismic frequency, especially for the (b) intermediate and (c) complex models.44

Figure 2.15: Frequency influence on the TCE for densely interpreted volumes. The accuracy of the chronostratigraphic correlation tends to improve with the increasing seismic frequency, especially for the (b) intermediate and (c) complex models. In the layer-cake model (panel [a]), the TCE is small at all frequencies, with the best interpretation from 80 Hz.....44

Figure 2.16: Observed correlation between lateral variations in the impedance models and amplitude variances calculated from their seismic records. Multiple variance time slices (60, 80, 100, 120, 140, and 160 ms) show similar distributions within models (a) I, (b) II, and (c) III. However, the amplitude variance increases when the range of lateral impedance variation increases from model I to model III. Note the changes in the horizontal scale of variance.47

Figure 2.17: Power relationship between the lateral relative distance in impedance model and the median value of the amplitude variance, calculated from the synthetic seismic volume.48

Figure 2.18: Workflows for generating the hybrid RGT volume. The author propose to use a special seismic attribute to replace human judgment for a quantitative and practical procedure.50

Figure 3.1: Permian San Andres-Grayburg stratigraphy, and challenges in seismic stratigraphic interpretation of shelf-margin reservoirs. (a) stratigraphic column and (b) regional stratigraphic cross-section are modified from Kerans et al.(2013). (c) a local dip-oriented seismic section. The annotated red and green box represents outcrop- and subsurface-constrained modeling interval in this study, with study areas shown in Figure 3.2.59

Figure 3.2: Study areas and subsurface productions. (a) Middle Permian stratigraphy showing LCC outcrop study area (red box) and CBP subsurface study area (green box), which is located within Dutton et al. (2004)’s Play 127 reservoir trend. (b) 2015 statistics on Play 127, the subsurface data is from a top producing field. (c) A zoomed-in LCC outcrop study area showing dataset. (d) A zoomed-in CBP subsurface study area showing dataset.61

Figure 3.3: 3D depositional and facies model from previous studies, with facies codes in this study. (a) and (b) show 3D depositional model of G9 HFS in PCS-10 and G11 HFS in PCS-11 (Kerans et al., 2013). (c) Facies model for an idealized HFC in G9 HFS, proposed based on LCC observations (Scott, 2007). (d) Facies model for a single timeline in G11 HFS, proposed based on field observations in Shattuck Escarpment (Hiebert, 2012). Other modeled facies in PCS10 and 11 are listed at the bottom, with more details in methodology section.66

Figure 3.4: Geocellular and seismic modeling workflow.69

Figure 3.5: 3D visualization of LIDAR-image of canyon walls, showing high-resolution of stratigraphic correlation for G9 HFC5~14 up to HFC scale.74

Figure 3.6: An example showing molded stratigraphic surfaces of a HFC. Stratigraphic contacts for the top, flooding surface and base of HFC6 were mapped on LIDAR image of canyon walls, then interpolated using Kriging. Results are shown in (b), (c) and (d).75

Figure 3.7: Selected surfaces for three sub-models. (a) and (b) are LIDAR-constrained G9 top and MFS flattened to Hayes sandstone to mitigate effect from Tertiary uplift. (c) is the cropped subsurface model to a similar size of LCC model, it shows a similar topography with (a) after rotating 30o clockwise. (d) is the G9 MFS as the top of lower PCS-10 model which assumed little along-strike topographic variation, thus the author deformed all these lower PCS-10 surfaces in relative to the LIDAR-constrained G9 MFS in (b).78

Figure 3.8: Dip-oriented well panel (see Figure 3.2d for location), showing stratigraphic correlation and zonation for subsurface-constrained PCS-11.80

Figure 3.9: Outcrop photos showing along-strike facies variability and dimensionality (modified from Scott, 2007). (a) LIDAR image of canyon walls showing outcrop photo locations. (b)~(d) along-strike outcrop photos from updip to downdip. (e) in the vicinity of Gilson Canyon, showing a major reef development in HFC11b, and its affected HFC12a.86

Figure 3.10: Modeled stratigraphic surfaces and along-strike interpretations, with locations shown in Figure 3.9a. (a) Dip-oriented section showing Sonnenfeld and Cross (1993)'s cross-section from measured section 14 to 27. (b) Along-stick cross-sections showing facies interpretation within modeled stratigraphic surfaces, along the East walls of (b1) White Oaks Canyon, (b2) Sitting Bulls Canyon, and (b3) Gilson Canyon.87

Figure 3.11: Observed width and maximum thickness for localized objects from outcrop photos, including the turbidite channels (F7-fpS) and mounds/bioherms (F6-M/B). In both case, most localized objects are well below vertical seismic resolution of their background facies, whereas above horizontal seismic resolution at a dominant frequency of 27 Hz or peak frequency at 35Hz.89

Figure 3.12: An example of modeling highly-ordered facies transition using TGS with Trend, as applied to HFC8-R hemicycle. (a) 3-D visualization of HFC8-R, with measured sections and result displayed in fence diagram, (b) Trend map used for facies modeling, (c) and (d) are resultant facies model near the promontory and reentrant, compared with layering/stratifications.....93

Figure 3.13: Examples of parameters used for simulating localized object of (a) turbidite channels, and (b) mound/buildups. In both case, the author assigned the highest demand to honor hard data of measured sections, and conservatively only generate object that intersect wells.95

- Figure 3.14: An example of modeling adaptive turbidite channel using SOM, as applied to HFC8 transgressive hemicycle. (a) 3-D visualization of measured sections in HFC8-T, (b) 3-D visualization of modeling results, where the background F8-bS is tuned as transparent.....96
- Figure 3.15: An example of Scenario 4 as applied for HFC10. (a) input measured sections for HFC10, where a bioherm was interpreted in measure section #V. (b) primary fabric modeled for HFC10, using TGS with trend. (c) a dip-view showing simulated bioherm in upper slope location, where previous layering follows a reference surface, (d) a map-view k-layer in HFC10 showing modeled bioherm within bioturbated sandstone near #V.....98
- Figure 3.16: An example of modeling complex stratigraphy in Grayburg-Lower Queen Formation, as applied to zone 7 (Figure 3.8). (a) Lithotype proportion matrix LPM and (b) Lithotype rule are two major inputs to generate (c) facies modeling results, as displayed in a chronostratigraphic k layer. (a) was generated by extrapolating from vertical proportion curves (a1) to a dense grid (a2) using Linear Model Kriging. (b1) and (b2) are two lithotype sets combining into the lithotype rule (b).....101
- Figure 3.17: Data source for acoustic property. (a) outcrop plugs in Sonnenfeld and Cross (1993)'s HFC6, laboratory measurements from Kenter et al. (1997, 2001). (b) A type well from CBP dataset with sonic and density logs.....103

Figure 3.18: P-wave velocity and impedance relationship of (a) PCS-10 and (b) PCS-11. The colored dots shows samples from outcrop plugs for PCS-10, and a type well for PCS-11, whereas the blue line shows predicted P-wave impedance (I_p) from P-wave velocity (V_p), where density is estimated from velocity using Gardner’s equation (1974). The author focused on velocity modeling, since I_p is highly predictable from V_p for both outcrop and subsurface datasets.....104

Figure 3.19: P-wave velocity distribution of (a) subsurface-constrained Grayburg Formation, and outcrop-constrained Upper San Andres Formation, before (b) and after (c) adjustments. The author elevated the mean and compressed the spread per lithofacies for outcrop-constrained uSA Formation (compare b and c) in order to image a realistic uSA-Grayburg sequence boundary.....108

Figure 3.20: Three-dimensional modeling results. (a) outcrop-constrained and subsurface constrained facies model. (a) Lithostratigraphic model, (b) Facies-averaged impedance model, and (c) 0° -phase 35Hz seismic model.....110

Figure 3.21: G9 top and bottom horizon interpretation following conventional seismic stratigraphic interpretation approach. (a) and (b) show IL116 of 90° synthetic seismic ($f_d=27\text{Hz}$) before and after interpretation. (c) highlights a comparison between seismic horizon of G9 top and base against modeled G7~G13 top. (d) interpreted horizon overlying on lithostratigraphic model.112

Figure 3.22: 2D example showing the colorcode of the difference between interpretation and modeled chronostratigraphic surface, where the red represents scenarios when interpretation is shallower than modeled surface, thus an over-estimation of relative geologic time if using the seismic horizon as geologic timeline. In contrast, the blue indicates an under-estimation of relative geologic time, and the white represents a well match.113

Figure 3.23: 3D example showing evaluation method of chronostratigraphic significance of interested horizons, such as G9 HFS bottom. (a) Interpretation without smoothing, by tracking seismic peak underneath coastal onlaps. (b) Modeled stratigraphic surface of G9 HFS bottom. (c) Difference map between interpretation and model (a) and (b). Map size is 4940 by 2880 meters, contoured every 10 meters.114

Figure 3.24: XL198. (a) seismic section showing seismic horizon versus modeled G9 HFS bottom. (b) Modeled G9 MFS and bottom. Interpreted and modeled G9 MFS bottom overlying on facies (c) and impedance model.115

Figure 3.25: an alternative practical interpretation approach combining (a) partial interpretation, (b) autotracking with defined polygon and (c) interpolation. The resultant difference map (d) shows an improved overall interpretation quality, as compared with Figure 3.23(d). (e) and (f) shows comparison on IL116 and XL198.118

Figure 3.26: an alternative practical approach to interpreted G9 HFS top. The G9 HFS interpreted as a seismic trough is systematically one event higher than the modeled stratigraphic surface (as shown in Figure 3.14c, 16c and d). If interpreting the underneath seismic peak as G9 HFS, its discontinuity would result in great difficulties in interpretation. Alternatively, the author shifted the previously interpreted seismic peak for 45 meters (a), and the difference (c) between the current interpretation (a) and modeled surface (b) is within $\frac{1}{4}$ wavelength (b). Selected IL116 (d) and (e) XL198 are shown for comparison.120

Figure 4.1: Study interval and areas, highlighted on (a) a Leonardian-Guadalupian stratigraphic column and (b) Middle Permian paleogeography map (Kerans et al., 2013). Constructed in Chapter 3, Case 1 used an outcrop dataset from Last Chance Canyon (blue box), and a subsurface dataset from Central Basin Platform (blue arrow). Case 2 in this study referred to Kingdom Field interpretations (red box) and facies model observed in Apache Canyon (red arrow) for a comparison with Case 1. The author consistently used red for Case 1 and blue for Case 2 for all applicable figures.125

Figure 4.2: Case 1 datasets, including (a) a 3D lithostratigraphic model constructed in Chapter 3, as the skeleton for this study, and (b) 64 outcrop plugs from Kenter et al. (2001) for acoustic property analysis of Upper San Andres Formation. (c) wells and cores from the CBP producing field for Kerans and Sitgreaves (2015)'s facies modeling and acoustic property analysis for Grayburg-Lower Queen Formation in this study.127

Figure 4.3: Kingdom Field dataset projected on a depth structure map of Abo Formation top, which was interpolated among 99 well picks. This dataset includes a time-domain seismic volume, 166 wells, and two described cores. This author projected the 1300-m depth contour from this structure map of Abo Formation top as the terminal Abo shelf margin on the stratal slice shown in Figure 4.5a2.128

Figure 4.4: Workflow in this study for a comparative analysis of mixed carbonate/clastic (Case 1) versus pure carbonate (Case 2) shelf margin. For each case, the author modeled five different scenarios of spatial velocity distribution, and then simulated their seismic responses at three frequencies as low-, normal-, and high-frequency representations of field seismic data. Consequently, the author evaluated 30 seismic models in this study for a broad discussion on possible subsurface scenarios. 129

Figure 4.5: Comparisons between two cases for lithofacies substitution and stratigraphic adjustment. (a) A 3D comparison between (a1) Kerans et al. (2013)'s depositional model for G9 HFS of uSA Fm., and (a2) interpretation on a stratal slice along Abo Fm. top. (b) A comparison of a dip-oriented seismic section between (b1) synthetic 35Hz- 90°-phase seismic section of uSA shelf margin with overlying modeled stratigraphic surfaces (solid canyon lines), and (b2) field seismic section of Abo shelf margin, with inferred HFC clinoformal surfaces (solid canyon lines). The synthetic seismic model in (b1) was simulated from a facies-averaged velocity and density model. (c) a comparison of HFC-clinoform facies model between (c1) uSA clinoform observed in Last Chance Canyon and described by Scott (2007) and (c2) Abo clinoform observed in Apache Canyon and described by Kerans (1995).135

Figure 4.6: Described cores by Kerans (modified from internal course slides) from Kingdom Field, including (a) ML&C 77 and (b) Gordon 31 with locations shown in Figure 4.3. The lithofacies assemblage shown in these cores is similar to Kerans (1995)'s facies model for a typical HFC clinoform proposed from Apache Canyon (Figure 4.5c2), with the development of reefal boundstone in reefal shelf facies belt.136

Figure 4.7: Velocity modeling of five scenarios for Case 1, reflecting five levels of intra-facies heterogeneity. Velocity was modeled using Janson and Fomel (2011)'s method, where spatial velocity continuity is equivalent to a combination of velocity spread and spatial velocity continuity. The intermediate velocity model (S3) was constructed using experimental normalized velocity distribution per facies (Figure 4.8b) and experimentally fitted velocity variogram per zone (Table 4.1b). The four realistic end members (S1, S2, S3 and S4) were constructed by adjusting velocity distribution per lithofacies and velocity variograms for selected zones.139

Figure 4.8: Normalized velocity distribution per facies with (a) small-, (b) medium, and (c) large spread of velocity values.140

Figure 4.9: Velocity modeling of five scenarios for Case 2, reflecting five levels of intra-facies heterogeneity. Velocity was modeled using Janson and Fomel (2011)'s method, where spatial velocity continuity is equivalent to a combination of velocity spread and spatial velocity continuity. Compared with Case 1 velocity models, the author referred to same/similar lithofacies in Case 1 (Figure 5.8) to assign velocity distribution per lithofacies in Case 2. Besides, the velocity variograms for pure carbonate clinoform HFC's was assigned using that from the carbonate-dominant regressive hemicycle in uSA Formation (G9 HFS-HFC6-R, Table 4.1).142

Figure 4.10: Seismic frequency spectrum extracted from the uSA-Grayburg reservoir interval of a producing field along the Eastern flank of CBP.143

Figure 4.11: Case 1 seismic models at a dominant frequency of 13.5, 27 and 54Hz, as low-, normal-, and high-frequency representations of subsurface seismic, generated from five different levels of intra-facies heterogeneity represented as different spatial velocity variations (S1~S5).....145

Figure 4.12: Case 2 seismic models at a dominant frequency of 13.5, 27 and 54Hz, as low-, normal-, and high-frequency representations of subsurface seismic, generated from five different levels of intra-facies heterogeneity represented as different spatial velocity variations (S1~S5).....146

Figure 4.13: An example of evaluating the chronostratigraphic significance for a targeted horizon of G9 HFS bottom. (a) and (b) are dip- and strike-sections showing interpretations against modeled stratigraphy. (c) and (d) are respectively the interpretation of G9 HFS bottom following the ‘chronostratigraphic significance of seismic reflections’ and the modeled G9 HFS bottom. (e) and (g) are the original TCE map and its histogram, whereas (f) and (h) are zero-centered TCE map and histogram. The following examples all use zero-centered TCE maps and histograms to facilitate cross-comparison.149

Figure 4.14: A comparative example on interpretations of G9 HFS bottom from multi-frequency seismic volumes simulated from Case 1 - S1 velocity and density models. (a) Modeled G9 HFS bottom surface, (b)~(d) are interpretations from multi-frequency seismic volumes, whose TCE maps and histograms are respectively shown in (e)~(g) and (h)~(i).....152

Figure 4.15: Modeled G12 HFS top and its interpretations from 30 seismic models.155

Figure 4.16: Zero-centered TCE maps for G12 HFS top from 30 seismic models.156

Figure 4.17: Zero-centered TCE histograms for G12 HFS top from 30 seismic models.....157

Figure 4.18: Modeled G9 HFS bottom and its interpretations from 30 seismic models.161

Figure 4.19: Zero-centered TCE maps for G9 HFS bottom from 30 seismic models.162

Figure 4.20: Zero-centered TCE histograms for G9 HFS bottom from 30 seismic models.....163

Figure 4.21: A comparison of diachronous internal reflections within G9 HFS in 35Hz seismic models on IL135. (a1) and (b1) are Case 1 seismic models, generated from (d1) a mixed carbonate/clastic lithostratigraphic model, which was assigned with a velocity/ impedance model with S3 intra-facies heterogeneity. In comparison, (a2)~(d2) are Case-2 equivalent IL135 sections, showing (a2) and (b2) of seismic models, (c2) impedance model, and (d2) lithostratigraphic model. The dashed lines in all subplots are interpreted G9 HFS top following a +/- zero-crossing based on termination relationship (single- and double-sided arrows) interpreted in Figure (a1) and (a2) per case. The eclipses highlights zones with diachronous landward-dipping seismic reflections, whereas the white guiding solid lines aligned the same locations among different models for a convenient comparison.....166

Figure 4.22: Interpretation of diachronous landward-dipping internal HFC-scale reflectors within G9 HFS for the mixed successions at (a1) low-, (b1) medium-, and (c1) high-frequency, and for the carbonate successions at (a2) low-, (b2) medium-, and (c2) high-frequency.167

Figure 4.23: A comparison of dip for these diachronous reflectors (magenta boxes in Figure 4.22) following the shelf-margin and upper-slope reservoir trend. (a), (b) and (c) are respectively dip of these horizon patches at low-, medium-, and high-frequency, whereas (d), (e) and (f) are their histograms.168

Figure 4.24: A comparison example explaining why diachronous HFC-scale reflector is more extensive and steeper in the carbonate shelf margin in Case 2. (a) dip-oriented seismic sections, (b) impedance models, and (c) facies models.171

Figure 4.25: Data preparation for different frequency volumes as inputs for the decision tree in Figure 4.26. (a) Input seismic volume. In this case, IL116 from the normal-frequency time-domain seismic model was used for an illustration. (b)~(d) are resultant low-, medium-, and high-frequency sections from selective frequency filtering using CWT.173

Figure 4.26: A solution tree proposed based on forward modeling results in Chapter 4.175

Figure 4.27: An attribute-driven volumetric picking scheme to tie the chronostratigraphic significance of seismic reflections (quantified as TCE here) with a particular seismic attribute. Chapter 2 proves the mean of amplitude variance to be highly correlated with TCE for flat-lying siliciclastic reservoirs.176

Figure A.1: Velocity variogram analysis per HFS for subsurface constrained G10~G13 HFS of Grayburg and Lower Queen platforms. (a) experimental standardized variance map showing velocity anisotropy. (b) Experimental variogram along major (green dots) and minor orientation (magenta dots), where a spherical variogram was fitted along the minor orientation by least-square regression. (c) Manually-fitted vertical range after fixing the variogram nugget and sill from (b). (d) a table showing resultant velocity variogram parameters.....185

Figure A.2: Velocity variogram analysis for the transgressive/T-hemicycle and regressive/R-hemicycle of Sonnenfeld and Cross (1993)'s HFC6 in G9 HFS. (a) up-scaled velocity samples to the stratigraphic grid of HFC5 in G9 HFS, which contains two zones of T-hemicycle and R-hemicycle, (b) variogram models fitted by least-square regression for two zones, and (c) recorded variogram parameters.....186

Chapter 1: Introduction

In this chapter, the author starts with an introduction to the research topic on the fundamental premise of seismic stratigraphy regarding ‘the chronostratigraphic significance of seismic reflection’, its first and present applicable scales, and its values in petroleum geosciences. Subsequently, the author moves on to motivations and then specific research questions to be addressed in this dissertation. After the delineation of research questions, the author provides an overview of the experimental design with controllable variables. Finally, this chapter closes with a structure of this dissertation.

1.1 RESEARCH TOPIC AND SIGNIFICANCE IN PETROLEUM GEOSCIENCES

1.1.1 Chronostratigraphic significance of seismic reflections – the fundamental assumption for seismic stratigraphy

The year 1977 witnessed a breakthrough in petroleum geosciences, as brought by the publication of AAPG Memoir 26. Entailing the introduction of ‘seismic stratigraphy’ by Fisher et al. (1973), this volume documented in detail of the seismic stratigraphy analysis approaches by Mitchum et al. (1977a and b) and Vail et al. (1977a, b, and c). With an emphasis on chronostratigraphic analysis of reflection seismic data, it represents a landmark for seismic interpretation and provides an invaluable tool for petroleum and mineral exploration (Brown and Fisher, 1980; Posamentier and Vail, 1988; Catuneanu, 2006; Hart, 2013). In this memoir, Vail and his colleagues published their innovative techniques at Esso Production Research to interpret seismic cross-sections. Assuming seismic reflections to follow chronostratigraphic surfaces, namely stratal surfaces and unconformities (Vail et al., 1977c), one can track seismic reflection pattern as stratifications, and then delineate significant sequence boundaries from a seismic reflection image (Mitchum et al., 1977b). Subsequently, as stratigraphic information is successively

presented on the seismic image and conforms to the ‘Law of Superposition’, these interpreted seismic horizons could be linked to globally significant tectono-eustatic and eustatic events that can be dated (Vail et al., 1977b). This application further provides valuable insights into the age, distributions, and facies within depositional sequences of exploration plays (Vail et al., 1977b).

This fundamental assumption of seismic stratigraphy is also known “chronostratigraphic significance of seismic reflection”. It has two-fold of meanings. First of all, it assumes seismic reflections to follow chronostratigraphic/time-significant surfaces, including the stratigraphic surfaces following the geologic timelines, or the unconformities separating the overlying younger strata from the underlying older ones. On the other hand, this fundamental assumption for seismic stratigraphy also asserted that seismic reflections should not follow lithostratigraphic surfaces, which transect geologic timelines and thus regarded as 'diachronous'.

1.1.2 Scale of applications of this fundamental assumption: original versus present

At the time when Vail and his colleagues (1977a, b, and c; Mitchum et al., 1977a and b) proposed this fundamental assumption, they suggested two major applications, including the delineation of depositional sequences (Mitchum et al., 1977b), and the construction of chronostratigraphic correlative curve or Wheeler Diagram (1960). Assuming seismic reflections represent stratifications, one can delineate depositional sequences based upon seismic reflection terminations, such as baselap, toplap and truncation (Mitchum et al., 1977a). Furthermore, these interpretations on seismic termination relationship lead to a seismically-interpreted cross-section showing the lateral extensions of both coastal and marine deposits (Figure 1.1a). By transforming this depth-domain cross-section into the geologic-time domain (Figure 1.1b), the Wheeler Diagram

is constructed (Figure 1.1b) with a further estimated regional relative sea-level curve (blue solid line, Figure 1.1b; Vail et al., 1977a). Finally, by comparing this estimated regional curve against other regional curves around the world from areas with mature explorations, one can more confidently predict the age, distribution, and facies of depositional sequences before drilling in a seismic-covered area (Vail et al., 1977b and c). This scale of applications have turned out highly successful in petroleum and mineral exploration (Posamentier and Vail, 1988; Catuneanu, 2006; Hart, 2013) when applied to low-order (up to third-order) seismic stratigraphy (Mayer, 1979 a, b; Mayer et al., 1986).

Recent decades have witnessed a boom in the use of seismic data, when seismic reflection-based seismic stratigraphy has become a standard geophysical approach for subsurface mapping of sedimentary basins, showing responses of petrophysical interactions between seismic wave and sedimentary rocks (Grogery, 1977; Watkins and Drake, 1982; Bally, 1983; Weimer and Davis, 1996; Eberli et al., 2001). Inevitably, it gradually becomes a standard practice to extend the fundamental assumption for seismic stratigraphy regarding the 'chronostratigraphic significance of seismic reflections' from its originally-recommended applicable basinal and regional scales for exploration (Vail et al., 1977a) to a local or prospect scale for reservoir development. With the advent of the computational seismic chronostratigraphy (Stark et al., 2013), advanced geophysical algorithms such as Predicative Painting (Fomel et al., 2010) has equipped the seismic interpreters with the power to automatically and densely pick seismic events (Figure 1.1c). If assuming these densely-picked horizons as chronostratigraphic surfaces, one can further deform these automated interpretations to a seismic relative geologic time/RGT domain (Stark, 2004), and then construct a seismic Wheeler Diagram (Figure 1.1d).

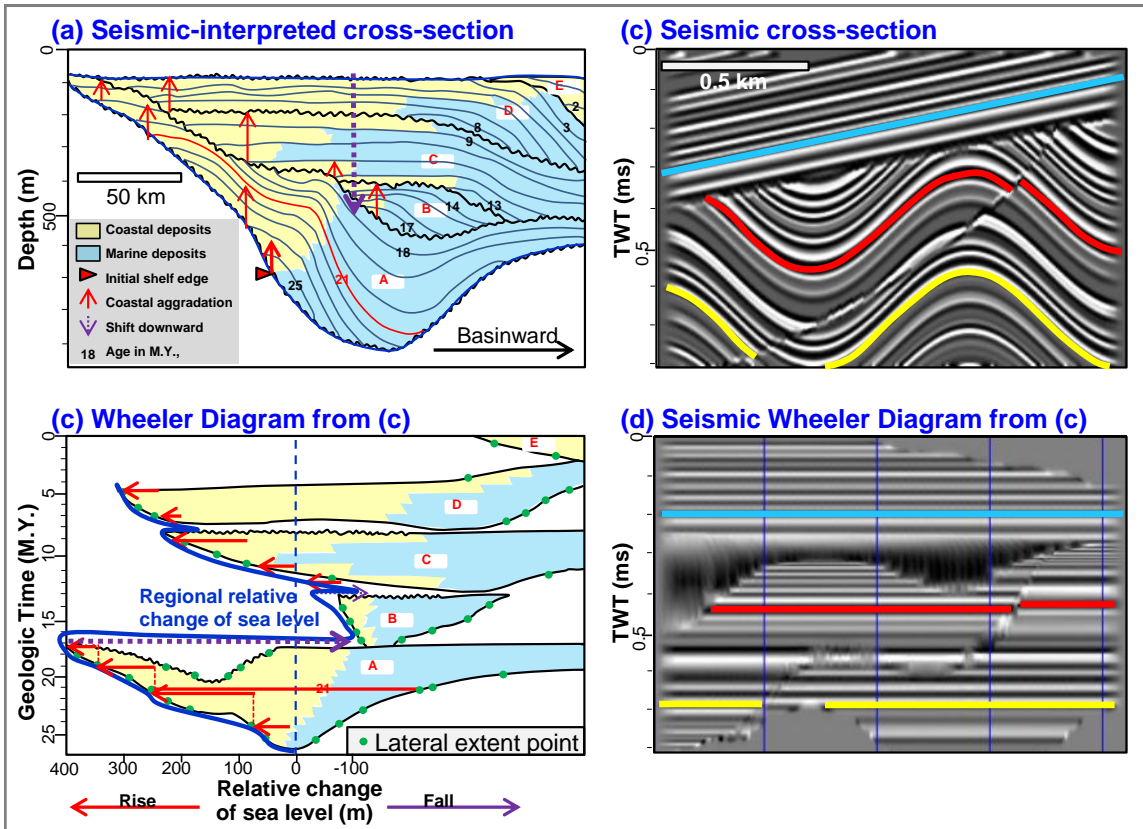


Figure 1.1: Seismic chronostratigraphic correlation applied to conventional seismic stratigraphy and modern computational seismic chronostratigraphy. Modified from Vail et al. (1977a), (a) and (b) show applications of seismic stratigraphy to interpret stratigraphic cross-section in (a), as well as Wheeler Diagram and then regional relative sea-level curve in (b). Modified from Fomel (2010), (c) and (d) present an advanced automated picking algorithm of predicative painting in computational seismic chronostratigraphy, which is capable of densely picking all seismic reflections in (c) and then reconstruct a seismic Wheeler Diagram in (d).

1.1.3 Significances of the research topic

An in-depth evaluation of the chronostratigraphic significance of seismic reflections beyond its initially recommended scale of applications would facilitate the development of computational seismic stratigraphy for reservoir-scale applications, and then contribute to the improvement of static reservoir model constructions. Upon a better

understanding of chronostratigraphic significance of seismic reflections at the reservoir scale, one can tell apart the densely-picked seismic reflections that truly honors chronostratigraphic surfaces apart from those following diachronous lithostratigraphic surfaces. This knowledge could more broadly contribute to the subsequent applications of computational seismic chronostratigraphy (Stark et al., 2013), including the trap prediction, the static reservoir model construction, the facies prediction, the thin-bed interpretation and the low-frequency model building for seismic inversion.

In terms of further applications discussed above, this dissertation focused on improving seismic chronostratigraphic correlation/ 3D horizon interpretation at HFS scale for an ultimate improvement on static reservoir model construction. During static reservoir model construction, among these seismically-derived model inputs, 3D seismic horizons at high frequency sequence (HFS) scale were presumed to be important time-markers or geologic timelines in seismic stratigraphic interpretation, and thus contribute to multiple stages of static reservoir model construction. Most directly at the stage of stratigraphic modeling/framework construction, 3D seismic horizons serve as reference surfaces for stratigraphic layering if interpreted in/converted to depth domain (Doyen, 2007). This ensures as true a representation of stratigraphic patterns and geometries as possible. Subsequently, at the stage of facies modeling, horizon-based attribute maps, if extracted from a true time surface, can provide a snapshot into a contemporaneous depositional system when integrated with cores and wireline logs (Posamentier et al., 1996; Zeng et al., 1998a, b; Posamentier and Kolla, 2003; Chopra and Marfurt, 2007). Attribute maps can also be integrated into facies modeling (Behrens et al., 1998; Yao and Chopra, 2000). In addition, at the final stage of property modeling, 3D seismic horizons can be optionally used to guide the extrapolation of wireline logs to build a low-frequency model for seismic

inversion, which further provide volumetric constraints for property estimation (Hampson et al. 2000; Chopra and Marfurt, 2007).

1.2 MOTIVATIONS AND RESEARCH QUESTIONS

1.2.1 Motivations

The author was motivated to evaluate the applicability of this fundamental assumption of seismic stratigraphy regarding the 'chronostratigraphic significance of seismic reflections' at the reservoir scale. More specifically, it refers to the scales of high-frequency sequence (HFS) and high-frequency cycle (HFC), compared with the initially recommended applicable scales up to defining a depositional sequence, which is one magnitude smaller than the supersequence (Sloss, 1963). The primary motivation herein is the increasing reported cases of failures of this fundamental assumption as applied for reservoir characterization, where the next paragraphs provide a concise review. The author is also intrigued by contemplations on Vail et al. (1977c)'s experiment design with a focus on exploration-scale validation, which calls an introduction of more variables when addressing reservoir-scale seismic stratigraphy (discussed in Section 1.3).

Discussions on whether the extension is appropriate started from concerns about seismic resolution, which is controlled by seismic frequency, as well as by acquisition, processing, and display techniques. Aigner et al. (1989) and Lawrence et al. (1990) observe differences between the seismically interpreted and the simulated buildup architectures, indicating the limitations of interpreting stratigraphic development from normal-frequency seismic data. Seismic resolution imposed a threshold that constrains the ability to define stratigraphic sequence using seismic data and to restore detailed models of the geologic history. Biddle et al. (1992) use a synthetic seismic model of outcrops to show, in low-frequency seismic, “aliased” onlapping surfaces may be present where the retrograding

platform was “still shedding sediment and no simple onlapping surface exists in the outcrops.”

Studies by Tipper (1993), Stafleu and Sonnenfeld (1994), Zeng et al. (1998), Zeng and Kerans (2003), and Hardage et al. (2007) reveal other contributors of inconsistencies between seismic reflections and geologic timelines. Tipper (1993) initializes an open debate, using the accretion dominated “unsteady sedimentation” model, which revealed “recognizable, apparently continuous reflections parallel to diachronous lithofacies boundaries.” Inspired by this study, Hardage et al. (2007) define the Tipper point for a reflection as the critical point at which the reflection begins to show a more time-transgressive/diachronous pattern. As a result, the Tipper point is jointly determined by the relative bed and interlayer thickness in wavelength units and the amount younger beds overlapping older beds. Zeng et al. (1998a) recognize basic conditions of the time transgression of a seismic event, including inadequate seismic resolution and an indented stack (en echelon or ramp) of thickness or impedance anomalies. Additional factors causing diachronous reflections, revealed by other studies, include but are not limited to complex depositional facies transitions (Stafleu and Sonnenfeld, 1994; Zeng and Kerans, 2003) and meteoric or burial-diagenetic alteration of carbonate rocks (Fournier and Borgomano, 2007).

1.2.2 Research questions

With an ultimate goal of improving the seismic stratigraphic interpretation to construct more accurate chronostratigraphic bounding surfaces for reservoir characterization, the research questions to be addressed focus on three aspects:

- For the evaluation of fundamental assumption of seismic stratigraphy at the reservoir scale, the research question to be address include (1) in what systems is it

- most appropriate? (2) And in what settings is it violated by complex 3D arrangements of lithofacies in prograding sequences?
- For the model construction of reservoir geologic model with hierarchical heterogeneity and seismic responses, the research questions to be addressed include (3) what are best techniques for modeling flat versus clinoformal stratigraphic architecture? And for facies and petrophysical properties in carbonate versus mixed successions? (4) What is the impact of intra-facies heterogeneity reflected as spatial velocity variation on seismic responses?
 - For recommendations on improving seismic chronostratigraphic correlation, the research questions to be addressed focus on what are alternative interpretation approaches if not directly picking seismic events and their suitable conditions? in cases (5) with and (6) without geoscientists' expert knowledge as critical inputs?

1.3 EXPERIMENTAL DESIGN AND CONTROLLABLE VARIABLES

1.3.1 Five variables to test at the reservoir scale

Similar to Vail et al. (1977c)'s experiment design, the author also adopted a forward modeling on geologic models as this approach allows a comparison of seismic stratigraphy against its definite and known chronostratigraphy in its input geologic model. Afterward, the author defined five variables which were less tested or insignificant for the initial validation of the chronostratigraphic significance of seismic reflections at the exploration scale (Vail et al., 1977c, p. 100~104); while can potentially influence its validity at the reservoir scale (Table 1.1).

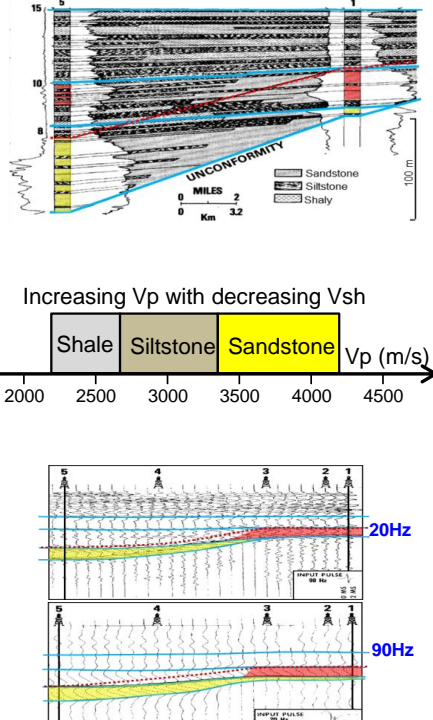
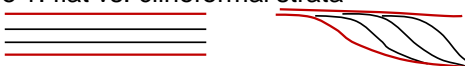

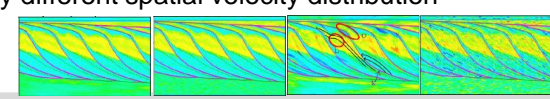
Vail et al. (1977)'s original experiment at exploration scale (up to CS)		New variables tested in this study at reservoir scale (HFS, HFC)
 <p>Increasing Vp with decreasing Vsh</p> <p>Shale Siltstone Sandstone Vp (m/s)</p> <p>2000 2500 3000 3500 4000 4500</p> <p>20Hz</p> <p>90Hz</p>	<p>Geologic model</p> <ul style="list-style-type: none"> Gently-dipping (0.36°) strata onlapping an UNC Very gentle lateral lithofacies variation (5~17 km per bed) <p>Sonic velocity model</p> <ul style="list-style-type: none"> Relatively linear lithofacies-Vp relationship in siliciclastic system No overlap between Vp per facies <p>Seismic model</p> <ul style="list-style-type: none"> Frequency-independent: works at both 20 and 90 Hz 	<p>Variable 1: flat vs. clinoformal strata</p>  <p>Variable 2: different lateral lithofacies variation</p>  <p>Variable 3: Complex lithofacies-Vp relationship in mixed and pure carbonate system</p> <p>Variable 4: intra-facies heterogeneity, represented by different spatial velocity distribution</p>  <p>Variable 5: Frequency-dependent? If so, proper interpretation strategy?</p>

Table 1.1: Five variables to be tested in this study for a reservoir-scale evaluation, compared with Vail et al. (1977c)'s original experiment design targeted at exploration scale.

During geologic modeling, Vail et al. (1977) designed an example of gently-dipping (0.36°) strata onlapping an angular unconformity, with very gentle lateral lithofacies variation containing laterally-extensive sandstone, siltstone and shale beds of 5~17 kilometers. Therefore, this dissertation further works on the validity of the 'chronostratigraphic significance of seismic reflections' on

- clinoformal versus flat stratal geometry (Variable 1)
- fast versus gentle lateral lithofacies variation (Variable 2)

As for the sonic velocity model as an input seismic modeling, the previous experiment does not explicitly include sonic velocity modeling details. Instead, it included the range of velocities per lithofacies. The high-velocity sandstone, medium-velocity siltstone and low-velocity shale in the pure siliciclastic system respectively has a velocity range from 3,300 to 4,200m/s, 2,700 to 3,300 m/s and 2,200 to 2,700 m/s. In general, this lithology-sonic velocity/acoustic impedance relationship is relative simple, with increasing sonic velocity responding to decreasing shale contents, as well as no overlap of velocity distribution among different lithofacies. This dissertation further probe into the validity of the 'chronostratigraphic significance of seismic reflections' on

- more complex lithofacies-sonic velocity relationship in mixed carbonate/clastic and carbonate system (Variable 3)
- different spatial velocity variation, as a combination of velocity value spread and spatial continuity (Janson and Fomel, 2011) to reflect intra-facies heterogeneity (Variable 4). He et al. (2015) studied its impact on HFS- and HFC-scale seismic chronostratigraphic interpretation upon a simplified 2D model of strongly-prograding mixed carbonate/clastic clinoforms, and illustrated the different associated challenges in interpreting both time-significant HFS boundaries and

diachronous lithofacies boundaries separating zones of contrasting petrophysical properties.

The last but not the least, Vail et al. (1977c) simulated vertical-incidence synthetic seismic models at 20- and 90-Hz, as representations of comparable subsurface normal- and high-frequency seismic sections from South America. In these seismic models, the interpreted seismic horizons follow the chronostratigraphic surfaces (Horizon 8, 10, 15 and UNC, Table 1.1), and can both tell apart the sandstones of different ages (shaded in yellow and orange, Table 1.1). Therefore, the proposal of 'chronostratigraphic significance of seismic reflections' indicates its frequency-independent nature for exploration-scale applications. The author's doubts on it first originates from He and Zeng (2014a)'s experiment on a duplicated Vail et al. (1977c) geologic section, where they observed apparent diachronous reflections following lithostratigraphic surfaces in both an intermediate-frequency (40Hz) and a low-frequency (8Hz) seismic model. Thus this study further tested

- the frequency-dependency for the 'chronostratigraphic significance of seismic reflections' (Variable 5) – would an intuitive solution on increasing seismic frequency help improve the seismic chronostratigraphic interpretation? If yes, what are its applicable conditions? If no, would any other alternative interpretation strategies contribute to improving this seismic chronostratigraphic correlation?

1.3.2 An overview of experimental design

In this study, the author probe into these five variables (Table 1.1) using a forward seismic modeling upon high-resolution geologic models with known chronostratigraphic framework. The standard workflow (Figure 1.2) used in this study contains a forward seismic modeling workflow, followed by an evaluation workflow on the validity of the

fundamental assumption of seismic stratigraphy as applied to high-order seismic stratigraphy. Despite the variations in the selection of geostatistical modeling methods and the different levels of integrations with other multi-scale constraints (such as LIDAR data, wireline logs, cores, and field analogs) during geologic, acoustic property and seismic forward modeling workflow, the overall evaluation workflow remains consistent. It typically includes the geologic modeling, petrophysical modeling, and eventually seismic modeling, followed by an optional further calculation of seismic attributes.

During the assessment/evaluation, the author interpreted the resultant synthetic seismic models by following seismic reflections as stratifications for reflection termination relationship, upon which a further delineation of HFS boundaries proceeds. The author then compared an interested interpreted seismic horizon following the 'chronostratigraphic significance of seismic reflections' with its modeled corresponding chronostratigraphic surface, by calculating their difference between the interpretation and the model. We termed this difference as 'time-correlation error/TCE' in this study, as it serves as a good indicator for using a given seismic horizon as a 'time-significant' surface: the less this TCE, the more valid the 'chronostratigraphic significance of this seismic reflection' is. Chapter 2 gives an introductory example for the calculation of TCE for both a single horizon and a densely-picked horizon volume, as well as how this concept in the forward modeling studies can tie to field applications.

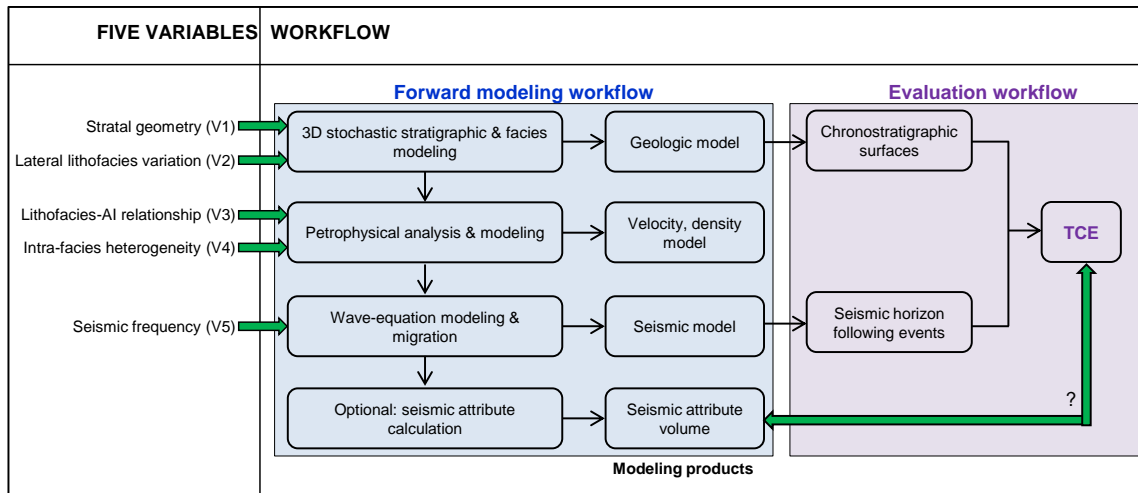


Figure 1.2: An overview of experiment design, containing a forward modeling and evaluation workflow, and five predefined controllable variables.

1.4 STRUCTURE OF THIS DISSERTATION

This dissertation is composed of five chapters:

Chapter 1 reviews the significance of seismic stratigraphy in petroleum geosciences, the research topic on testing the validity of its fundamental assumption regarding the chronostratigraphic significance of seismic reflections. It also introduces an overview of experiment design and controllable variables, followed by the structure of this dissertation.

As there is not a single geologic model to exclusively address all these five variables, the author designed three interconnected experiments (Figure 1.2), which will be addressed as stand-alone chapters in this dissertation in Chapter 2 to 4.

- Chapter 2 serves as an introductory case for the entire dissertation project (Figure 1.3a). In this study, the author constructed a series of the conceptual siliciclastic reservoir models using a fluvial-shallow marine dataset in Starfak Field, GoM. The author chose this geologic setting due to (1) its relatively flat-lying simple stratigraphy, and (2) an eligibility of using acoustic impedance as a proxy of

lithofacies variation for a reduction of variables to be discussed. These simplifications further allow a focused discussion on the influence of the lateral lithofacies variation (Variable 2), as well as seismic frequency (Variable 5). Furthermore, the author established an evaluation scheme for the chronostratigraphic significance of seismic reflections, which applies both for a single interested seismic horizon, and a horizon volume with a pile of densely-picked horizons. Finally, the author implemented some initial search for a potential seismic attribute to predict the chronostratigraphic significance of a seismic reflector and established an attribute-driven volumetric picking scheme for a future field application.

- Chapter 3 inherited the evaluation scheme on the chronostratigraphic significance of seismic reflections, by applying it to a real data to evaluate a particular HFS (G9 HFS in PCS-10) for a mixed carbonate/clastic reservoir equivalency of Upper San Andres-Grayburg reservoirs in the Permian Basin (Figure 1.3b). Advancing from the conceptual models in Chapter 2, Chapter 3 honors the published 3D depositional model, discrete high-resolution measured sections/cores, and continuous lateral constraints of stratigraphic contacts, so that it makes a real-world case, by honoring the reservoir geology of Upper San Andres-Grayburg reservoirs as carefully as possible. More specifically, the outcrop data set at Last Chance Canyon, Guadalupe Mountains, allows a characterization of complex clinoformal stratigraphy up to HFC scale of Upper San Andres shelf margin. In comparison, the subsurface data set from a producing field of Central Basin Platform allows a modeling of complex lithofacies variation within relatively flat-lying strata of Grayburg and Lower Queen Formation. Finally, the author simulated a single seismic model from a facies-averaged velocity and density model, and applied an evaluation on the G9

- HFS top and bottom, which can commonly serve as bounding surfaces for modeling Upper San Andres mixed carbonate/clastic shelf and shelf-margin reservoirs.
- Chapter 4 utilized the skeleton of the 3D lithostratigraphic model from Chapter 3 for a broader discussion on multiple variables potentially influencing the chronostratigraphic significance of seismic reflections. First of all, the author applied a 3D lithofacies substitution on the siliciclastic-rich lithofacies and stratigraphic adjustments on the 3D lithostratigraphic model from Chapter 3 (Case 1), for the sake of constructing a carbonate reservoir model analogous to Early Permian Abo shelf margin - Clear Fork platform (Case 2, Figure 1.3c). The subsurface interpretations of Abo Formation from Kingdom Field in Terry and Hockley County of West Texas provides critical references for this comparative study, whereas the outcrop studies from Apache Canyon provides insights on facies model. Resultantly, this pair of mixed carbonate/clastic and pure carbonate reservoir shelf margin - platform models allow an evaluation of the influences from flat versus clinoformal stratal geometry (Variable 1), respectively with gentle and fast lateral lithofacies variation (Variable 2). Besides, these two cases also represent situations with complicated lithofacies-sonic velocity relationship in mixed carbonate/clastic successions and carbonate successions. During velocity modeling, instead of assigning a constant velocity-density pair per lithofacies in Chapter 3, the author evaluated five different spatial velocity variations ($S_1 \sim S_5$) to reflect intra-facies heterogeneity (Variable 4). Finally, the author simulated seismic models at low-, medium-, and high-frequency (Variable 5) referring to a frequency spectrum from a producing field at the reservoir interval. The evaluations focused on HFS surfaces such as the flat-lying G12 HFS top and clinoformal G9 HFS bottom. Moreover, the author also compared the HFC-scale diachronous reflections

that follow porous reservoir-prone lithofacies in mixed and carbonate successions. Finally, the author addressed potential field applications based on main learnings from the forward modeling studies in this dissertation, in scenarios with or without sufficient geoscientists' expert knowledge.

At this stage, Chapter 4 has summarized the influences of five predefined variables from Chapter 1 on the chronostratigraphic significance of seismic reflections at the HFS and HFC scale, as well as discussed potential field applications upon main learnings from the forward modeling results from Chapter 2 to 4. Herein, Chapter 5 only provides a brief summary of conclusions, followed by two directions of suggested future works.

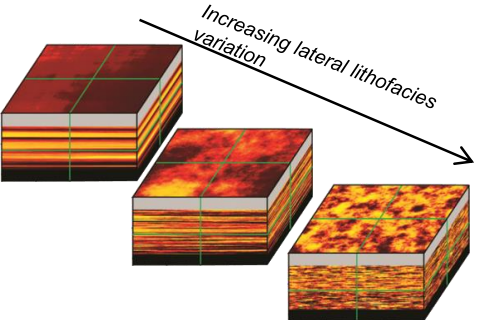
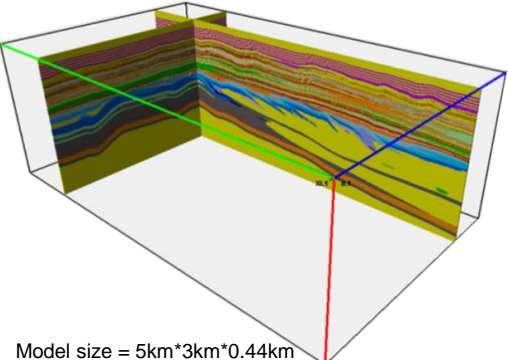
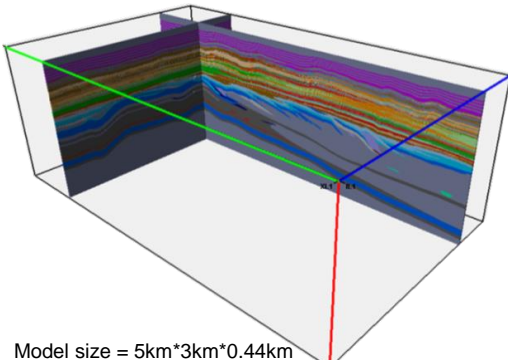
(a) Chapter 2: an introductory example	(b) Chapter 3: an outcrop- and subsurface-based example	(c) Chapter 4: a discussion of multiple variables
<p>Overview</p> <p>Conceptual siliciclastic reservoir models with simple flat-lying stratigraphy, constrained by</p> <ol style="list-style-type: none"> (1) Well-based characterization 	<p>Mixed carbonate/clastic reservoir equivalency with complex stratigraphy, constrained by</p> <ol style="list-style-type: none"> (1) Digital outcrop model (2) Integrated subsurface characterization 	<p>Mixed carbonate/clastic (Case 1) & carbonate (Case 2) reservoir equivalency and analog, constrained by</p> <ol style="list-style-type: none"> (1) Outcrop analog by lithofacies replacement (2) Integrated subsurface characterization
<p>Study interval & area</p> <p>Miocene interbedded sandstone-shale interval</p> <ol style="list-style-type: none"> (1) Starfak Field, GoM 	<p>Permian San Andres-Grayburg shelf margin</p> <ol style="list-style-type: none"> (1) Last Chance Canyon, Guadalupe Mountains (2) A producing field, Central Basin Platform, Permian Basin 	<p>Permian Abo shelf margin</p> <ol style="list-style-type: none"> (1) Apache Canyon analog, Sierra Diablo Mountains (2) Kingdom Field, NW shelf, Permian Basin
<p>2D/3D geological and seismic models</p>  <p>Model size = 1km*1km*200ms</p>	 <p>Model size = 5km*3km*0.44km</p>	 <p>Model size = 5km*3km*0.44km</p>
<p>Objectives</p> <p>An introductory example to establish an evaluation scheme and conduct feasibility analysis</p> <ol style="list-style-type: none"> (1) Evaluate the influence by Variable 2 and 5 (2) Investigate the feasibility of using seismic attributes to approximate TCE 	<p>Extend the established evaluation scheme to real data on a normal-frequency seismic model to</p> <ol style="list-style-type: none"> (1) Model hierarchical heterogeneity (2) Implement a case study on G9 HFS top and bottom 	<p>Discuss multiple variables on the seismic chronostratigraphy at the HFS and finer scale</p> <ol style="list-style-type: none"> (1) Evaluate the influence of Variable 1~5 (2) Discuss on practical approaches in improving the seismic chronostratigraphic interpretation

Figure 1.3: Focus of three dissertation projects. Chapter 2 to 4 presents these projects as stand-alone elements. Note their interrelations as stated in objectives.

Chapter 2: An introductory example – conceptual siliciclastic reservoirs with flat-lying stratal geometry

This chapter presented a conceptual example of Miocene fluvial-marine siliciclastic reservoir in Starfak Field, GoM¹. This study area was chosen as the introductory example for this dissertation, due to its simple flat-lying stratal geometry, along with its relatively explicit lithology–impedance relationship, which allows an approximation of low-impedance unit as reservoir-prone facies of porous sandstone. These simplifications allow the author to focus on evaluating the influence on the chronostratigraphic significance of seismic reflections from two variables, including the lateral lithofacies continuity/reservoir continuity and the seismic frequency. A series of geologic model with increasing lateral lithofacies variation were constructed, succeeded by seismic simulation at multiple frequencies.

The time-correlation error (TCE) is defined as the difference between seismic events and relative geologic time (RGT). A series of statistically simulated impedance models with flat chronostratigraphic surfaces was generated from a subsurface data set to describe gradual lithofacies changes in contemporaneous strata and to account for vertical cyclicity from seed wireline logs. The author converted these models to realistic seismic records using an exploding-reflector algorithm. The TCE from the seismic models was positively correlated to the lateral impedance variation, in which the TCE magnitude for a model of complex impedance variation could be quite significant. For example, a maximum, two-event, 32.5-m TCE had been observed in a small 1 × 1-km model. An increase in wavelet frequency in general reduced the TCE and improved the seismic chronostratigraphic correlation. In addition, a preliminary test confirmed that amplitude

¹Figures and major contents of this chapter were from He et al. (2015a), being published in Interpretation Journal on May 2015 (v. 3, no.2, p. SN69-SN87, doi: 10.1190/INT-2014-0136.1.

variance in the seismic model was related to lateral impedance variation and could be used to predict TCE. Therefore, certain attributes (such as amplitude variance) were useful in developing tools for generating TCE-based, hybrid, and RGT volumes from field seismic data. This strategy integrated the advantages, and avoided the disadvantages, of the present methods.

2.1 INTRODUCTION

The seismic-stratigraphy analysis approach of Mitchum et al. (1977a and b) and Vail et al. (1977a, b, and c), with an emphasis on chronostratigraphic analysis of reflection seismic data, represents a landmark for seismic interpretation and provides an invaluable tool for petroleum and mineral exploration (Posamentier and Vail, 1988; Catuneanu, 2006; Hart, 2013). Vail et al. (1977a) propose that stratigraphic information is successively presented in seismic images and conforms to the law of superposition. To the extent that seismic reflections are assumed to follow chronostratigraphic surfaces (stratal surfaces and unconformities), seismic data can be linked to globally significant tectonoeustatic and eustatic events providing valuable insights into the age, distributions, and facies of depositional sequences of exploration plays (Vail et al., 1977b). Seismic reflections are chronostratigraphically significant or time significant when they represent stratal surfaces that are isochronous in geologic time scale or unconformities that are important markers separating younger strata from older rocks. In contrast, lithostratigraphic surfaces transact geologic timelines and are time transgressive or diachronous.

Vail et al.'s (1977c) fundamental assumption of chronostratigraphic significance of seismic reflections was applied successfully to low-order (third- or lower order sequences) seismic stratigraphy (e.g., Mayer et al., 1986; Eberli et al., 2002). Vail et al. (1977c) expect all reflections to follow chronostratigraphically significant surfaces with a

chronostratigraphic correlation error of approximately $+1/2$ wavelength (one peak or trough of seismic events). In conventional, low-frequency (20–50 Hz) seismic data, thick depositional sequences are adequately imaged by reflection configuration and geometry, as long as the thickness reaches two to three wavelengths. As a result, seismic reflections have chronostratigraphic meaning at large scale (Macurda, 2012). These practices successfully applied to lower order seismic stratigraphy, at the regional/basinal scale, primarily include the delineation of depositional sequence (Mitchum et al., 1977b) and the construction of chronostratigraphic correlation curves.

In recent decades, the seismic-stratigraphy approach has been extended, with some controversy, from basinal and regional scale to prospect and reservoir scale (<50 m). Discussions on whether the extension is appropriate started from concerns about seismic resolution, which is controlled by seismic frequency, as well as by acquisition, processing, and display techniques. Aigner et al. (1989) and Lawrence et al. (1990) observe differences between the seismically interpreted and the simulated buildup architectures, indicating the limitations of interpreting detailed stratigraphic development from normal-frequency seismic data. Seismic resolution imposed a threshold that constrains the ability to define stratigraphic sequence using seismic data and to restore detailed models of the geologic history. Biddle et al. (1992) use a synthetic seismic model of outcrops to show, in low-frequency seismic, “aliased” onlapping surfaces may be present where the retrograding platform was “still shedding sediment and no simple onlapping surface exists in the outcrops.”

Studies by Tipper (1993), Stafleu and Sonnenfeld (1994), Zeng et al. (1998), Zeng and Kerans (2003), and Hardage et al. (2007) reveal other contributors of inconsistencies between seismic reflections and geologic timelines. Tipper (1993) initializes an open debate, using the accretion dominated “unsteady sedimentation” model, which revealed

“recognizable, apparently continuous reflections parallel to diachronous lithofacies boundaries.” Inspired by this study, Hardage et al. (2007) define the Tipper point for a reflection as the critical point at which the reflection begins to show a more time-transgressive/diachronous pattern. As a result, the Tipper point is jointly determined by the relative bed and interlayer thickness in wavelength units and the amount younger beds overlapping older beds. Zeng et al. (1998a) recognize basic conditions of the time transgression of a seismic event, including inadequate seismic resolution and an indented stack (en echelon or ramp) of thickness or impedance anomalies. Additional factors causing diachronous reflections, revealed by other studies, include but are not limited to complex depositional facies transitions (Stafleu and Sonnenfeld, 1994; Zeng and Kerans, 2003) and meteoric or burial-diagenetic alteration of carbonate rocks (Fournier and Borgomano, 2007). In summary, time-transgressive reflections may be expected when geologic timelines are flat and dipping (Figure 1, compare Figure 1a and 1b) and in prograding, or retrograding, settings (Figure 1, compare Figure 1b and 1c).

In the era of “computational seismic chronostratigraphy” (Stark et al., 2013), an entire 3D seismic volume can be processed to generate a relative geologic time (RGT) volume (Stark, 2004), in which an arbitrary isosurface is ostensibly comprised of a single RGT. At present, there are two different ways to build an RGT volume, following the alternative views on the chronostratigraphic nature of seismic events. Applying the assumption of Vail et al. (1977c), one can pick seismic events manually followed by interpolation or, alternatively, one can use an autotracking algorithm to generate RGT (horizon) slices that strictly follow an equal phase (event). Many innovative methods have been developed to automatically flatten seismic events for an RGT volume (Stark, 2004; Groot et al., 2006; Lomask et al., 2006; Bruin et al., 2007; Fomel, 2010). Acknowledging that some seismic events have a tendency to be diachronous, phantom slices (time slice,

horizon slice, and stratal or proportional slice) do not necessarily follow an equal seismic phase, yet they still honor geologic timelines. In particular, the stratal-slicing approach (Zeng, 1994; Zeng et al., 1998a, 1998b) applies a linear interpolation model among selected geologic time-equivalent seismic reference events to generate proportional slices (Posamentier et al., 1996) for an RGT volume.

Here, the author developed the foundation of a hybrid scheme that sufficiently integrates tracked time-equivalent seismic surfaces and phantom stratal surfaces by starting from impedance models with known flat chronostrati-graphic surfaces (similar to Figure 1a). To validate such a scheme, the author tested two assumptions: that (1) the quality of seismic chronostratigraphic correlation can be measured and (2) this measurement can be correlated with certain seismic attributes. The author defined a measurement for seismic chronostratigraphic correlation, and the author observed how it responds to stratigraphic and lithofacies complexity, as well as the seismic frequency. Last, an example is provided to suggest a potential linkage between the proposed measurement and a particular seismic attribute, which may lead to the future development of an automatic hybrid method to better represent seismic information on geologic time surfaces.

2.2 METHODS

For this study, the author started by building geologic/lithofacies models with a known flat chronostratigraphic relationship. A set of geologic models with various geologic complexities are required for systematic consideration of the chronostratigraphic meaning of primary seismic reflections. In addition, these various geologic complexities were expected to incorporate reservoir-scale heterogeneity. These two requirements were satisfied by adjusting the lateral lithofacies variation/discontinuity between the same set of seed wells. In this experiment, the Gaussian random function simulation (GRFS) (Daly et

al., 2010) was applied to generate lithofacies models; by decreasing the lateral correlative distance/range of an input variogram, models with increasing lateral lithofacies variation/discontinuity were built.

The input of seismic simulation requires the property of acoustic impedance (AI) as a product of velocity and density. The relationship between AI and petrophysical properties can be complicated because the velocity alone can be case-by-case dependent on multiple factors, including mineral composition, porosity and pore type, diagenesis, etc. (Christensen and Szymanski, 1991; Marion et al., 1992; Vernik and Nur, 1992; Anselmetti and Eberli, 1993, 1997, 2001). In this study, the author assumed a linear relationship between AI and effective porosity, on the basis of a reported observation of wireline log data in a Gulf Coast Miocene study (Zeng et al., 2001), in which AI was negatively correlated with the effective porosity. Then, the author generated synthetic models using the exploding-reflector algorithm (Loewenthal et al., 1976), which simulates wave propagation in 3D and thus produces more realistic records than do convolution models. Afterward, considering the thin-bedded nature of sandstone and shale beds in models of this study, synthetic records were shifted 90°-phase, for an easier visual linkage between an impedance unit and a seismic event (Zeng and Backus, 2005a, 2005b).

After generating models of various complexities and their seismic records, the author defined a measurement on the quality of seismic chronostratigraphic correlation and studied its responses to multiple variables. This measurement, called the time-correlation error (TCE) herein, was defined to quantitatively describe to what extent seismic reflections depart from geologic timelines. Using prepared models of various complexities with a definite chronostratigraphic relationship, the author analyzed how TCE responds to lateral impedance variation and seismic frequency.

2.3 MODEL DESIGN: IMPEDANCE AND SEISMIC MODELS

Various modeling techniques exist to simulate different geologic complexities. Early models for seismic simulation include simple conceptual models (e.g., Meckel and Nath, 1977; Neidell and Poggiagliolmi, 1977; Schramm et al., 1977; Tipper, 1993) featuring simplified facies with constant AI and stratigraphic surfaces designed in 2D with simple geometries. Honoring the more confidently mapped/correlated surfaces and using AI from the subsurface analog, more realistic outcrop and subsurface models were introduced to simulate geologic complexities (e.g., Biddle et al., 1992; Zeng et al., 1994). Again, the assignment of the AI property remained constant for each facies. The introduction of statistical stratigraphic and reservoir models (Issaks and Srivastava, 1989; Goovaerts, 1997; Dubrule, 1998) could be perceived as an improvement, by honoring AI variations within each facies in a predefined range. The author designed statistical models in 3D to investigate the chronostratigraphic significance of seismic reflections, replacing conceptual or “layer-cake” models commonly used for this topic. Statistical models can better describe gradual lithofacies changes in contemporaneous strata and avoid unnatural seismic diffractions at abrupt lithofacies boundaries seen in other models. Additionally, statistical models can account for vertical cyclicity from seed wireline logs, which are usually disregarded in non-statistical models.

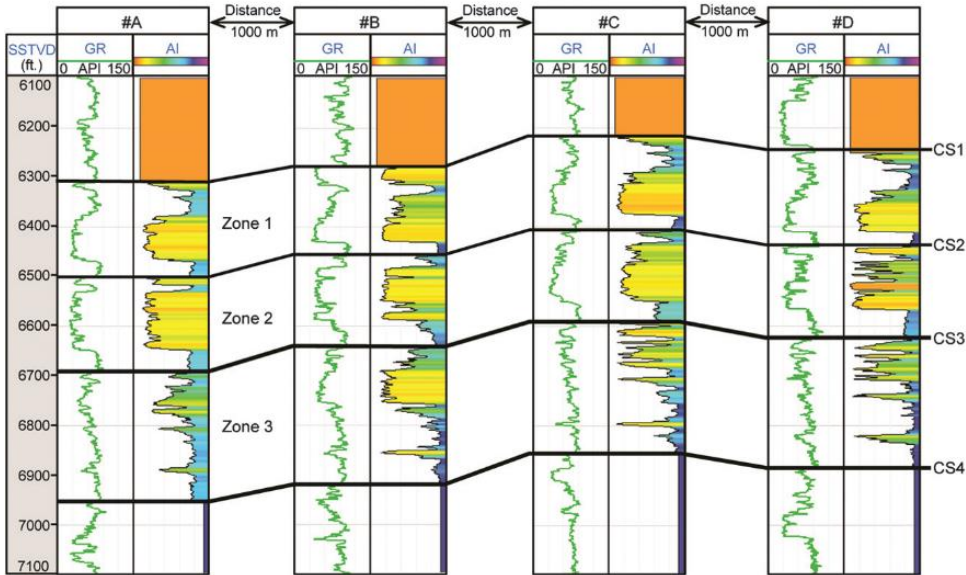
2.3.1 Impedance models

As the input for the statistical AI models, four seed wells (A, B, C, and D) were selected from the upper Miocene Starfak Field, offshore Louisiana (Figure 2.1). The selected interval (1860–2164 m [6100–7100 ft]) is fluvial -shallow marine in origin (Hentz and Zeng, 2003). Seismic and wireline correlations (cs1–cs4, Figure 2.1a) show no unconformities or discordant surfaces along the seed wells; thus, the three stratigraphic zones (zones 1–3) are considered chronostratigraphic units. In this sandstone/shale

sequence, a measured relationship between AI and lithology in a Gulf Coast field (Zeng et al., 2001) was adopted, which shows AI to be linearly related to effective porosity (ϕ_e). As a result, variation in impedance reflects complexity of lithofacies.

To simulate a definite flat chronostratigraphic relationship in this study, the author applied a depth to time conversion and a slight stretching or compression. The wireline logs were converted to two-way traveltime (TWT). To simplify the modeling and interpretation, the four chronostratigraphic surfaces (cs1–4), along with the three stratigraphic units (zones 1–3), were flattened (Figure 2.1b). This adjustment removes the structural background with limited changes to thickness (Figure 2.2a). Wireline logs experienced little distortion within 5% in terms of time thickness during the adjustment (Figure 2.2b). In the new adjusted correlation scheme, all simulated chronostratigraphic surfaces/geologic timelines are flat in TWT. The local dip of a reflection is indicative of the magnitude of time transgression (Figure 2.2c), as explained later in the section “Results and interpretations.”

a) Original well correlation



b) Adjusted well correlation

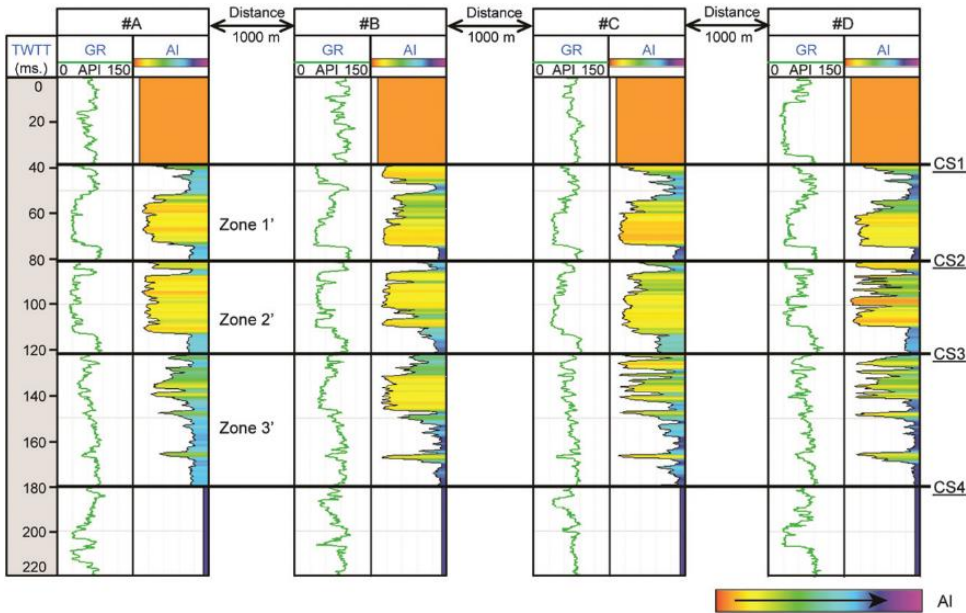


Figure 2.1: Correlation between seed wells. (a) Original correlation in subsea true vertical depth. Interpreted chronostratigraphic surfaces (cs1–4) defined three chronostratigraphic units (zones 1–3) and (b) adjusted correlation in TWT. Flattened chronostratigraphic surfaces (cs1–4) bounded three slightly compressed/ stretched chronostratigraphic units (zones 1'–3'). The AI for sandstone is lower in this study.

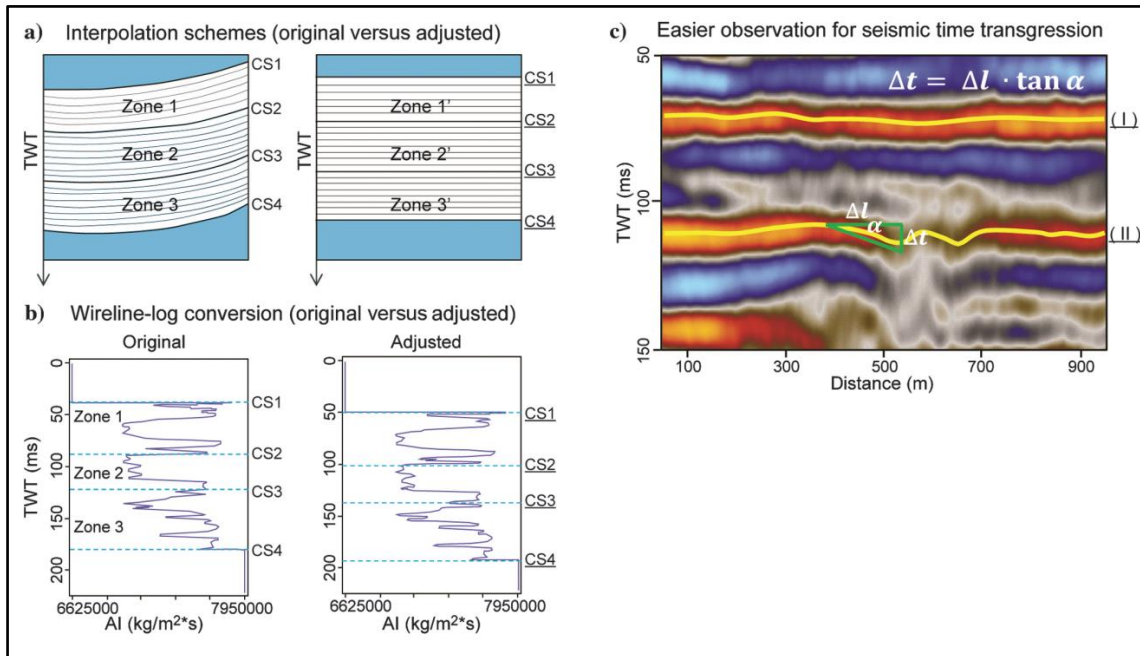


Figure 2.2: A 2D illustration of the interpolation scheme used in this study. (a) Conversion from the original scheme (left) to the correlation scheme (right), where all chronostratigraphic layering (gray solid lines) is horizontal. (b) Little wireline-log distortion resulted during the conversion (average of 2% for each zone). The original and adjusted chronostratigraphic surfaces (cs1–4 and cs1–4) are marked with dashed orange lines, and (c) the adjusted scheme facilitates easier observation of seismic time transgression. Time transgression Δt is proportional to dip α (compare I and II).

Using the same four seed impedance logs and the same adjusted correlation scheme discussed above, impedance models of variable complexities (Figure 2.3) were simulated using GRFS (Daly et al., 2010). The lateral impedance variation, which is related to the lithofacies complexity in this study, could be adjusted by changing the correlative distance/range of the input variogram (Figure 2.3a). By reducing the lateral range in the input variogram, more lateral impedance variation/discontinuity is simulated (Figure 2.3b–2.3d).

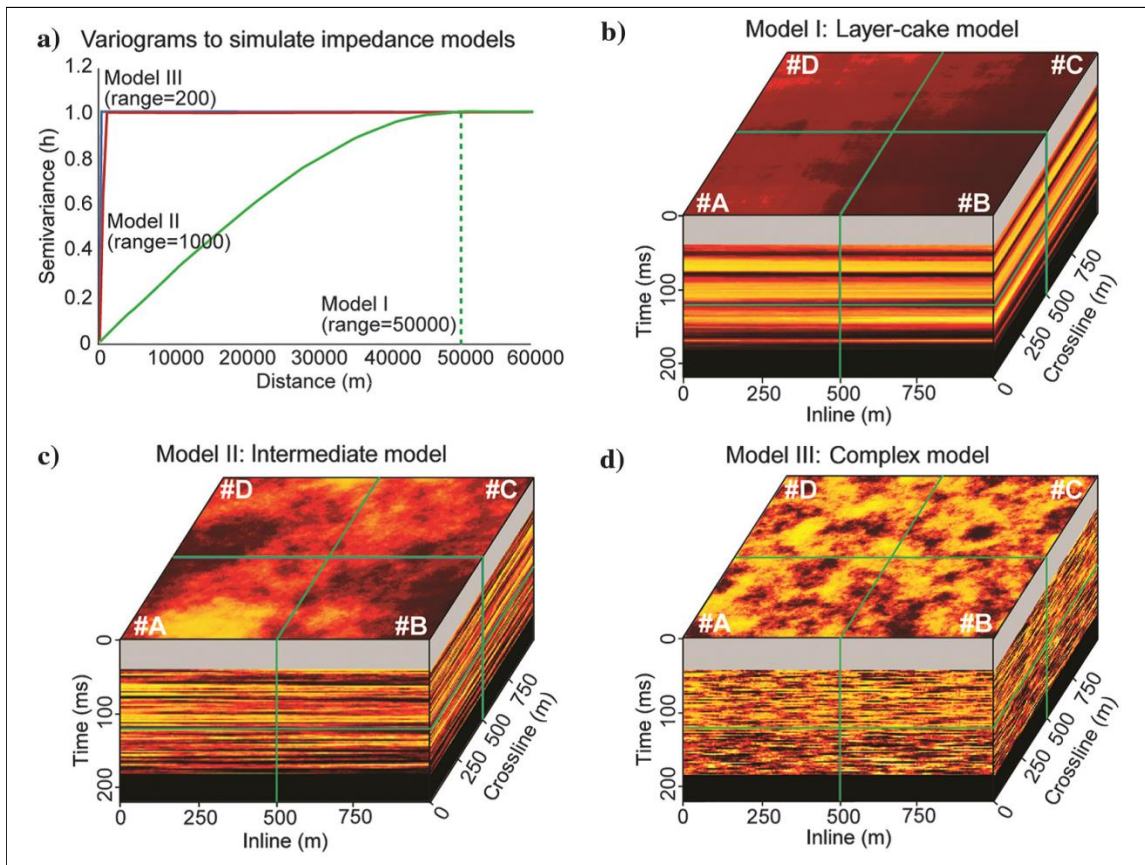


Figure 2.3: Impedance models with increasing lateral lithofacies variation. (a) Variograms to simulate impedance models via GRFS. Given the same seed wells (A, B, C, and D), the decreased lateral range in the input variogram produces increased lateral impedance complexity. (b) Layer-cake model I, generated with a lateral correlative distance/range of 50,000 m, 50 times its model size (1000 m). (c) Intermediate model II, generated with a lateral range of 1000 m. (d) Complex model III, produced with a lateral range of 200 m.

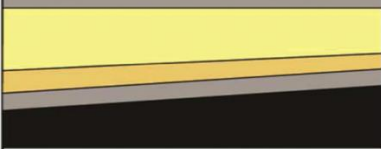
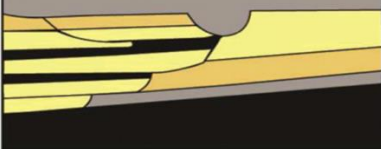

Conceptual model	Descriptions
a) Layer-cake reservoir type 	Distinct layer with marked continuity and gradual thickness variation
b) Jigsaw puzzle reservoir type 	Different sand bodies fitting together without major gaps
c) Labyrinth reservoir type 	Complex arrangements of sand pods and lenses, often appearing discontinuous in sections

Table 2.1: Engineering description of geologic complexity (Weber and van Geuns, 1990). The reservoir heterogeneity is characterized by different extents of lateral lithofacies discontinuity/variation.

These simulated models resemble the Weber and van Geuns' (1990) engineering description of reservoir heterogeneity (Table 2.1). The layer-cake model (model I, Figure 2.3b) is similar to their layer-cake reservoir type, featuring distinct layering with marked continuity and gradual thickness variation. The intermediate model (model II, Figure 2.3c) resembles their "jigsaw-puzzle" reservoir type, in which different sand bodies fit together without major gaps. The complex model (model III, Figure 2.3d) is analogous to the labyrinth reservoir type, in which sand pods and lenses are complexly and discontinuously arranged.

2.3.2 Seismic models

The author applied a noise-free, exploding-reflector algorithm (Loewenthal et al., 1976) to generate seismic responses from the impedance models (Figure 2.3b–2.3d). A built-in package from the open-source geophysics software Madagascar (Janson and

Fomel, 2011) was used. The extended split-step method (Kessinger, 1992) was used to implement wave propagation in the frequency domain. One merit of this approach was the accommodation of lateral slowness variation, by introducing multiple reference slowness logic to the split-step Fourier method (Stoffa et al., 1990). Besides, compared with the conventional, idealized 1D convolution model, this wave-equation-based model simulates wave propagation in 3D and produces more realistic seismic records, especially in cases in which the geologic model is complex with many small, patchy impedance anomalies (Figure 2.4). More specifically, for a layer-cake impedance model (Figure 2.3b), convolutional and exploding-reflector modeling work well (Figure 2.4a). However, for an intermediate model (Figure 2.3c), seismic records modeled by the exploding-reflector modeling look more realistic, and they have enhanced horizon continuity (Figure 2.4b). For a complex model (Figure 2.3d), seismic records modeled by the convolution modeling will be even more chaotic and too noisy to apply autotracking in the following experiments.

Because most of the sandstone and shale units in the seed wells are below seismic resolution limits at examined frequencies (Figure 2.5), a 90°-phase shift was applied to the synthetic records to improve the correlation between amplitude/polarity and relative AI/lithology (Figure 2.6). Interpretive advantages of the 90° phase wavelet for thin beds are discussed by Zeng and Backus (2005a, 2005b). In a 90°-phase seismic model, the center of a high-impedance unit is expressed as maximum amplitude (compare Figure 2.6a and 2.6b). In comparison, in a zero-phase seismic model, the top and bottom of each unit are, respectively, represented by a peak and a trough (compare Figure 2.6a and 2.6c). Therefore, the 90°-phase seismic models were used because of this straightforward correlation to the impedance model. Therefore, the 90°-phase seismic models were used because of this straightforward correlation to the impedance model.

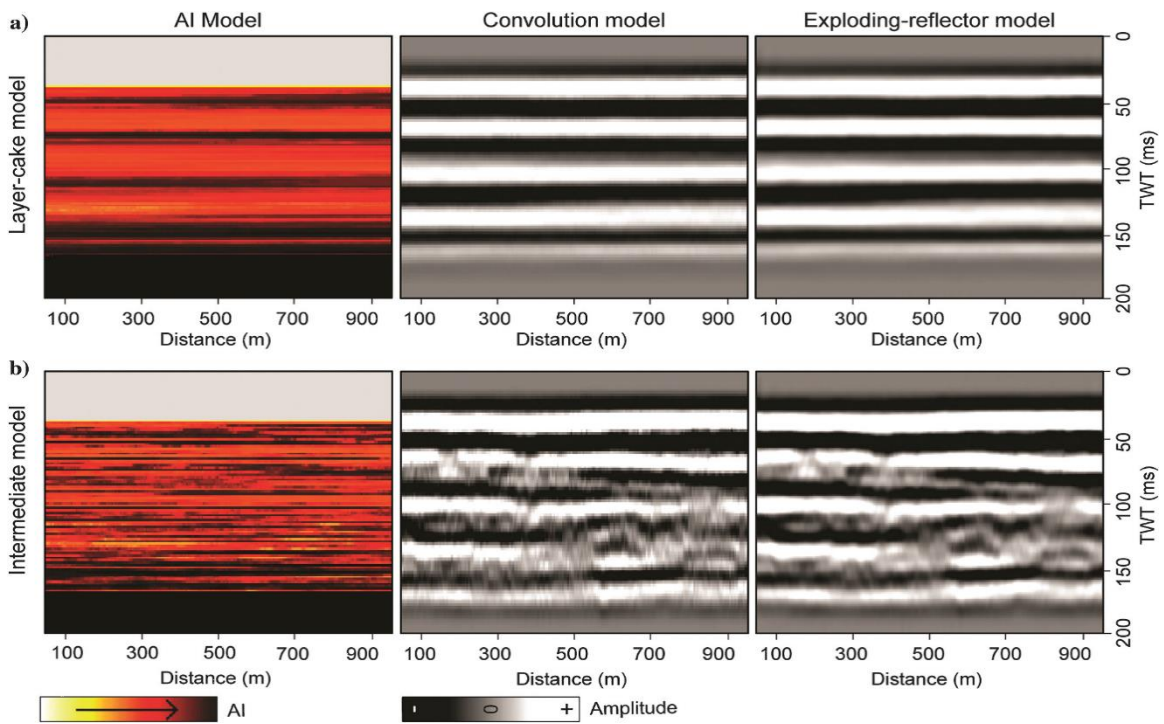


Figure 2.4: Comparison of seismic models: convolution versus exploding-reflector. (a and b) In layer-cake cases, both models work well. In more complex cases, the exploding-reflector model provided more realistic synthetics, with enhanced horizon continuity, than did the convolution model. Thus, the exploding-reflector model was used in this study.

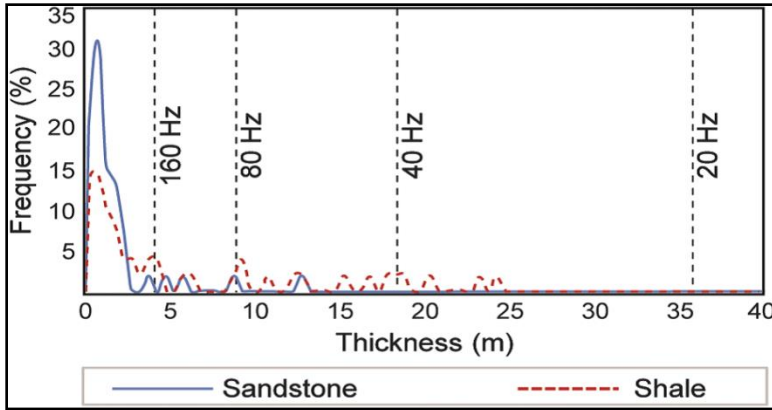


Figure 2.5: Most of the impedance/lithofacies units in this study are below seismic resolution. More than 70% of high-impedance shaly units (blue curve) and low-impedance sandstone units (red curve) were irresolvable at ultiple frequencies.

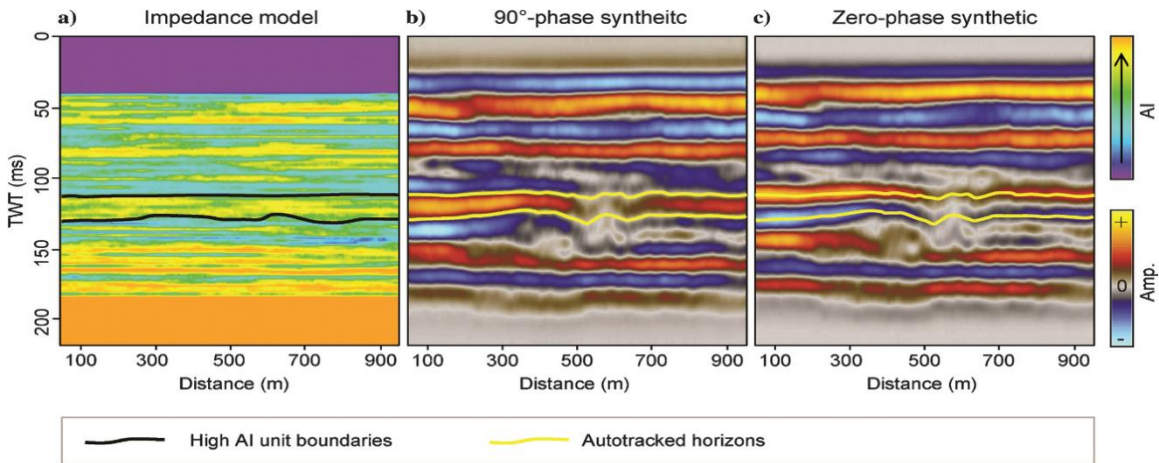


Figure 2.6: Comparison between 90°- and zero-phase seismic models. (a) Impedance section, (b) 90° seismic model, in which the top and bottom of a high-impedance unit (black lines) are, respectively, expressed as a $-t$ zero crossing and a t^- zero crossing (yellow lines), and (c) zero-phase seismic model, in which the top and bottom of the unit are, respectively, represented as a peak and a trough (yellow lines). Panel (b) was used in this study for its straightforward correlation to the impedance model (panel [a]).

2.4 QUANTIFY THE QUALITY OF RELATIVE GEOLOGIC TIME CORRELATION

In this study, the author define the TCE to evaluate the quality of seismic chronostratigraphic correlation between simulated geologic surfaces in an impedance model and tracked seismic events in the corresponding seismic model. The author begin by defining the TCE for a single, manually tracked event. To evaluate TCEs for an entire seismic volume, the author use the RGT volume (Stark, 2004), which contains densely mapped seismic events.

2.4.1 The time-correlation error for a manually tracked seismic event

Vail et al. (1977c) refer to a “time-equivalent” reflection as a reflection following/ paralleling geologic timeline(s). Following this notion, the difference between a seismic reflection h_k and its nearest stratigraphic surface CS_k in TWT (t) is defined as a TCE:

$$TCE_{h_k}(x, y) = t_{h_k}(x, y) - t_{CS_k}(x, y) \quad (1)$$

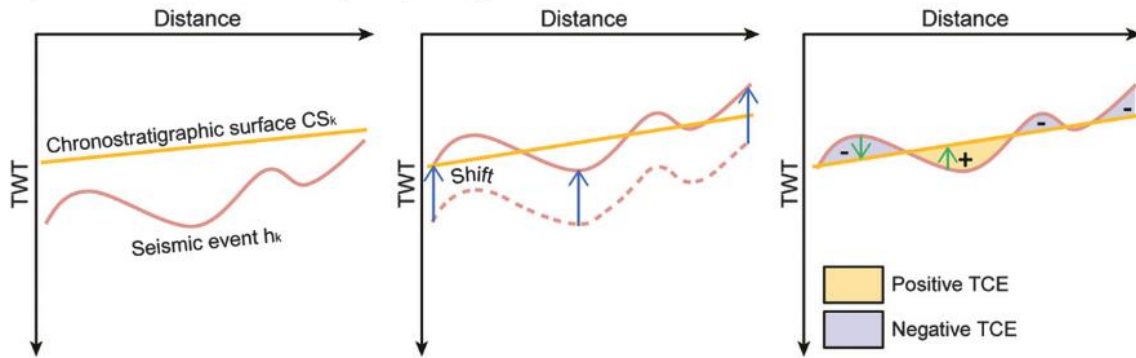
The word “parallel” suggests that there is a shift of reflection h_k toward its nearest stratigraphic surface CS_k (Figure 2.7a). In that way, the distribution of TCEs is expected to spread around zero. In this specific correlation scheme, in which all chronostratigraphic surfaces are flat, the calculation of the TCE is simpler (Figure 2.7b). It is merely necessary to compare a tracked seismic reflection h_k against its own median value to obtain a zero-centered distribution:

$$TCE_{h_k}(x, y) = t_{h_k}(x, y) - \text{median}[t_{h_k}(x, y)] \quad (2)$$

The histogram of TCEs from a tracked event measures the quality of seismic chronostratigraphic correlation when using that event. The width of the TCE distribution (δ) equals the difference between the maximum positive and negative departures from the chronostratigraphic surfaces, and thus it refers to the magnitude for the time transgression. The standard deviation (std. dev.) of the TCE distribution refers to the degree

in which a given measurement deviates from the mean, and it is indicative of the representative ranges of TCEs.

a) Time-correlation error (TCE) in a general case



b) Time-correlation error (TCE) in our horizontal chronostratigraphic scheme

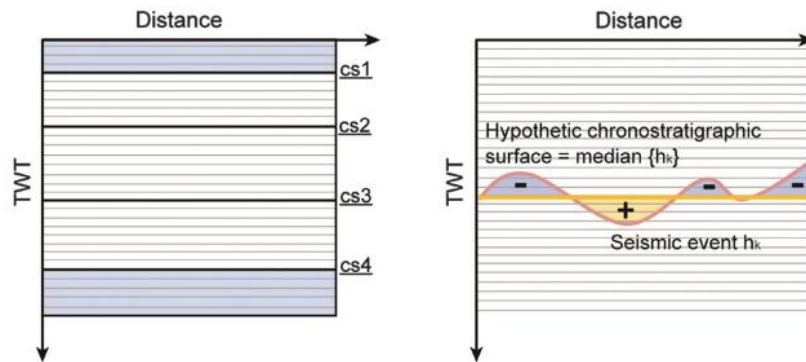


Figure 2.7: The TCE of a horizon, measuring the time difference between a seismic event h_k and the nearest chronostratigraphic surface CS_k . (a) In a general case, a shift of the seismic event is needed to measure only the minimum time difference. (b) In this specific scheme, a seismic event h_k is compared with an arbitrary flat geologic timeline, e.g., the median value for the seismic event h_k .

2.4.2 The time-correlation error for a manually tracked seismic event

To estimate the quality of the seismic chronostratigraphic correlation for an entire 3D volume, the author have to obtain the TCE at each sample point in that volume. The RGT volume (Stark 2004; Figure 2.8) provides a convenient platform for the TCE

calculation (Figure 2.9). By definition, an arbitrary constant surface/isosurface within a seismically estimated RGT represents an autotracked seismic horizon; therefore, an RGT volume could be viewed as a densely autotracked seismic cube in terms of relative geologic time registration. Furthermore, a TCE volume (Figure 2.9c) is taken as the difference between the seismically estimated RGT volume (Figure 2.9a) and the predefined linear RGT volume from the geologic/impedance model (Figure 2.9b). Where seismic events closely follow geologic timelines, the TCE is small (box I). Where reflections are apparently transacting geologic timelines, the TCE is large. Depending on the sign of the apparent seismic dip, the true RGT could be either overestimated (box II) or underestimated (box III).

In this study, the predictive painting technique (Fomel, 2010) was used to generate the RGT volume. This technique is appropriate to evaluate the quality of seismic chronostratigraphic correlation, due to its event-based nature. In other words, information in the multiple seed reference lines was spread through the entire volume following the local inline and crossline dip fields, which were estimated by the method of plane-wave destruction (Claerbout, 1992).

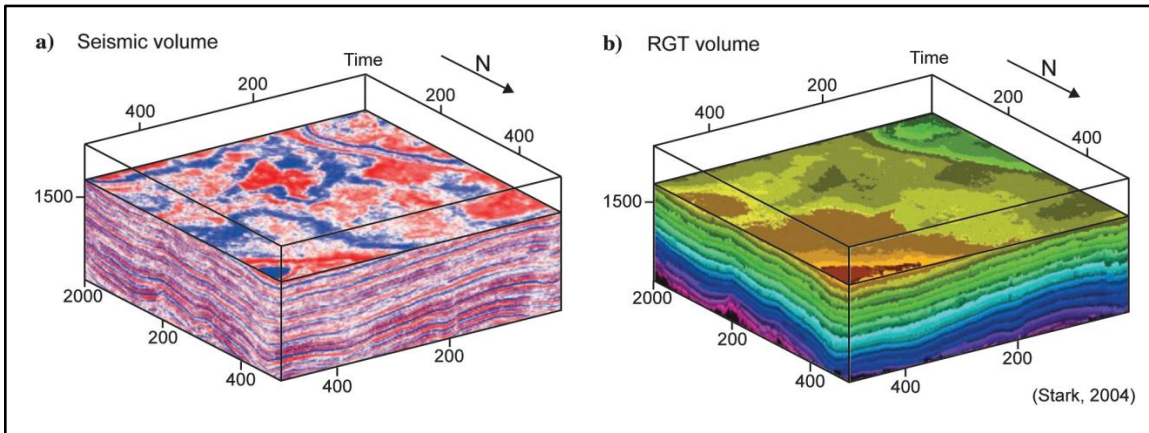


Figure 2.8: An RGT volume estimated from a seismic time-amplitude volume (from Stark, 2003). (a) Seismic cube and (b) estimated RGT volume, in which the constant-value surface is equal to a seismic horizon. Therefore, the RGT volume could be viewed as a densely interpreted cube.

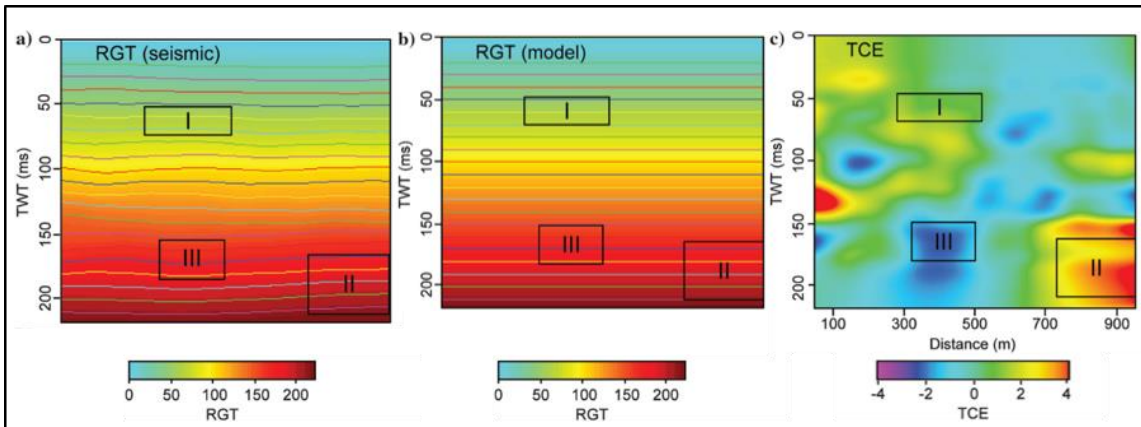


Figure 2.9: TCE for a seismic RGT cube. (a) RGT volume from the seismic model, with curved RGT lines and (b) RGT volume from the impedance model, with flat RGT lines. Contours = 10 ms in panels (ab,). (c) The difference between panels (ab) is an estimation of TCE. Where reflections follow geologic timelines, the TCE is small (box I). Boxes II and III show positive (overestimated) and negative (underestimated) TCE, respectively. Note that higher TCE offset values around the margins result from a seed reference trace employed in the center.

2.5 RESULTS AND INTERPRETATIONS

The quality of the seismic chronostratigraphic correlation can be evaluated by either describing TCEs corresponding to lateral lithofacies/impedance changes in seismic models of fixed frequency (Figures 2.10–2.12) or by studying TCE trends in a frequency range within the same impedance model (Figures 2.13–2.15). For each case, the author started from a visual comparison of TCEs, followed by statistical analyses for selected manually tracked horizons and autotracked seismic volumes, respectively.

2.5.1 The time-correlation error distribution related to lateral impedance variation

The models with increasing lateral impedance variation (models I to III) and their corresponding 40-Hz, 90°-phase seismic models (Figure 2.10) were generated for an initial visual evaluation of how the quality of the seismic chronostratigraphic correlation responds to the impedance (lithofacies) complexity. Note that in these simulated geologic models, all chronostratigraphic surfaces/geologic timelines are flat in TWT. In other words, any local dipping of a seismic event in the synthetic seismic records indicates a departure from chronostratigraphic surfaces (Figure 2.2c). Therefore, the observed smooth and flat seismic reflections in the layer-cake model (model I, Figure 2.10d) follow (are parallel to) the geologic time surfaces defined in the impedance model (Figure 2.10a). In comparison, reflections in the intermediate model (model II, Figure 2.10e) contain a mixture of long, continuous reflections and relatively short, dipping events, indicating a deteriorating quality of geologic time correlation. Furthermore, in the complex model (model III, Figure 2.10f), seismic events are very chaotic with steep local dips, suggesting deviations from true modeled timelines, which are flat.

Subsequently, TCE responses to the lateral impedance (lithofacies) variation were evaluated using manually picked horizons (horizons h1, h2, and h3) in these three seismic models, respectively (Figure 2.11). As discussed in the last section, greater spreading of a

TCE distribution (delta) generally indicates less accurate chronostratigraphic interpretation by tracking seismic events. Clearly, all three manually picked horizons become more and more time-transgressive when the author increase the lateral litofacies variations in the impedance models (models I to III, Figure 2.11). The maximum TCE in the 40-Hz complex model (model III, Figure 2.11) can be as great as the width of two seismic events, or 31.25 m in a 2500 m/s sandstone formation.

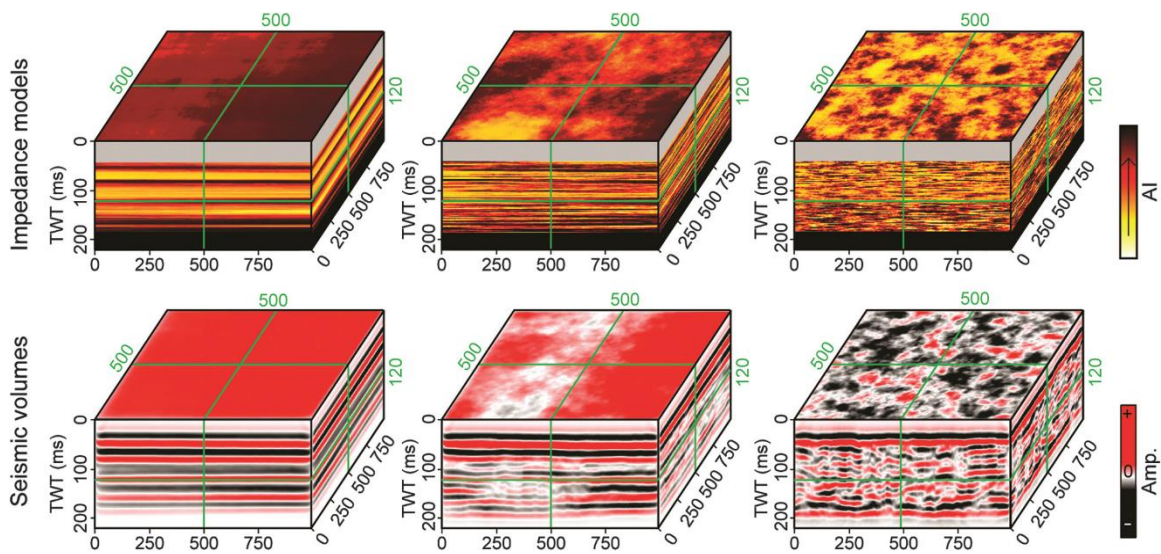


Figure 2.10: Visual comparison for geologic time correlation of seismic events, among models with increasing lateral impedance variation. From models I to III, there is an increase in dipping and chaotic reflections, indicating increased TCE. The front, side, and top frames of a cube, respectively, show the center crossline (crossline = 500 m), inline (inline = 500 m), and time slice (time = 120 ms). The same visualization cube also applies to Figure 2.12.

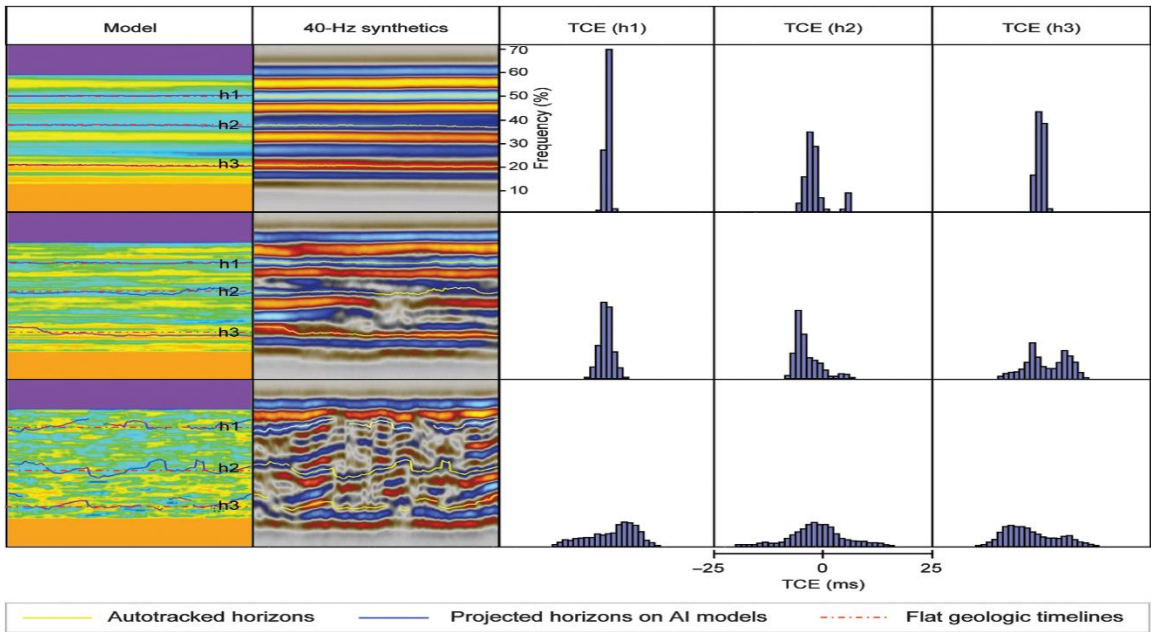


Figure 2.11: TCEs for selected horizons (h1, h2, and h3) at 40 Hz, showing an increasing trend with increasing lateral impedance variation. Event width = 12.5 ms. Units for the maximum time transgression (delta) and standard deviation (std. dev.) are milliseconds (ms).

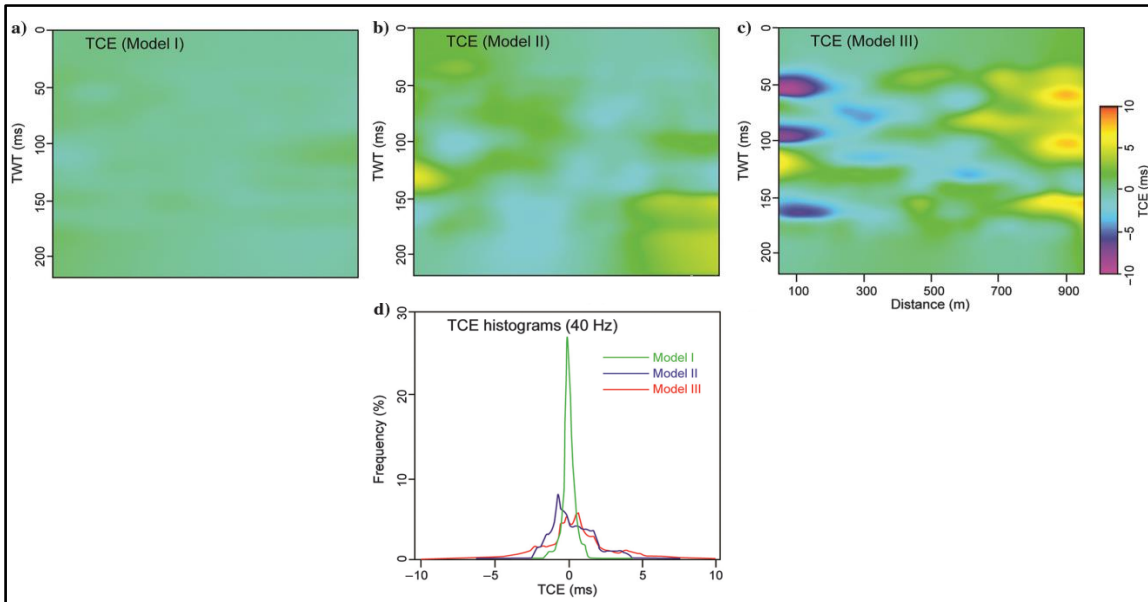


Figure 2.12: TCEs for the same intersection extracted from 40-Hz seismic volumes. Panel (a-c) are the TCEs for models I to III. The same inline was visualized in the same color scheme. (d) Overlaying TCE histograms of three models. The visual comparison among (a-c) and histograms in panel (d) show increasing TCEs with increasing lateral lithofacies variation.

In addition, TCE responses to lateral impedance (lithofacies) variation were also evaluated for an entire volume by calculating the difference between the seismically tracked and geologically simulated RGT volumes. In Figure 2.12, the same intersection from the 40-Hz seismic models (Figure 2.10d, 2.10e, and 2.10f) was extracted to calculate TCEs. As a result, in impedance models with increasing lithofacies variation (models I to III), TCEs tend to have greater magnitudes and are increasingly less accurate for reproducing chronostratigraphic relationships. Note that the overlaying TCE histograms (Figure 2.12d) for models I to III also show a wider TCE distribution for models with increasing lithofacies variation.

2.5.2 The time-correlation error distribution related varying seismic frequencies

The secondary aim of this section is to evaluate the influence of wavelet frequency on the TCE distribution of seismic events from various impedance models. Therefore, the same experiment at 40 Hz (Figure 2.10) was expanded to include seismic models generated with 90°-phase-shifted Ricker wavelets at different predominant frequencies, ranging from 20 to 160 Hz (Figure 2.13).

Resembling the case of 40-Hz models (Figure 2.10), all other seismic models at different frequencies (20-, 80-, and 160-Hz; Figure 2.13) demonstrate a similar trend: More dipping and discontinuous events are associated with more complex lateral impedance (lithofacies) variations. However, visual examination of seismic models at various frequencies against their impedance models (Figure 2.13a–2.13c) alone leads to inconclusive observations. Therefore, quantitative TCE evaluations are essential for capturing the impact of frequency and heterogeneity.

A manually tracked horizon (horizon h2) was selected for analysis of the TCE versus frequency (Figure 2.14). The TCEs calculated from the intermediate and complex models (Figure 2.14b and 2.14c) show a decreased magnitude with increased frequency in TCE histograms, indicating improved time-correlation accuracy at higher seismic frequencies. Estimation for the layer-cake model (Figure 2.14a) at examined frequencies shows similar small departures from real geologic timelines. Though still small in absolute value, the TCE distribution at 40 Hz is about two times wider than that at other frequencies. Probably at 40 Hz, the relative bed and interlayer thickness in wavelength units and the amount younger beds overlapping older beds jointly contribute to more reflections that reach the Tipper point (Hardage et al., 2007).

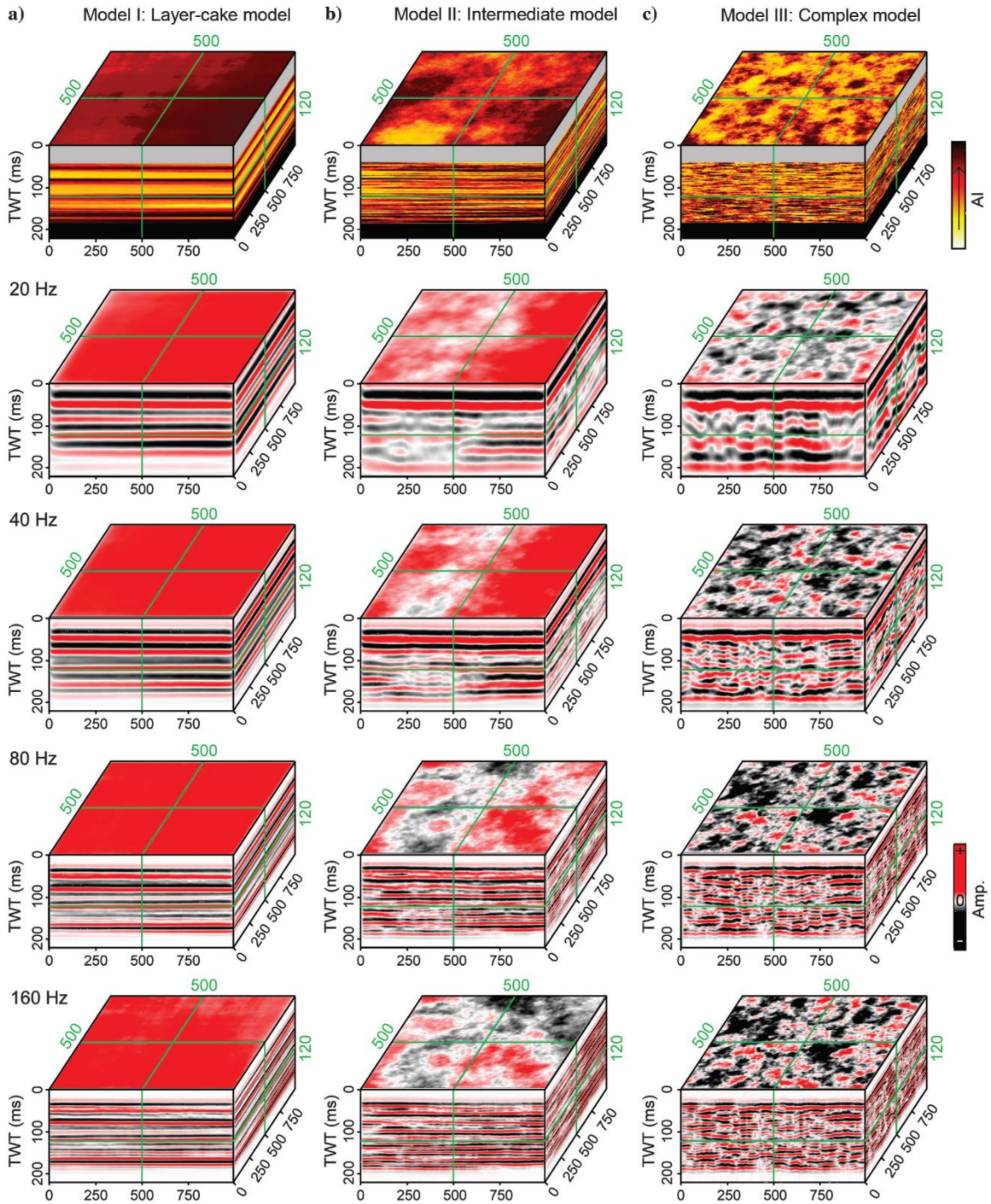


Figure 2.13: Visual comparison for geologic time correlation of seismic events at multiple frequencies. The TCE tends to decrease with increasing seismic frequency for the (b) intermediate and (c) complex models. It is difficult to visually identify a trend for the layer-cake model (a).

Besides, for a more complete evaluation, TCE volumes were also calculated for the seismic models at different frequencies in Figure 2.12. Again, in the intermediate and complex models (Figure 2.15b and 2.15c), higher frequencies in general lead to smaller TCE magnitudes and more accurate seismic chronostratigraphic interpretation. Similarly, inconclusive results occur in the layer-cake model (Figure 2.15a), probably suggesting that a highly continuous impedance model with few lithofacies anomalies tends to generate highly chronostratigraphic reflections, regardless of the wavelet frequency.

These results, achieved by evaluating TCEs for all reflections in 3D seismic volumes, agree with early studies by Zeng et al. (1998a) and Zeng and Kerans (2003) that are dependent on visual inspection of individual seismic events. As supported by all these studies, improved resolution in higher frequency seismic data reduces lithofacies interferences and creates more geologic time-equivalent reflection events, unless there is very little geologic heterogeneity.

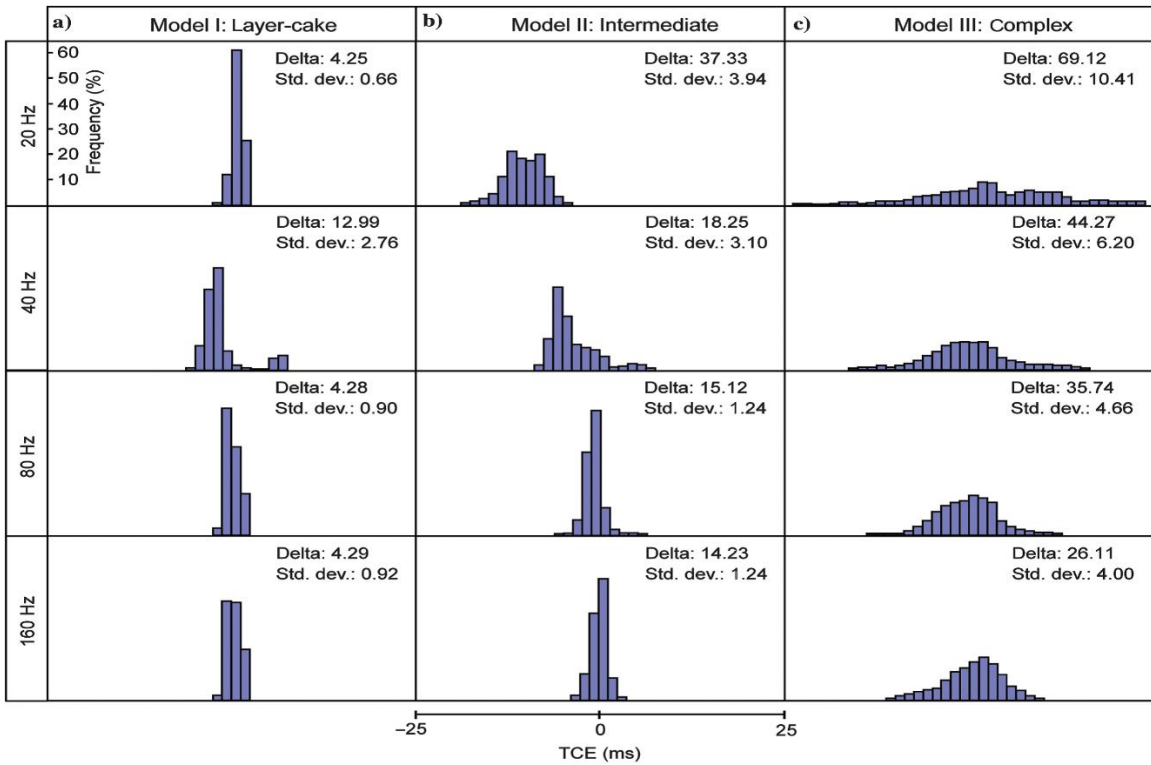


Figure 2.14: TCEs for seismic event h2 (see Figure 2.10 for position) at different seismic frequencies. The accuracy of the chronostratigraphic correlation tends to improve with the increasing seismic frequency, especially for the (b) intermediate and (c) complex models.

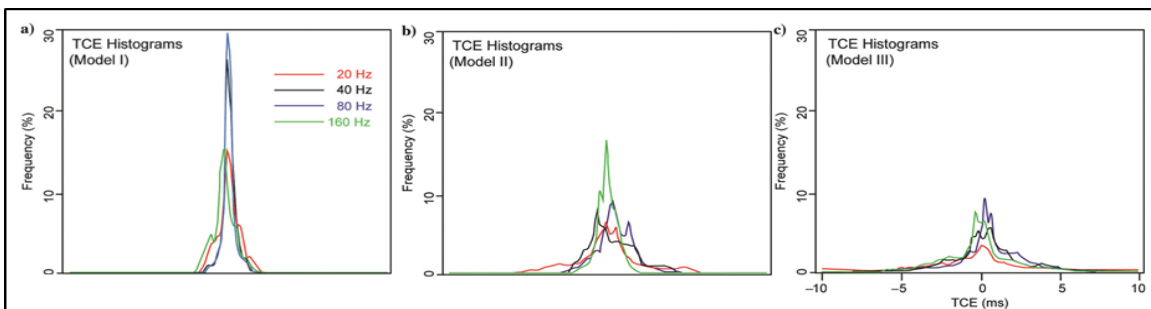


Figure 2.15: Frequency influence on the TCE for densely interpreted volumes. The accuracy of the chronostratigraphic correlation tends to improve with the increasing seismic frequency, especially for the (b) intermediate and (c) complex models. In the layer-cake model (panel [a]), the TCE is small at all frequencies, with the best interpretation from 80 Hz.

Note that TCEs calculated in this study are a conservative estimation of true TCEs. The TCEs calculated in these models are probably smaller than those in field observations. This phenomenon results from the way the author designed geologic models, in which a small vertical correlative distance is assigned by assuming good stratification. In reality, a much larger TCE can occur in field data, as suggested by Zeng et al. (1998b). Moreover, as for an autotracked seismic volume, estimated TCEs can be even smaller than manually tracked horizons. For instance, predictive painting (Fomel, 2010) follows the continuous dip field, which is smoothed by shaping regularization (Fomel, 2007). The smoothing effect smeared local features of dipping and chaotic reflections, further resulting in TCEs smaller than those of manually tracked horizons.

2.6 POTENTIAL APPLICATIONS TO SEISMIC CHRONOSTRATIGRAPHY

To generate RGT volumes from field seismic data, autotracking and stratal slicing have advantages and disadvantages. Autotracking of all primary reflections can capture all geologic time-equivalent seismic events, but many of the picks may be diachronous. In comparison, stratal slicing, is designed to replace diachronous horizons with phantom slices that statistically better track geologic time, while omitting many time-equivalent reflections. To more accurately track horizons without omitting detailed information, the author propose an integration of the above two processes. As discussed in previous sections, the TCE could be a measurement to evaluate seismic chronostratigraphic correlation, although it is not a variable measurable directly from the field data. So the key is to identify a seismic attribute (or combination of attributes) that is indicative of the quality of seismic chronostratigraphic correlation (i.e., as an approximation of the TCE, He and Zeng, 2014b). The application of this selected attribute with limited human

intervention would improve the integration process and make a hybrid RGT volume a reality.

2.6.1 Looking for a useful attribute

In this study, a limited number of seismic attributes have been tested for their relationship with the TCE. Amplitude variance is highlighted here; it measures how amplitude values spread out around a sample point and is a first-order approximation of amplitude energy (Barnes, 2001). In a thick homogeneous medium, the author expected to see zero amplitude variance in a seismic model. For models with abrupt impedance change, greater amplitude variance is expected near the lithofacies boundary. In other words, amplitude variance increases in models with increasing impedance variability and with increasing facies heterogeneity in this study.

Volumes of amplitude variance were calculated for the 40-Hz seismic models related to impedance models I, II, and III, respectively (Figure 2.10a–2.10c). Six extracted time slices in each of the three volumes demonstrate similar variance histograms (e.g., the time slice at 100 ms, Figure 2.16). The log-normal distribution of variance varies greatly among different models. Minimal variance is related to models of the least lateral impedance changes (model I, Figure 2.16a), whereas dramatically increased variances are observed in models of increasing impedance variations (models II and III; Figure 2.16b and 2.16c).

To observe a relationship between a specific seismic attribute with lateral impedance variation, more impedance models beside the original three ones have been simulated, with a lateral correlative distance/range ranging from 20×100 to 29×100 m. As observed, it exhibits a power relationship between the median amplitude variance from the seismic models and the lateral correlative distance/range used in simulating the

impedance model (Figure 2.17). Therefore, the author expect to predict geologic (lithofacies) heterogeneity from a specific seismic attribute, for example, the medium amplitude variance in this case.

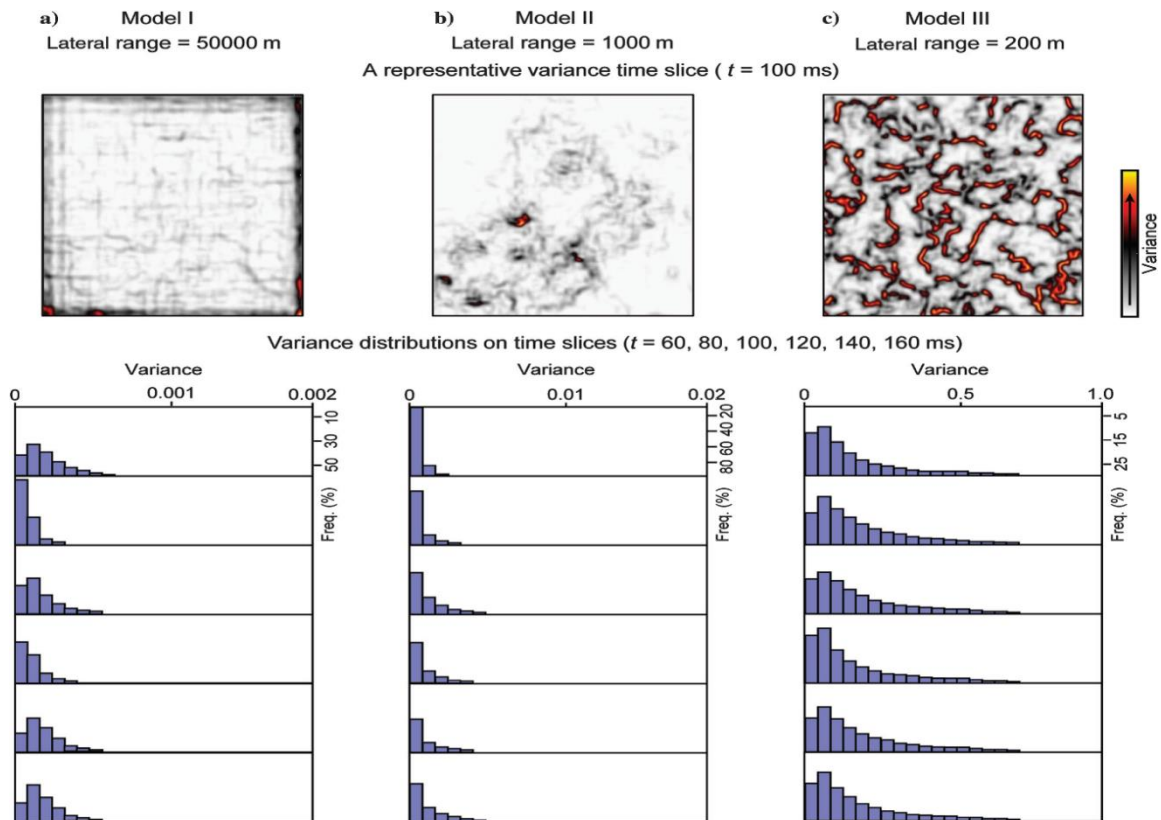


Figure 2.16: Observed correlation between lateral variations in the impedance models and amplitude variances calculated from their seismic records. Multiple variance time slices (60, 80, 100, 120, 140, and 160 ms) show similar distributions within models (a) I, (b) II, and (c) III. However, the amplitude variance increases when the range of lateral impedance variation increases from model I to model III. Note the changes in the horizontal scale of variance.

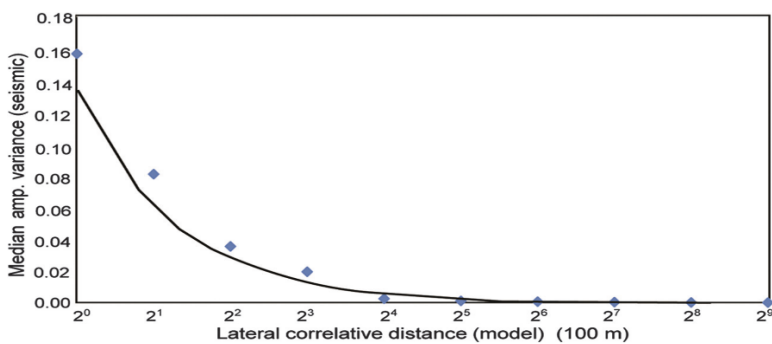


Figure 2.17: Power relationship between the lateral correlative distance in impedance model and the median value of the amplitude variance, calculated from the synthetic seismic volume.

Notice that the TCE, measured either for manually tracked seismic events or for an autotracked seismic volume, is also positively related to the lateral correlative distance used to build impedance models (Figures 2.11 and 2.12); this result suggests that the seismic attribute, medium amplitude variance, may help to predict/ approximate the TCE, which is useful for the development of TCE-based, hybrid RGT, and stratal slice volumes.

2.6.2 Integrating autotracking and phantom slicing (stratal slicing)

At present, in determining the chronostratigraphic significance of a seismic event, two popular approaches include seismic modeling of either a conceptual model or a target-oriented geologic model. A conceptual model is built through consultation with experts who have sufficient experience with regional and local geologic settings, reservoir distribution patterns, depositional/production history, and local seismic interpretation. And the target-oriented geologic model is built from subsurface data (e.g., wireline logs) that capture certain depositional/reservoir architectures. Note that designing these models is experience guided. Moreover because judgment for seismic chronostratigraphic significance is based on visual comparison between the model and synthetic seismic

records, these two approaches are difficult, if not impossible, to apply to the generation of a hybrid RGT volume.

The author recommend a new, attribute-based flattening scheme that makes use of the TCE information automatically estimated from the 3D seismic data that is to be stratal sliced (Figure 2.18). Assuming a particular seismic attribute that highly correlated with the TCE has been found through the above/similar forward modeling experiments, this key learning could be extended to field data. The procedure includes two steps: First, a specific seismic attribute (e.g., amplitude variance in this study) is calculated from the original 3D seismic volume as an approximation for TCEs of each seismic event. Then, interpreters could set a threshold value for this particular attribute to judge the chronostratigraphic significance of seismic events and thus to select the method for predicting RGT: If an event is estimated to follow geologic timelines, an autotracking operation would be performed on the event; otherwise, a phantom stratal slice would be chosen. Eventually, a hybrid RGT volume could be generated.

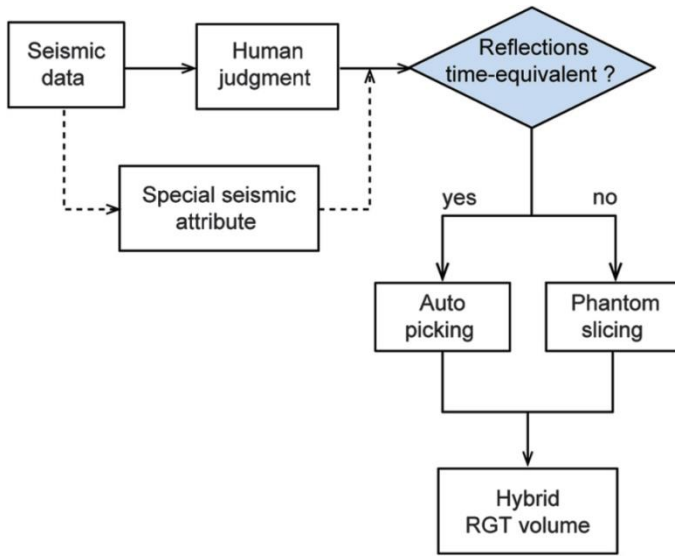


Figure 2.18: Workflows for generating the hybrid RGT volume. The author propose to use a special seismic attribute to replace human judgment for a quantitative and practical procedure.

Note that the optimum threshold value for this particular seismic attribute could be determined by multiple runs. By comparing multiple test results against the predetermined geologic model, this limited human intervention helps to improve the accuracy of the newly generated RGT volume.

2.7 CONCLUSIONS AND FUTURE WORKS

2.7.1 Conclusions

Statistically simulated impedance models with flat chronostratigraphic surfaces at reservoir scale have been used to study the quality of relative geologic time correlation of seismic reflections/seismic chronostratigraphic correlation. The observed difference between simulated geologic time surfaces in an impedance model and tracked seismic events in the corresponding seismic is quantified as the TCE. The TCEs for selected manually tracked horizons and also for autotracked seismic volumes reveal increased

seismic time transgression with increased lateral impedance variation. Observed TCEs can be as large as the width of two seismic events, or 32.5 m in a small, complex impedance model. Higher frequency models in general tend to generate more accurate seismic chronostratigraphic interpretations.

A preliminary test showed that medium amplitude variance calculated from seismic models has a power relationship with the lateral impedance variability (range), which is in turn negatively related to TCE. Consequently, medium amplitude variance could be useful for generating TCE-based, hybrid RGT volumes from field seismic data. The proposed procedure integrates two present techniques, autotracking and phantom slicing (stratal slicing), and it can be practical and economical when implemented in an automated computer algorithm.

2.7.2 Future Works

The statistical modeling procedure used in this study can produce impedance models and associated seismic models. They simulate flat relative geologic time surfaces and lateral impedance/lithofacies variations within each chronostratigraphic unit. These simplified models can be viewed as geologically reasonable; however, they represent limited scenarios. Among the many other factors that can be tested, the most important is to search for more efficient ways to calculate and interpret TCEs in complex stratigraphic frameworks. This requires expanding the approach to models with dipping geologic time surfaces, unconformities, and faults; sequence- stratigraphic frameworks and depositional system tracts can be introduced so that TCEs can be evaluated in real space and time.

A digital outcrop model (DOM) built from detailed geologic mapping constrained by highly accurate spatial data, such as terrestrial LIDAR data, can provide an important platform for this research. When built in a high-frequency sequencestratigraphic

framework, a high-quality DOM model can demonstrate realistic stratigraphic and lithofacies complexities, while honoring detailed observations following multiple outcrop-defined surfaces (Bellian et al., 2005). Many DOMs have been built and studied in the past decade (e.g., Enge et al., 2007; Janson et al., 2007; Bellian et al., 2012). The DOM models will provide opportunities to discuss conditions and procedures for realistic applications of hybrid RGT.

Clearly, a critical test will be using real field data, in which a combination of core, logs, and high signal-to-noise ratio 3D seismic provide adequate geologic constraint. This test should confirm that a hybrid RGT volume should be a better representation of a true RGT cube in that it tends to integrate advantages and avoid disadvantages of autotracking and phantom slicing. By finding a calculated and highly TCE-indicative seismic attribute (amplitude variance or other candidates), the procedure should be practical and economical when implementing as an automated computer algorithm.

Chapter 3: Improving 3D seismic horizon interpretation for reservoir model construction: an example of 3D geocellular and seismic model of Permian San Andres shelf-Grayburg platform mixed carbonate/clastic strata

Seismic horizons are a significant component for reservoir model construction, commonly serving as reference surfaces for stratigraphic layering and a contemporaneous snapshot into depositional system from which to extract seismic attributes, as well as guiding the construction of low-frequency model for seismic inversion. This study² tests limitations of using horizons extracted from 3D seismic as bounding surfaces in building an accurate reservoir model, as applied on Permian mixed siliciclastic-carbonate shelf reservoirs, whose seismic stratigraphic interpretation is challenged by its internal complex shelfal stratal geometry and its interference with overlying platforms containing numerous laterally-continuous but vertically-thin fluid barriers. To investigate the seismic response of this mixed system, a hybrid model was built from both high-resolution outcrop and subsurface data, and then populated with lithostratigraphic and acoustic properties. Geostatistical interpolations were used extensively during model construction, in order to simultaneously honor high-resolution discrete vertical measurements, the lateral continuous constraints, and published 3D depositional models. Relationship between lithofacies and acoustic properties were established from outcrop measurement and well logs. Forward acoustic-wave equation modeling/migration was then applied to investigate seismic response at an analogous peak frequency of field seismic at 35 Hz. Subsequently, reflection-geometry-based conventional seismic stratigraphic interpretation was used to pick the maximum flooding surface and top of a well-constrained high frequency sequence

²Figures and major contents of this chapter were from a manuscript completed in March 2017 (He et al., 2017c, in preparation) for a submission to AAPG Bulletin, which is currently undergoing data sponsors' final review and approval.

(HFS) as the base and top of strongly-progradational shelf reservoirs. In both cases, spatial discrepancies exist between the interpreted seismic horizon and the input stratigraphic surface, thus the author made recommendations to improve practical seismic interpretation.

3.1 INTRODUCTION

Derivative products from the analysis of 3D seismic data are important components of modern reservoir characterization. Such products provide essential map-view or three-dimensional constraints for 3D static reservoir models, and guide stratigraphic, facies, and property modeling via a variety of forms, including seismic horizons, horizon-based attribute map analysis, volume-based attribute analysis, and seismic inversion results (Grötsch and Mercadier, 1999; Chopra and Marfurt, 2007). Among these seismically-derived model inputs, 3D seismic horizons were presumed to be important time-markers or geologic timelines in seismic stratigraphic interpretation (Vail et al., 1977c), and thus contribute to multiple stages of static reservoir model construction. Most directly at the stage of stratigraphic modeling/framework construction, 3D seismic horizons serve as reference surfaces for stratigraphic layering if interpreted in/converted to depth domain (Doyen, 2007). This ensures as true a representation of stratigraphic patterns and geometries as possible. Subsequently, at the stage of facies modeling, horizon-based attribute maps, if extracted from a true time surface, can provide a snapshot into a contemporaneous depositional system when integrated with cores and wireline logs (Posamentier et al., 1996; Zeng et al., 1998a, b; Posamentier and Kolla, 2003; Chopra and Marfurt, 2007). Attribute maps can also be integrated into facies modeling (Behrens et al., 1998; Yao and Chopra, 2000). In addition, at the final stage of property modeling, 3D seismic horizons can be optionally used to guide the extrapolation of wireline logs to build

a low-frequency model for seismic inversion, which further provide volumetric constraints for property estimation (Hampson et al. 2000; Chopra and Marfurt, 2007).

Many of these significant roles of seismic horizons for the static reservoir model construction are explicitly or implicitly based on the fundamental assumption of seismic stratigraphy (Vail et al., 1977c), which presumes seismic reflections to chronostratigraphic surface/geologic timelines, rather than lithostratigraphic surfaces. Therefore, one can interpret ‘seismic sequence/depositional sequence’ as the ‘basic unit’ (Mitchum et al., 1977b) based on seismic reflection patterns (Mitchum et al., 1977a), including the reflection terminations at the sequence boundary, the reflection configurations within sequence, and the external forms of sequences and seismic facies. The suggested basic interpretation unit of ‘depositional sequence’ was defined as ‘a stratigraphic unit composed of a relatively conformable succession of genetically related strata and bounded at its top and base by unconformities or their correlative conformities’ (Mitchum et al., 1977b), and one magnitude smaller than Sloss (1963)’s supersequence (Mitchum et al., 1977b).

This fundamental assumption for seismic stratigraphic interpretation has facilitated many great successes in petroleum exploration and low-order (3rd-or lower-order) seismic stratigraphy (Brown and Fisher, 1980; Posamentier and Vail, 1988; Eberli et al., 2002; Catuneanu, 2006; Hart, 2003), while requires additional validations when extending to the smaller-scale seismic stratigraphy to define high frequency sequence (HFS’s) and high frequency cycles (HFC’s) in scenarios of complicated lithofacies-acoustic impedance relationship, complex stratigraphy, and typical normal-frequency industrial seismic data. First of all, the original authors have stated a rule of thumb that ‘the greater the sea-level fall the easier it is to recognize sequence boundaries’ by reflection terminations (p. 65, Vail et al., 1977a). Therefore, small-scale events during paracycles or shorter pulse, especially during greenhouse with low-amplitude and faster sea level variation (Read, 1985), could

fall below the seismic resolution (Sheriff, 1977), thus requires additional data such as outcrops and tightly-spaced wells with adequate cores (p.64, Vail et al., 1977a). In addition, the original synthetic experiment to propose this fundamental assumption (p. 103, Vail et al., 1977c) was drawn upon a siliciclastic geologic cross-section with both simple lithofacies-impedance relationship and simple stratigraphy of flat strata onalp a 0.36° angular unconformity, thus the author was motivated to test the model-dependency of this assumption by applying to a shelf-margin mixed siliciclastics-carbonate model in this study. Most importantly, the applicability of this fundamental assumption has been reported for being venerable to seismic resolution (Aigner et al., 1989; Lawrence et al., 1989), indented lithofacies stack pattern (Zeng et al., 1998a; Hardage, 2007), and meteoric or burial-dagenetic alternation of carbonate rocks (Fournier and Borgomano, 2007). Therefore, when applied to reservoir-scale interpretation, these uncertainties could lead to seismic reflections not follow chronostratigraphic layering at the high-resolution scale (Grammer et al., 2004), and further result in misinterpretation of depositional environment and reservoir compartmentalization (Zeng and Kerans, 2003), as well as stratigraphic architecture and thus misinterpretation of facies model and inaccurate volumetric calculation (Stafleu and Sonnenfeld, 1994).

In this study, with an ultimate goal to improve 3D seismic horizon interpretation for the static reservoir model construction, the author tested the validity of the fundamental assumption of seismic stratigraphy as applied to higher-order seismic stratigraphy of a mixed siliciclastic-carbonate shelf margin with complex stratigraphy, and then make recommendations on practical interpretation accordingly. More specifically, the author chose Permian mixed siliciclastic-carbonate Upper San Andres (uSA) shelf-margin reservoirs as an example, due to its significance in Permian production, challenges in seismic stratigraphic interpretation, and multi-scale (regional- to core-scale) data

availability. Subsequently, the author applied 3D geocellular modeling for stratigraphy, facies, and acoustic properties, and then seismic modeling. Implementing a conventional seismic stratigraphic approach by assuming seismic reflections represents chronostratigraphic stratifications, the author interpreted the top and base of strongly-progradational reservoirs. Finally the author compared the seismic horizons against the geologic model for their discrepancies, as a proxy to evaluate the applicability of fundamental assumption of seismic stratigraphy as applied to reservoir model construction.

3.2 STUDY TARGET AND CHALLENGES

Permian Upper San Andres (uSA, Figure 3.1) mixed-system shelf reservoirs were chosen as the target for this study. These reservoirs have contributed significantly to Permian cumulative production numbers, and continued extraction through both waterflooding and Tertiary recovery is ongoing. Besides its significance in Permian production, the author chose this target for its challenges in seismic stratigraphic interpretation, as well as and its good data availability to construct both a 3D high-resolution stratigraphic model and forward seismic model for a comparison between an idealized seismic stratigraphy against high-resolution stratigraphy.

3.2.1 Seismic stratigraphic interpretation challenges for uSA shelf reservoirs

The seismic stratigraphic interpretation for the top and base of the uSA prograding shelf reservoirs showcased challenges in an HFS- and smaller-scale seismic stratigraphy. One can chose the top and bottom of G9 HFS as the bounding surfaces of these reservoirs, as (1) the G9 top segmented uSA shelf reservoir and Grayburg platform reservoir compartment and (2) the G9 bottom featured in a transition from aggradational to progradational geometry. Applying the conventional seismic stratigraphic interpretation approaches (Mitchum et al., 1977a), the author identified the shingled to sigmoidal reflections as clinoforms prograding toward the basin (Figure 3.1c, magenta arrows). These clinoforms terminate downdip (downlap) against a continuous and gently-inclined seismic trough at the toe of slope, thus the author interpreted this seismic trough as the G9 bottom/reservoir model base (Figure 3.1c, the lower white lines). In addition, these clinoforms terminated updip (toplap) against a relatively flat-lying seismic trough, thus the author interpreted this seismic trough as the G9 top/model top (Figure 3.1c, the upper white lines). However, when applying this conventional seismic stratigraphic interpretation approach to HFS- and smaller scale, the key encountered challenges include but not limit

to (1) the difficulties in characterization of complex stratigraphic architecture at a typical seismic peak frequency of 35 Hz (Figure 3.1c) for accurate reflection terminations and internal reflection configurations, (2) the uncertainties in interpreting the uSA reservoir top, as seismic reflections may follow low-impedance reservoir compartments and thus cross uSA-Grayburg sequence boundary, where these reservoir compartments include both uSA porous carbonate and Grayburg porous carbonate and sandstone/siltstone (Dutton et al., 2004, Play 127 – Grayburg Platform Mixed Clastic/Carbonate Play), and (3) the lack of deep wells and cores for an integrated interpretation.

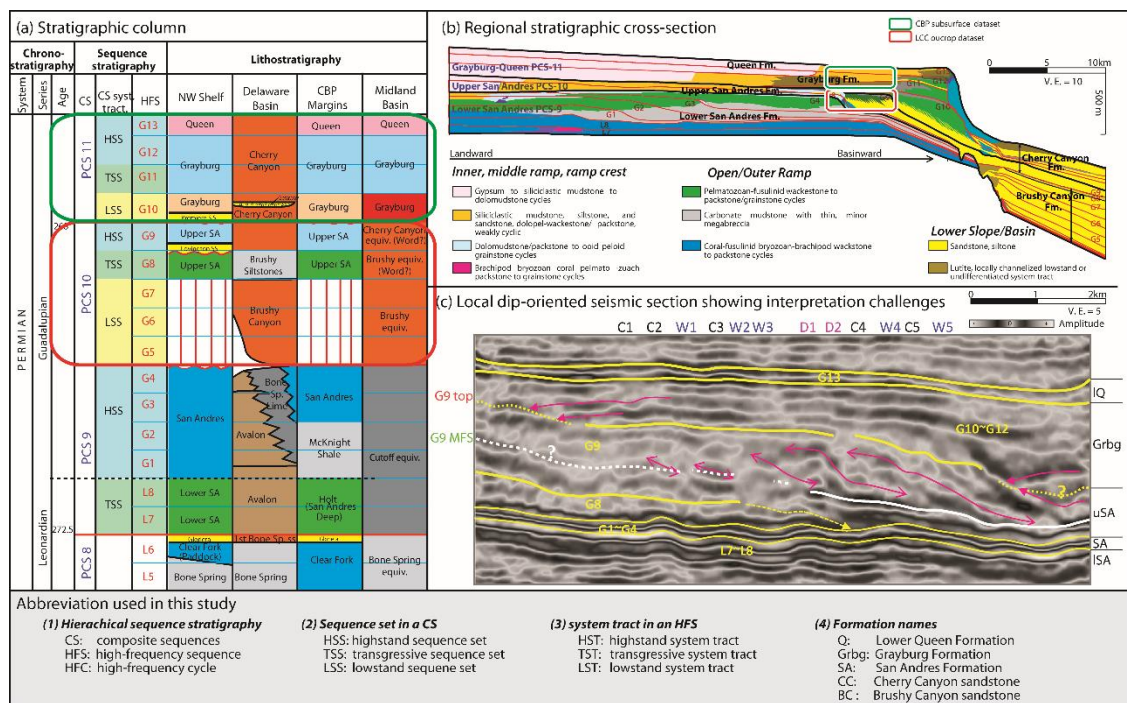


Figure 3.1: Permian San Andres-Grayburg stratigraphy, and challenges in seismic stratigraphic interpretation of shelf-margin reservoirs. (a) stratigraphic column and (b) regional stratigraphic cross-section are modified from Kerans et al.(2013). (c) a local dip-oriented seismic section. The annotated red and green box represents outcrop- and subsurface-constrained modeling interval in this study, with study areas shown in Figure 3.2.

3.2.2 An opportunity to investigate seismic stratigraphy through forward modeling

A forward seismic modeling on a 3D geologic model would allow a validation of this conventional seismic interpretation results against the reality. An advantage of the Permian mixed system dataset used in this study is the availability of other significant multi-scale (core- to regional scale) inputs for use in the interpretation/model-building process, including core and wireline logs as well as close outcrop analogs. This allows analysis of the idealized seismic responses and limitations of using 3D seismic horizons in reservoir model construction through forward modeling. Core-scale characterization provides high-resolution 1D and 2D stratigraphic descriptions (Kerans and Tinker, 1996) but these are inherently limited in terms of uncertainties in correlation and interpolation, especially in scenarios of sparse or clustered well distributions. Outcrop analog data provide 2.5D information of stratigraphic layering and distribution of petrophysical properties, but will always be limited in their applicability by the degree to which these datasets are indeed “analogous” to subsurface field data, in terms of geologic settings, depositional and post-depositional history, and lithofacies assemblage. Fortunately, regional geologic frameworks allows for more effective leveraging of analogs for seismic stratigraphic analyses (Shepherd, 2009), therefore joint examination of outcrop analogs and a subsurface field provides a unique opportunity in this study.

3.3 STUDY AREAS, GEOLOGIC SETTING AND DEPOSITIONAL MODELS

3.3.1 Study areas and datasets

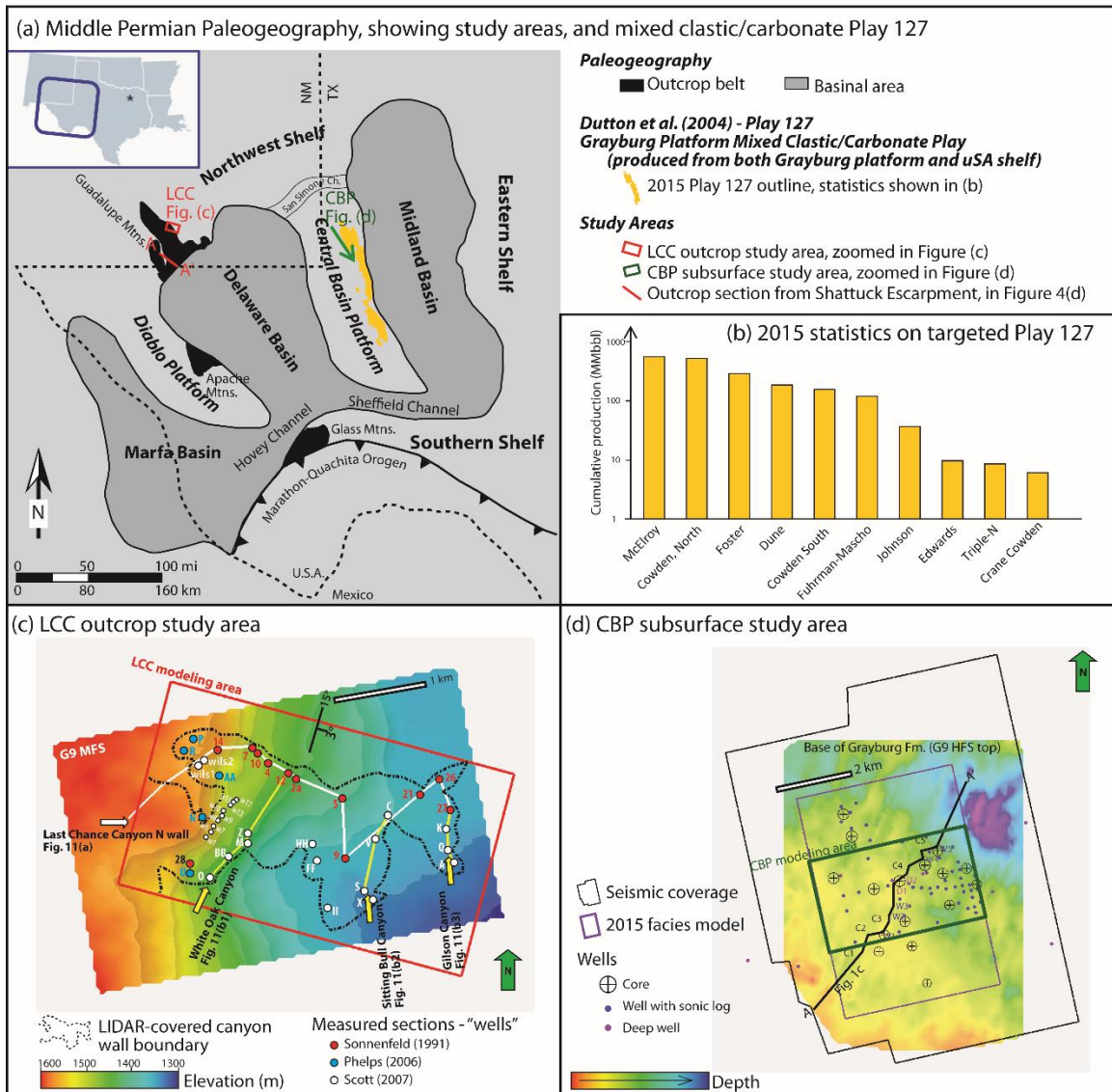


Figure 3.2: Study areas and subsurface productions. (a) Middle Permian stratigraphy showing LCC outcrop study area (red box) and CBP subsurface study area (green box), which is located within Dutton et al. (2004)'s Play 127 reservoir trend. (b) 2015 statistics on Play 127, the subsurface data is from a top producing field. (c) A zoomed-in LCC outcrop study area showing dataset. (d) A zoomed-in CBP subsurface study area showing dataset.

The two study areas for this modeling research are from the well-studied San Andres and Grayburg outcrops of Last Chance Canyon in Guadalupe Mountains

(Sonnenfeld and Cross, 1993; Stafleu and Sonnenfeld, 1994; Phelps and Kerans, 2012, Phelps, 2006, and Scott, 2007) and a subsurface reservoir setting from the eastern margin of the Central Basin Platform (Figure 3.2a). These settings are closely analogous geologically and examining the two together affords a unique opportunity to test limits of seismic imaging for analysis of reservoir architecture. The author use the regional stratigraphic framework (Figure 3.1a) proposed by Kerans and Fitchen (1995) and Kerans and Kempter (2002) that recognizes three scales of stratigraphic cycles, with five composite sequences (PCS's), 32 high frequency sequences (HFS's) and numerous high frequency cycles (HFC's). The San Andres and Grayburg units at Last Chance Canyon and surrounding canyons have been shown to define two PCS's with distinctly different stratal architectures.

The upper San Andres Formation G8 HFS was the focus of Phelps' (2006) work, whereas Sonnenfeld (1991a,b) and Scott (2007) were focused on the G9 HFS. The focus in this study is the upper San Andres composite sequence or PCS 10 (both G8 and G9 HFS's, Figure 3.1a, red box). The specific model area covers approximately 15 square kilometers, including four canyons which are altogether shortened as LCC (Figure 3.2a, red box; Figure 3.2c). The Upper San Andres at LCC consists of mixed siliciclastic-carbonate oblique to complex oblique-sigmoidal HFC clinofolds (Sonnenfeld and Cross, 1993) with distinctive promontory-reentrant along-strike variability, generally prograding to the east (Figure 3.2c) with a maximum topset to bottomset relief of approximately 140 meters (Sonnenfeld and Cross, 1993; Scott, 2007). Grayburg strata onlap the top-San Andres karstic unconformity (Scott, 2007) and form a landward (Western locally) tapering onlap wedge of shallow subtidal carbonates and sandstones that upon detailed inspection can be further subdivided into 3 high-frequency sequences of which two are present at LCC (Hiebert, 2012). The author revisited this outcrop as recent data acquisition on this outcrops

allows a 3D stratigraphic and facies modeling: Phelps (2006) and Scott (2007) supplemented along-strike measured sections to the classic dip-oriented ones by Sonnenfeld (1991a), compiling a dense network of 42 measured sections with spacing between sections varying between 50 m and 700 m (Figure 3.2a), and acquired ground-based Light Detection and Ranging (LIDAR, Bellian et al., 2005; Buckley et al., 2008, Janson et al., 2010) to provide a merged visualization of the LCC canyons walls using Bellian et al. (2005)'s methodology.

The subsurface study area is from a top producing Grayburg waterflooding field on the eastern margin of the Central Basin Platform (Figure 3.2a, green box). This field produces from Grayburg units within the transgressive to early highstand sequence set of PCS 11 (Figure 3.1, green box), with only minor contribution from the underlying San Andres Formation. Regionally this field is part of the Grayburg mixed siliciclastic-carbonate play (Play 127 in Dutton et al. 2004) which had produced 669.7 MMbbl cumulatively as of 2000, and is currently under secondary recovery in the Basin today (Figure 3.2a and b). This field was selected for this study because (1) it has a geologic setting that is closely analogous to the LCC study area and (2) it has a dataset (Figure 3.2d) consisting of 16 cored wells (2,931 feet in total), 64 wells with good-quality log suites penetrating the Grayburg Formation, 8 deep wells penetrating the San Andres Formation, and a modern 3D seismic volume with a 35-Hz peak frequency. This field is both representative of the larger producing play and is an excellent dataset to interrogate and demonstrate the ability to correctly model the subsurface, revealing key reservoir heterogeneities at a scale analogous to that observed in this outcrop model.

3.3.2 Geologic setting

Paleogeographic reconstructions place the Permian Basin within 0 to 5° North of the equator during Middle to Late Permian (Coffin et al., 1992; Lottes and Rowley, 1990; Scotese, 2004). Outcrop and subsurface studies both suggest a long-term arid environment, supported by the abundance of evaporites and eolian terrigenous clastics (Fischer and Sarnthein, 1988; King, 1948) and the lack of clay-rich fluvial runoff in both outcrop and subsurface (Kerans and Tinker, 1999). During the Guadalupian, the LCC outcrop and CBP subsurface study areas were located near the periphery of the shallow-water shelf of the Permian Basin. Reciprocal sedimentation, where shallow-water carbonate sedimentation on the shelf alternated with basin-centered terrigenous siliciclastic deposition (Silver and Todd, 1969), occurs during both the San Andres and Grayburg times. At the basinal scale, eolian terrigenous sands are transported into the basin during low relative sea level, followed by shelf-centered shallow-water carbonate deposition during relative high sea level, when the broad backreef lagoon prevented the terrigenous sediments from reaching the basin. The basinal equivalent of San Andres and Grayburg strata, the Brushy Canyon/Cherry Canyon formations of the Delaware Mountain Group, mark distinct lowstand events (Harms, 1974; King, 1942) of bypass of eolian sandstone and siltstone, whose lack of clay was explained by detritus segregation in eolo-marine model (Sarnthein and Diester-Haass, 1977; Sarnthein and Koopmann, 1980) and whose sand origin was recently revealed to be sourced from south of Ouachita-Marathon suture using detrital-zircon geochronology (Soreghan and Soreghan, 2013).

3.3.3 Depositional models for San Andres-Grayburg strata

The PCS 10 (Figure 3.1) chronologically contains 3 lowstand HFS's of the Brushy Canyon Formation (G5-G7 HFS) without shelf equivalency (Gardner and Borer, 2000), the G8 HFS and basinal Brushy Canyon Formation (transgressive sequence set), and G9 HFS of uppermost San Andres Formation affinity (highstand sequence set). The Lower Cherry Canyon Formation or Cherry Canyon Tongue is the lowstand to transgressive element of the G9 HFS. According Kerans et al. (2013)'s 3D depositional models of Upper San Andres Formation, the G8 HFS has gentle depositional profiles with average depositional dip less than 5°, and is characterized by upper-slope fusulinid-rich mounds or shoals, lower-slope small-scale channel-levee complexes and basinal hemipelagic mudstone blanket (Phelps and Kerans, 2007). In comparison, the sandier G9 HFS exhibits steepened depositional profiles and sinuous promontory-reentrant shelf margins (Figure 3.3a). Its adjacent shelf-margin promontories are spaced at 200~500 meters apart along-strike and serve as preferential sites for patch reef growth, whereas its shelf-margin reentrants were favorable for siliciclastic bypass (Scott, 2007). Sonnenfeld (1991) and Scott (2007) both divided an idealized HFC clinoform into a lower siliciclastic-rich transgressive (T) hemicycle and an upper carbonate-dominant regressive (R) hemicycle (Figure 3.3c). The author applied Scott (2007)'s facies model to Sonnenfeld (1993)'s cross-section, and then get a measurements on the dimensions per strongly-progradational HFC, namely the HFC6~14 in Sonnenfeld (1993): its bottomset-topset elevation can reach up to 158 meters. In addition, its width of outer ramp, upper slope and low-slope facies belt respectively ranges from 827~1604 meter, 607~1020 meter, and more than 2237 meters. In comparison, Phelps and Kerans (2007)'s 3D model for distally steepened ramp clinoforms in G8 HFS of Last Chance Canyon shows more straight or linear along-strike boundaries between various facies tracts.

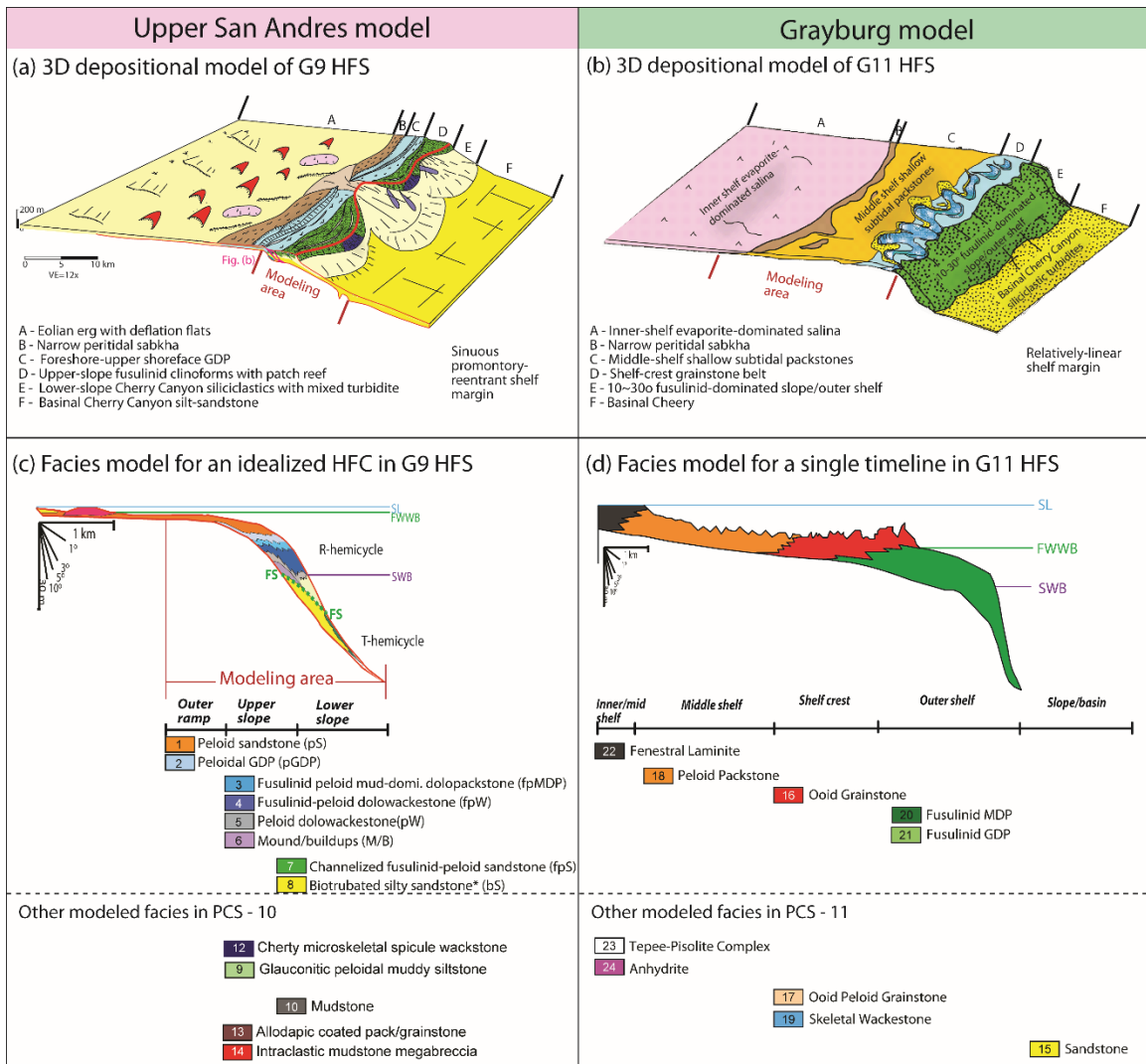


Figure 3.3: 3D depositional and facies model from previous studies, with facies codes in this study. (a) and (b) show 3D depositional model of G9 HFS in PCS-10 and G11 HFS in PCS-11 (Kerans et al., 2013). (c) Facies model for an idealized HFC in G9 HFS, proposed based on LCC observations (Scott, 2007). (d) Facies model for a single timeline in G11 HFS, proposed based on field observations in Shattuck Escarpment (Hiebert, 2012). Other modeled facies in PCS10 and 11 are listed at the bottom, with more details in methodology section.

The PCS 11 herein (Figure 3.1) includes the G10 HFS (lowstand sequence set, lower Grayburg Formation), G11 HFS (transgressive sequence set, middle Grayburg

Formation), and G12-G13 HFS (highstand sequence set, upper Grayburg-Lower Queen Formation). Kerans et al. (2013) proposed 3D depositional models of G10-G13 HFS. In general, the depositional profiles evolve from distally steepened ramp to reef-rimmed shelf with relief of 80-100 m in the G12 HFS. For the inner/mid ramp, the G10 HFS displays a sabkha facies with localized tepee island complexes, compared with the G11 and G12 HFSs which contain an evaporite-dominated salina and oolitic barrier. The carbonate factory for the G11 and G12 is much broader than that of the G10 HFS (10 km compared with 5 km). As shown in an example of the G11 HFS (Figure 3.3b), depositional profiles steepen with clinoform slopes of 10-30°. The model interval in this study corresponds to the landward platform area, with a mixed siliciclastic-carbonate-evaporite association. Hiebert (2012) proposed a single timeline facies model using measured sections from the Shattuck Escarpment (Figure 3.3d), showing a basinward facies transition from inner/middle-ramp facies belt of dominantly fenestral laminate (<1 km width), to middle ramp facies belt of peloid packstone (3~4 km width), to shelf crest facies belt of ooid grainstone (2~3 km width), and then to Fusulinid-rich outer shelf facies belt (4~5 km width). Compared with the facies model of upper San Andres Formation, the Grayburg model shows greater lateral facies continuity.

3.4 MODELING WORKFLOW AND METHODOLOGY OVERVIEW

The overall modeling interval (Figure 3.1) contains two PCS's of mixed clastic-carbonate systems, including (1) PCS-10 of uSA Formation and its equivalent Brushy Canyon and Lower Cherry Canyon basinal deposits, and (2) PCS-11 including Grayburg and Lower Queen formations, whose flat-lying inner to middle ramp onlaps the subaerial unconformity on the karst-modified top uSA sequence boundary (Fitchen, 1993). The geocellular forward model draws upon detailed LCC outcrop data (Figure 3.2c) for its lower San Andres-equivalent portion and subsurface data for the upper Grayburg-equivalent portion (Figure 3.2d). A single high-resolution reservoir model was constructed based the San Andres outcrop- and Grayburg subsurface geocellular model, which were built separately using different geostatistical methods driven by the different input data types and geological complexity. This section presents a six-step (Figure 3.4) geocellular and seismic modeling workflow with an overview of methodology, with a focus on inter-connection among steps. For those complex steps (Step 2~3, 4, and 5), the author will present detailed methodology, parameters and examples in separate subsequent sections.

3.4.1 Workflow

Six steps were followed to build the 3-D geocellular and then seismic model (Figure 3.4), including

1. Lithofacies definition
2. High-resolution sequence stratigraphic correlation
3. Stratigraphic modeling and gridding
4. Facies modeling
5. Petrophysical analysis, adjustment and modeling
6. Seismic modeling

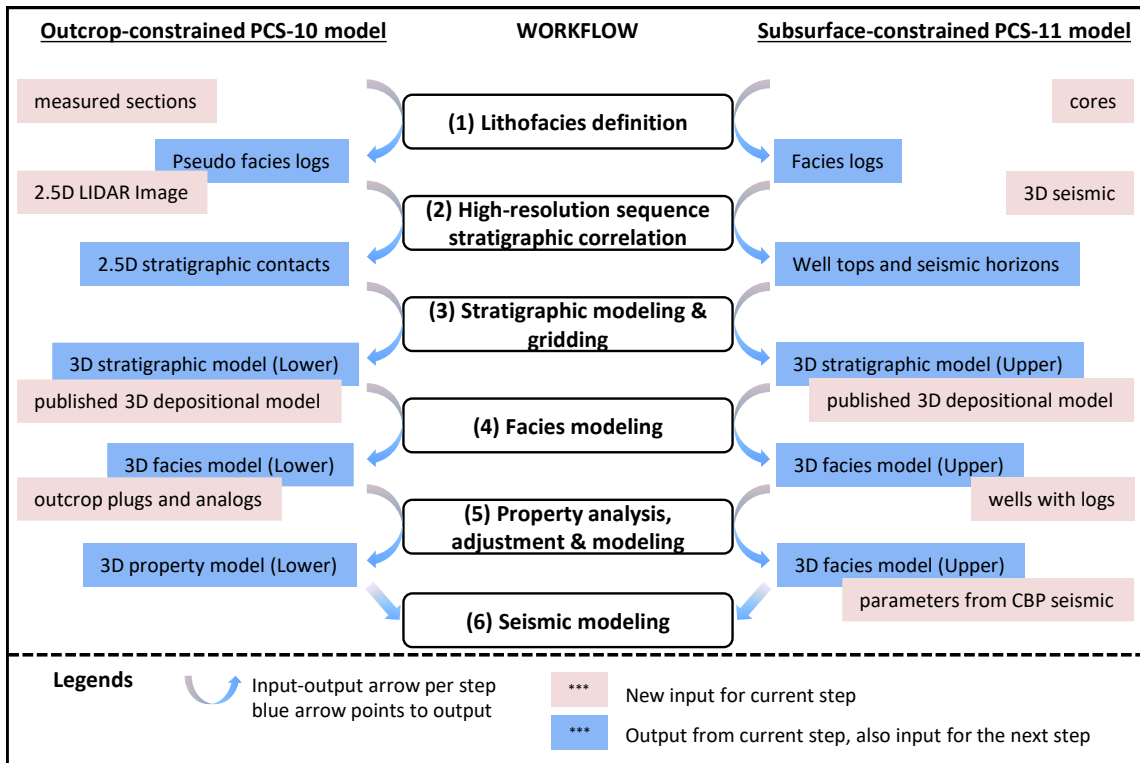


Figure 3.4: Geocellular and seismic modeling workflow.

3.4.2 Methodology overview

For both outcrop and subsurface datasets, Embry and Klovan (1971)'s modification of Dunham (1962)'s classification system for carbonate rocks was used for lithofacies definition (Step 1), and resulted in 14 lithofacies for PCS-10 and an additional 10 for PCS-11. Afterward, high-resolution sequence stratigraphic correlation up to HFC scale was applied (Step 2). For the outcrop dataset, 19 stratigraphic contacts between G9 MFS and G9 top was digitized on LIDAR image of canyon walls by Scott (2007), and 19 lower stratigraphic contacts below G9 MFS were digitized on the georeferenced Sonnenfeld and Cross (1993)'s cross-section. As for the subsurface dataset, Kerans and Sitgreaves (2015) interpreted well tops for 15 surfaces and two seismic horizons.

In this study, the author defined a 105°-oriented 20×20m grid in an area of approximately 5×3-km for stratigraphic modeling, and then chose 105° as its updip-downdip orientation for facies modeling. This decision was supported by Scott (2007)'s reconstruction of strongly-progradational clinoforms between G9 MFS to its top. Scott (2007) reconstructed surfaces in a 78°-oriented 5.7×3.6km rectangular area (Figure 3.2c), in order to optimally bounding the LIDAR-coverage, by using Sequential Gaussian Simulation (SGS, Deutsch and Journel, 1998) with a Gaussian variogram to extrapolate surfaces from 2.5D stratigraphic contacts. As the best-constrained G9 MFS has a 105° dip orientation, the author adopted this orientation as the updip-downdip orientation in this study. Applying to this map-view grid, the author constructed 38 outcrop-constrained PCS-10 surfaces and 15 subsurface surfaces (Step 3) by (1) extrapolating from digitized stratigraphic contacts below G9 MFS, (2) resampling from Scott (2007)'s surfaces between G9 MFS, and (3) deforming Kerans and Sitgreaves (2015)'s subsurface-constrained 15 PCS-11 surfaces, which was extrapolated using refinement gridding (Shi et al., 2013). Subsequently, the author layered the stratigraphic model vertically to an average thickness of 1~2ft to capture subtle vertical facies variation to mimic the stratification style per zone (Janson et al., 2007). Details of stratigraphic correlation, modeling and gridding will be presented in a subsequent section, including examples for three sub-models and their integration into one stratigraphic model.

The author upscaled facies logs to the vertical scale of this stratigraphic grid, and then extrapolated facies from these upscaled logs using a variety of facies modeling method (Step 4), including Constant Facies Value (CFV), Stochastic Object Modeling (SOM, Adam et al., 2005), Truncated Gaussian Simulation (TGS) with Trend (Matheron et al., 1987, Ravenne and Beucher, 1988, Rudkiewicz et al., 1990, Galli et al., 1994, Labourdette et al., 2008; ; Amour et al., 2013), and Pluri-Gaussian Simulation (PGS, Le Loc'h et al.,

1994, Galli et al., 2006; Yarus et al. 2012), depending on the heterogeneity per zone. Details of facies modeling will be presented in a subsequent section, starting with a decision tree for method selection/combination per zone in outcrop-constrained PCS-10 model, and the resultant four scenarios (S₁, S₂, S₃, and S₄) in facies modeling per zone. After an information extraction from outcrop photos, the author presented examples respectively for S₂, S₃, and S₄, as S₁ is merely assigning a constant facies for some highly-homogeneous zones. Finally, the author presented a facies modeling example of subsurface-constrained PCS-11 using PGS (Kerans and Sitgreaves, 2015).

Here lithofacies was chosen as the primary unit for property analysis and modeling (Step 5), as it represent distinct rock elements with characteristic grain types, compositions, and sedimentary structures that form the basic modeling component, and incorporate key factors influencing the sonic velocity of mixed carbonate-siliciclastic units, including porosity, primary pore type, quartz content, and dolomite content (Anselmetti and Eberli, 1993; Kenter et al., 2001; Kenter et al., 1997; Janson et al, 2007; Janson and Fomel, 2010). After velocity and density analysis per facies using outcrop plugs and six type wells, the author assigned an average velocity-density pair per lithofacies to build the velocity and density models for both outcrop and subsurface dataset. Note a systematically slower velocity measurement from outcrop plugs, the author made adjustment for a better analog of CBP field seismic. Details of acoustic property analysis, adjustment, and modeling will be presented in a subsequent section.

Finally, the author stitched the subsurface-constrained acoustic property model (sonic velocity and density) above the G9 HFS top of outcrop-constrained model along a 105° dip, then generated a single synthetic forward model (Step 6) in the depth domain for future direct comparison with the stratigraphic model. The forward-seismic modeling approach applied here uses a waveform-based exploding reflector model (Claerbout et al.,

1985; Janson and Fomel, 2010). This model simulates the acoustic wavefield and then migrates this to the depth domain, where the acoustic wave equation is solved using extended split-step Fourier method (Kessinger, 1992) with its advantage to accommodate for fast lateral velocity changes. For a close analog with the CBP field seismic, the author resampled the velocity and density model of a stratigraphic grid to a regular grid of $20 \times 20 \times 1\text{m}$ to mimic the receiver alignment in the CBP field (65ft/19.8m). Moreover, the CBP field seismic serves as a quality control during the synthetic seismic modeling.

3. 5. STRATIGRAPHIC CORRELATION, MODELING AND GRIDDING (STEP 2~3)

3.5.1 An overview of hard constraints and modeling methods

The stratigraphic model was integrated from three sub-models with distinct hard constraints and methods during surface modeling (Table 3.1). In the subsequent subsections, the author introduce the stratigraphic correlation, modeling, and gridding workflow, with examples of resultant stratigraphic surfaces for three sub-models (Section 5.2~5.4), followed by their stratigraphic model integration into a single seamless model.

	Constraints	Surface modeling methods	Stratigraphic model integration
PCS-11	(1) Well tops for 15 surfaces (2) Seismic horizon for G9 top and the base of main evaporite	Refinement gridding by Kerans and Sitgreaves, 2015)	(1) Deform relative to G9 top from PCS-10 upper model (2) Crop an area with similar size as PCS-10 upper model (3) Rotate 30° clockwise to align with PCS-10 upper model
PCS-10 upper	Digitized 2.5D stratigraphic contacts on LIDAR canyon wall by Scott (2007)	(1) Sequential Gaussain Simulation (SGS), and flattened to a local datum of 'HSS' (Scott, 2007) (2) Surface resampling to the new 105° oriented grid	Remain the same
PCS-10 lower	Digitized 2.5D stratigraphic contacts on georeferenced Sonnenfeld and Cross (1993)'s cross-section	Convergent interpolation	Deform relative to G9 MFS from PCS-10 upper model

Table 3.1: Surface modeling methodology overview and integration of three sub-models.

3.5.2 Outcrop-constrained upper PCS-10 flattened to HSS (Model I-b)

The PCS-10 upper model between G9 MFS and G9 top is the core modeling interval in this study (shaded in gray, Table I), being made up of strongly-progradational mixed clastic-carbonate clinoforms (G9-HFC5~14, Figure 3.6b) with 42 measured sections, thus ground-based LIDAR images acquired by Phelps (2006) and Scott (2007), combined these detailed measured section data permit high-resolution mapping of this complex stratigraphy (Figure 3.5, Bellian et al. 2005; Janson et al., 2007; Buckley et al., 2008; Burton et al., 2011). Scott (2007) digitized stratigraphic contacts of 19 surfaces between G9 MFS and G9 top, including each cycle top and some flooding surface per cycle for HFC5~14 (Figure 3.5), and then extrapolated to 19 surfaces using SGS (Deutsch and Journel, 1998) with a Gaussian variogram, which randomly placed highs and lows between data in a manner that honors the Gaussian variogram, thus particularly suitable for modeling the strongly-progradational PCS-10 upper model with shelf-margin promontories and reentrants (Scott, 2007). In order to mitigate the effect of tilting associated with Tertiary uplift, Scott (2007) flattened these surfaces relative to Hayes Sandstone (Figure 3.5, yellow line annotated as 'HSS'), as it was interpreted as a local datum within the lower few meters of Grayburg Formation (Sonnenfeld and Cross, 1993). In this study, the author resampled his flattened surfaces to the new 20×20m grid in an area of 5×3-km with x axis along 105° (compare Figure 3.2c for original and this modeling area), and enforced an additional rule to impose the law of superposition, where younger surfaces never crosscut older surfaces for resampled surfaces in this study.

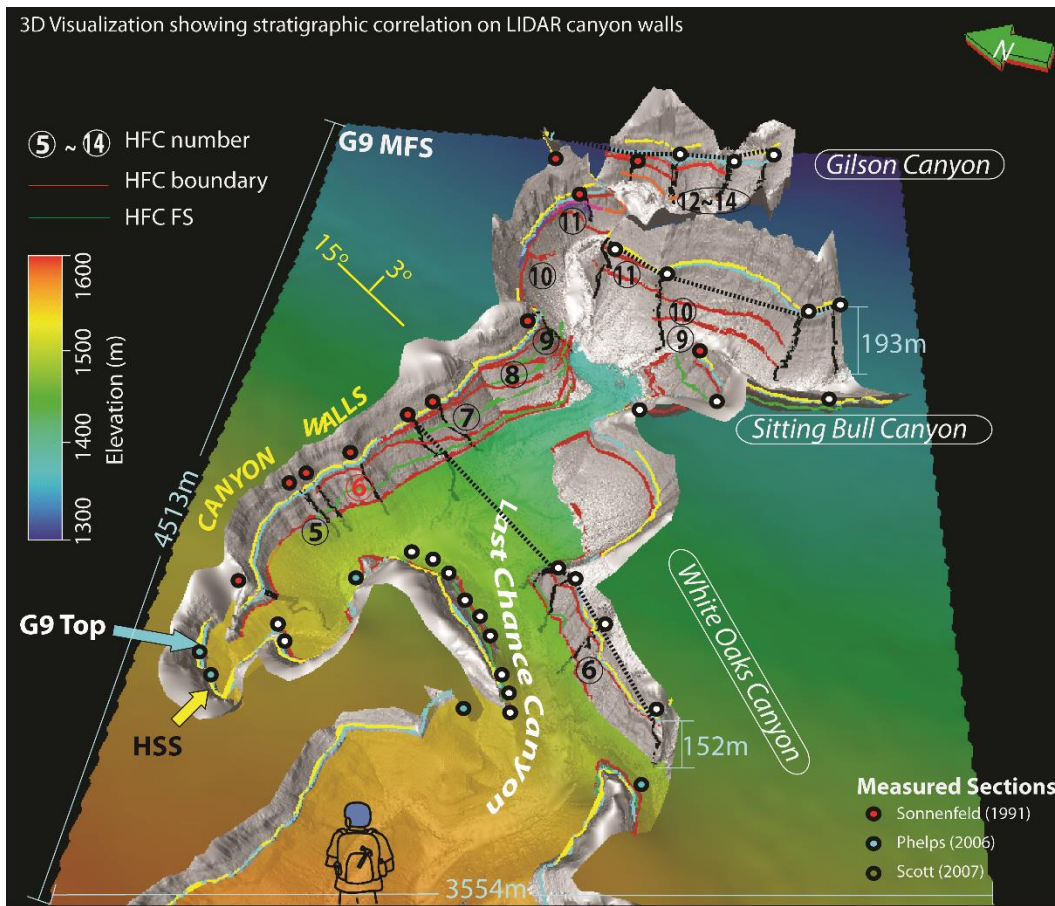


Figure 3.5: 3D visualization of LIDAR-image of canyon walls, showing high-resolution of stratigraphic correlation for G9 HFC5~14 up to HFC scale.

A map-view resampled key stratigraphic surfaces for HFC6 clinoform before flattening is provided as an example (Figure 3.6), including its base, flooding surface and top. The LIDAR image (Figure 3.6a) is predominantly a high resolution DOM, containing both (X, Y, Z) for geometry of canyon walls and intensity (I) information as a sensor for rock properties (Bellian et al., 2005; Burton et al., 2011), thus allows stratigraphic surface mapping on it. Note that the most strongly-prograding clinoforms of these restricted shelves have limited lateral extension (stratigraphic contacts shown as white lines in Figure 3.6b-d), thus the author ensured that the present modeled surface always gradually draped

on its underlying adjacent surface, in the way that the flooding surface of HFC6 conforms to its base surface (compare Figure 3.6b and c), and the top of HFC6 drapes on its respective flooding surface (compare Figure 3.6c and d). After flattening of all surfaces between G9MFS to G9 top (Figure 3.7a and b), the author obtained a more gentle topography. For instance, the slope at the upper slope of G9 MFS is now approximately 3.5~9.4°.

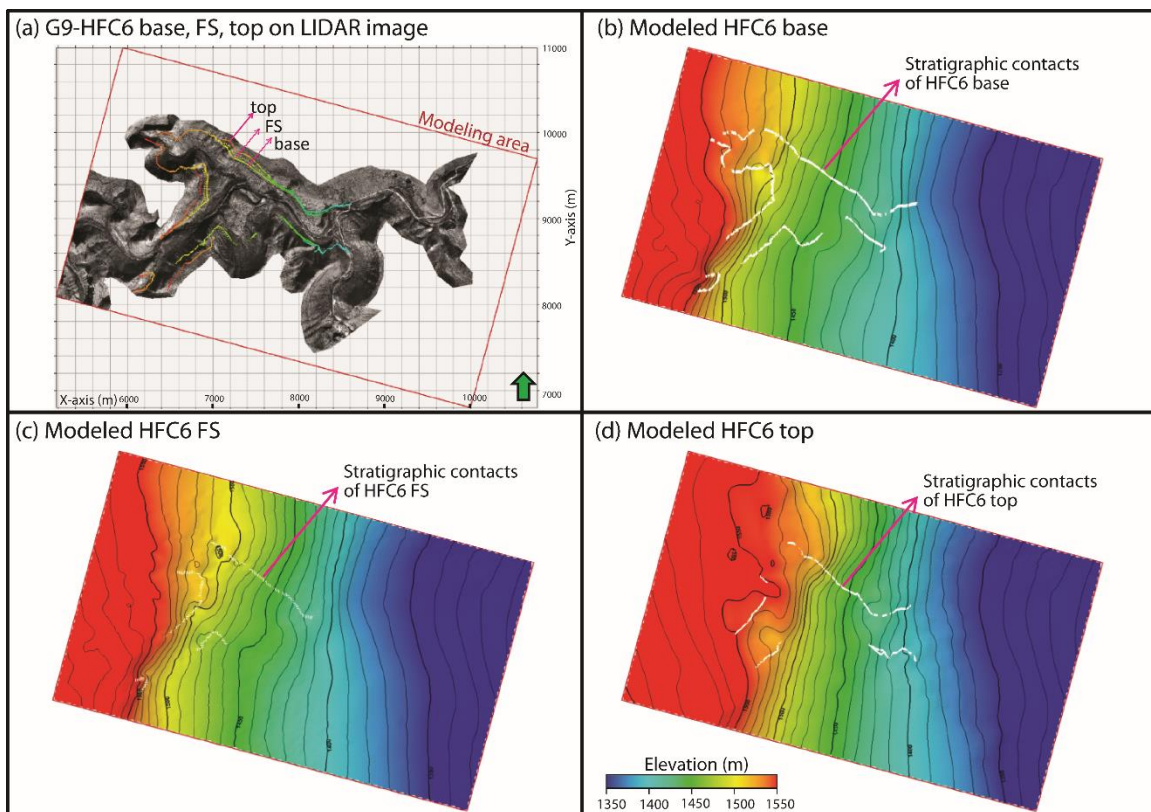


Figure 3.6: An example showing molded stratigraphic surfaces of a HFC. Stratigraphic contacts for the top, flooding surface and base of HFC6 were mapped on LIDAR image of canyon walls, then interpolated using Kriging. Results are shown in (b), (c) and (d).

Subsequently, the author layered the upper PCS-10 stratigraphic model to an average layer thickness of 1ft. A zone of transgressive hemicycle was layered by following

the zone top/cycle top. In comparison, a zone of regressive hemicycle was layered by following its reference surface, which is the average of the zone base and top, namely the flooding surface and top of this regressive hemicycle. Examples of layering will be given when presenting facies modeling examples in the next section.

3.5.3 Outcrop-constrained lower PCS-10 (Model I-a)

In comparison, the lower PCS-10 lower model below G9 MFS, that is made up of distally-steepened ramp strata (G9-HFC1~4 and lower HFS's) lacks sufficient controls from measured sections and outcrop plugs to model deterministically in this study. Fortunately, there is less along-strike lithostratigraphic variability with more linear/stratigraphic facies boundaries, as shown in Phelps and Kerans (2007)'s 3D depositional of G8 HFS exposed at Last Chance Canyon and surface-based facies model. Therefore, the author georeferenced Sonnenfeld and Cross (1993)'s cross-section, and digitized 2.5D stratigraphic contacts of the high-frequency cycle boundaries and flooding surfaces. Assuming a very gentle along-strike stratigraphic and facies variation, the author shifted and duplicated these stratigraphic contacts along strike as additional constraints, from which the author extrapolated 3D stratigraphic surfaces using polynomial-interpolation-based normal convergent interpolation in Petrel, as this method uses a series of refinements to locally tune the surface to neighboring data and reduces wild extrapolations (SCM, 2014), thus is suitable for modeling these gently-dipping surfaces.

As shown in the example of G9 MFS as the top of this modeling interval, the author digitized the G9 MFS stratigraphic contacts (shown as purple solid line in Figure 3.7d) on the georeferenced section, and then shifted and duplicated it along the strike orientation (15°) forward/southward for 1160m and 1740 meters, and northward/backward for 580 meters as three additional constraints (shown as purple dashed line in Figure 3.7d). The

resultant surface has exhibited little along strike variations, with a dip angle of oscillating slightly around 5° at the upper slope.

Subsequently, the author layered the stratigraphic model to an average thickness of 2 feet, by applying proportional layering for most zones. Exceptions are a few zones of transgressive sandstone or siltstone (such as G9-HFC1), where the author layered by following the top for an onlapping stratification.

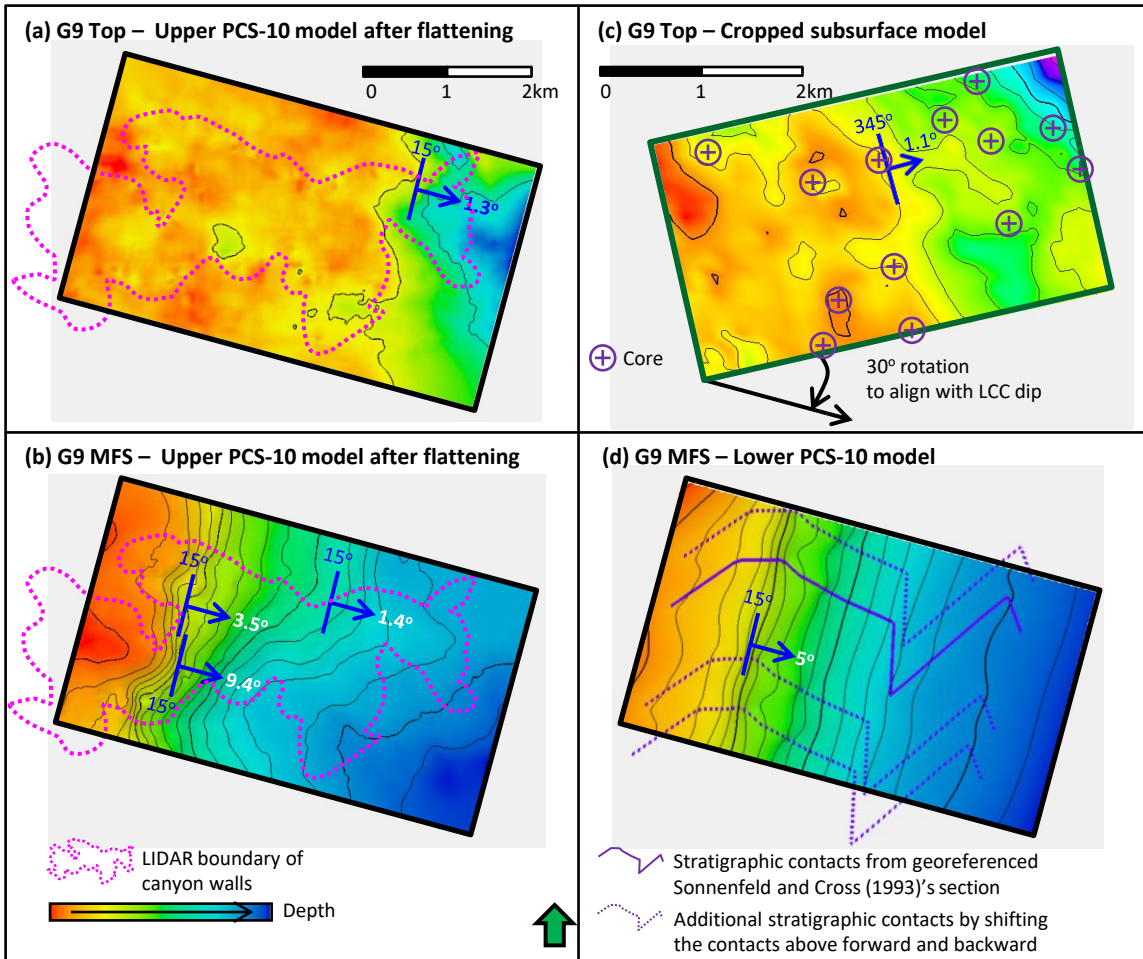


Figure 3.7: Selected surfaces for three sub-models. (a) and (b) are LIDAR-constrained G9 top and MFS flattened to Hayes sandstone to mitigate effect from Tertiary uplift. (c) is the cropped subsurface model to a similar size of LCC model, it shows a similar topography with (a) after rotating 30° clockwise. (d) is the G9 MFS as the top of lower PCS-10 model which assumed little along-strike topographic variation, thus the author deformed all these lower PCS-10 surfaces in relative to the LIDAR-constrained G9 MFS in (b).

3.5.4 Cropped subsurface-constrained PCS-11 (Model II)

For this seismic-covered subsurface modeling area (purple outline, Figure 3.2d), wells penetrating PCS-11 are clustered in the center area and sparsely distributed in toward the North and South ends. Therefore, Kerans and Sitgreaves (2015)'s stratigraphic

correlation and modeling utilized both 16 cores and seismic data for high-resolution stratigraphic correlation. Kerans and Sitgreaves (2015) interpreted well tops for 15 surfaces (Figure 3.8), including G9, G10, G11, and G12 HFS tops (Figure 3.8, black lines), along with a few intermediate surfaces within the Grayburg Formation of G10~G12 (Figure 3.8, green lines), and key datum surfaces within Lower Queen Formation of G13 (Figure 3.8, pink lines). This correlation is based upon Kerans et al. (2014)'s updated Grayburg model, which was supported by Hiebert (2010) and Parker (2010)'s studies of Shattuck Escarpment. These interpreted well tops as the primary control, combined with selected seismic horizons (i.e. the base of main evaporite and the G9 top), allows the construction of 15 key surfaces on a map-view regular grid of 150×150ft (45.7×45.7m) using refinement gridding (Shi et al., 2013), which conducts a series of refinements until the target grid cell size is reached, by passing the surface model through a biharmonic filter to produce a smooth surface with minimum curvature in area without a fault. The resultant 14 intervals were mostly layered by proportional layering to an average thickness of 2 ft, except for Zone 6 (Figure 3.8) being layered by following its top. In this study, the author cropped a 4.1×2.5km center area (green box in Figure 3.2d) from Kerans and Sitgreaves (2015)'s 4.1× 5.8km model (black box in Figure 3.2d), and then named it as 'Model II'. This area was chosen both for its densest well control, and for its similar reconstructed topography of G9 top (Figure 3.7c) with that from outcrop-constrained PCS-10 model (Figure 3.7a).

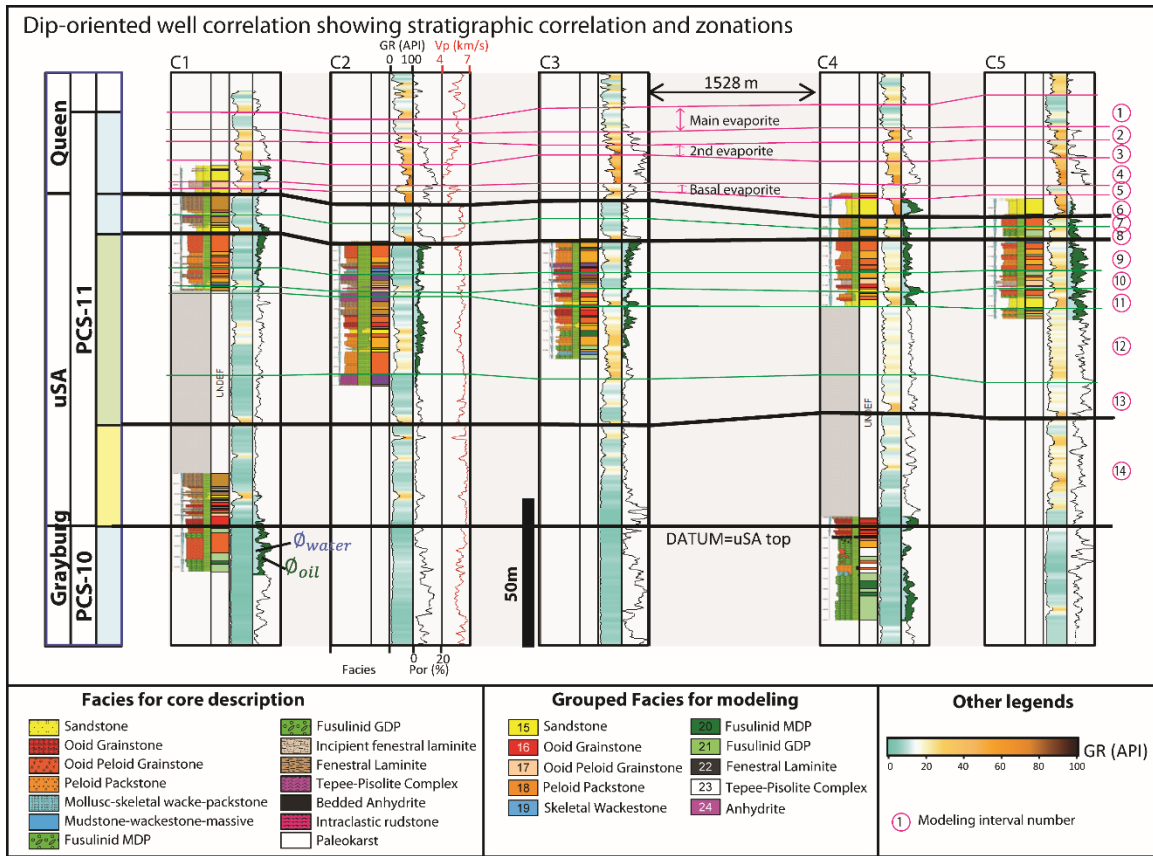


Figure 3.8: Dip-oriented well panel (see Figure 3.2d for location), showing stratigraphic correlation and zonation for subsurface-constrained PCS-11.

3.5.5 Integration for a single stratigraphic model

Since the above stratigraphic model construction was implemented separately, the author made certain adjustments for a single stratigraphic model. As the outcrop-constrained upper PCS-10 (Model I-b) is the core modeling interval all of its surfaces from G9 MFS to G9 top remained unchanged. The author deformed all surfaces in outcrop-constrained Lower PCS-10 model (Model I-a) in relative to G9 MFS from Model I-b, and then obtained a composite outcrop-constrained PCS-10. As a result, the adjusted 38 stratigraphic surfaces in PCS-10 on the dip-oriented section (Figure 3.10a) are closely comparable to Sonnenfeld (1991)'s interpretation, that showed clinofolds evolving from

oblique to complex oblique-sigmoidal. Besides, three strike cross-sections (Figure 3.10b1, b2, and b3) are taken to highlight the younger strongly-progradational clinoforms (HFC6~HFC14), which all show moderate to strong along-strike topographic variability near the shelf margin, featured by promontories and reentrants, where Scott (2007) interpreted the distance between adjacent promontories being 200 to 500 meters.

Next, the author needed to stitch the cropped subsurface-based PCS-11 model (Model II) above this outcrop-constrained PCS-10 model (Model Ia+Ib). The author scaled up the 4.1×2.5km cropped subsurface PCS-11 model (Model II) to the same size of 5×3km PCS-10 model, and then rotated the new PCS-11 model clockwise for 30° (Figure 3.8c) so that its dip is aligned with that of PCS-10. Finally the author deformed all surfaces in this model relative to the G9 top from Model I-b, and eventually constructed a seamless San Andres-Grayburg stratigraphic model.

3.6 FACIES MODELING (STEP 4)

3.6.1 PCS-10 facies modeling overview and method selection per zone

In order to populate lithofacies across the stratigraphic grid of PCS-10, measured sections were upscaled and then extrapolated per zone, using one or a combination of three following geostatistical methods (Table 3.2). Constant Facies Value (CFV) assigns a constant facies for a relatively homogenous zone of sandstone or mudstone. Pixel-based Stochastic-Object Modeling (SOM) enables a simulation of localized objects, such as turbidite channels (Falivene et al., 2006) and bioherms (Adam et al., 2005). In addition, Truncated Gaussian Simulation (Matheron et al., 1987, Ravenne and Beucher, 1988, Rudkiewicz et al., 1990) ensures an ordered basinward facies transition in shoreface and carbonate ramps/slopes (Galli et al., 1994, Labourdette et al., 2008; Amour et al., 2013).

In practice, the author designed a two-step query tree to select and combine these three methods, in order to accommodate for four scenarios that may occur for a zone (Table 3.3). This query essentially questioned a larger- and smaller- scale of heterogeneity within a zone, by sequentially examining if the modeling zone exhibits highly-ordered basinward facies transition, and if it includes localized objects. Consequently, in cases of relatively homogeneous sandstone/mudstone without both features (Scenario 1/ S_1), CFV was used to assign a constant facies for these HFC's. In cases of no highly-ordered facies transition but containing localized objects (Scenario 2/ S_2), SOM was used alone to insert localized objects in homogeneous background. In cases of highly-ordered facies transition without any additional localized objects (Scenario 3/ S_3), TGS with trend ensured this transition. In the most complicated scenario (Scenario 4/ S_4), a certain modeling zone/hemicycle both exhibit strongly-ordered basinward facies transition and certainly contain localized mounds/buildups (F6-M/B), the author used TGS with trend to model a primary facies fabric of basinward facies transition, and then inserted bioherms within its upper slope facies tract (F3-fpMDP, F4-fpW, F5-pW). In a few extreme cases when bioherm strongly affected the overlying facies, two iterations may be necessary to fit local deposition pattern strongly influenced by bioherms. Examples will be presented for S_2 , S_3 , and S_4 , after an analysis of outcrop photos for along-strike facies variability and dimensionality.

	System Tract	Zone	Sections	Layering methods	Facies modeling methods					
					Scenario	CFV	SOM	TGS, facies transition type		
Model b	G9-IHST	HFC14 proximal	6	Follow top	S3			F1->F2->F3->F4->F8	III	
		HFC13 proximal	8	Follow ref. surface	S3			F1->F2->F3->F4->F8	III	
		HFC12b proximal	7	Follow ref. surface	S4		bioherm (F2)	F1->F2->F3->F4->F8	III	
		HFC12a upper	9	Follow ref. surface	S3			F1->F2->F3->F4->F8	III	
		HFC12a sand onalp	5	Follow top	S3			F2->F3->F8	III	
		HFC11b reef1	2	Proportional	S3			F6->F13	III*	
			HFC11a	9	Follow ref. surface	S4		bioherm (F2)	F1->F2->F3->F4->F5->F8	III
			HFC10	11	Follow ref. surface	S4		bioherm, channel	F1->F2->F3->F4->F8	III
			HFC9-R	9	Follow ref. surface	S3			F1->F2->F3->F4->F8	III
			HFC9-T	9	Follow top	S3			F1->F2->F3->F4->F5->F8	III
			HFC8-R	7	Follow ref. surface	S3			F1->F2->F3->F4->F8	III
			HFC8-T	7	Follow top	S2		channel (F7)		
			HFC7-R	11	Follow ref. surface	S4		bioherm (F2)	F1->F2->F3->F4->F8	III
			HFC7-T	15	Proportional	S4		channel (F7)	F1->F2->F3->F4->F8	III
			HFC6-R	28	Follow ref. surface	S4		channel (F7)	F1->F2->F3->F4->F5->F8	III
			HFC6-T	28	Follow top	S3			F1->F2->F3->F4->F5->F8	III
	G9-eHST	HFC5	16	Proportional	S4		bioherm (F2)	F2->F3->F4->F12->F10	I	
Model a	G9-TST	HFC4-R	13*	Proportional	S3			F3->F4->F12->F10	I	
		HFC4-T	13*	Follow top	S3			F4->F12->F10	I	
		HFC3-R	13*	Proportional	S3			F4->F12->F9->F10	II	
		HFC3-T	13*	Follow top	S1	F10				
	G9-LST	HFC2-R	13*	Proportional	S3			F12->F9	II	
		HFC2-T	13*	Follow top	S3			F12->F9->F10	II	
		HFC1-Lower Cherry Canyon	13*	Follow top	S1	F8				
	G8	HFC5	13*	Proportional	S3			F4->F12->F10	I	
		HFC4-R	13*	Follow top	S3			F12->F10	I	
		HFC4-T	13*	Proportional	S2		intraclstics (F14)	F4->F12->F10	I	
		HFC2-R	13*	Proportional	S1	F10				
		HFC2-thin layer	13*	Proportional	S1	F13				
		HFC2-T	13*	Proportional	S1	F14				
		mudstone 2	13*	Proportional	S1	F10				
		a thin sandstone layer	13*	Follow top	S1	F3				
		Brushy Canyon Sandstone	13*	Follow top	S1	F3				
mudstone 1		13*	Follow top	S1	F10					
		below mud	13*	Follow top	S1	F8				
Notes	System tract, HFC number, and digitized vertical measured section (denoted with *) refers to Sonnenfeld and Cross (1993) See Table 3.3 for the selection of facies modeling methods for four scenarios (S1, S2, S3, and S4) See Table 3.4 for parameters used in SOM, and Table * for three types of basinward facies transition simulated by TGS with Trend									

Table 3.2: Facies modeling overview, with zonation information, as well as number of measured sections, layering and modeling method per zone.

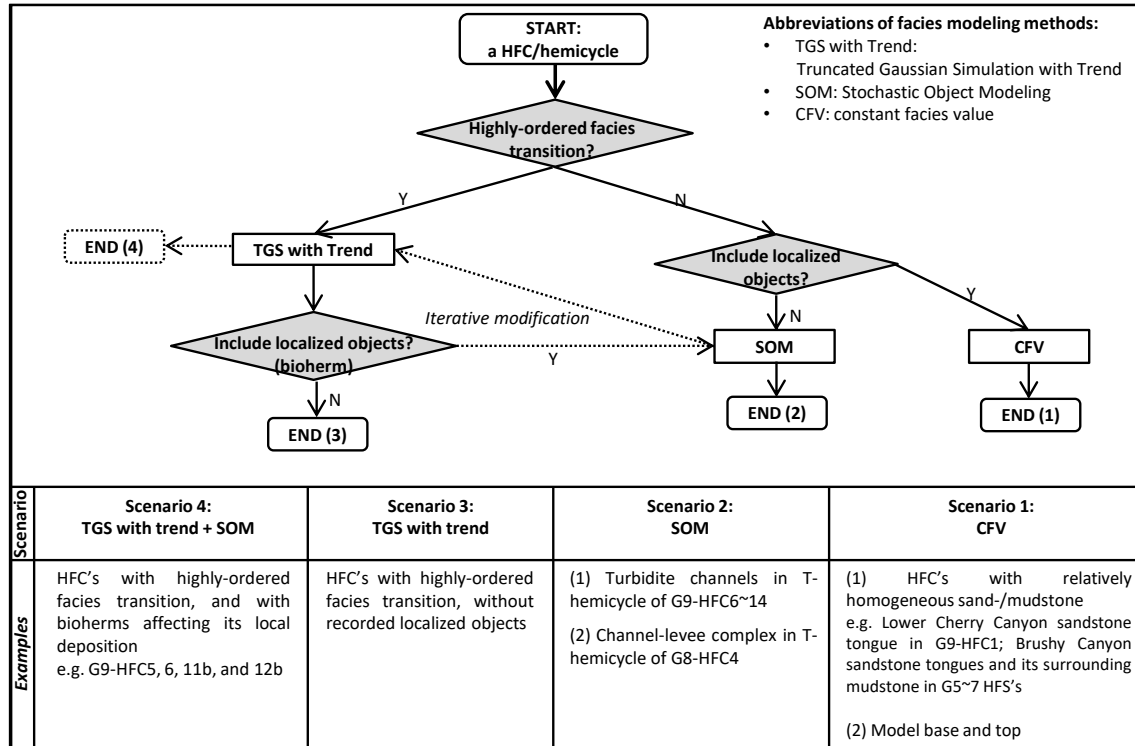


Table 3.3: The decision tree to select and combine facies modeling methods, and four scenarios.

3.6.2 PCS-10 along-strike facies variability and dimensionality from outcrop photos

The author used Scott (2007)'s outcrop photos (Figure 3.9) to interpret cross-well along-strike facies variability within stratigraphic surfaces (Figure 3.10, He et al. 2016), and to obtain facies dimensionality information for localized objects (Figure 3.11). The selected along-strike photos (Figure 3.9a) are from the West and East wall of White Oaks Canyon (Figure 3.9b and c) and the East wall of Sitting Bulls Canyon (Figure 3.9d). Besides, a dip-oriented photo was chosen near the vicinity of Gilson Canyon (Figure 3.9e), as it highlights a special HFC of major reef development (HFC11b) and its affected HFC12a.

As exhibited in the large outcrop photo at the East Wall of White Oak Canyon (Figure 3.9c), the lateral facies variability for strongly-progradational HFC's above G9 MFS is much stronger than that of weakly-progradational HFC's below G9 MFS. This observation agrees with Phelps and Kerans (2007)'s 3D idealized facies model showing a more linear/straight facies boundaries. Therefore, the author assumed a moderate to strong along-strike facies variability for G9 HFC5~14 and a weak one for the lower HFC's in PCS10.

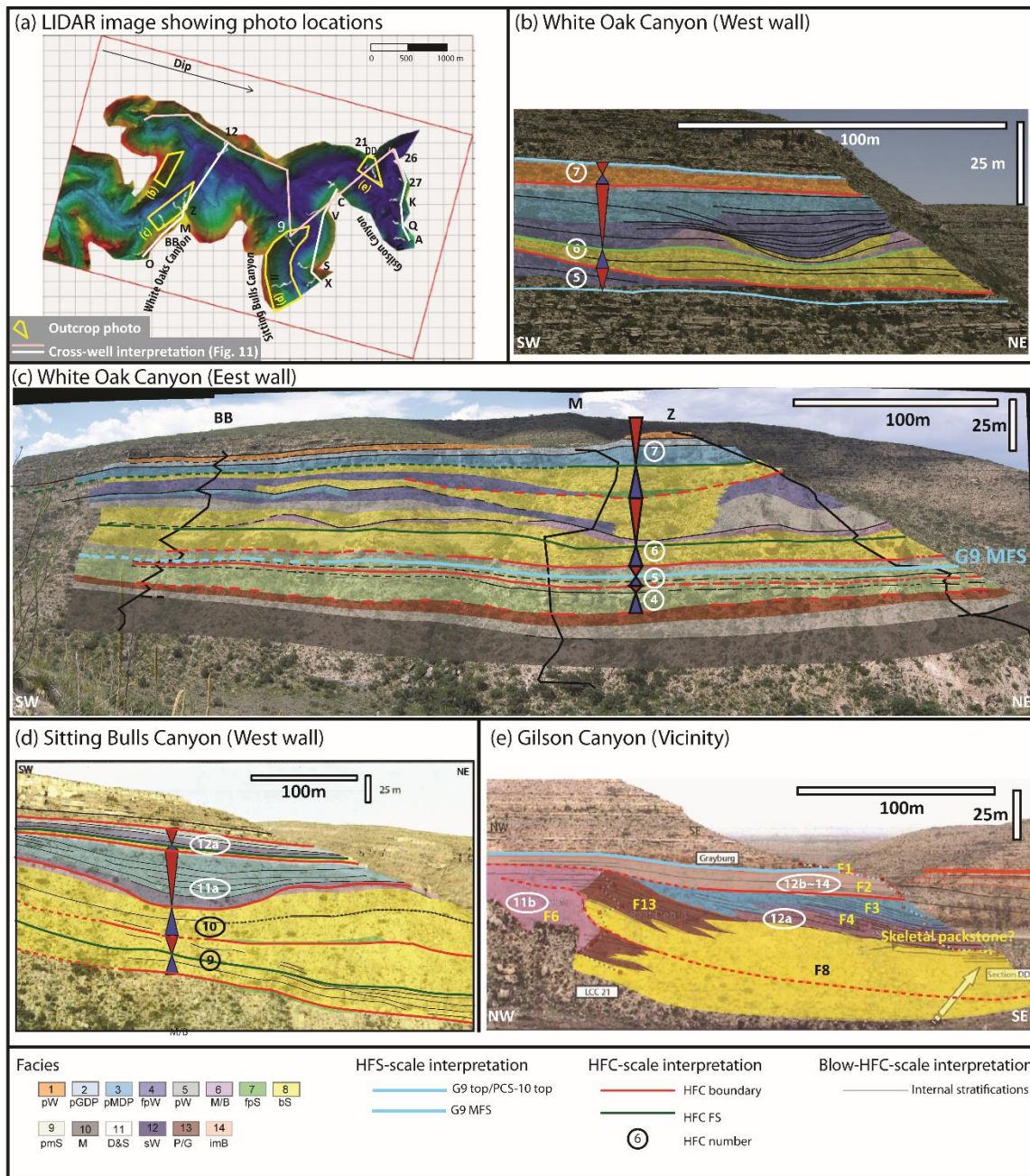


Figure 3.9: Outcrop photos showing along-strike facies variability and dimensionality (modified from Scott, 2007). (a) LIDAR image of canyon walls showing outcrop photo locations. (b)~(d) along-strike outcrop photos from updip to downdip. (e) in the vicinity of Gilson Canyon, showing a major reef development in HFC11b, and its affected HFC12a.

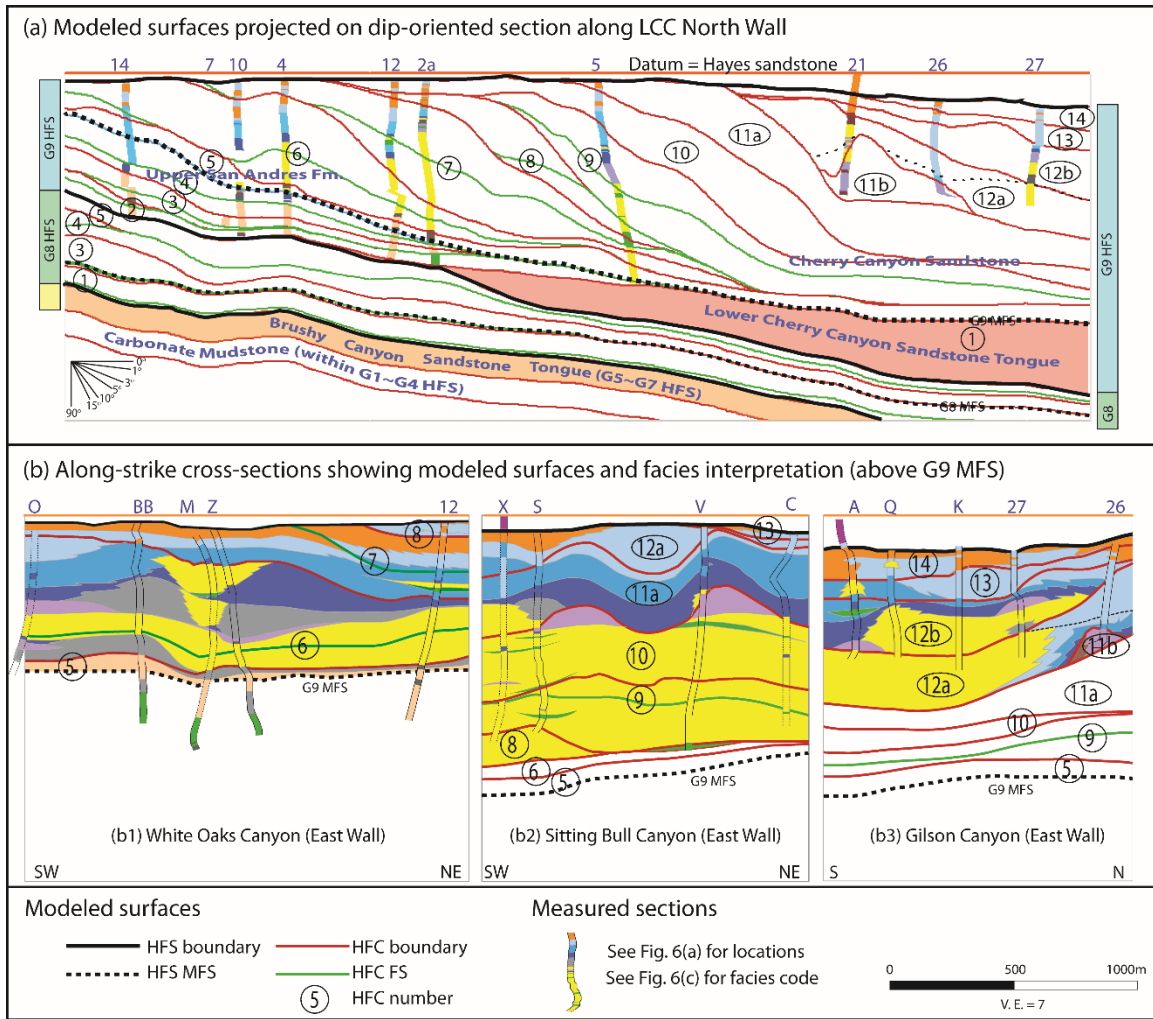


Figure 3.10: Modeled stratigraphic surfaces and along-strike interpretations, with locations shown in Figure 3.9a. (a) Dip-oriented section showing Sonnenfeld and Cross (1993)'s cross-section from measured section 14 to 27. (b) Along-stick cross-sections showing facies interpretation within modeled stratigraphic surfaces, along the East walls of (b1) White Oaks Canyon, (b2) Sitting Bulls Canyon, and (b3) Gilson Canyon.

The shelf-margin promontory/reentrant topography for G9 HFC5~14 resulted in along-strike differential deposition, thus further leads to sinuous facies boundaries in plane view. The shelf-margin reentrants served as preferential pathways for siliciclastic bypass (Scott, 2007, Kerans et al., 2013), as shown in the HFC6 (Figure 3.9b, c, Figure 3.10b1),

HFC-11a (Figure 3.10b2), HFC12a and 12b (Figure 3.10b3). In comparison, with their elevated topography and shallower water depth, the shelf-margin promontories became the preferential sites for authigenic carbonate deposition, especially for the reef/bioherm deposition, as shown in (Scott, 2007, Kerans et al., 2013), as shown in the HFC6-R (Figure 3.9a,b, and Figure 3.10b1), HFC10 (Figure 3.9d, Figure 3.10d), as well as HFC11b and Figure 3.11a (Figure 3.9e and Figure 3.10b3). Therefore, in the map view, the resultant carbonate-siliciclastic facies boundary curves landward at the shelf-margin reentrants, while curves basinward at the shelf-margin promontories (Figure 3.3a).

Outcrop photos, combined with upscaled measured sections, also provided us some basic information for section-view geometry of localized objects (Figure 3.11a), including the turbidite channels (F7-fpS) encased in bioturbated sandstone (F8-pS), and mounds/bioherms (F2-M/B) deposited within upper-slope facies (F3-fpMDP, F4-fpW, F5-fpW). From the above outcrop photos and an additional along-strike photo from Scott (2007, Figure 3.1.14), the author located six bioherms and six turbidite channels, measured their observed maximum thickness and width from DOM for improved accuracy and then plotted the results in the crossplot shown in Figure 3.11. Given these measurements are highly dependent on its azimuth when exposing on the way and its internal position, thus can not provide us actual maximum width and thickness per localized object, they do provide some typical values to set up a size distribution for these localized objects (Table 3.4) when combining with thickness measurements from measured sections (Figure 3.11b), and referring to similar scenarios. Meanwhile, the author also calculated the seismic resolution of their surrounding rocks at a 35Hz peak frequency/27 Hz dominant frequency, where that of bioturbated sandstone is 38.6m and of Fusulinid peloid wackestone is 43.6m. A comparison with the observed object size (Figure 3.11a) shows that most of these localized objects are below vertical seismic resolution, while resolvable in map view. An

exception of F6 herein is the major reef development in HFC11b and HFC12a (Figure 3.9e), whose cumulative thickness reaches 47 meters and thus anticipated to be resolvable from seismic. Therefore, during facies modeling, the author modeled all these sub-seismic-resolution localized objects using SOM, while modeled the major reef development and its debris (F13- Allodapic coated pack/grainstone) using TGS with trend.

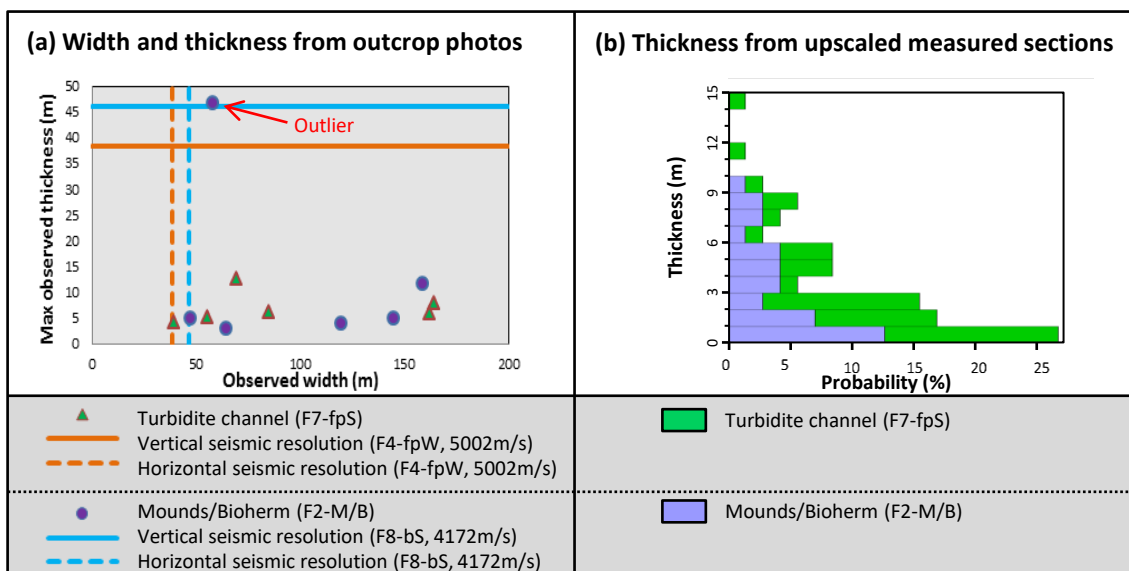


Figure 3.11: Observed width and maximum thickness for localized objects from outcrop photos, including the turbidite channels (F7-fpS) and mounds/bioherms (F6-M/B). In both case, most localized objects are well below vertical seismic resolution of their background facies, whereas above horizontal seismic resolution at a dominant frequency of 27 Hz or peak frequency at 35Hz.

3.6.3 Modeling highly-ordered facies transition using TGS with trend – an example of Scenario 3

Three types of highly-ordered basinward facies transition were classified in this study (Table 3.4), on the basis of the order of facies occurrence and their along-strike facies variability. The author named the Type I-III in their order of relative geologic time from older to younger, where Type I, II, III facies transition, which respectively characterized

the carbonate-dominant ramps of G8-HFC2~5, the upper carbonate-lower silty-clastics weekly-progradational shelf of G9-HFC1~5, and the upper carbonate-lower sandstone strongly-progradational shelf of G9-HFC6~14. In general, the author observed increasing siliciclastic contents from Type I to Type III facies transition. Besides, as discussed in the outcrop photo analysis, Type III exhibits stronger facies variability than Type I and II, thus the author assumed sinuous map-view facies boundaries for Type III, and linear/straight ones for Type I and II.

Facies transition	Applicable targets	Idealized order for basinal facies transition	Along-strike facies variability
Type-III	Upper carbonate-lower sandstone strongly-progradational shelf e.g. G9-HFC6~14	F1->F2->F3->F4->F5->F8	Moderate to Strong
		F6->F13, an exception for HFC11b	
Type-II	Upper carbonate-lower silty clastics weekly-progradational shelf e.g. G9 - HFC2~3	F4->F12->F9->F10 Featured in the inclusion of F9-Glaucinite peloid muddy siltstone	Weak (assumed)
Type-I	Carbonate-dominant ramps and weekly-progradational shelf (G8 - HFC4~5, G9-HFC1,4,5)	F3->F4->F12->F10	

Table 3.4: Three types of facies transition, modeled by TGS with Trend in this study, for Scenario 3 or Scenario 4.

The author present an example from the regressive hemicycle of HFC8 here to illustrate the simulation of Type III – highly-ordered facies transition (Figure 3.12). TGS with trend (Matheron et al., 1987, Ravenne and Beucher, 1988, Rudkiewicz et al., 1990) requires a facies proportion volume to define the likelihood of a facies to occur per cell, and a variogram to control the lithofacies continuity along major orientation, minor orientation and vertical direction.

The facies proportion volume, also known as probability volume per facies, defines the likelihood for a certain lithofacies to occur per cell. As the input for facies proportion

volume per zone, the author used a horizontal trend map instead of vertical proportion curve, as lithofacies changes fast along a contemporaneous layer, which makes the simulation result highly-dependent on layering accuracy and available measured section numbers (ranging from 2~28 with a median of 9, Table I) if using the vertical proportion curves. Alternatively, the author draw a horizontal trend map per zone, as it both ensures an definite order of basinward facies transition, and is eligible to control the inclination of lithostratigraphic units to mimic Scott (2007)'s conceptual diagram. More specifically, the author defined a map view basinward facies transition from outer ramp (F1-pS, F2-pGDP), to upper slope (F3-pMDP, F4-fpW), then to lower slope (F8-bS) facies belt, as previously illustrated in Scott (2007)'s idealized facies model (Figure 3.3c). Then the author shaped the map-view lithofacies boundaries to a sinuous pattern (Figure 3.12b) by referring the zone base, namely the HFC8 flooding surface (contoured surface in Figure 3.12a and colored surface in Figure 3.12b), as its topography provided information on both an approximate updip-downdip extension of each facies belt and the locations of shelf-margin promontories and reentrants. In this case, the author identified a dominant promontory (blue arrow, Figure 3.12), and reentrant (red arrow, Figure 3.12). As discussed in the last section, the development of these shelf-margin topographic features led to sinuous facies boundaries in map view, with carbonate-siliciclastic facie boundary curves landward near the reentrant, and basinward near the promontory. Therefore, the author draw the basinward facies boundaries accordingly (denoted as b_1, b_2, b_3, b_4, b_8 with black solid lines, Figure 3.12b). In addition, the landward limits (denoted as l_1, l_2, l_3, l_4, l_8 , black dashed lines, Figure 3.12b) are critical to define, as the along-dip distance between the landward and basinward limit of a facies/the lateral extension of the facies, controls the manner it follows the layering/stratification: a larger distance (blue double-sided arrow, Figure 3.12b) contributes to a better conformance of this lithofacies unit to the stratigraphic

layering (Figure 3.12c), whereas a smaller distance (red double-sided arrow, Figure 3.12b) led to the lithostratigraphic unit to intersect with the layering at a more oblique angle (Figure 3.12d).

Using this trend map along with a Gaussian variogram (Figure 3.12b) to control spatial continuity, the author effectively reproduced Scott (2007)'s 3D conceptual facies transition diagram (Figure 3.1.7 in Scott, 2007) via TGS with Trend. For the variogram the author defined, the author set up the major, minor and vertical range (Figure 3.12b) referring to the typical dip-oriented clinoform size, the distance between adjacent shelf-margin promontories, and the vertical thickness per facies as observed from upscaled facies logs. The nugget and sill controls the lower and upper limit of similarity for two points at an infinitesimally small distance and large distance, where the author chose 0.05 and 1 for this interval. In addition, the variance controls the width of interfingerring facies transition zone, where the small variance here contributes to a shorter facies transition zone.

The resultant facies model for HFC8-R is shown using a fence diagram in Figure 3.12a. As one can compare between the dip-oriented facies fence at the shelf-margin promontory (labeled with blue arrow, Figure 3.12a) and at the reentrant (labeled with red arrow, Figure 3.12a), the author effectively reproduced elevated carbonate/siliciclastic proportion at the shelf-margin promontory than at the reentrant. Besides, the reconstructed vertical lithofacies contacts agree with Scott (2007)'s idealized dip-oriented facies models crossing shelf-margin promontory and reentrant (Figure 3.1.7 in Scott, 2007): the lithostratigraphic units in upper-slope facies tract (F2, F3, F4) is slightly basinward dipping at a shelf-margin promontory, while landward dipping at the reentrant.

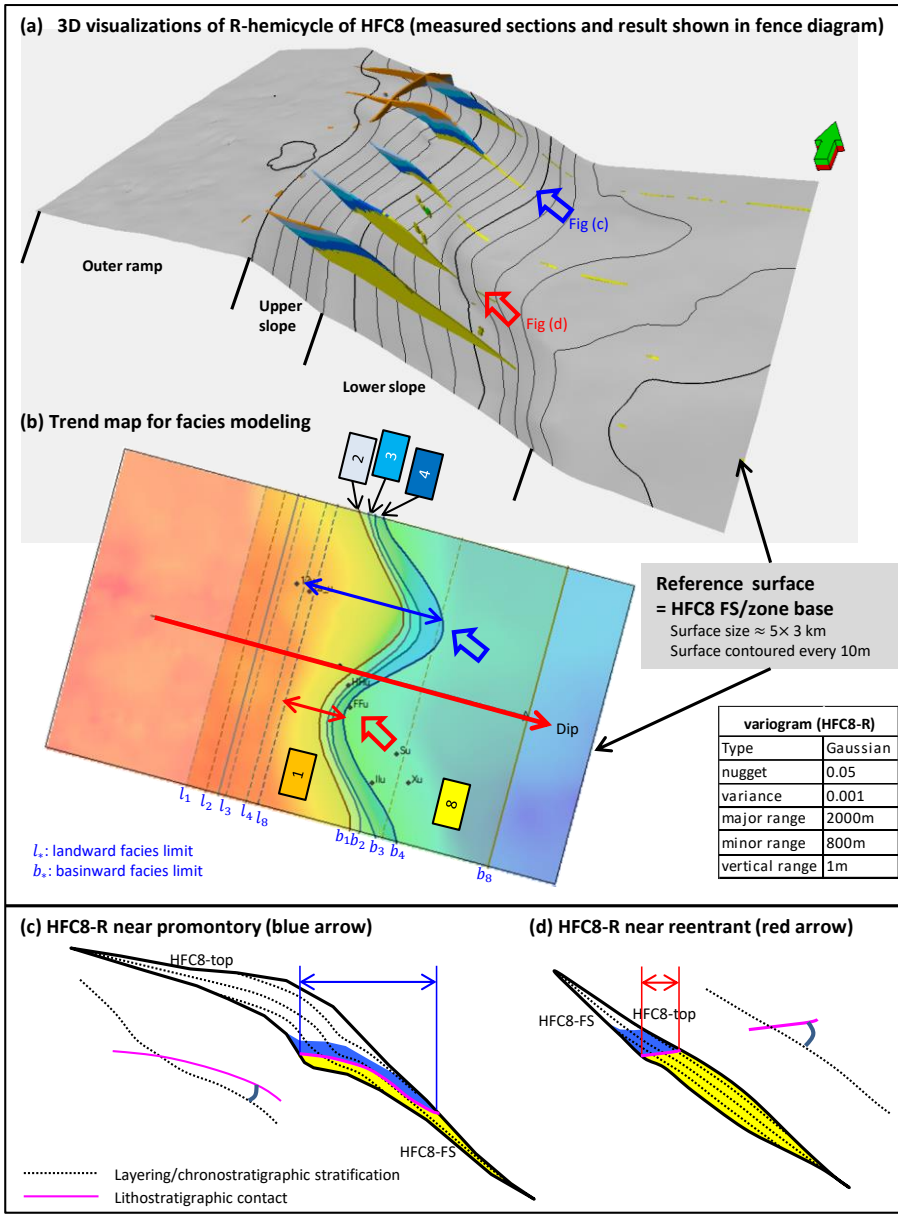


Figure 3.12: An example of modeling highly-ordered facies transition using TGS with Trend, as applied to HFC8-R hemicycle. (a) 3-D visualization of HFC8-R, with measured sections and result displayed in fence diagram, (b) Trend map used for facies modeling, (c) and (d) are resultant facies model near the promontory and reentrant, compared with layering/stratifications.

3.6.4 Modeling localized objects using SOM – an example of Scenario 2

Pixel-based Stochastic Object Modeling (SOM) was used to simulate two localized objects, including turbidite channels (Falivene et al., 2006) and mounds/buildups (Adam et al., 2005) in the mixed clastic-carbonate strongly-progradational HFC6~14 within G9 HFS. Outcrop photos and measured sections (Figure 3.11) has provided thickness and width information for defining section-view geometry, whereas the author referred to similar settings to define plane-view layout. Figure 3.13 shows an illustration and typical parameters used in modeling turbidite channels within bioturbated sandstone as an example of Scenario 2 (Figure 3.13a), and up-rounded bioherms within the upper-slope facies tract of highly-ordered basinward facies transition, as an example of Scenario 4 (Figure 3.13b). Note that, another example of Scenario 2 is the localized intraclastic mudstone megabreccia (F14-imB) within the mudstone (F10-M) G8-HFC4-T (Table I). Without sufficient along-strike hard constraints in this less interested lower interval, the author simplified inserted an elongated intraclastic mudstone megabreccia along the plane of geospatially-corrected Sonnenfeld (1991a)'s cross-section.

Serving as an example of Scenario 2 in facies modeling (Table 3), the author present the modeling of turbidite channels in the transgressive hemicycle of HFC8 (HFC8-T), where channelized Fusulinid peloid sandstone deposits (F7-fpS) were found in erosional contact with bioturbated sandstone (F8-bS, Sonnenfeld and Cross, 1993; Scott, 2007). Since its updip point-source remains unknown (Scott, 2007), the author fitted data-driven adaptive turbidite channels within a bioturbated sandstone matrix. Using the parameters as defined in Figure 3.13a, the author obtained the facies model by assigning the highest priority to honor the hard data of measured sections and by conservatively extrapolating only assured turbidite channels that intersecting with measured sections. The adaptive channels fitted in the resultant model (Figure 3.14b) suggest a preferential updip-source

from shelf-margin promontories, and thus well agrees with Scott (2007)'s interpretation and Kerans et al. (2013)'s 3D depositional model of G9 HFS (Figure 3.3a). Section-view facies model along reentrant and promontories (Figure 3.14c) exhibits these simulated turbidite channels well following the layering/stratifications as localized discontinuities in bioturbated sandstone.

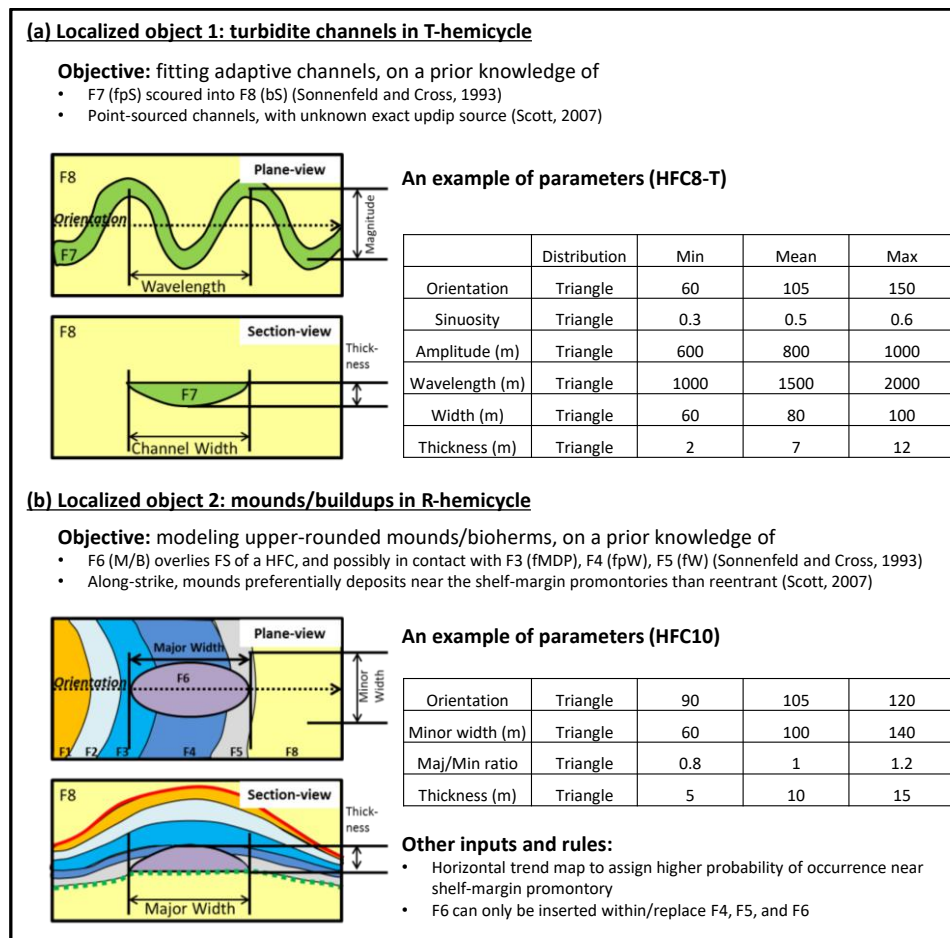


Figure 3.13: Examples of parameters used for simulating localized object of (a) turbidite channels, and (b) mound/buildups. In both case, the author assigned the highest demand to honor hard data of measured sections, and conservatively only generate object that intersect wells.

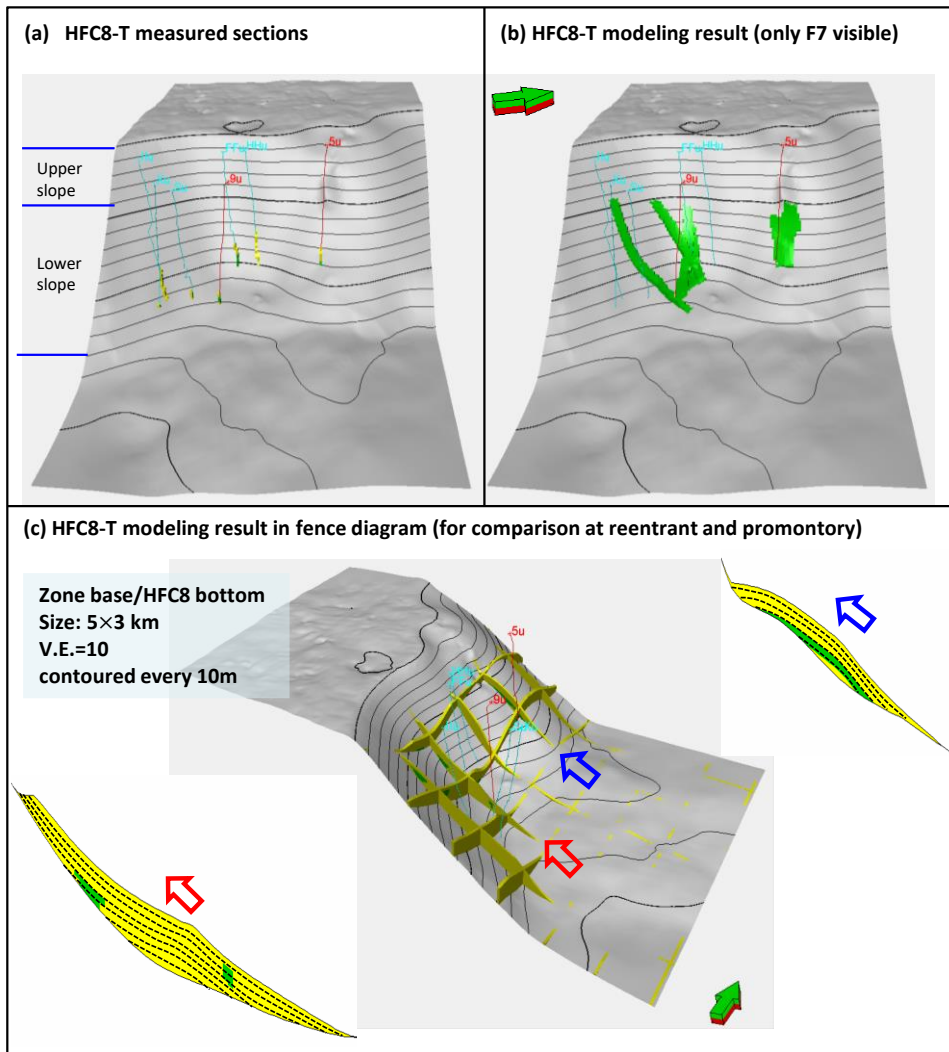


Figure 3.14: An example of modeling adaptive turbidite channel using SOM, as applied to HFC8 transgressive hemicycle. (a) 3-D visualization of measured sections in HFC8-T, (b) 3-D visualization of modeling results, where the background F8-bS is tuned as transparent.

3.6.5 Modeling both large- and small-scale heterogeneity – an example of Scenario 4

The last example in PCS-10 shown in this study is the most complicated example of Scenario 4 in facies modeling (Table 3). Scenario 4 was regarded as the most complicated scenario in facies modeling of this study, as it exhibits large-scale heterogeneity of highly-ordered facies transition, as well as localized objects of both

turbidite channels and bioherms. In addition, the HFC10 is a complex S₄ example. For a typical HFC with both transgressive and regressive hemicycle, such as the discussed HFC8, its zonations have implicitly imposed preferred locations for localized object, where turbidite channels were simulated in the transgressive hemicycles to ensure their lower-slope locations (Figure 3.14), while bioherms were inserted within the upper-slope facies in regressive hemicycles. However, this implicit preferred location for localized object does not directly apply to HFC10, as it has no flooding surface mapped and thus no zonation of transgressive and regressive hemicycle.

Therefore, alternatively, the author simulated the gradual basinward facies transition between 11 measured sections (Figure 3.15a) as a primary facies fabric using TGS with trend, using a similar approach as applied in the previous S₃ example. The resultant shows a thicker and more carbonate-dominant deposition toward the North (Figure 3.15b), with deposition affected by more densely-spaced promontories than the S₃ example. Subsequently, the author modeled the secondary fabric of bioherms using parameters in Figure 3.13b. Note the preferred locations of bioherms herein is enforced by a facies replacement rule, where the author regulated the bioherms to be inserted only within the upper-slope facies belt (F4-fpMDP, F5-fpW), or uppermost bioturbated sandstone (F8-bS), as observed from outcrop photos of HFC6-R (Figure 3.9b) and HFC10 (Figure 3.9d), also as that Scott (2007) reported the gradational contacts between bioherms and F4 or F5, and then interpreted these bioherm communities to be tolerable of limited carbonate debris until eventually being smothered by progradational upper slope deposits. Similar to the previous S₂ example, the author only conservative interpolated bioherms intersecting with the measured sections. The resultant facies model (Figure 3.15c) shows bioherms to follow chronostratigraphic layering as localized discontinuity, where HFC10

was layered by paralleling its middle surface. In the map view, this resultant bioherm is approximately 80×80 in a selected contemporaneous k layer (Figure 3.15d).

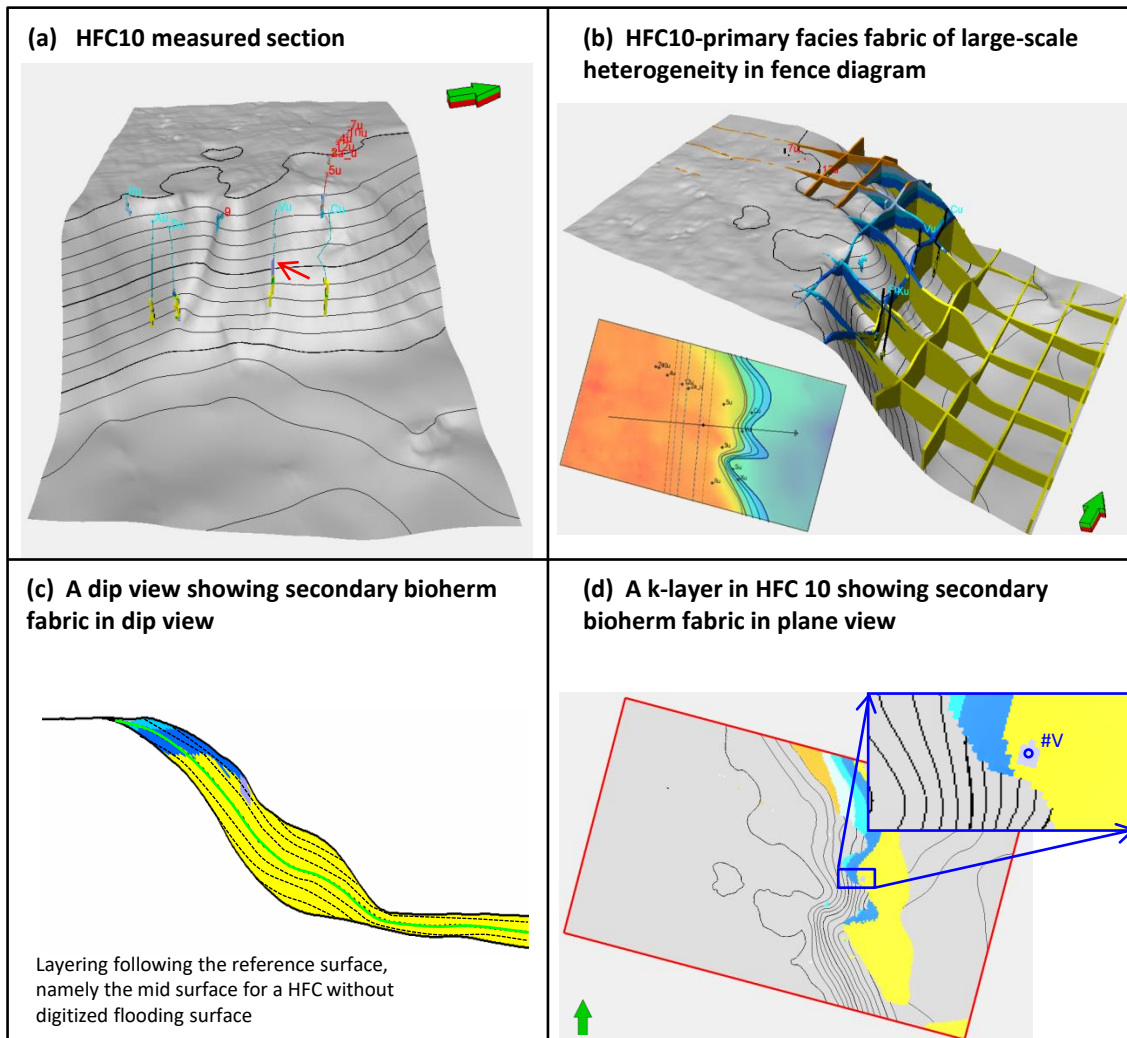


Figure 3.15: An example of Scenario 4 as applied for HFC10. (a) input measured sections for HFC10, where a bioherm was interpreted in measure section #V. (b) primary fabric modeled for HFC10, using TGS with trend. (c) a dip-view showing simulated bioherm in upper slope location, where previous layering follows a reference surface, (d) a map-view k-layer in HFC10 showing modeled bioherm within bioturbated sandstone near #V.

3.6.6 Modeling complex facies distribution using PGS – an subsurface example

Since the facies distribution of subsurface-constrained PCS-11 is more complex than the highly-ordered facies transition in PCS-10, a pixel-based Pluri-Gaussian Simulation algorithm (PGS, Le Loc'h et al., 1994), as an extension of TGS, was used to handle the complex facies transition in Grayburg-Lower Queen platform (G10~G13HFS). As an extension of TGS (Amstrong et al., 2003), PGS allows a definition of a lithotype rule containing 2 different lithotype rule set with two variograms to model complex stratigraphy. Back in 2012, Yarus et al. successfully applied this method in modeling an alternating dolomite and siltstone distribution in Grayburg platform in a west Texas Field, which is located slightly south of the area of interest in this study along the same reservoir trend, and proved the benefits of using two different lithotype rule set and variogram in modeling complex stratigraphy in a similar setting.

An example presented here are from Kerans and Sitgreaves (2015). Lithotype proportion matrix/LPM (Figure 3.16a) along with two lithotype sets and their variograms (Figure 3.16b) are two significant inputs to model complex stratigraphy using PGS (Figure 3.16c). For each cell or grouped cell in LPM (Figure 3.16a), it contains the probability per lithofacies (Beucher et al., 2006; Amstrong et al., 2011; Hamon et al., 2011; Yarus et al., 2012), and was obtained by extrapolating from lithofacies proportion curves at core locations (Figure 3.16a1) to a coarse grid (Figure 3.16a2), using Linear Model Kriging in DecisionSpace, which is a special kriging which does not requires the user to compute and model a variogram. Instead, an map-view isotropic model was assumed as an input. Afterward, for the lithotype rule (Figure 3.16b) used in this zone, it contains two lithotype sets (Figure 3.16b1, b2) with distinct variogram. These user-defined rule sets were based on observed contact relationship from cores and 3D conceptual geologic model, and was user-defined to regulate facies spatial relationships of Grayburg Formation, whereas the

cubic variograms controls facies continuity per lithotype rule set, where F15 and F19 in lithotype set 1 (Figure 3.16c1) were assumed to be less continuous than the rest lithofacies in lithotype set 2 (Figure 3.16c2). As shown in a resultant example (Figure 3.16c) of a chronostratigraphic layer within interval 7 (Figure 3.8), one can observe a facies transition from fenestral laminites (F22) and a tepee-pisolite complex (F23) in the inner platform, to ooid grainstones (F16) of the shallow shoreline setting and ooid peloid packstone (F17) and peloid packstone (F18) in the outer platform.

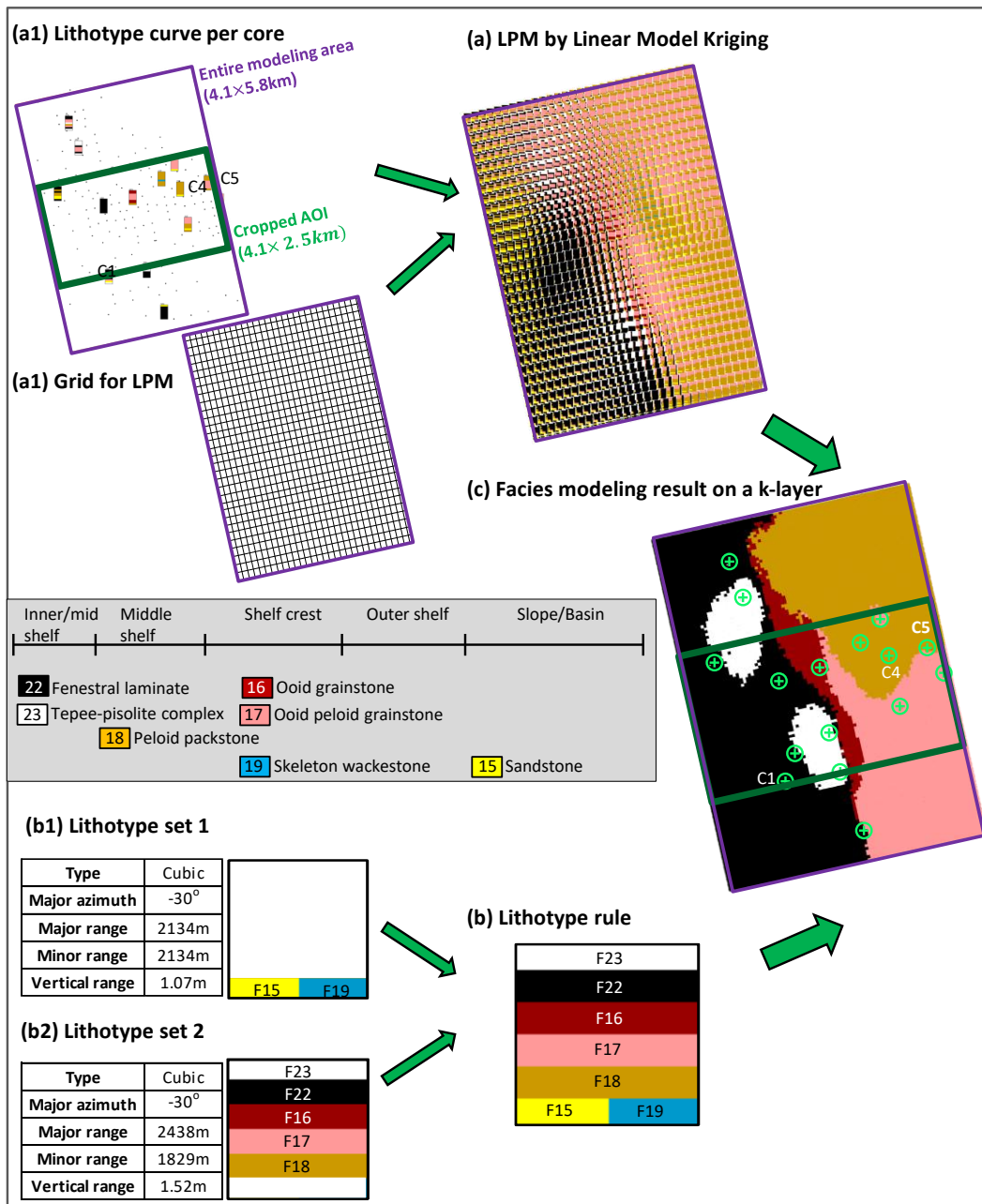


Figure 3.16: An example of modeling complex stratigraphy in Grayburg-Lower Queen Formation, as applied to zone 7 (Figure 3.8). (a) Lithotype proportion matrix LPM and (b) Lithotype rule are two major inputs to generate (c) facies modeling results, as displayed in a chronostratigraphic k layer. (a) was generated by extrapolating from vertical proportion curves (a1) to a dense grid (a2) using Linear Model Kriging. (b1) and (b2) are two lithotype sets combining into the lithotype rule (b).

3.7. PROPERTY AND SEISMIC MODELING (STEP 5~6)

3.7.1 Data sources for acoustic properties (outcrop and subsurface)

The availability of P-wave velocity (V_p) and bulk density (ρ) data from both LCC outcrop and CBP subsurface dataset (Figure 3.17) allows one to apply seismic modeling using the acoustic wave equation. Kenter et al. (1997, 2001) collected 1-inch core plugs from the LCC outcrops to measure bulk density, porosity, mineral composition, as well as P- and S-wave velocity at a confining and pore pressure of 40-10MPa. These confining and pore pressure conditions correspond to burial depths of 750–2500m and are analogous to those of typical producing fields in the Permian Basin (Kenter et al., 2001). In terms of spatial distribution, these plugs were collected within Sonnenfeld and Cross (1993)'s HFC6, being sampled with the strategy of capturing the petrophysical variability associated with the facies within a single HFC (Figure 3.17a). For other facies (Facies 9-14) in G9 and G8 HFS's, the author use the mean velocity-density pair per facies in Stafleu and Sonnenfeld (1994). As for the CBP subsurface dataset, the author used six type well (Figure 3.17b) with sonic, bulk density logs, and described cores for acoustic property analysis.

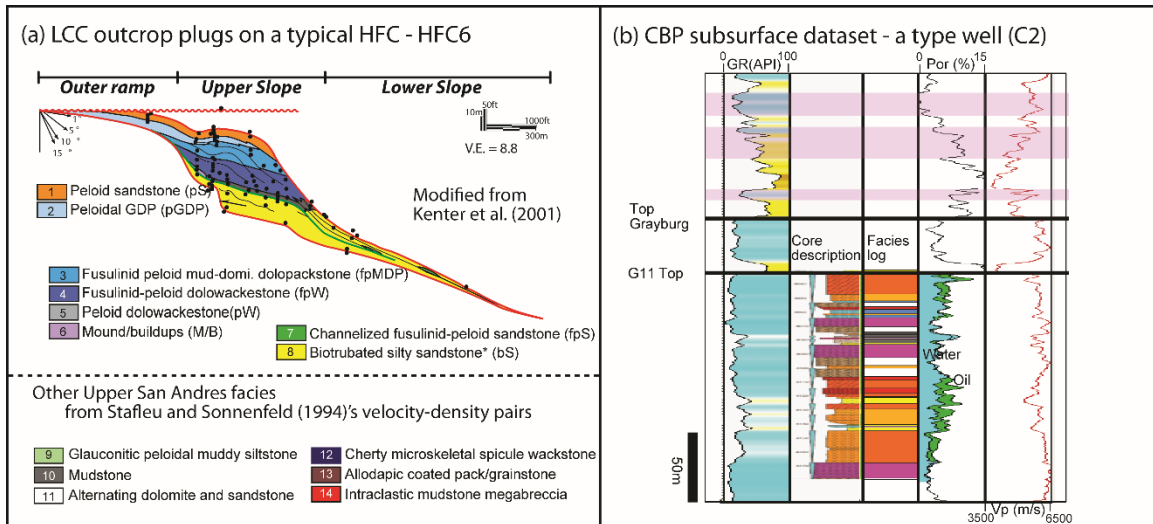


Figure 3.17: Data source for acoustic property. (a) outcrop plugs in Sonnenfeld and Cross (1993)'s HFC6, laboratory measurements from Kenter et al. (1997, 2001). (b) A type well from CBP dataset with sonic and density logs.

3.7.2 Relationship between acoustic velocity and impedance

Instead of jointly considering the two variables of P-wave velocity and bulk density per location, the author focused on modeling velocity as a single variable, and then estimated bulk density (ρ') using Gardner's equation (Gardner et al., 1974). The resultant further estimated P-wave impedance (I_p') is highly correlated with actual measured impedance (I_p) from both outcrop (Figure 3.18a) and subsurface (Figure 3.18b).

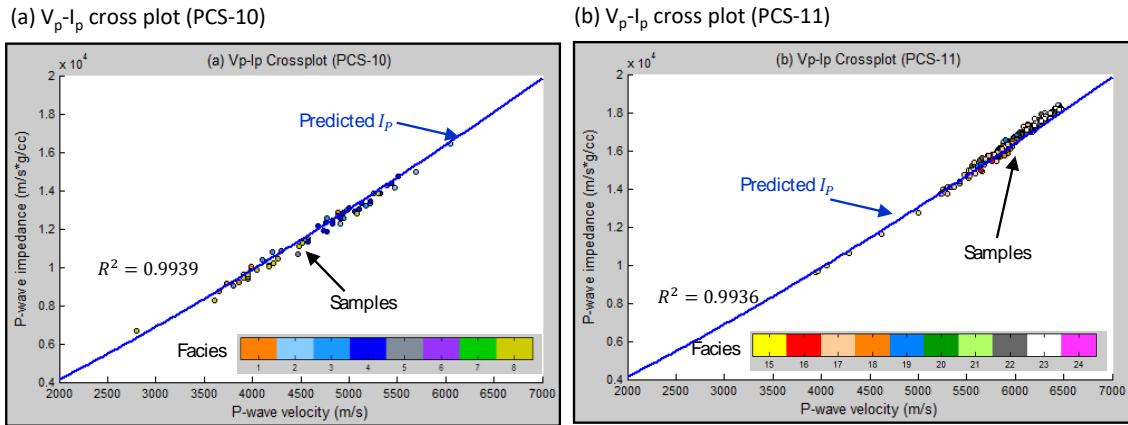


Figure 3.18: P-wave velocity and impedance relationship of (a) PCS-10 and (b) PCS-11. The colored dots shows samples from outcrop plugs for PCS-10, and a type well for PCS-11, whereas the blue line shows predicted P-wave impedance (I_p) from P-wave velocity (V_p), where density is estimated from velocity using Gardner's equation (1974). The author focused on velocity modeling, since I_p is highly predictable from V_p for both outcrop and subsurface datasets.

3.7.3 Acoustic velocity analytic results and adjustments

Following Janson and Fomel (2010) workflow, facies-based velocity modeling as the definition of lithofacies itself has already incorporated some key factors influencing the sonic velocity of mixed carbonate-siliciclastic systems, including porosity and primary pore type, quartz content and dolomite content (Anselmetti and Eberli, 1993). For a less controversial discussion on seismic stratigraphy, the author assigned an average velocity-density pair per facies as the most common inputs for seismic modeling, which assumes little intra-facies heterogeneity (Meckel and Nath, 1977; Neidell and Poggiagliolmi, 1977; Schramm et al., 1977; Biddle et al., 1992; Tipper, 1993). In comparison, in an accompany study (He et al., 2016), the author incorporated the analytic intra-facies heterogeneity for a discussion on its effect on the interpretation of key chronostratigraphic surfaces. This consideration of intra-facies heterogeneity could be necessary, considering that the large size of a sandstone (F8-bS) in transgressive hemicycle, which could reach up to 2200 m

laterally and 120 m vertically. Both of its lateral and vertical dimensions are beyond seismic resolution at 35 peak frequency, when the acoustic wave propagates through strata with an average velocity around 5000m/s.

			1. Facies-Averaged Model				2. Facies-Static Model				
			Distribution				Variogram				
	Codes	Facies Name	constant value	mean	std	min	max	azimuth	major range	minor range	vert.range
Model Top Section	15	Sandstone	5018 (w)	5018 (w)	568 (w)	3314	6722	15	2500	1000	7.5
	24	Anhydrite	5821 (w)	5821 (w)	345 (w)	5209	6661	15	2500	1000	7.5
G10~G13 HFS, PCS-11	15	Sandstone	5018 (w)	5018 (w)	568 (w)	3314	6722	15	2500	1000	7.5
	16	Ooid Grainstone	5935 (w)	5935 (w)	242 (w)	5209	6661	15	2500	1000	7.5
	17	Ooid peloid grainstone	5736 (w)	5736 (w)	416 (w)	4488	6984	15	2500	1000	7.5
	18	Peloid packstone	5839 (w)	5839 (w)	308 (w)	4915	6763	15	2500	1000	7.5
	19	Skeletal wackestone	5850 (w)	5850 (w)	321 (w)	4887	6813	15	2500	1000	7.5
	20	Fusulinid MDP	5819 (w)	5819 (w)	234 (w)	5117	6521	15	2500	1000	7.5
	21	Fusulinid GDP	5788 (w)	5788 (w)	273 (w)	4969	6607	15	2500	1000	7.5
	22	Fenestral Laminite	5850 (w)	5850 (w)	408 (w)	4626	7074	15	2500	1000	7.5
	23	Tepee-pisolite complex	6115 (w)	6115 (w)	123 (w)	5746	6484	15	2500	1000	7.5
	24	Anhydrite	5821 (w)	5821 (w)	345 (w)	4786	6856	15	2500	1000	7.5
G9 clinofoms, PCS-10	1	Peloid Sandstone	4101 (k)	4101 (k)	424 (k)	2829	5373	isotropic	400	400	4
	2	Peloid GDP	5280 (k)	5280 (k)	556 (k)	3612	6948	isotropic	300	300	3
	3	Fusulinid peloid dolopackstone	4781 (k)	4781 (k)	414 (k)	3539	6023	isotropic	300	300	3
	4	Cherty Fusulinid dolowackestone	5002 (k)	5002 (k)	267 (k)	4201	5803	isotropic	300	300	3
	5	Peloid dolowackestone	4203 (k)	4203 (k)	289 (k)	3336	5070	isotropic	300	300	3
	6	Mounds/buildups	5391 (k)	constant = 5391 (k)				NA			
	7	Channelized fusulinid-peloid sandstone	5255 (k)	constant = 5255 (k)				NA			
	8	Bioturbated silty sandstone	4172 (k)	4172 (k)	524 (k)	2600	5744	isotropic	400	400	4
Other facies in PCS-10	9	Glauconite peloid muddy siltstone	3865 (s)	3865 (s)	400 (a)	2665	5065	isotropic	400	400	4
	10	Mudstone	4877 (s)	4877 (s)	400 (a)	3677	6077	isotropic	300	300	3
	11	Alternating dolomite and sandstone	NA in composite model				NA in composite model				
	12	Cherty microskeletal spicule wackestone	4572 (s)	4572 (s)	300 (a)	3672	5472	isotropic	300	300	3
	13	Allodapic coated pack/grainstone	5486 (s)	5486 (s)	300 (a)	4586	6386	isotropic	300	300	3
	14	intralastic mudstone megabreccia	6005 (s)	6005 (s)	300 (a)	5105	6905	isotropic	300	300	3
Model Base Section	1	Peloid Sandstone	4101 (a)	4101 (a)	424 (a)	2829	5373	isotropic	1000	1000	10
	10	Mudstone	4877 (a)	4877 (a)	400 (a)	3677	6077	isotropic	1000	1000	10

Data Source for velocity distribution (mean and std)

(k) - calculated from Kenter et al. (1997, 2001)'s measurements of LCC outcrop plugs
(w) - calculated from 6 out of 16 wells with both cores and sonic logs (truncated 10% values)
(s) - referred to Stafleu and Sonnenfeld (1994)
(a) - analogous to similar facies

Data source for velocity variogram

The current variograms are our best estimation using limited available samples.
The variogram ranges are roughly estimated from experimental variogram.
The variogram azimuth of Grayburg and Queen Formation is determined from variance map.
The variogram azimuth of Upper San Andres Formation remains unknown, thus assumed isotropic.

Table 3.5: Raw analytic results of P-wave velocity before adjusting systematic differences, which was originated from different acoustic property data sources.

Initial petrophysical analysis (Table 3.5) shows systematic discrepancies between the outcrop-based lower model and the subsurface-based upper model (Figure 3.19). Normalized velocity distributions from outcrops plugs (Figure 3.19b) of uSA Formation measured at 30MPa effective pressure are not only systematically much slower than that from sonic logs of Grayburg and Lower Queen, but also exhibit a wider distribution and a more dramatic contrast between siliciclastics and carbonates (Figure 3.19a). Beyond the difference in input frequency for laboratory ultrasonic (300~800kHz, Kenter et al., 2001) versus subsurface sonic (3~7kHz, Haldorsen, 2006) measurements, these differences were likely caused by multiple other factors. Petrographic analysis shows extensive anhydrite cements for Grayburg subsurface samples, compared with those of uSA outcrop samples that are devoid of anhydrite cements (Kenter et al., 1997). Anhydrite cements occluded some interparticle porosity in the subsurface (Murray, 1960), contributing to a more rigid rock matrix (Brie, 1985; Anselmetti and Eberli, 1993). In addition, the pore fluid contents (Batzie and Wang, 1992) and effective pressure (Anselmetti and Eberli, 1993) may cause an even more minor difference, as laboratory measurements for the 100%-water-saturated outcrop plugs were taken at an effective pressure at 30 MPa, whereas the Grayburg sonic logs actually penetrated 50%-brine-and-50%-oil-saturated reservoirs.

If this raw separate analysis for the subsurface-constrained Grayburg-Lower Queen model (Figure 3.19a) and outcrop-constrained uSA model (Figure 3.19b) were directly used, the resultant seismic reflections near the San Andres-Grayburg sequence boundary would be unrealistically stronger and more continuous than the subsurface seismic (Figure 3.1c). Therefore, the author adjusted the outcrop-constrained velocity distribution (Figure 3.19c) to match a common facies in subsurface data: the outcrop-derived Gaussian distribution of F8 was elevated and then compressed to match the distribution of subsurface-constrained F15.

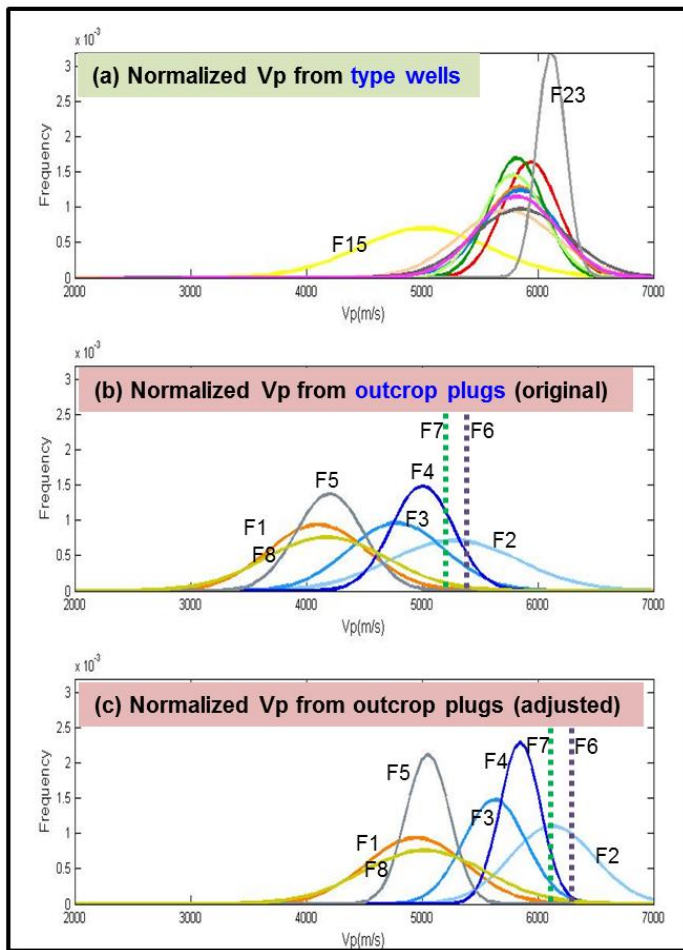


Figure 3.19: P-wave velocity distribution of (a) subsurface-constrained Grayburg Formation, and outcrop-constrained Upper San Andres Formation, before (b) and after (c) adjustments. The author elevated the mean and compressed the spread per lithofacies for outcrop-constrained uSA Formation (compare b and c) in order to image a realistic uSA-Grayburg sequence boundary.

3.7.4 Seismic modeling parameters

As the direct input for the exploding-reflector imaging/migration package of Madagascar (Janson and Fomel, 2011; Fomel et al., 2013), the velocity and density model was resampled to a regular spacing of 20 meters, in order to mimic receiver geometry in CBP subsurface seismic (65ft/19.8m). Besides, since the frequency spectrum at the

reservoir level shows a peak frequency at 35Hz, and a bandwidth of 0~80 Hz. The author simulated 0°-phase seismic model at a peak frequency of 35 Hz, or dominant frequency of 27Hz as an analog for CBP seismic.

3.8. RESULTS AND DISCUSSIONS ON CHRONOSTRATIGRAPHIC SIGNIFICANCE FOR A RESERVOIR TOP AND BASE

3D lithostratigraphic model (Figure 3.20a), acoustic impedance model (Figure 3.20b), and 35-Hz normal-frequency seismic model (Figure 3.20c) were ready for further evaluation on the conformance or discrepancy of HFS and higher-order seismic stratigraphy as compared with the high-resolution modeled stratigraphy. The author started with a 2D and then 3D example to illustrate the evaluation of the difference between a seismic horizon interpreted by conventional seismic stratigraphic interpretation approach (Mitchum et al., 1977a) against the actual modeled stratigraphic surface. The author evaluated two important seismic horizons, including the base and top of G9 which covers from the platform to the toe-of-slope, as well as the segmented uSA shelf and Grayburg platform reservoirs in subsurface fields. Finally, the author analyzed the cause of apparent discrepancy in the most error-prone area, and then propose potential alternative practical solutions.

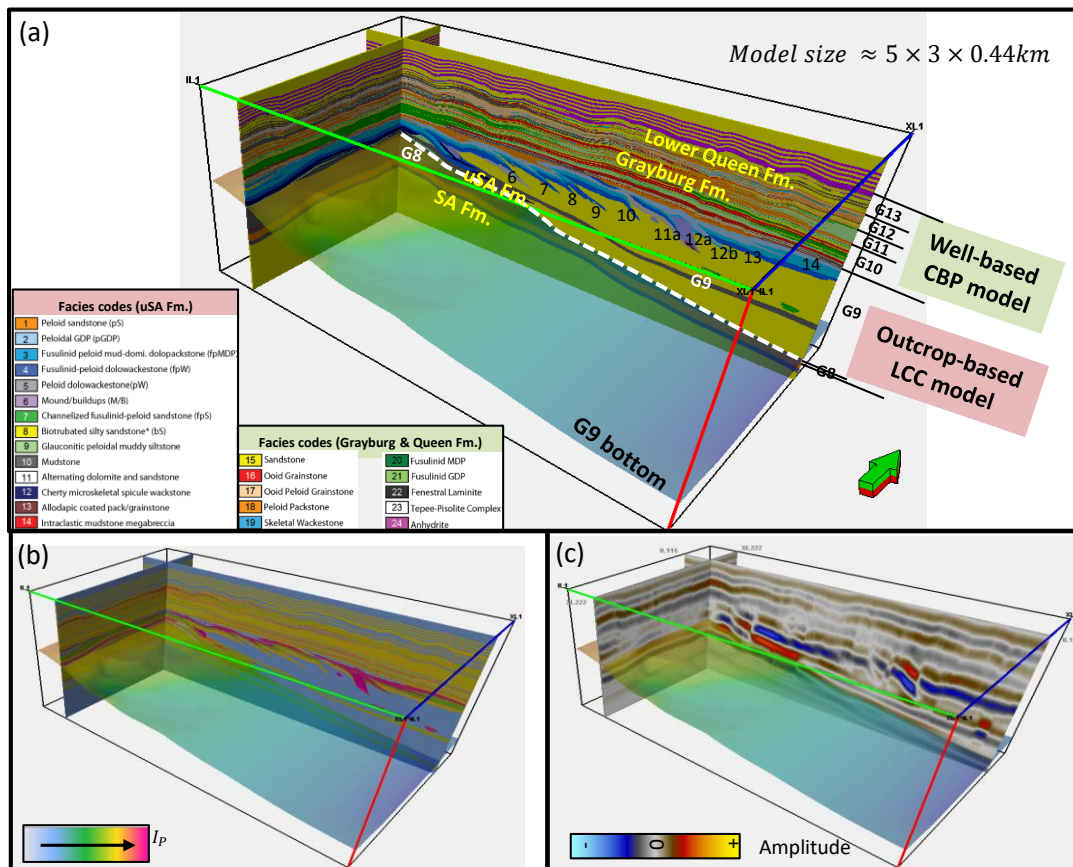


Figure 3.20: Three-dimensional modeling results. (a) outcrop-constrained and subsurface constrained facies model. (a) Lithostratigraphic model, (b) Facies-averaged impedance model, and (c) 0°-phase 35Hz seismic model.

3.8.1 2D and 3D evaluation methods and examples

In previous published 2D comparison of seismic stratigraphy against actual stratigraphy (Stafleu and Sonnenfeld, 1994), important actual chronostratigraphic surfaces were projected on seismic models, so that one can visually compare how an interested seismic reflector would agree/deviate from the reality. The author started with a similar logic for the evaluation of an interested seismic horizon (Figure 3.21). For instance, an uninterpreted IL116 is shown in Figure 3.21a. Assuming seismic reflections follows stratigraphic surfaces and unconformities (Vail et al., 1977c), the author interpreted the top

and base of G9 HFS based on reflection termination relationship (red arrows in Figure 3.21b). More specifically, G9 HFS base was interpreted as a seismic peak (green line, Figure 3.21b) underneath marine onlaps, where the author had the most confidence when tracking at the base of a thick Lower Cherry Canyon Sandstone Tongue (A-B, Figure 3.21d), and then started to lose confidence when approaching the shelf margin (B-C), with even less certainty near the outer ramp (C-D) when two seismic troughs converged (Figure 3.21b). Compared with the interpretation of G9 base, the interpretation of G9 top as a seismic peak (yellow line, Figure 22b) had less ambiguity when tracking the seismic peak above toplap of a few lower HFC clinoforms. Then the author projected the interpreted G9 top and base horizons on modeled stratigraphy (Figure 3.21c), upon which visual comparison can be easily made.

If the author further plot interpretations and modeled stratigraphic surface of the G9 base and top as a function of distance (Figure 3.22a and c), their difference could be easily calculated per location (Figure 3.22b and d). When interpretation is shallower than the modeled surface (such as Point C, Figure 3.22a), their positive difference (Point C, Figure 23, colorcoded with red) represents an over-estimation of relative geologic time at this location if using the interpreted horizon as an approximation of a geologic timeline. In contrast, when interpretation is below the modeled surface (such as Point A, Figure 3.21a), their negative difference (Point A, Figure 3.21b, colorcoded with blue) represents an under-estimation of relative geologic time at this location if using the interpreted horizon as an approximation of a geologic timeline. When interpretations almost coincide with the modeled surface (white arrow in Figure 3.17a), their difference is approaching zero (white arrow in Figure 3.22b, colorcoded with white). Using this evaluation approach, the 2D example of G9 bottom horizon follows the geologic timeline well at the platform and along the slope, however it becomes convex-up near the shelf margin, and slightly convex-down

near toward the basin. In comparison, the example of G9 HFS top horizon (Figure 3.22c and d) suggested a systematically shallower (10~70m) interpretation than modeled surface.

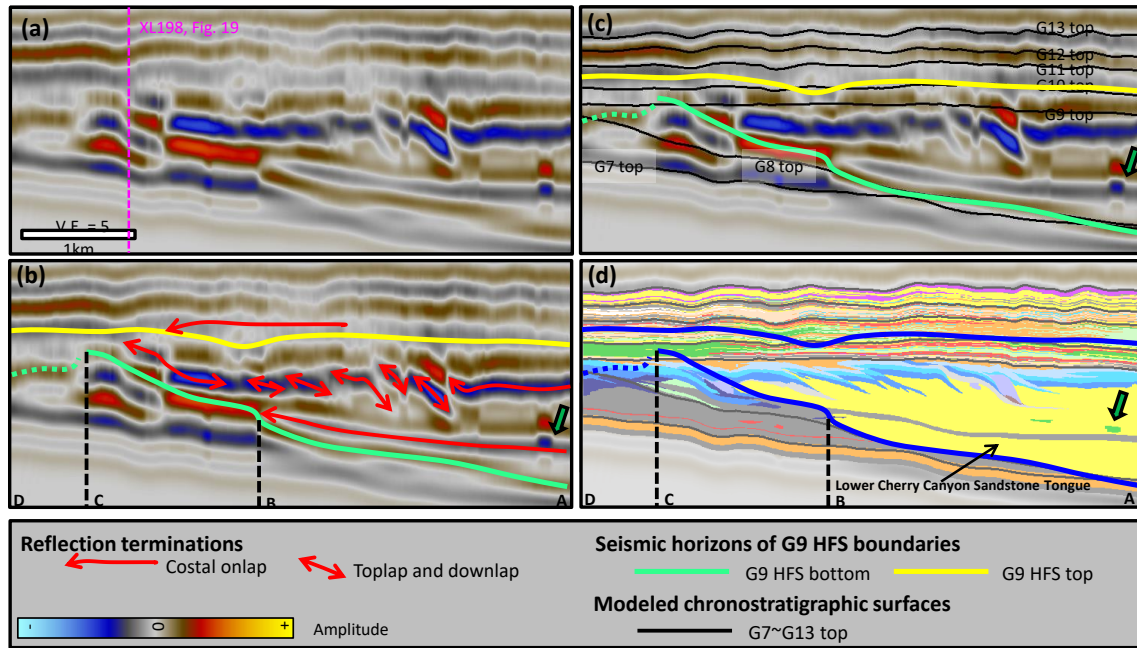


Figure 3.21: G9 top and bottom horizon interpretation following conventional seismic stratigraphic interpretation approach. (a) and (b) show IL116 of 90° synthetic seismic ($f_d=27\text{Hz}$) before and after interpretation. (c) highlights a comparison between seismic horizon of G9 top and base against modeled G7~G13 top. (d) interpreted horizon overlying on lithostratigraphic model.

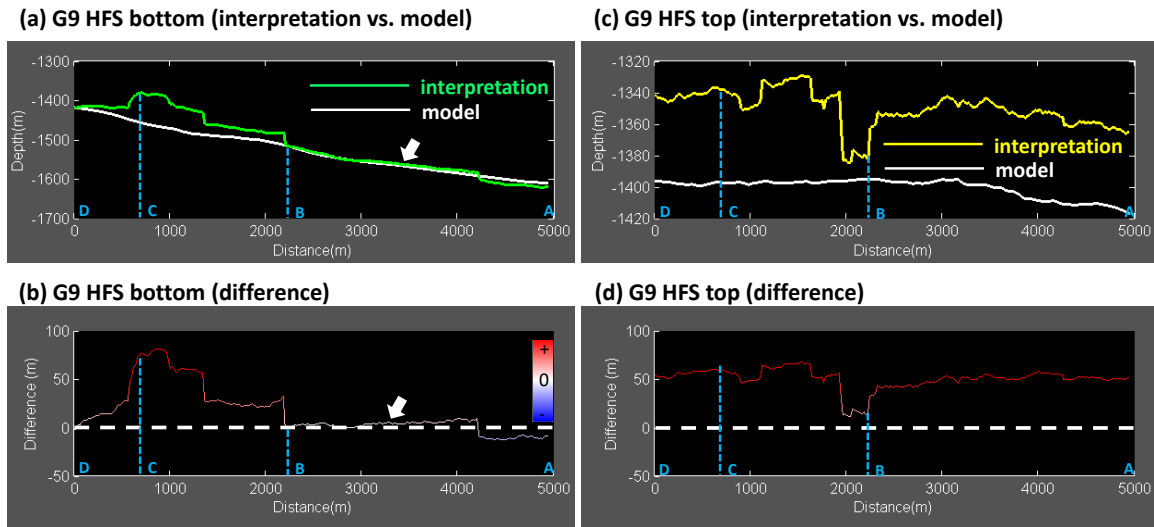


Figure 3.22: 2D example showing the colorcode of the difference between interpretation and modeled chronostratigraphic surface, where the red represents scenarios when interpretation is shallower than modeled surface, thus an over-estimation of relative geologic time if using the seismic horizon as geologic timeline. In contrast, the blue indicates an under-estimation of relative geologic time, and the white represents a well match.

Extending the above 2D interpretation to 3D, the author sparsely picked and then autotracked the seismic peak at G9 HFS bottom (Figure 3.23a). Comparing this seismic horizon (Figure 3.23a) with the actual modeled G9 HFS bottom (Figure 3.23b), its more densely-spaced contours near the shelf margin of the seismic horizon suggests a steeper interpretation than the modeled stratigraphy. Subsequently, the author computed the difference between seismic horizon (Figure 3.23a) and modeled surface (Figure 3.23b), and then colored using RWB color scheme as in the previous 2D example. The difference map (Figure 3.23c) suggested the most predominant error occurs near the shelf margin, and becomes more severe near the shelf margin promontories, which is also shown in XL198 (Figure 3.24).

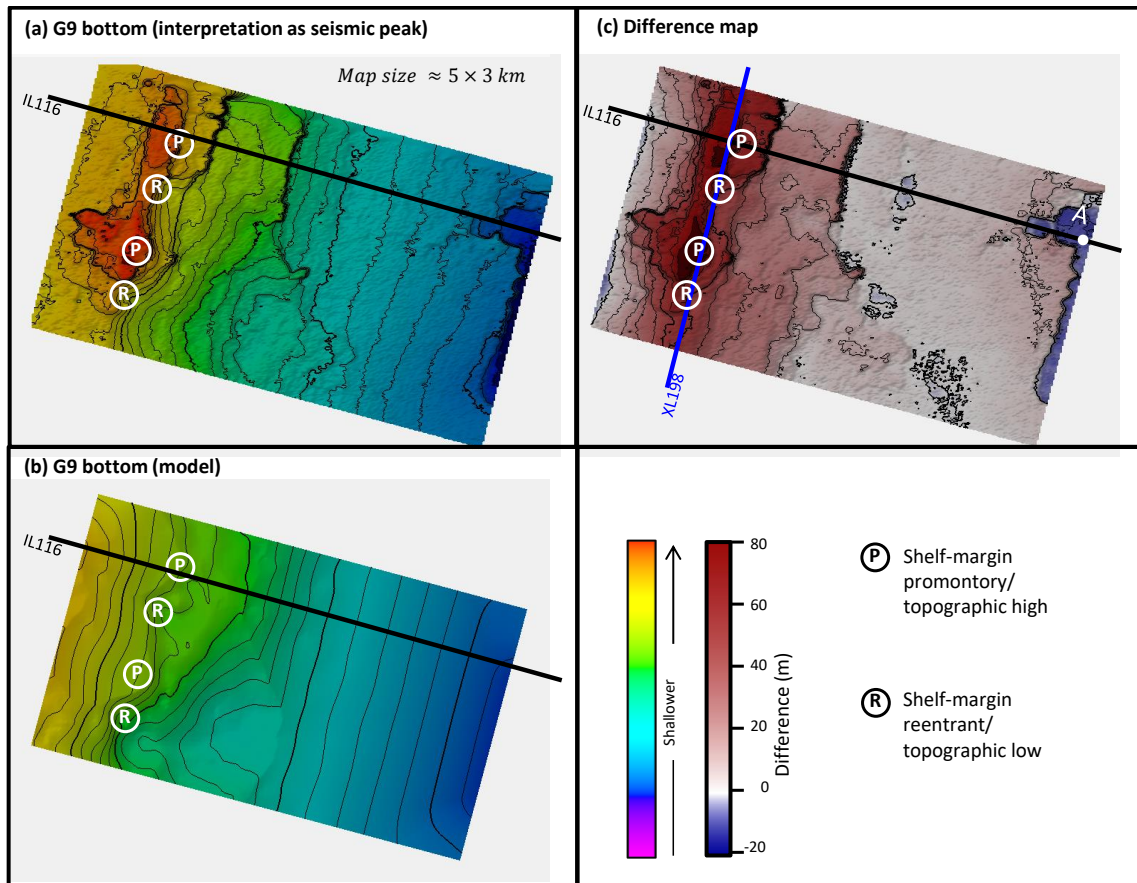


Figure 3.23: 3D example showing evaluation method of chronostratigraphic significance of interested horizons, such as G9 HFS bottom. (a) Interpretation without smoothing, by tracking seismic peak underneath coastal onlaps. (b) Modeled stratigraphic surface of G9 HFS bottom. (c) Difference map between interpretation and model (a) and (b). Map size is 4940 by 2880 meters, contoured every 10 meters.

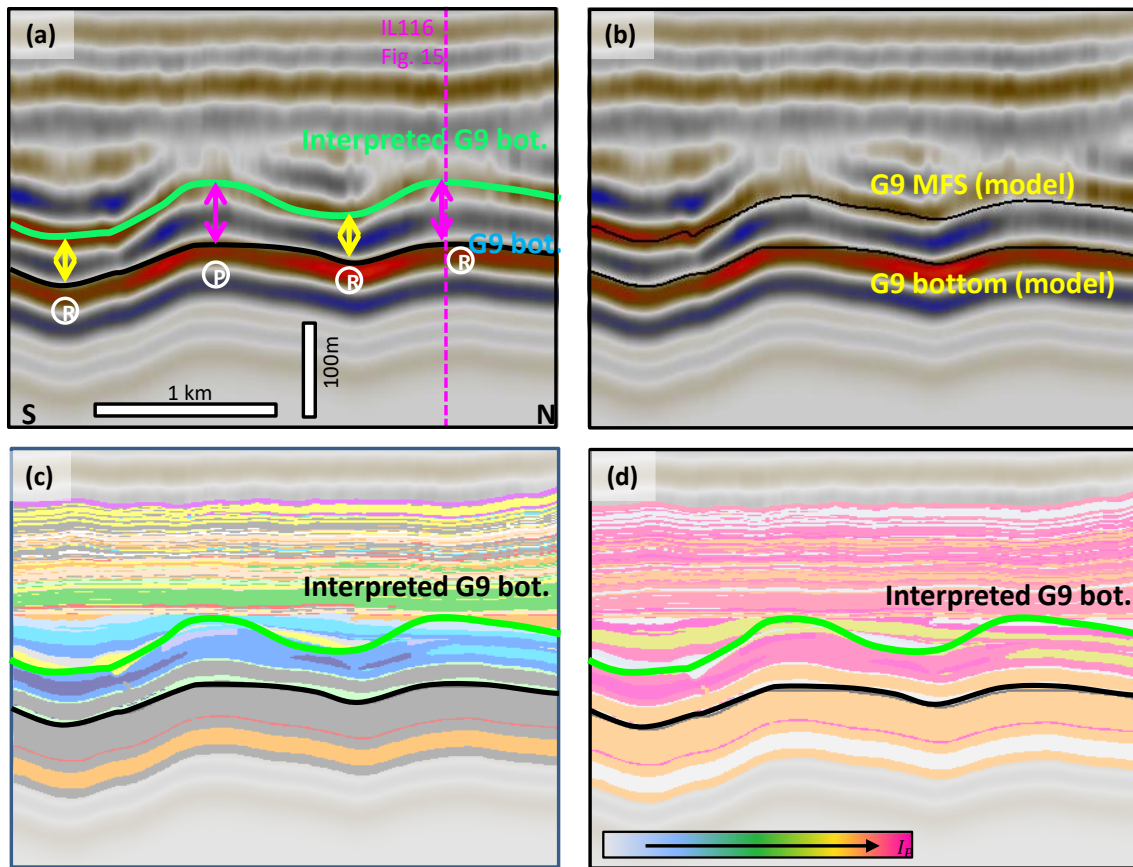


Figure 3.24: XL198. (a) seismic section showing seismic horizon versus modeled G9 HFS bottom. (b) Modeled G9 MFS and bottom. Interpreted and modeled G9 MFS bottom overlying on facies (c) and impedance model.

3.8.2 Discussion and recommendations

As shown in the above 2D and 3D example (Figure 3.21~24), G9 HFS top and bottom were interpreted using a conventional seismic stratigraphic interpretation workflow, by assuming the seismic reflections follow stratigraphic surfaces/unconformities, thus G9 HFS top and bottom were interpreted by following events and termination relationships. The discrepancy between the interpreted horizon and its corresponding stratigraphic surface suggests further actions to should be made to improve seismic stratigraphic interpretation at HFS scale.

3.8.2.1 Interpreted G9 HFS bottom and interpretation strategy

In general, at the lower slope, the seismic peak representing G9 HFS bottom agrees well with the modeled chronostratigraphic surfaces, with minor discrepancies less than +/- 25 meters (shown as blue, white and pink in Figure 3.23c). The maximum negative discrepancy occurs near Point A (Figure 3.26c), where the higher-impedance turbidite channel (pointed by the green arrow in Figure 3.26d) above the mudstone near G9 maximum flooding surface generates localized seismic amplitude anomalies, which slightly interfere with the seismic peak at the bottom of Cherry Canyon sandstone, and then caused the local interpretation to be deeper than the modeled G9 HFS bottom (compare Figure 3.23 a and b). Most importantly, significant discrepancies occur near the shelf margin, where the positive discrepancy could reach up to 80 meters (shown as red to dark red in Figure 3.23c). The more closely spaced contours in the G9 bottom horizon (Figure 3.23a), as compared with the G9 bottom surface (Figure 3.23b) indicate an over-steepened interpretation between Point B and C in IL116 (Figure 3.26c). Along the strike orientation, the positive discrepancy seems to further increase near the shelf margin promontories, compared with the shelf margin reentrants (Figure 3.23c). As shown in a crossline transecting the shelf margin (Figure 3.24), the interpreted G9 top as a seismic peak seems better follow the modeled G9 MFS instead of G9 top, while imaged much lower than the reality (approximately more than 3/4 wavelength).

Considering the large discrepancy between the seismic horizon and modeled surface at G9 HFS bottom, the author are more concerned about the areal discrepancies along the shelf-margin trend, compared with the localized discrepancy resulting from the interference of turbidite channels. Furthermore, the author suggest an alternative practical interpretation approach (Figure 3.25), starting with a partial grid (Figure 3.25a), where interpretation is stopped wherever the interpreter loses confidence in correlating further

(Figure 3.25a). Next the author suggest use of automated 3D tracking within defined patch polygons (Figure 3.25b). Finally, convergent interpolation or other interpolation can be applied to fill in the holes (Figure 3.25c). This practical approach improves the overall discrepancy between the seismic horizon and the actual G9 HFS bottom (Figure 3.25d). However, the interpolation across shelf-margin trend results in a smoothed shelf margin (Figure 3.25e and f), losing the ability to present all shelf-margin reentrant and promontories. Thus an interpolation with well tops near the shelf margin could further improve the interpretation.

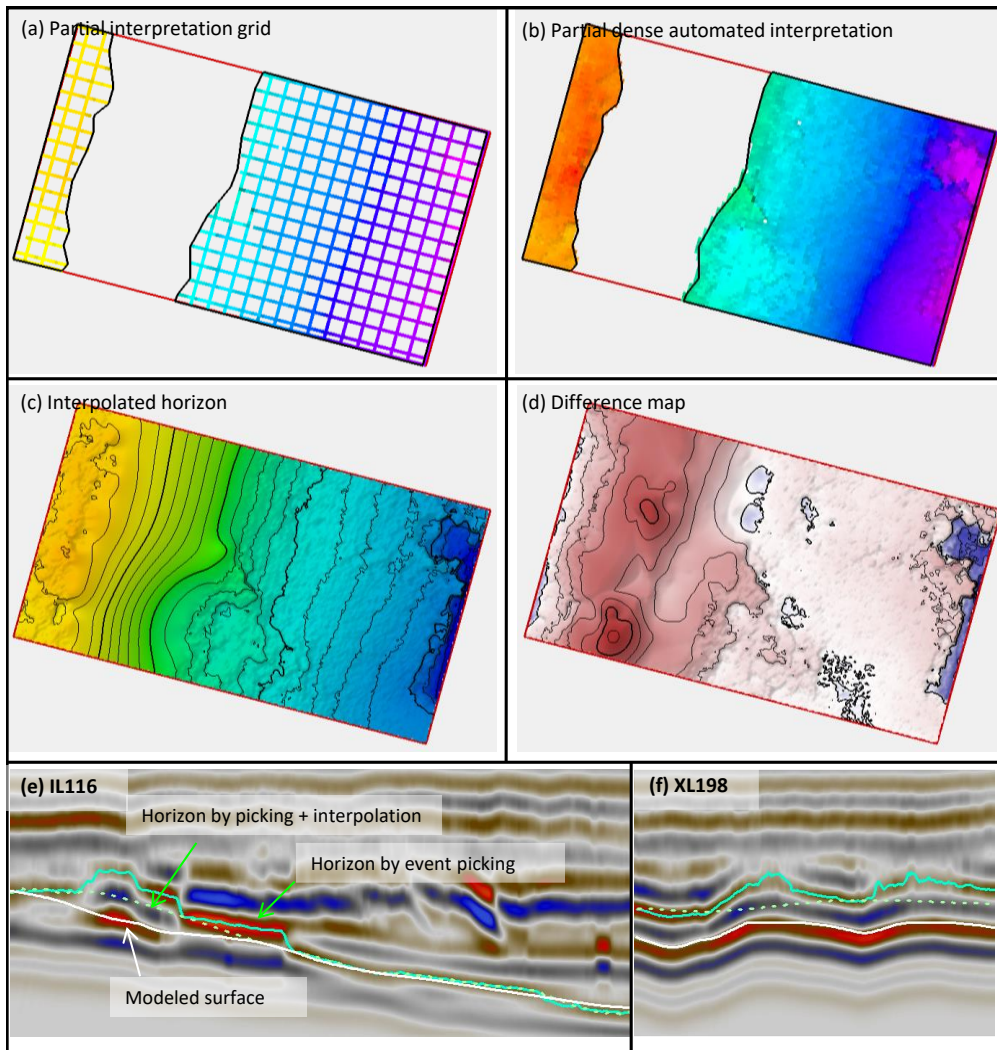


Figure 3.25: an alternative practical interpretation approach combining (a) partial interpretation, (b) autotracking with defined polygon and (c) interpolation. The resultant difference map (d) shows an improved overall interpretation quality, as compared with Figure 3.23(d). (e) and (f) shows comparison on IL116 and XL198.

3.8.2.2 Interpreted G9 HFS top and alternative interpretation strategy

Tracking the seismic trough to interpret the G9 HFS results in an interpretation one HFS higher than it should be. In the selected cross-section view on IL116 (yellow solid line, Figure 3.26c), the interpreted G9 topseismic trough) is 10~65m shallower than the

modeled G9 top (Figure 3.22d), and more closely resembles the actual modeled stratigraphy of G10 HFS top (Figure 3.26c). It seems more likely that the underlying adjacent seismic peak better reflects the location of G9 HFS top. Since this seismic peak is far less continuous and more difficult to follow, the author took an alternative approach in practical chronostratigraphic interpretation (Figure 3.26), where an overall depth shift of 45 meters was applied to the interpreted seismic trough (Figure 3.26a). The resulting discrepancy (Figure 3.26c) between interpreted (Figure 3.26a) and modeled (Figure 3.26b) G9 top is now reduced within ± 32 meter, which is less than the $\pm 1/4$ wavelength of a normal-frequency ($f_p=35\text{Hz}$) seismic data. By using this shifted horizon as the base of the Grayburg reservoir model, it a more realistic thickness of the pay zones may be achieved, compared with using the original seismic trough.

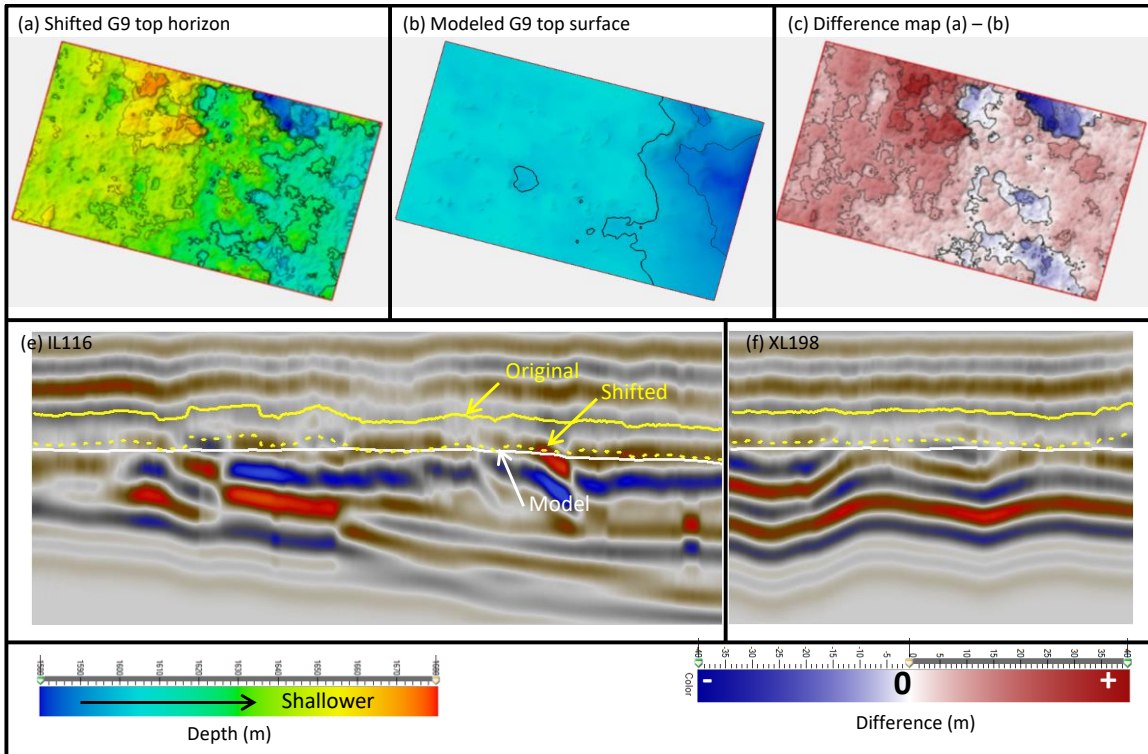


Figure 3.26: an alternative practical approach to interpreted G9 HFS top. The G9 HFS interpreted as a seismic trough is systematically one event higher than the modeled stratigraphic surface (as shown in Figure 3.14c, 16c and d). If interpreting the underneath seismic peak as G9 HFS, its discontinuity would result in great difficulties in interpretation. Alternatively, the author shifted the previously interpreted seismic peak for 45 meters (a), and the difference (c) between the current interpretation (a) and modeled surface (b) is within $\frac{1}{4}$ wavelength (b). Selected IL116 (d) and (e) XL198 are shown for comparison.

3.9 CONCLUSIONS AND FUTURE WORK

The author presented an innovative 3-D lithostratigraphic modeling workflow to reconstruct the hierarchically-embedded high-resolution mixed clastic-carbonate strata of the San Andres-Grayburg-Lower Queen formations that serve as high-resolution analogs for the Grayburg Platform Mixed Clastic/Carbonate Play (Dutton et al., Play 127). This workflow started with reconstruction of hierarchically-embedded stratal surfaces, followed by facies interpolation using a mixture of geostatistical modeling approaches to reconstruct

large-scale natural facies transitions, and localized objects. Consequently, the resultant model in this study effectively characterized complex uSA clinoformal stratigraphy, and contained horizontally-extensive and vertically thin fluid barriers, which have imposed key challenges in utilizing seismic inputs in static reservoir modeling. Velocity analysis per facies revealed a systematic error between laboratory measurements of uSA outcrop plugs and Grayburg core plugs, and thus adjustments were made according to seismic reflection magnitude at the San Andres-Grayburg unconformity. With the facies-averaged velocity and density model as an input, the author simulated waveform-based acoustic seismic response at 35 Hz. Finally, the author evaluated the discrepancy of seismically-interpreted horizons versus modeled stratigraphic surfaces of G9 HFS top and bottom, and then discussed a potential practical interpretation approach to mitigate these discrepancies for more accurate HFS-scale seismic stratigraphic interpretation.

Only a seismic model generated from facies-averaged P-wave impedance model was presented and discussed in this study, and it was assumed that intra-facies heterogeneity is negligible in terms of HFS-scale seismic stratigraphic interpretation. In an accompany study in the next chapter, more variables will be considered that potentially influence the HFS-scale seismic stratigraphic interpretation for shelf reservoirs, as predefined in Chapter 1.

Chapter 4: Improving 3D seismic stratigraphic correlation for reservoir model construction: evaluation and discussions³

Upon the constructed high-resolution 3D lithostratigraphic model of Upper San Andres shelf margin-Grayburg and Lower Queen platforms in the last chapter, herein the author used this skeleton to discuss the predefined factors in Chapter 1 that potentially influence the chronostratigraphic significance of seismic reflections at the high-frequency sequence and cycle (HFS and HFC) scale. The author started with constructing an analogous model of pure carbonate successions of Early Permian Abo shelf margin and its overlying Clear Fork platform, via lithofacies substitution and stratigraphic adjustment. The resultant model allows a comparative study between mixed carbonate-siliciclastic successions (Case 1) and pure carbonate successions (Case 2) with the same stratal geometry. Subsequently, the author modeled a variety of intra-facies heterogeneity per case represented as five scenarios of spatial velocity variations (S_1 , S_2 , S_3 , S_4 and S_5), which further accommodates for the possible subsurface situations. Upon these ten models, the author simulated 90°-phase seismic data at a dominant frequency of 13.5Hz, 27 Hz, and 54 Hz. These seismic data served as the low-, normal-, and high-frequency representation of subsurface seismic in Central Basin Platform (CBP), referring to the extracted frequency spectrum at the reservoir interval from a producing field along the eastern flank of CBP.

The evaluation of the chronostratigraphic significance of seismic reflections was applied at both HFS and HFC scale, compared with the typical application scale up to a scale using the depositional sequence as the basic interpretive unit (Mitchum et al., 1977b). Using a similar approach as showcased in the evaluation workflow in Chapter 3, the author compares the interpreted seismic horizon following the 'chronostratigraphic significance

³This chapter is edited from an unpublished manuscript of the author, containing partially published figures from He et al. (2017a) presented in AAPG ACE 2017 and He et al. (2017b, in review) for SEG 2017.

of seismic reflections' against the modeled chronostratigraphic surface, and then termed their discrepancies as time-correlation error/TCE. TCE serves as a proxy for the validity of 'chronostratigraphic significance of seismic reflections', where a larger value at a given location represents a severe violation of this fundamental assumption for seismic stratigraphy. The author firstly applied evaluations on two types of HFS surfaces, by comparing their respective interpretation from 30 seismic models against the modeled stratigraphy. The evaluated surfaces include a clinoformal G9 HFS bottom as it spans from the platform to the toe-of-slope and a flat-lying G12 HFS top as it is atop of Grayburg platform reservoirs. Furthermore, the author also extended the evaluation to HFC scale using an alternative approach, by manually picking horizon patches for landward-dipping diachronous seismic reflections and then cross-comparing for their areal pattern and structural dip within the mixed (Case 1) versus carbonate (Case 2) successions.

4.1 INTRODUCTION

In this study, the author tested the validity of 'chronostratigraphic significance of seismic reflections' when interpreting HFS and higher-order seismic stratigraphy. The author adopted the same forward modeling and then evaluation workflow as in Chapter 3, while extended its model design for a comprehensive consideration of possible subsurface scenarios. During geologic modeling, besides the original Middle Permian mixed carbonate/clastic shelf margin-platform lithostratigraphic model from Chapter 3 (shortened as 'Case 1' in this study), the author built an analogous model of Early Permian carbonate shelf margin-platform model via lithofacies substitution and stratigraphic adjustment. The comparisons of published and the author's recent works on Case 1 against subsurface interpretations from Kingdom Field on Case 2 provided important references during geologic modeling of Case 2. Subsequently, this pair of 3D high-resolution

lithostratigraphic models benefited the discussion of the chronostratigraphic significance of seismic reflections in three aspects. It allows a comparison between flat versus clinoformal stratigraphy, the fast versus gentle lateral lithofacies variation, and the mixed-versus pure-lithology (Variable 1, 2, and 3 predefined in Chapter 1). Furthermore, upon these two cases, the author tested the influence of intra-facies heterogeneity reflected as spatial velocity and then density variations, as well as the effect of seismic frequency (Variable 4 and 5 predefined in Chapter 1). Finally, upon the evaluations of 30 resultant seismic models, the author made recommendations on potential interpretation strategies to improve seismic chronostratigraphic correlation at the reservoir scale and then listed their applicable conditions.

4.2 MODELING AREAS AND DATASETS

4.2.1 Modeling areas

The author targeted at two types of shallow-water reservoirs in Permian Basin for a comparative study (Figure 4.1a), including the Grayburg Platform Mixed Clastic/Carbonate Play (Play 127) and the Abo Platform Carbonate Play (Play 116) in Dutton et al. (2004)'s Permian Basin Play Portfolio. Play 127 (Figure 4.1, shaded in yellow) is located in the Eastern Margin of Central Basin Platform. Despite its name of 'Grayburg' mixed carbonate-siliciclastic reservoirs, Play 127 has been producing from both porous carbonates and siliciclastics in Grayburg Formation, as well as porous carbonates in San Andres Formation ((Entzminger et al., 2000; Petersen and Jacobs, 2003; Ruppel, 2001). The reciprocal deposition of the Permian Basin (Silver and Todd, 1969) deposited these thick mixed carbonate-siliciclastic successions. In comparison, Play 116 (Figure 4.1, shaded in blue) has reservoirs developed along the southern margin of the Northwest Shelf and the West margin of the Central Basin Platform (Dutton et al., 2004).

This play type has in total contributed a production of 541.5 MMbbl till 2000, from the shelf and shelf-margin porous carbonates (Kerans, 2000; Kerans et al., 2000).

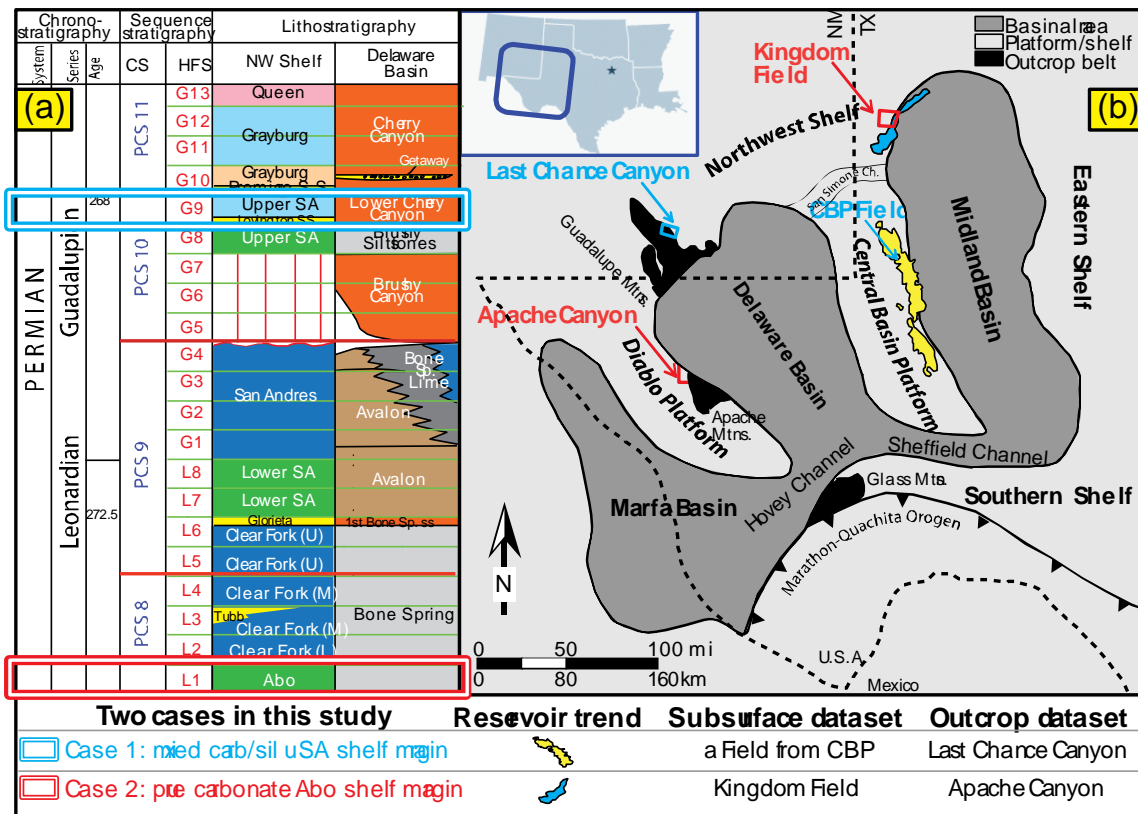


Figure 4.1: Study interval and areas, highlighted on (a) a Leonardian-Guadalupian stratigraphic column and (b) Middle Permian paleogeography map (Kerans et al., 2013). Constructed in Chapter 3, Case 1 used an outcrop dataset from Last Chance Canyon (blue box), and a subsurface dataset from Central Basin Platform (blue arrow). Case 2 in this study referred to Kingdom Field interpretations (red box) and facies model observed in Apache Canyon (red arrow) for a comparison with Case 1. The author consistently used red for Case 1 and blue for Case 2 for all applicable figures.

4.2.2 Datasets for Case 1 and Case 2

The previously constructed 5×3×0.44-km 3D lithostratigraphic model in Chapter 3 covers a stratigraphic interval of Upper San Andres shelf margin – Grayburg and Lower

Queen platform. An updated outcrop dataset constrained the lower portion of Upper San Andres Formation (G8~G9 HFS's). This dataset from Last Chance Canyon (LCC, blue arrow, Figure 4.1), Guadalupe Mountains, New Mexico, contains 42 measured sections, a merged LIDAR image of canyon walls where Scott (2007) mapped stratigraphic surfaces from G9 MFS to the G9 top, and digitized stratigraphic surfaces from Sonnenfeld and Cross (1993)'s 2D section for the lower stratigraphic surfaces. Moreover, Kenter et al. (2001)'s laboratory measurements of outcrop plugs (Figure 4.2b) in Sonnenfeld and Cross (1993)'s HFC6 in G9 HFS at 30MPa effective stress provides the basis for facies-based analysis of acoustic properties. In comparison, a subsurface dataset (Figure 4.2c) from a producing field in Central Basin Platform constrained the upper portion of Grayburg-Lower Queen platform (G10~G13 HFS's), with its densely-spaced 64 wells with sonic or density logs, 16 cores, and 3D seismic coverage.

As a major producing field within Early Permian Abo Platform Play/ Play 116 reservoir trend (Dutton et al., 2004), Kingdom Field is located along the Southern margin of Northwest shelf (Figure 4.1). The area of interest in this field is covered by a 3D time-domain seismic survey and has 166 dense well penetrations of complete or uppermost Early Permian pure carbonate Abo shelf margin reservoirs and its overlying Clear Fork platforms (Figure 4.3a). This field data, combined with Kerans (1995) and Courme (1999)'s outcrop studies in its analogous outcrops in Apache Canyon (Figure 1b), provides the basis for constructing an analogous carbonate model of Early Permian Abo shelf margin to its overlying Clearfork platform in Case 2.

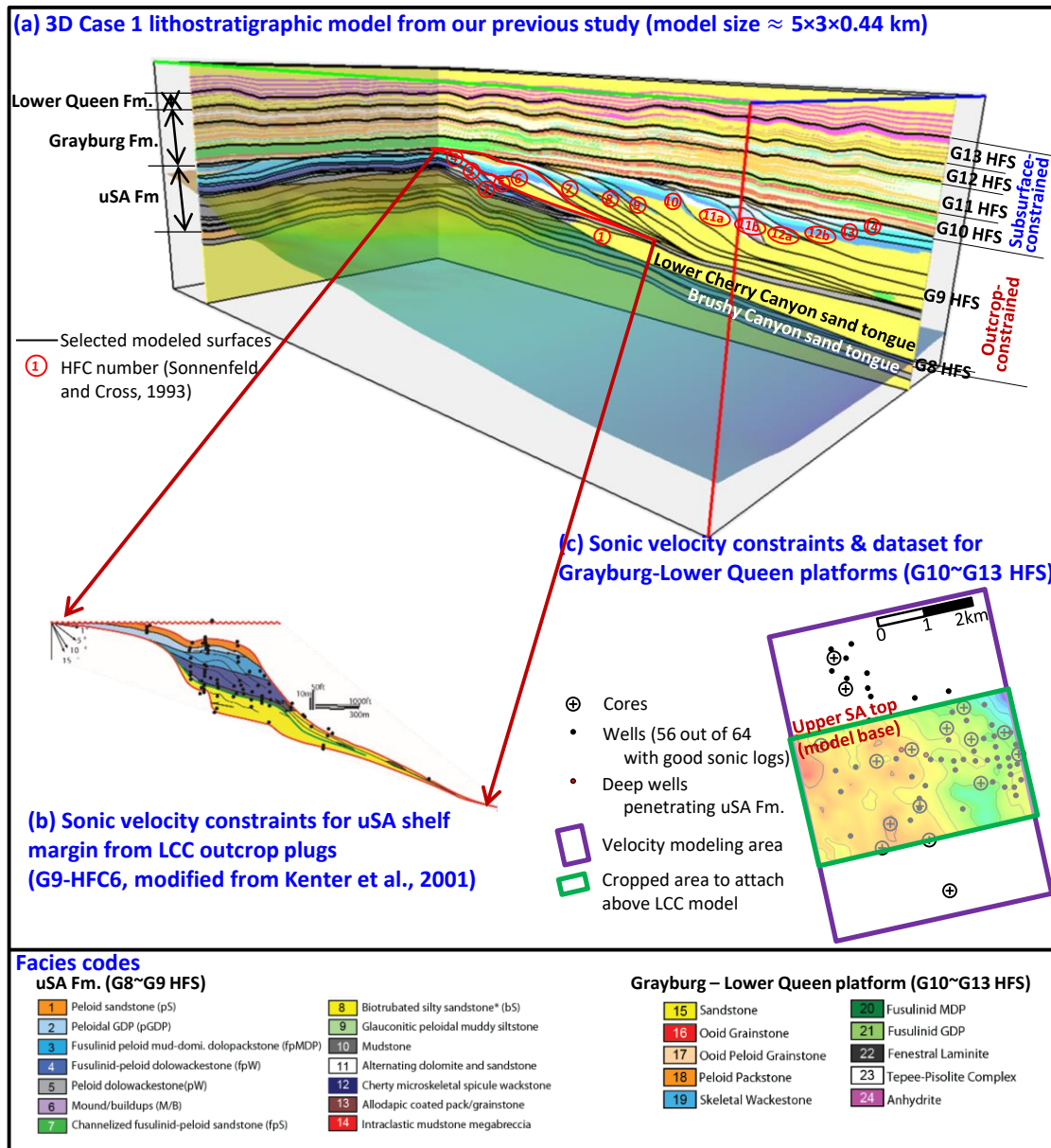


Figure 4.2: Case 1 datasets, including (a) a 3D lithostratigraphic model constructed in Chapter 3, as the skeleton for this study, and (b) 64 outcrop plugs from Kenter et al. (2001) for acoustic property analysis of Upper San Andres Formation. (c) wells and cores from the CBP producing field for Kerans and Sitgreaves (2015)'s facies modeling and acoustic property analysis for Grayburg-Lower Queen Formation in this study.

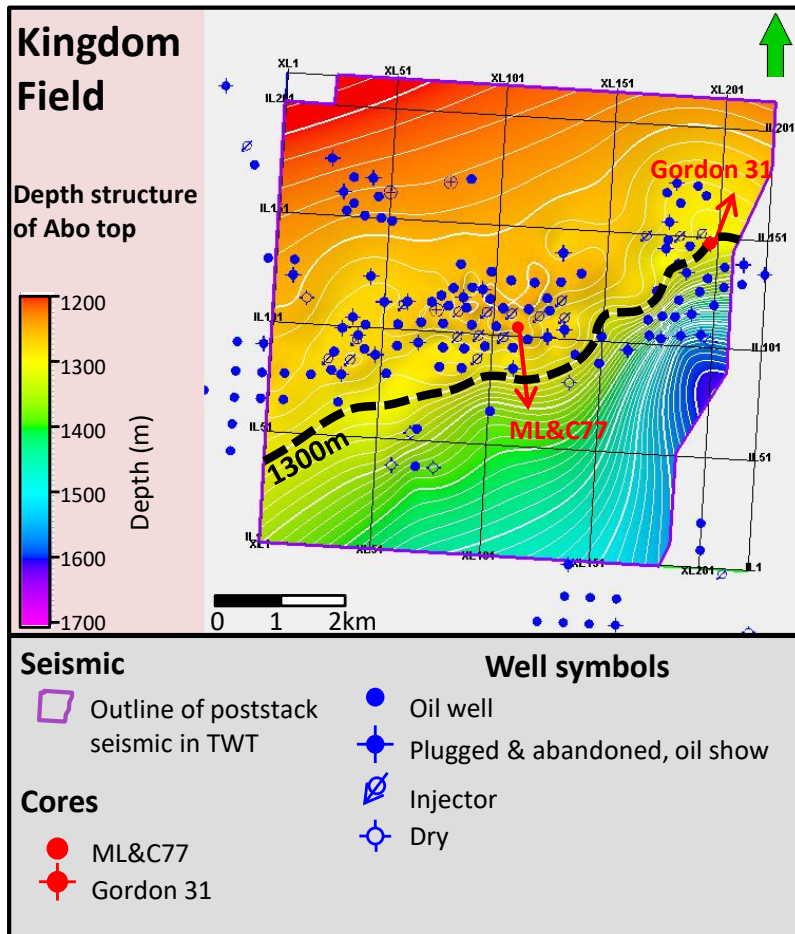


Figure 4.3: Kingdom Field dataset projected on a depth structure map of Abo Formation top, which was interpolated among 99 well picks. This dataset includes a time-domain seismic volume, 166 wells, and two described cores. This author projected the 1300-m depth contour from this structure map of Abo Formation top as the terminal Abo shelf margin on the stratal slice shown in Figure 4.5a2.

4.3 MODEL DESIGN: WORKFLOW AND RESULTS

4.3.1 An overview of modeling workflow

The author used a six-step workflow in this study (Figure 4.4) to develop a framework for comparative analysis of the two cases of mixed carbonate-siliciclastic (Case 1) versus pure carbonate (Case 2) shelf margin-platform successions.

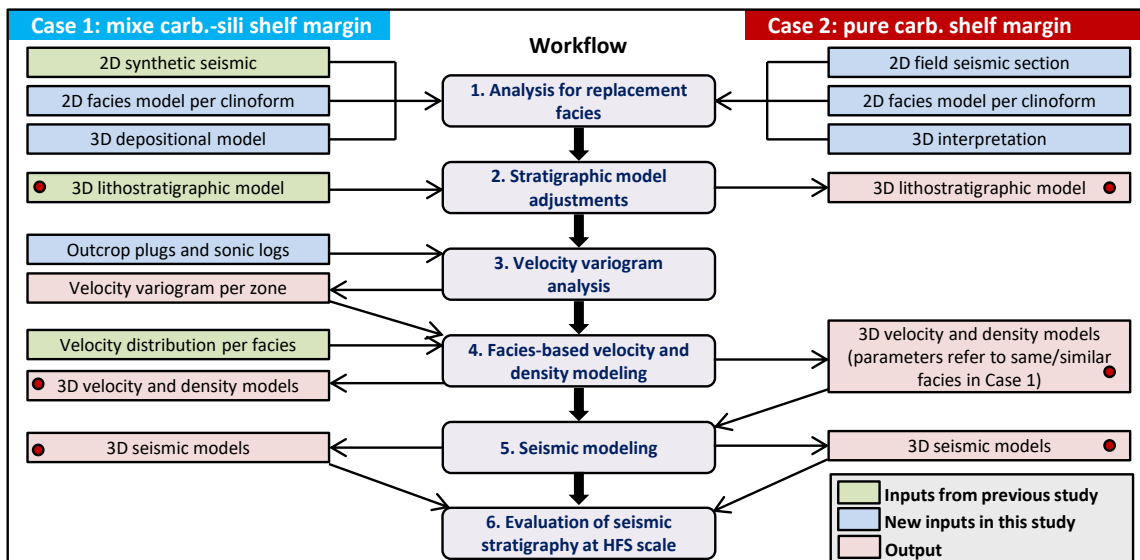


Figure 4.4: Workflow in this study for a comparative analysis of mixed carbonate/clastic (Case 1) versus pure carbonate (Case 2) shelf margin. For each case, the author modeled five different scenarios of spatial velocity distribution, and then simulated their seismic responses at three frequencies as low-, normal-, and high-frequency representations of field seismic data. Consequently, the author evaluated 30 seismic models in this study for a broad discussion on possible subsurface scenarios.

After lithofacies identification (Step 1) and stratigraphic adjustments (Step 2) upon the Case-1 3D lithostratigraphic model, the author obtained a pure carbonate lithostratigraphic model for Case 2. The completion of lithostratigraphic modeling and layering resulted in a simulation grid per case along the chronostratigraphic surfaces and contemporaneous layering, upon which the author can further simulated velocity and

density models (Step 3 and 4). The velocity models herein were extrapolated using Janson and Fomel (2011)'s method for an integration of intra-facies heterogeneity, where velocity extrapolation per facies was simulated along its contemporaneous slopes with user-defined (1) normalized velocity distribution controlling the possible velocity values and (2) velocity variogram controlling the spatial velocity continuity. During implementations, the author analyzed velocity variograms for selected zones (Step 3), using Kenter et al. (2001)'s outcrop plugs (Figure 4.2b) for Upper San Andres shelf margin and subsurface sonic logs (Figure 4.2c) for Grayburg-Lower Queen platforms. These variograms, along with normalized velocity distribution per facies from Chapter 3, serves as inputs for Janson and Fomel (2011)'s facies-based velocity modeling methods, where velocity was extrapolated along stratigraphic layering using Gaussian Random Function Simulation (Step 4, GRFS, Lantuéjoul, 2013). Subsequently, the author estimated a density model from the velocity model using Gardner (1974)'s equation, which was proven in Chapter 3 to be highly efficient for Case-1 datasets. Note that, instead of modeling a single pair of the velocity-density model as the inputs for acoustic wave equation seismic modeling/migration, this study considered five scenarios per case (Case 1 and Case 2) to accommodate for wider subsurface situations. Next, the author calculated a frequency spectrum from a Central Basin Platform producing field at its reservoir interval. This frequency spectrum served as a reference to select three wavelet frequencies for seismic simulation (Step 5) using an exploding-reflector modeling/migration package in Madagascar (Fomel et al., 2013), upon which the author further analyzed as the low-, medium-, and high-frequency representations of subsurface seismic. Finally, this chapter presents the evaluation of the resultant 30 seismic models (Step 6) in the next stand-alone section.

4.3.2 Results: Case 2 model construction

The author identified the siliciclastic-rich lithofacies for replacement in Case 1 by a multi-scale comparison between Middle Permian Upper San Andres (uSA) shelf margin in Case 1 and Early Permian Abo shelf margin in Case 2 (Figure 4.5).

First of all, both the 3D perspective (Figure 4.5a) and sectional comparison (Figure 4.5b) illustrated similar strong progradation and thus resembling stratal geometry near the terminal shelf margin of uSA Formation in Case 1 and of Abo Formation in Case 2. In the 3D perspective, the author compared Kerans et al. (2013)'s depositional model of G9 HFS in uSA shelf margin (Figure 4.5a1) with subsurface interpretations of Abo Fm. (Figure 4.5a2), where a seismic amplitude stratal slice was extracted slightly below Abo top (location shown as white dashed line in Figure 4.5b2) from a 90°-phase time-domain seismic volume. On this stratal slice, the author projected a 1300m-contour (green solid line, Figure 4.5a2) from the depth structure of Abo top (Figure 4.3) interpolated from 99 well picks as Abo terminal shelf margin. Moreover, as for the dip-oriented seismic sections, the author displayed a seismic section (an equivalent location shown as AA' in Figure 4.5a1) from a synthetic 90°-phase normal-frequency (dominant frequency/ $f_d = 27\text{Hz}$) seismic model, which was simulated from a Case1 facies-averaged velocity and density models. Next, the modeled stratigraphic surfaces of HFC6~14 in G9 HFS (solid canyon lines, Figure 4.5b1) were projected on this synthetic seismic section. In comparison, the author also showcased a seismic section (Figure 4.5b2, location shown as BB' in Figure 4.5b1) from a field 90°-phase seismic volume ($f_d = 30\text{ Hz}$, Zeng and Kerans, 2003), with its inferred interpretations of clinoforms. This interpretation mainly based on the outcrop analog from Apache Canyon (Kerans et al., 1995; Courme, 1999) and on 3D analysis from multiple stratal slices to differentiate individual clinoform (comparing the numbers annotated in Figure 4.5a2 and b2). As a result, the strong progradation near the terminal

shelf margin for the uSA Formation in Case 1 is apparently shown on its dip-oriented seismic section (Figure 4.5a2). In comparison, that for the Abo Formation in Case 2 is shown as (1) map-view closely-spaced seismic troughs paralleling the Abo terminal shelf margin on the amplitude stratal slice (Figure 4.5a2), and as (2) the inferred HFC clinoforms (cyan solid lines, Figure 4.5b2) on the field seismic section (Figure 4.5b2). The paralleling seismic troughs on the amplitude stratal slice were interpreted as a proxy of shelf-margin low-impedance porous reservoir facies (see Zeng et al., 2005a, b for the interpretive advantage of 90°-phase seismic volumes).

Moreover, the author anticipated resembling lithofacies spatial distribution pattern after a substitution of siliciclastic-rich lithofacies in Case 1 for carbonates lithofacies in Case 2. In general, both cases feature in a sinuous along-strike shelf margin trend (shown as a red solid line in Figure 4.5a1, and green solid line in Figure 4.5a2). For the mixed carbonate-siliciclastic G9 HFS in Case 1 (Figure 4.5a1, from Kerans et al., 2013), the shelf-margin reentrants became preferential pathways for sand bypass (F8) to the lower slope. In comparison, the promontories are dominated by carbonate deposition including the upper-slope bioherms (F6) and possibly serve as updip sources of mixed turbidite channels of Fusulinid peloid sandstone (F7). Therefore, during the lithofacies substitution of siliciclastic-rich lithofacies in this Case 1 for carbonate facies in Case 2,

- the author started with a comparison of ‘larger’-scale heterogeneity with highly-ordered basinward facies transition, by comparing the HFC clinoform model as observed from Last Chance Canyon for Case 1 (Figure 4.5c1, Sonnenfeld and Cross, 1993; Scott, 2007) and as observed from Apache Canyon for Case 2 (Figure 4.5c2). This comparison revealed a similar lithofacies assemblage (F2, F3, F4 and F5) in their shelf margin to upper-slope facies belt; thus the author kept them unchanged when constructing the Case 2 lithostratigraphic model. In contrast, the

- author replaced middle/outer shelf peloid sandstone (F1) with fenestratal laminate (F22), as well as the lower-slope bioturbated sandstone (F8) with Fusulinid peloid wackestone to mudstone (F26).
- subsequently, the author validated the existence of localized objects in Case 2, which were simulated in Case 1 using Stochastic Object Modeling as described in Chapter 3. First of all, the seismic anomalies on carbonate slope, which are perpendicular/oblique to Abo terminal shelf margin (green solid line, Figure 4.5a2), can be seismic geomorphologically interpreted as turbidite channels. This possibility was further tested by core descriptions (Figure 4.6) noting pure-carbonate turbidite channels of Fusulinid peloid pack- to wackestone (F27). Meanwhile, the core ML&C77 (Figure 4.6, location shown as a white triangle in Figure 4.5a2) also encountered an interval of upper-slope reefal boundstone (F6). Therefore, the author kept the F6 unchanged during lithofacies substitution, while replaced the mixed turbidite channels of fusulinid peloid sandstone (F7) with carbonate turbidite channels of Fusulinid peloid pack- to wackestone (F27). Using a similar comparative analysis approach, for the rest lithofacies not included in G9-HFC6 (Figure 4.5c1), the author replaced glauconite peloid muddy siltstone (F9) with F26.

After the lithofacies substitution, the author obtained a new Case 2 lithostratigraphic model, and then further re-layered this model to mimic the stratification of the HFC clinoform model as observed from Apache Canyon (Figure 4.5c2). This stratigraphic adjustment serves as a critical procedure before velocity modeling, whose extrapolation follows the real contemporaneous slopes. More specifically, the previous layering of a typical HFC in Case 1 (black dashed lines in Figure 4.5c1) has been applied separately for its transgressive/T- and regressive/R- hemicycle, referring to Sonnenfeld and

Cross (1993) and Scott (2007)'s observations on stratifications. The author layered the T-hemicycle by following its zone top (the flooding surface of this HFC), whereas layered the R-hemicycle by following an imaginary reference surface, which is the middle surface between the zone base and top (the flooding surface and cycle top of this HFC). After the stratigraphic adjustment referring to Kerans (1995)'s HFC clinoform facies model from Apache Canyon(Figure 4.5c2), the author re-layered the Case 2 by proportional layering upon corresponding entire HFC (illustrated on a Case 1 clinoform model as magenta dashed lines, Figure 4.5c1). As a result, the previous two-zone stratigraphic grid in Case 1 model has now changed into a single-zone proportionally-layered stratigraphic grid in the Case 2 lithostratigraphic model.

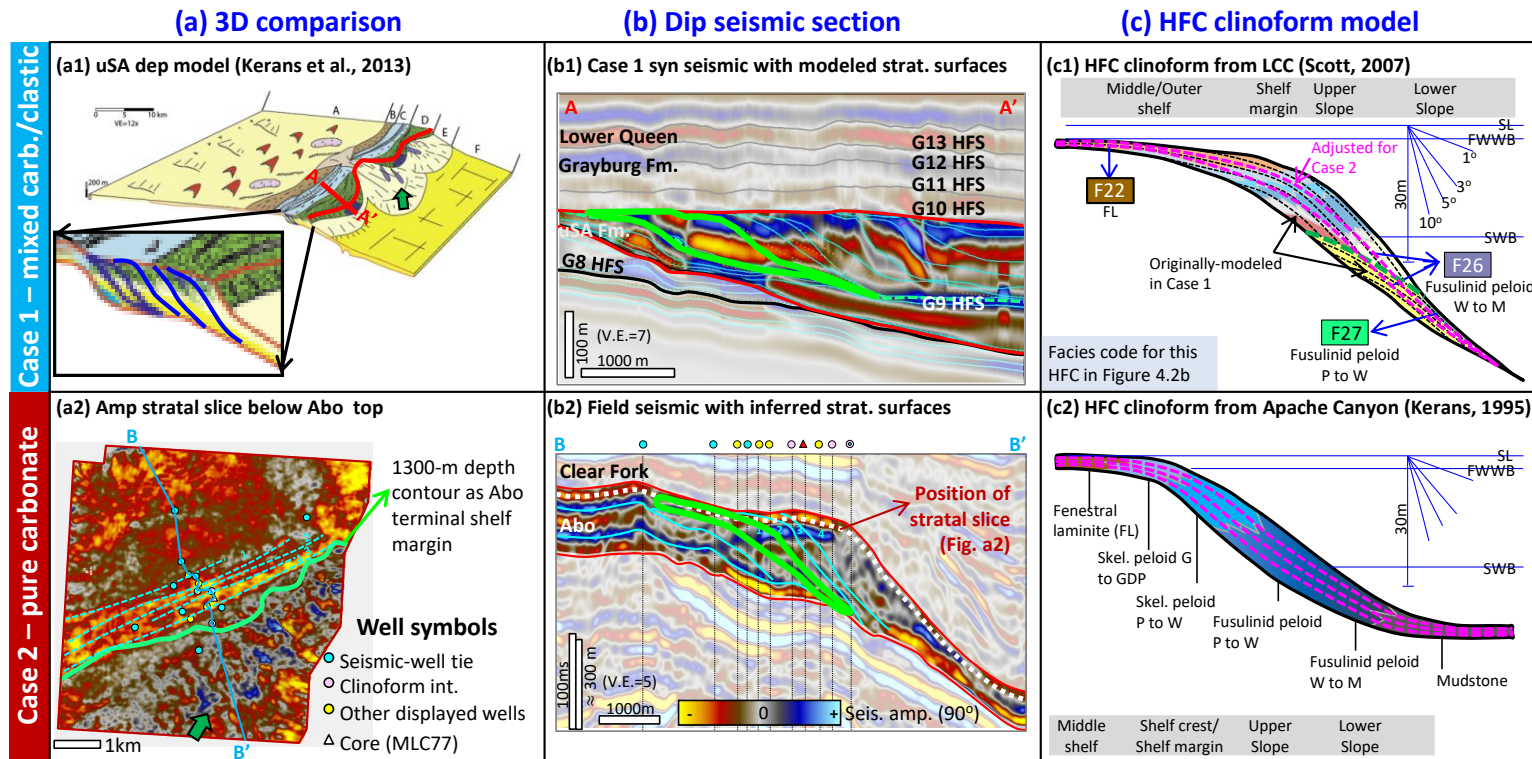


Figure 4.5: Comparisons between two cases for lithofacies substitution and stratigraphic adjustment. (a) A 3D comparison between (a1) Kerans et al. (2013)'s depositional model for G9 HFS of uSA Fm., and (a2) interpretation on a stratal slice along Abo Fm. top. (b) A comparison of a dip-oriented seismic section between (b1) synthetic 35Hz-90°-phase seismic section of uSA shelf margin with overlying modeled stratigraphic surfaces (solid canyon lines), and (b2) field seismic section of Abo shelf margin, with inferred HFC clinoformal surfaces (solid canyon lines). The synthetic seismic model in (b1) was simulated from a facies-averaged velocity and density model. (c) a comparison of HFC-clinoform facies model between (c1) uSA clinoform observed in Last Chance Canyon and described by Scott (2007) and (c2) Abo clinoform observed in Apache Canyon and described by Kerans (1995).

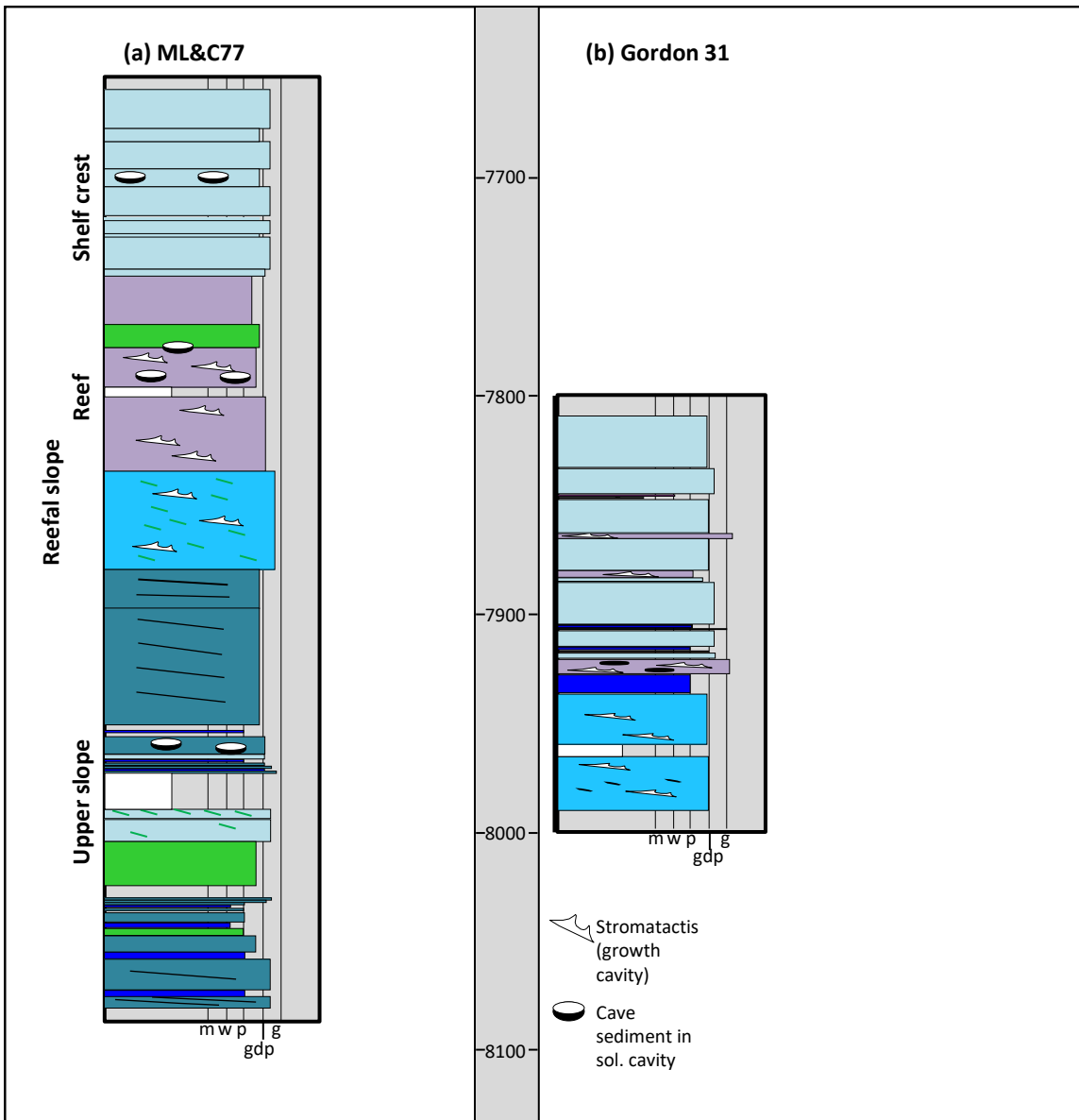


Figure 4.6: Described cores by Kerans (modified from internal course slides) from Kingdom Field, including (a) ML&C 77 and (b) Gordon 31 with locations shown in Figure 4.3. The lithofacies assemblage shown in these cores is similar to Kerans (1995)'s facies model for a typical HFC clinoform proposed from Apache Canyon (Figure 4.5c2), with the development of reefal boundstone in reefal shelf facies belt.

4.3.3 Results: velocity variogram analysis and models

He et al. (2015b) previously studied the influence of different spatial velocity variation on resultant reservoir-scale seismic models upon a simplified 2D geologic section of uSA HFC clinoforms exposed at Last Chance Canyon (modified from Kenter et al., 2001). That study proved the significance of integrating intra-facies heterogeneity represented as the spatial velocity variation for uSA modeling interval. In this study, the author utilized the same velocity modeling approach (Janson and Fomel, 2011) upon 25 lithofacies within 38 zones for five different spatial velocity variations. First of all, the author constructed the intermediate velocity model (Figure 4.7, S_3) with adjusted normalized velocity distribution per facies from Chapter 3 and experimental velocity variograms for selected zones in this study (Table 4.1). For the new experimental variogram analysis, the author conducted it separately for the outcrop-plug-constrained uSA shelf margin HFC clinoform/HFC6 (Figure 4.2b) versus the sonic-log-constrained Grayburg-Lower Queen platforms (Figure 4.2c). Detailed analysis has been included in Appendix I, with analytic results of the fitted variograms shown in Table 4.1b. As revealed by this analysis, the Grayburg-Lower Queen platforms fitted from upscaled sonic logs have apparently more continuous spatial velocity distribution (along both horizontal and vertical orientation) than that of Upper San Andres shelf-margin clinoform fitted from outcrop plugs. Moreover, within the upper platform interval, the spatial velocity distribution is more continuous along the strike than the dip orientation. Within the lower uSA shelf margin HFC (HFC6), its transgressive siliciclastic-rich hemicycle is less continuous than its regressive carbonate-dominant hemicycle.

This intermediate velocity model (S_3 , Figure 4.7) with experimental velocity distribution (Figure 4.8b) and spatial continuity (Table 4.1b) provided a reference to set

up four realistic end-member velocity models. The author shrank this intermediate velocity spread (σ) per facies in S_3 (Figure 4.8b) to half ($1/2 \sigma$, Figure 4.8a) for end-member velocity models with a small velocity spread (S_1 and S_2 , Figure 4.7). In contrast, the author whereas double-stretched it (2σ , Figure 4.8a) for end-member velocity models with a large velocity spread (S_4 and S_5 , Figure 4.7). Similarly, for the other variable of spatial velocity continuity, the author adjusted it by changing the range of the velocity variograms away from the intermediate velocity model (S_3) with an imaginary variogram range of a (Table 4.1b). Referring to this variogram range (major, minor horizontal range, and vertical range) in intermediate model per zone, the author obtained the end-member velocity models with twice as good spatial velocity continuity (range= $2 a$, Table 4.1a; S_1 and S_4 , Figure 4.7). In contrast, the author also obtained the end members with poor, half spatial velocity continuity (range= $1/2 \times a$, Table 4.1c; S_2 and S_5 , Figure 5.7). Note that, finally the author decided to use the facies-averaged velocity model as S_1 . Besides its significance as an extreme representation of S_1 with an infinitely narrow velocity distribution and great velocity continuity, the facies-averaged velocity model also serves as a benchmark model, as it has been most widely used as an input for seismic modeling of large outcrops.

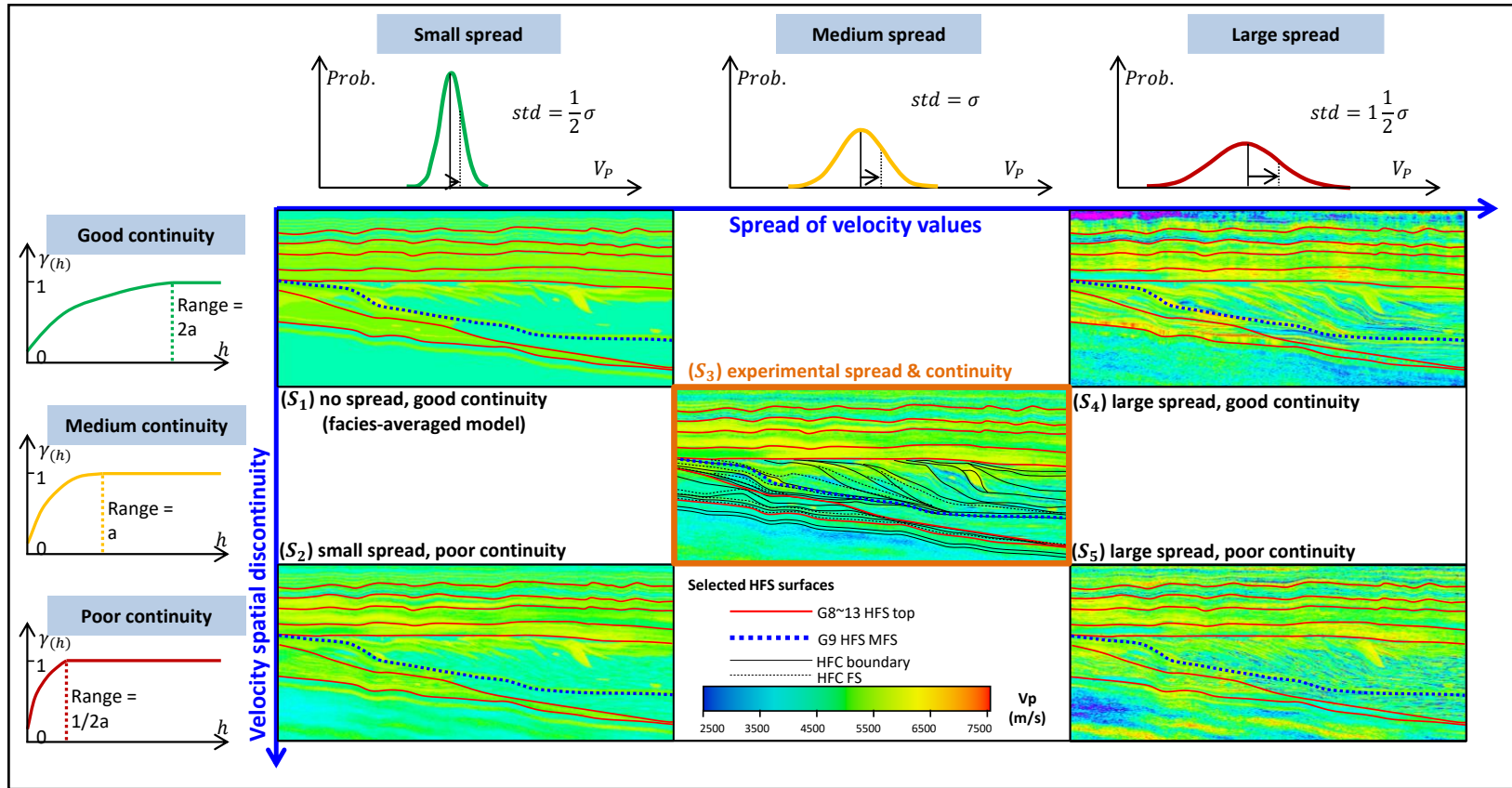


Figure 4.7: Velocity modeling of five scenarios for Case 1, reflecting five levels of intra-facies heterogeneity. Velocity was modeled using Janson and Fomel (2011)'s method, where spatial velocity continuity is equivalent to a combination of velocity spread and spatial velocity continuity. The intermediate velocity model (S_3) was constructed using experimental normalized velocity distribution per facies (Figure 4.8b) and experimentally fitted velocity variogram per zone (Table 4.1b). The four realistic end members (S_1 , S_2 , S_3 and S_4) were constructed by adjusting velocity distribution per lithofacies and velocity variograms for selected zones.

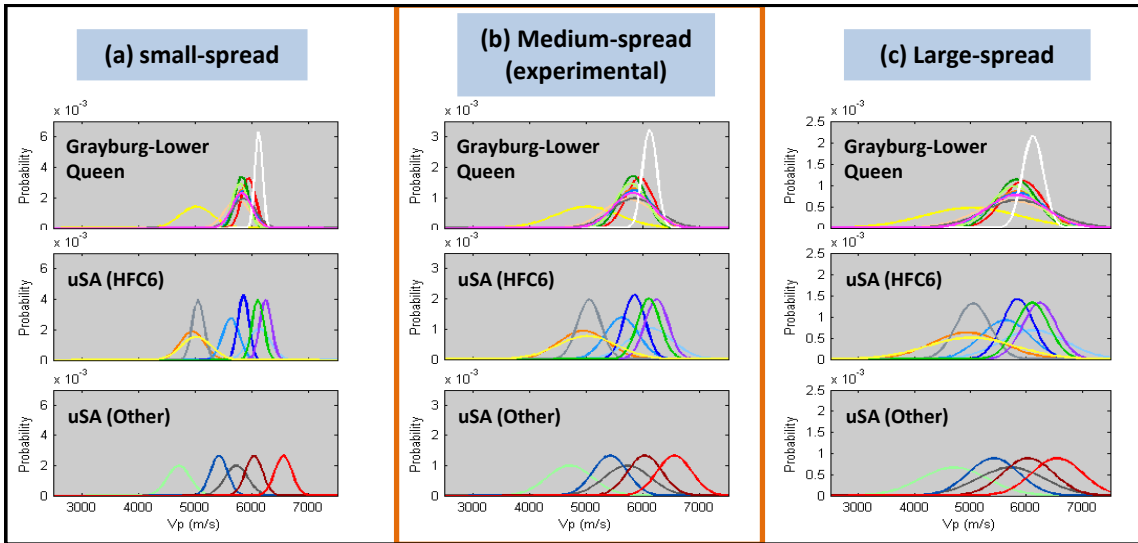


Figure 4.8: Normalized velocity distribution per facies with (a) small-, (b) medium, and (c) large spread of velocity values.

		type	nugget	sill	Range (m)		
					Minor	Major	Vertical
(a) Good velocity continuity	G13 HFS	spherical	0.2285	0.9729	6412	11043	30
	G12 HFS						44
	G11 HFS						118
	G10 HFS						120
	G9-HFC6-R	spherical	0	0.9949	1614	1614	3.86
	G9-HFC6-T	spherical	0.033	0.9822	534	534	6.8
(b) Medium velocity continuity (experimentally-fitted)	G13 HFS	spherical	0.2285	0.9729	3206	5515	15
	G12 HFS						22
	G11 HFS						59
	G10 HFS						60
	G9-HFC6-R	spherical	0	0.9949	807	807	1.93
	G9-HFC6-T	spherical	0.033	0.9822	267	267	3.4
(c) Poor velocity continuity	G13 HFS	spherical	0.2285	0.9729	1603	2757.5	7.5
	G12 HFS						11
	G11 HFS						29.5
	G10 HFS						30
	G9-HFC6-R	spherical	0	0.9949	403.5	403.5	0.965
	G9-HFC6-T	spherical	0.033	0.9822	133.5	133.5	1.7

Table 4.1: Velocity variograms for selected zones used in this study, with (a) good, (b) intermediate/experimentally-fitted, and (c) poor velocity continuity.

Similarly, five scenarios of velocity models (Figure 4.9) were constructed to accommodate a variety of intra-facies heterogeneity in Case-2 pure carbonate successions. The Case-2 velocity distribution per facies refers to that of the same or analogous lithofacies in Case 1 (Figure 4.8). Besides, as discussed in the facies modeling section, the siliciclastic-rich transgressive hemicycle and carbonate-dominant regressive hemicycle in a typical HFC of Case 1 have been grouped into a single pure carbonate HFC before proportional re-layering in Case 2 (compare Figure 4.5c1 and c2). Therefore, the author further assigned the velocity variogram of the carbonate-dominant regressive hemicycle in Case 1 (Table 4.1) to the new pure carbonate HFC's in Case 2 during the velocity modeling. Finally, these five velocity models per case (Figure 4.7 for Case 1 and Figure 4.9 for Case 2) serves as inputs for estimating their respective density model using Gardner (1974)'s equations. This estimation is highly-effective for the uSA-Grayburg modeling interval, as discussed in Chapter 3.

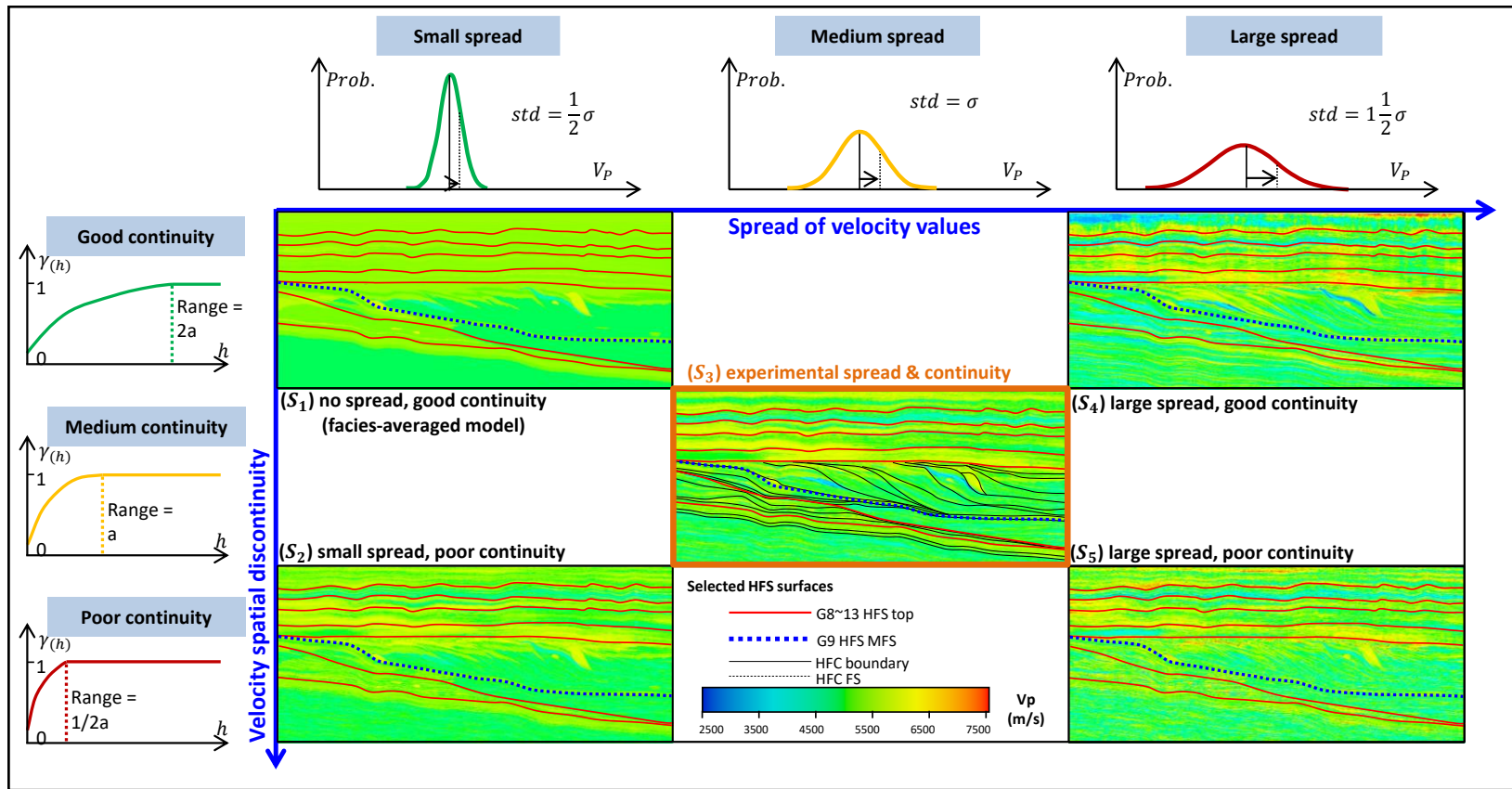


Figure 4.9: Velocity modeling of five scenarios for Case 2, reflecting five levels of intra-facies heterogeneity. Velocity was modeled using Janson and Fomel (2011)'s method, where spatial velocity continuity is equivalent to a combination of velocity spread and spatial velocity continuity. Compared with Case 1 velocity models, the author referred to same/similar lithofacies in Case 1 (Figure 5.8) to assign velocity distribution per lithofacies in Case 2. Besides, the velocity variograms for pure carbonate clinoform HFC's was assigned using that from the carbonate-dominant regressive hemicycle in uSA Formation (G9 HFS-HFC6-R, Table 4.1).

4.3.4 Results: seismic models

The author extracted a seismic frequency spectrum (Figure 4.10) from the stacked and migrated seismic data of uSA-Grayburg reservoir interval in the Central Basin Platform producing field (Figure 4.1). This seismic frequency spectrum has a dominant frequency at 35Hz and a bandwidth of 0~80 Hz. Since the author chose Ricker wavelet, whose dominant frequency is 1.3 times of its peak frequency, the author simulated seismic models at a peak frequency of 27 Hz as a 35 Hz subsurface representation. Afterward, the author chose half and double of this frequency, namely a dominant frequency of 17.5- and 70-Hz as the low- and high-frequency representations of subsurface seismic data.

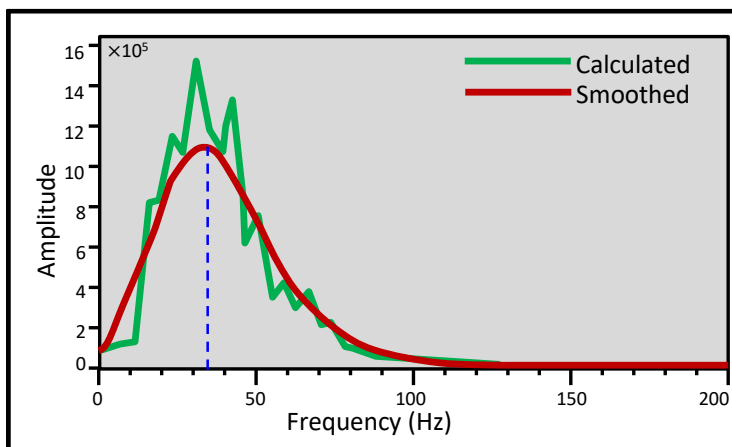


Figure 4.10: Seismic frequency spectrum extracted from the uSA-Grayburg reservoir interval of a producing field along the Eastern flank of CBP.

Eventually, this forward modeling workflow has obtained 15 90°-phase seismic models per case for the mixed carbonate/clastic successions in Case 1 (Figure 4.11) and for the pure carbonate successions in Case 2 (Figure 4.12). These models were generated as a result of five spatial velocity variations and three testing wavelet frequencies per case. To summarize, at this stage, the resultant lithostratigraphic models, acoustic property

models, and seismic models have incorporated five controllable variables potentially influencing the 'chronostratigraphic significance of seismic reflections' at the reservoir scale (as predefined in Chapter 1), including

1. flat versus clinoformal stratal geometry, by comparing uSA shelf margin versus Grayburg-Lower Queen platforms
2. gentle versus fast lateral lithofacies variation, by comparing the slower lateral lithofacies variations within Grayburg-Lower Queen platforms and fast lithofacies variations within uSA HFC shelf-margin clinoforms
3. mixed carbonate/clastic and pure carbonate successions (Case 1 and Case 2) with more complicated lithofacies-velocity relationship than that of the siliciclastic cross-section in Vail et al. (1977c)
4. different levels of intra-facies heterogeneity reflected as spatial velocity continuity, which can break down to velocity value spread and spatial velocity continuity, and
5. varied seismic frequencies to test the frequency-dependency for the fundamental assumption of seismic stratigraphy, which was proposed to be frequency-independent at exploration scale.

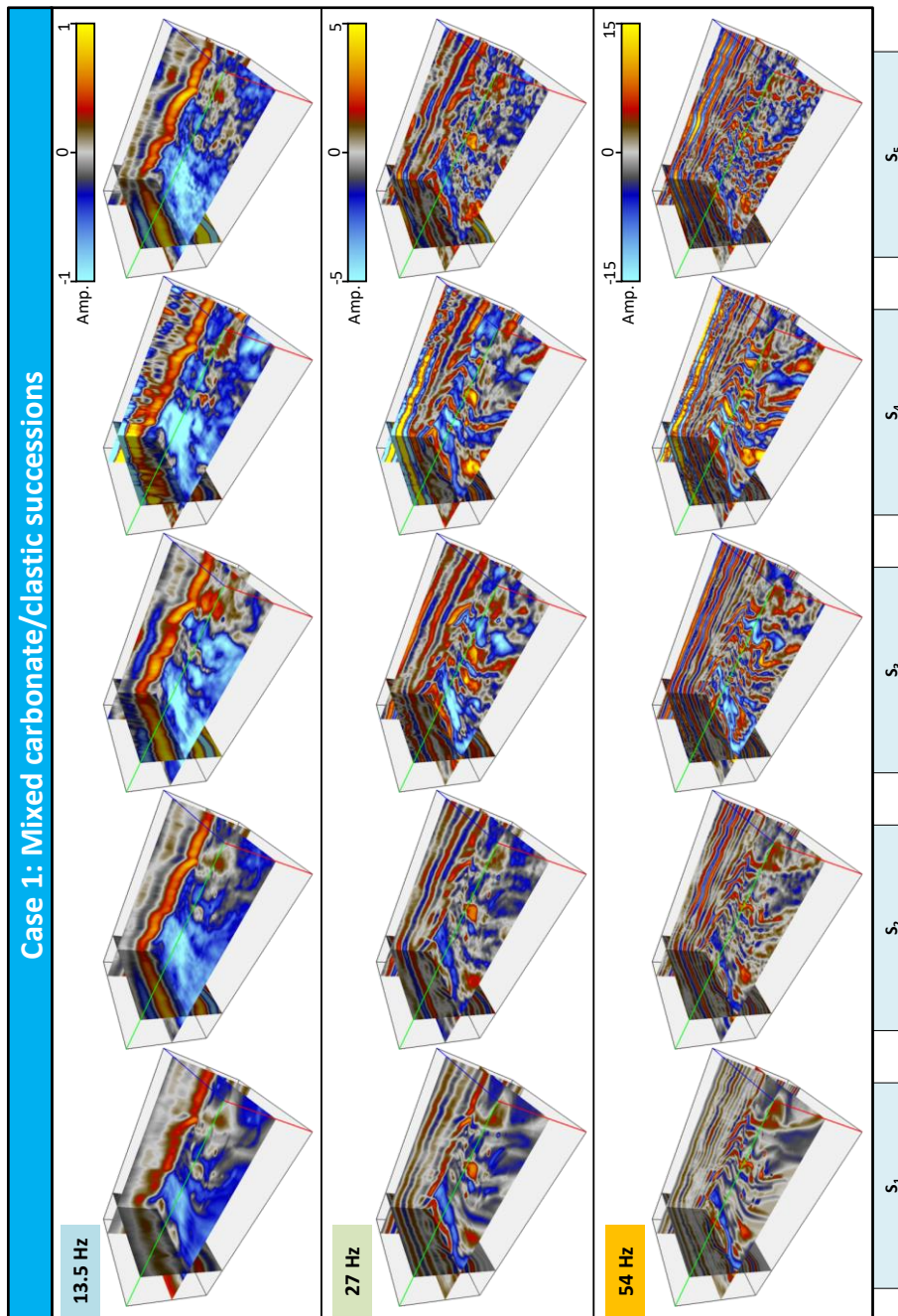


Figure 4.11: Case 1 seismic models at a dominant frequency of 13.5, 27 and 54Hz, as low-, normal-, and high-frequency representations of subsurface seismic, generated from five different levels of intra-facies heterogeneity represented as different spatial velocity variations ($S_1 \sim S_5$).

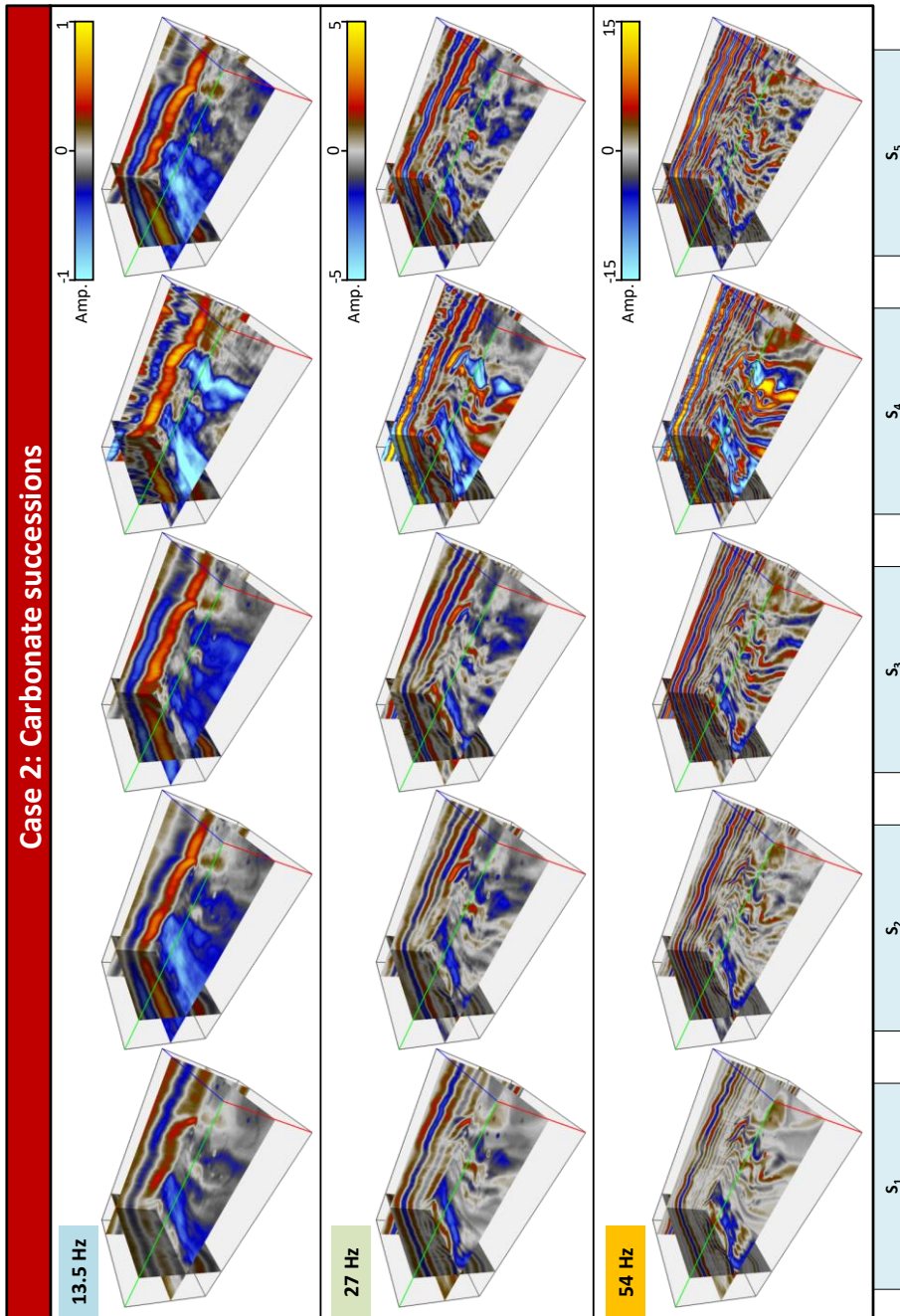


Figure 4.12: Case 2 seismic models at a dominant frequency of 13.5, 27 and 54Hz, as low-, normal-, and high-frequency representations of subsurface seismic, generated from five different levels of intra-facies heterogeneity represented as different spatial velocity variations (S₁~S₅).

4.4 EVALUATION METHODS AND EXAMPLES

The evaluation method in this study is an extension from He et al. (2015a) included as Chapter 2, which defined time-correlation error (TCE) as a measurement of discrepancy between the horizon interpreted following seismic reflection geometry against its corresponding modeled stratigraphic surface. In addition to the initial application of this TCE concept on conceptual flat-lying siliciclastic reservoir models in Chapter 2, this concept herein applies to the outcrop- and subsurface-constrained model (Case 1) as well as its analogous model. Moreover, the evaluation of the chronostratigraphic significance of seismic reflections is at the HFS and finer scale⁴.

4.4.1 An example on evaluating one horizon from one seismic model

The example shown in Figure 4.13 illustrated the evaluation on the chronostratigraphic significance of an HFS-scale interested seismic horizon from a 35-Hz 0°-phase seismic model constructed in Chapter 3, which was simulated from a facies-averaged velocity and density model for the mixed carbonate/clastic successions (Case 1 - S₁). Following the assumption of the chronostratigraphic significance of seismic reflections (Vail et al., 1977c), seismic reflections were assumed as internal stratifications so that termination relationships can be interpreted (red arrows and double-sided arrows, Figure 4.13a) on dip-oriented inlines. Upon the interpretations of the termination relationship, the author picked two HFS boundaries, including G9 HFS top as a seismic trough (solid yellow line, Figure 4.13a) and G9 HFS bottom as a seismic trough (green solid line, Figure 4.13a). Furthermore, the author focused on the evaluation of the G9 HFS bottom, by extending its interpretation to strike-oriented cross-lines (Figure 4.13b), and finally to the 3D seismic horizon (Figure 4.13c). Subsequently, the author compared this interpreted seismic horizon

⁴Figure 4.13 and 4.14 were modified from He et al. (2017a)'s AAPG ACE talk.

following the 'chronostratigraphic significance of seismic reflections' against its modeled surface (Figure 4.13d). This procedure resulted in a difference map known as TCE map in this study (Figure 4.13e), which allows identification of error-prone areas. For instance, a positive value on TCE map at a given location represent that the interpretation is higher than the modeled surface (such as Point A, Figure 4.13a), whereas its negative value (such as Point B, Figure 4.13a) represent an interpretation lower than the modeled surface. Furthermore, the histogram (Figure 4.13g) of this TCE map (Figure 4.13e) provides a likelihood distribution for a given error to occur. Note that, the author shifted the original TCE map (Figure 4.13e) in relative to its mean (17.66m, Figure 4.13g) so that one can obtain a zero-centered TCE map (Figure 4.13f) and then its histogram (Figure 4.13h) with a mean of zero. This procedure accommodates for the original definition of a 'time-significant' seismic reflection, which can be either coincide with or 'parallel to' its corresponding chronostratigraphic surface (Vail et al., 1977c). As another advantage of this shift, the resultant zero-centered TCE map and histogram (Figure 4.13 f and h) further facilitate cross-comparisons between evaluation results of multiple seismic models, as shown in the next example.

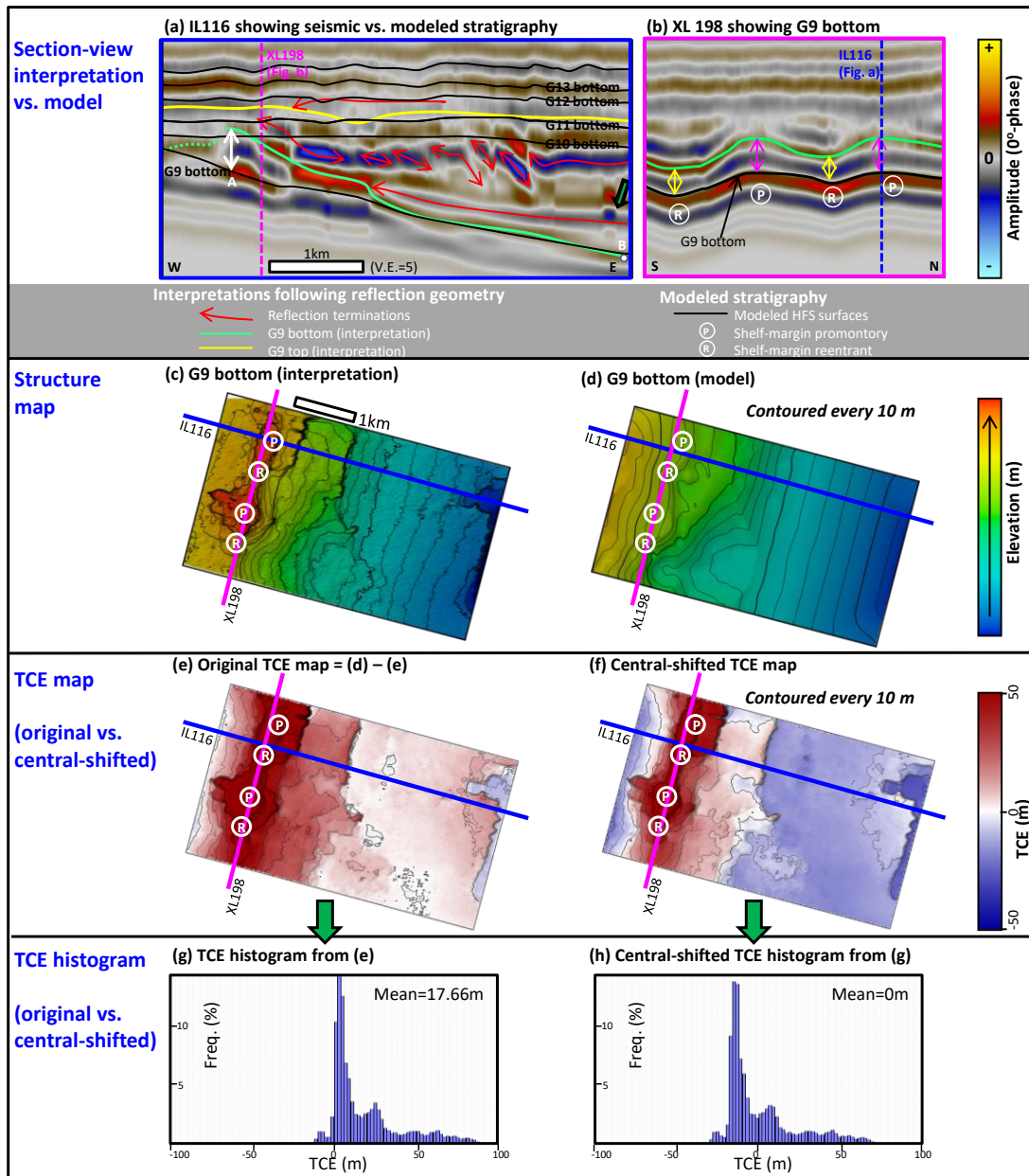


Figure 4.13: An example of evaluating the chronostratigraphic significance for a targeted horizon of G9 HFS bottom. (a) and (b) are dip- and strike- sections showing interpretations against modeled stratigraphy. (c) and (d) are respectively the interpretation of G9 HFS bottom following the ‘chronostratigraphic significance of seismic reflections’ and the modeled G9 HFS bottom. (e) and (g) are the original TCE map and its histogram, whereas (f) and (h) are zero-centered TCE map and histogram. The following examples all use zero-centered TCE maps and histograms to facilitate cross-comparison.

4.4.2 An example of cross-comparison among multi-frequency seismic models

Applying the above evaluation workflow to multi-frequency seismic models from the same velocity-density model allows a further discussion on frequency-dependency (Variable 5 predefined in Chapter 1) of the ‘chronostratigraphic significance of seismic reflections’, and then interpretation strategies to improve the seismic chronostratigraphic correlation. An example (Figure 4.14) shown here is a cross-comparison of evaluations on interpreted G9 HFS bottom from low-, normal-, and high-frequency 0°-phase seismic models, whose inputs were Case 1- S_1 velocity (Figure 4.7) and density model (Figure 4.9). Similar to the normal-frequency example illustrated in the last section (Figure 4.13), the interpreted seismic horizons of G9 HFS bottom (Figure 4.14b~d) from multi-frequency seismic volumes all follow a seismic peak based on termination relationship. Subsequently, the author obtained their zero-centered TCE map (Figure 4.14e~g) and then TCE histogram (Figure 4.14h~j).

In the next discussion section, the author will probe into three alternative solutions as suggested in this comparative example, including

- Option 1: using the high-frequency seismic components/volume to improve the seismic chronostratigraphic correlation. This option serves as an efficient approach if the TCE histogram distribution narrows with the increasing seismic frequency. In this example of Case 1- S_1 (Figure 4.14h-j), this option does not work well, as the interpretation from the low-frequency seismic model has exhibited the smallest discrepancy (Figure 4.14h), whereas that from the intermediate-frequency volume displays the widest TCE distribution (Figure 4.14i).
- Option 2: incorporating preferential interpretation with well-interpolation, based on the error distribution pattern from the forward seismic modeling studies. In this example, all of these three tested TCE maps (Figure 4.14 e~g) exhibit a linear/low-

sinuosity positive anomaly ridge near the shelf margin, with a larger error near the shelf-margin promontories than reentrants. Therefore, one can consider picking seismic events along dip-sections crossing less-error-prone shelf-margin reentrants and then integrate this preferentially-interpreted horizon patch with other horizon patches near the error-prone shelf-margin promontories constrained, which can be obtained by interpolation among well tops.

- Option 3: integrating horizon patches from multi-frequency seismic volumes. In this example, a comparison between interpreted structure maps from low-, medium-, and high-frequency seismic volumes (Figure 4.14b~d) against the modeled G9 HFS bottom (Figure 4.14a) revealed a promising application in combining horizon patches interpreted from different frequencies to obtain a composite surface better honoring the actual stratigraphy. In this example (Figure 4.14), one can consider integrating three horizon patches of different locations. For instance, the platform area of the low-frequency interpretation (labeled as ① in Figure 4.14a and b) most resemble the actual chronostratigraphic surface and thus can be cropped as a horizon patch. Similarly, a horizon patch upper to lower-slope from medium – frequency interpretation (labeled as ② in Figure 4.18a and c), and a horizon patch at the toe-of-slope from high-frequency interpretation (labeled as ③ in Figure 4.18a and d), would also help improve the seismic chronostratigraphic correlation.

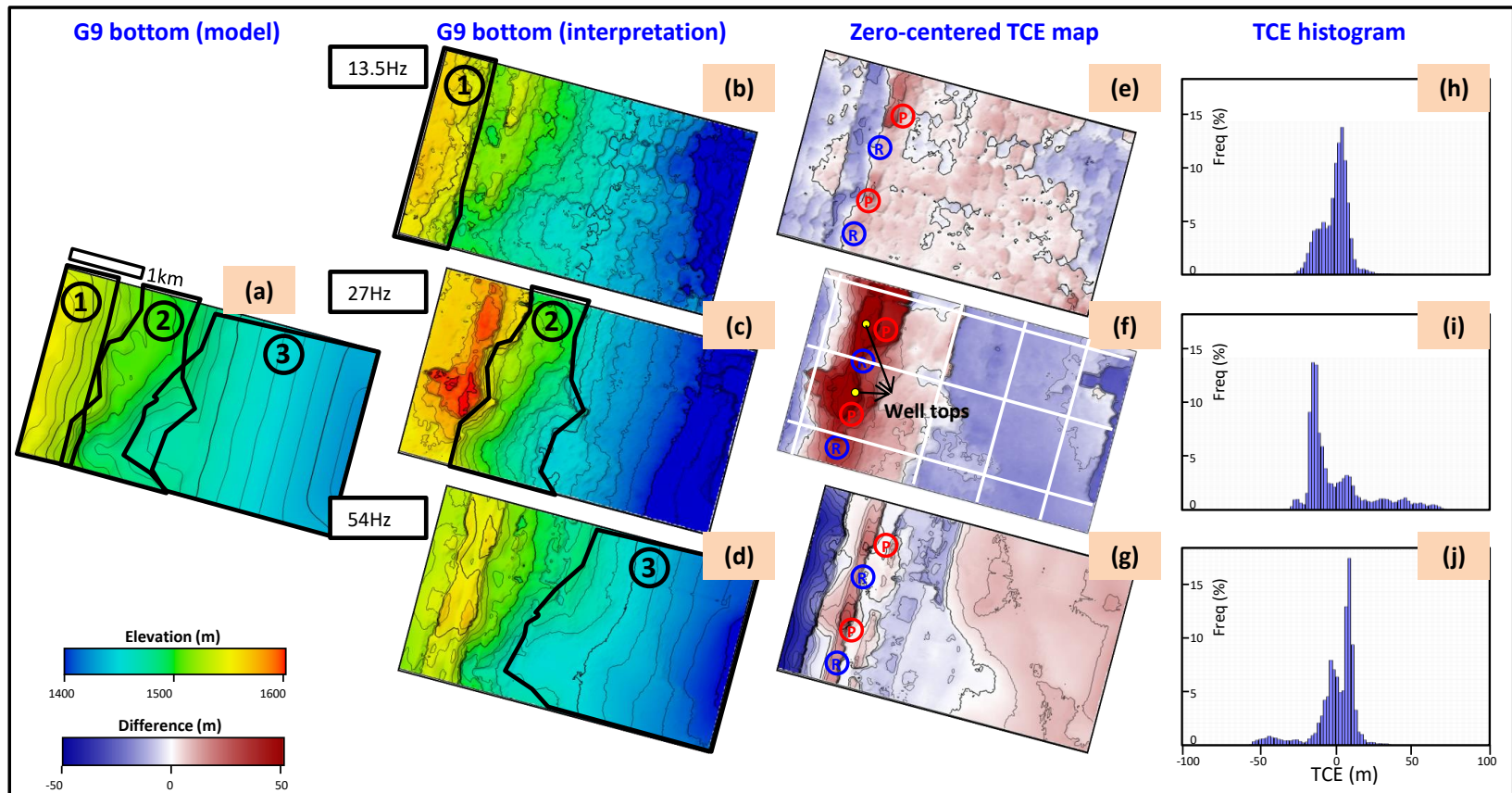


Figure 4.14: A comparative example on interpretations of G9 HFS bottom from multi-frequency seismic volumes simulated from Case 1 - S_1 velocity and density models. (a) Modeled G9 HFS bottom surface, (b)~(d) are interpretations from multi-frequency seismic volumes, whose TCE maps and histograms are respectively shown in (e)~(g) and (h)~(i).

4.5 EVALUATION RESULTS AT HFS AND HFC SCALE

This chapter further applied the above comparative evaluation approaches to five velocity and density models ($S_1 \sim S_5$, Figure 4.7 and 4.9) per case (Case 1 and Case 2) for a complete evaluation of 30 90°-phase seismic models (Figure 4.11 and 4.12). The author focused on the assessment of two HFS surfaces. One is the flat-lying G12 HFS top (Figure 4.2a), also known as the Grayburg Formation top and used as Grayburg reservoir-bounding surface. The other is the clinoformal G9 HFS bottom (Figure 4.2a), which is the same surface illustrated in the previous introductory examples, spanning from the platform to the toe-of-slope and can optionally serve as a significant surface in constructing uSA porous carbonate reservoirs. Finally, the author also extended the discussion to HFC scale, by manually picking landward-dipping diachronous horizon patches and then comparing their occurrences in mixed carbonate/clastic and carbonate shelf margins with the change of seismic frequency.

4.5.1 Evaluation results of flat-lying G12 HFS top

The seismic interpretations of G12 HFS top from 30 seismic models follow the most continuous reflector in the closet adjacent of the modeled G12 HFS top (Figure 4.15), referring to the termination relationships by assuming seismic reflections as stratifications. Subsequently, the author calculated their zero-centralized TCE maps (Figure 4.16) and histograms (Figure 4.17) using the method introduced in Section 4.4. Evaluation results suggest that

1. Mixed versus carbonate successions: the chronostratigraphic significance of G12 HFS top in carbonate platforms are in general better than that in mixed platforms, with narrower TCE distributions for all of the tested five intra-facies heterogeneity and at all of the three tested frequencies (Figure 4.17).

2. Regarding the three alternative options to improve the seismic chronostratigraphic correlation
 - Option 1: Increasing the seismic frequency significantly helps improve chronostratigraphic significance of G12 HFS top for all tested scenarios, with narrower TCE distributions with increasing seismic frequency (Figure 4.17).
 - Option 2: For both mixed carbonate/clastic (Case 1) and carbonate (Case 2) platforms, at low-frequency ($f_d = 13.5\text{Hz}$), TCE map suggested an over-steepened interpretation than the actual modeled G12 HFS top, with positive TCE updip and negative TCE downdip. In comparison, at medium to high frequency, TCE map illustrated a less steep interpretation than the actual modeled G12 HFS top (Figure 4.16). The TCE map-view distribution does not exhibit a consistent along-strike trend, thus not appropriate for the preferential picking with well-top-constrained interpolation.
 - Option 3: From the analysis in Option 2, integrating updip horizon patch from the low-frequency volume with downdip horizon patch from the medium/high-frequency volume, or vice versa, can potentially improve seismic chronostratigraphic interpretation.
3. Recommendations: In cases of available high-frequency volume, the author recommend an interpretation of flat-lying platform from this volume to most efficiently and conveniently improve seismic chronostratigraphic correlation; in cases of available only low- and medium-frequency volume, an integration of horizon patches worth further validation.

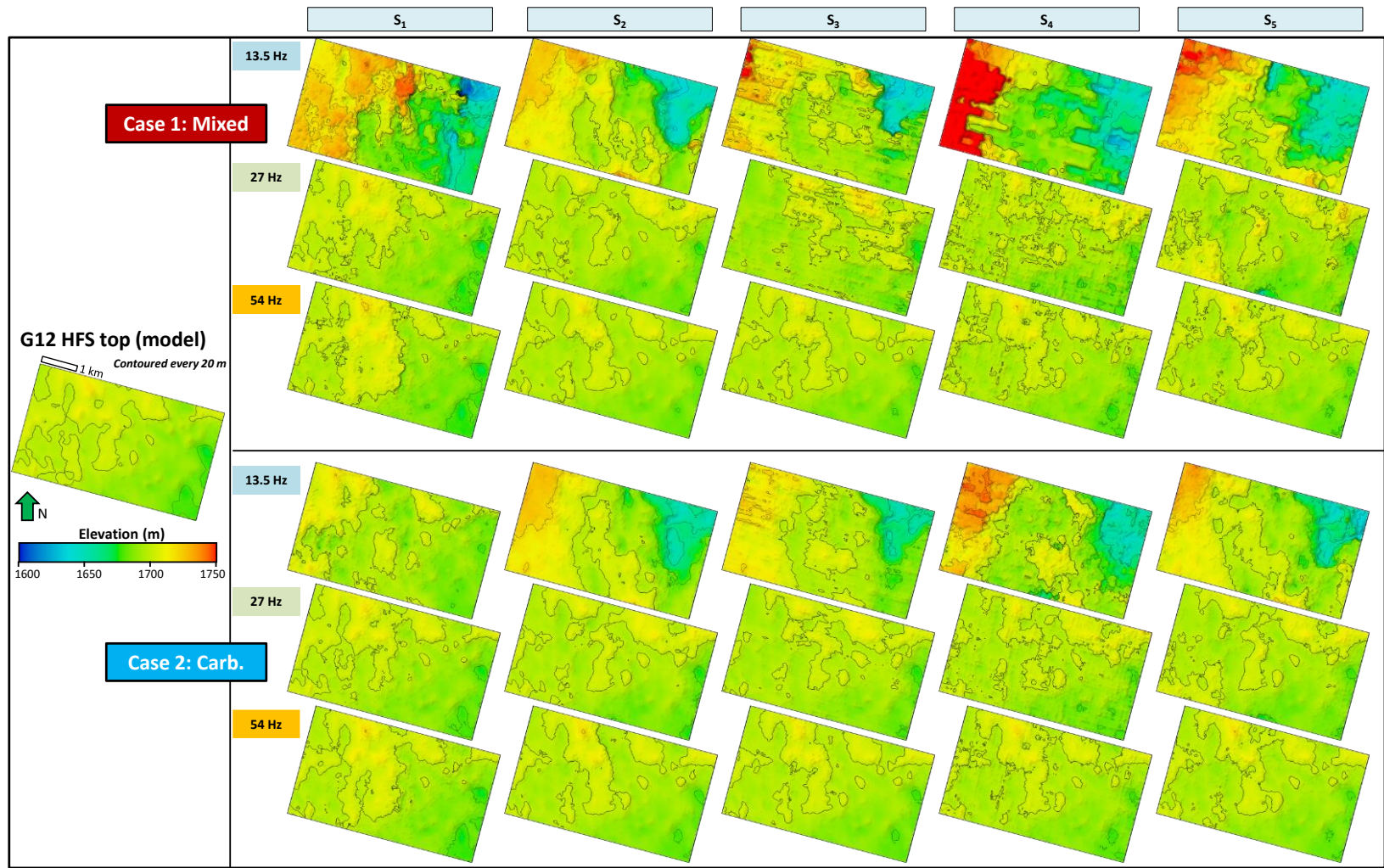


Figure 4.15: Modeled G12 HFS top and its interpretations from 30 seismic models.

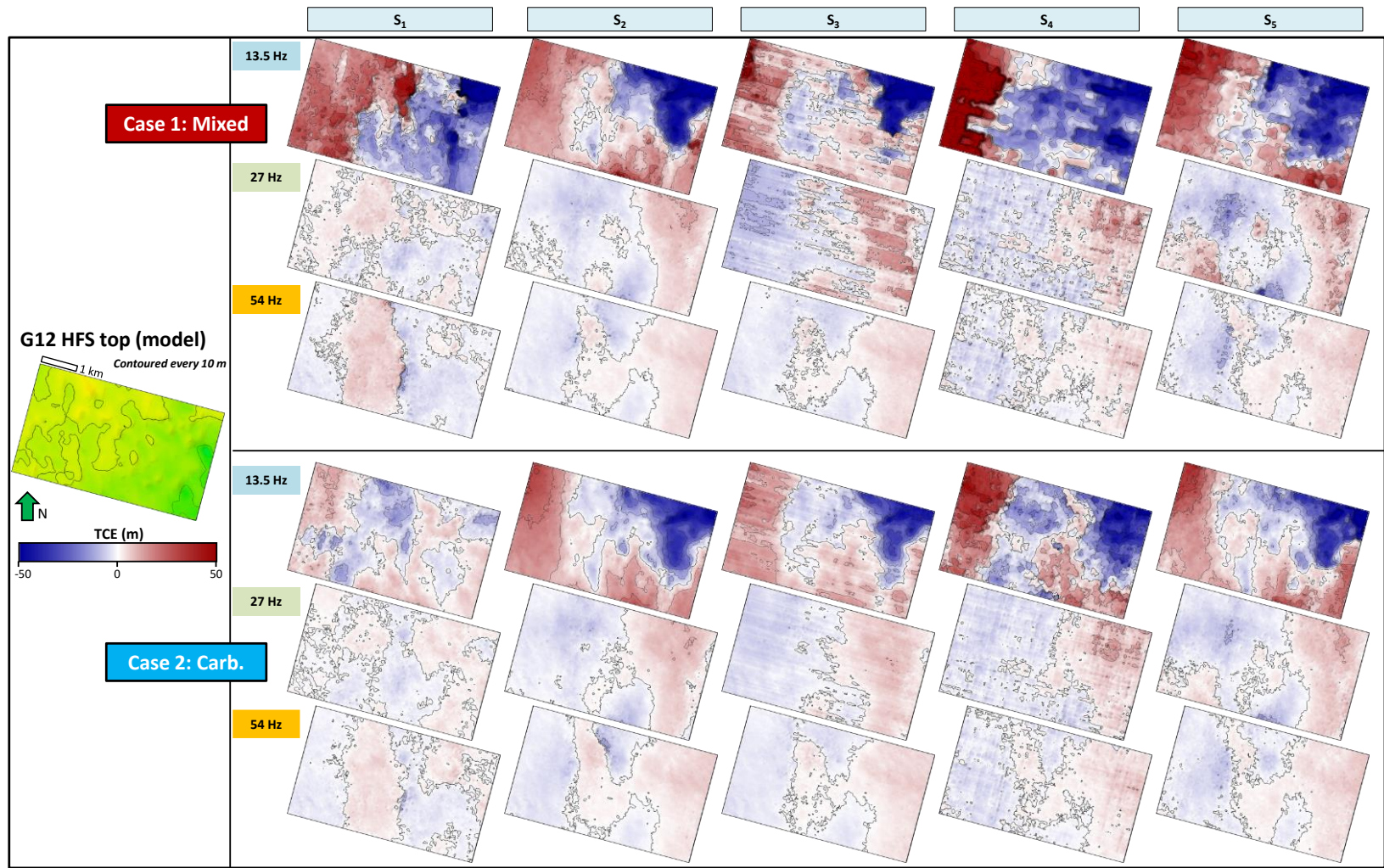


Figure 4.16: Zero-centered TCE maps for G12 HFS top from 30 seismic models.

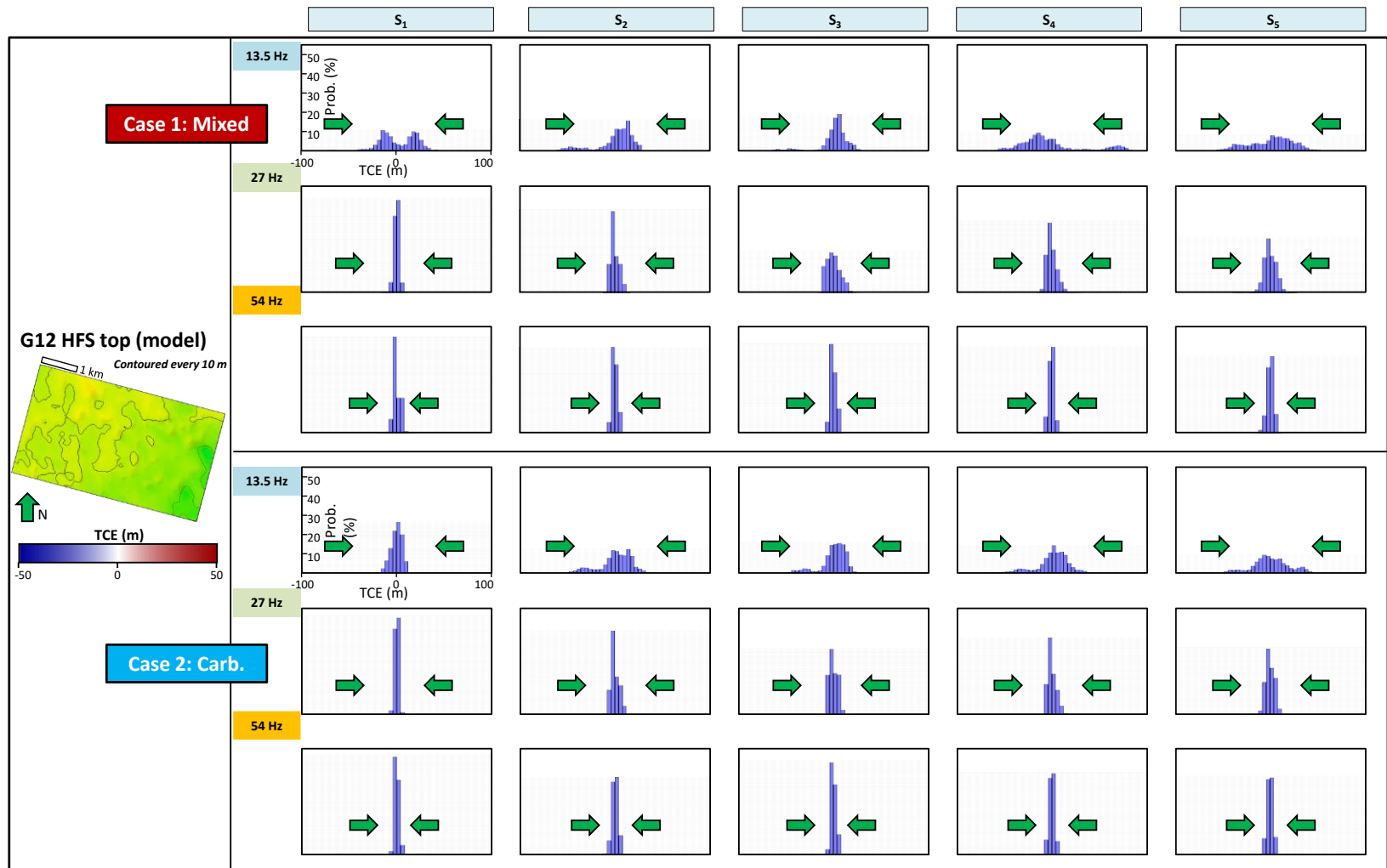


Figure 4.17: Zero-centered TCE histograms for G12 HFS top from 30 seismic models.

4.5.2 Evaluation results of clinoformal G9 HFS bottom

The seismic interpretations of G9 HFS bottom from 30 seismic models follow the most continuous horizon in the closet adjacent of the modeled G9 HFS bottom (Figure 4.18), referring to the termination relationships by assuming seismic reflections as stratifications. Subsequently, the author calculated their zero-centralized TCE maps (Figure 4.19) and histograms (Figure 4.20) using the method introduced in Section 4.4. Evaluation results suggest that

1. Mixed versus carbonate successions: the chronostratigraphic significance of G9 HFS bottom in carbonate platforms are in general better than that in mixed platforms, with narrower TCE distributions for 13 out of 15 tested five intra-facies heterogeneity and at three tested frequencies (Figure 4.17). Two exceptions are low-frequency seismic models from S_2 and S_4 models with good spatial velocity and density continuity (Figure 4.7 and 4.9).
2. Regarding the three alternative options to improve the seismic chronostratigraphic correlation
 - Option 1: Increasing seismic frequency more gently improve the seismic chronostratigraphic significance of G9 HFS bottom with a less apparent decreasing in TCE distribution (Figure 4.20), compared with G12 HFS top discussed above (Figure 4.17). Besides, there are a few exceptions where interpretation from the medium-frequency volume ($f_d=27\text{Hz}$) resulted in the worst seismic chronostratigraphic correlation, including models with narrower velocity spread or less intra-facies heterogeneity, such as the Case 1- S_1 , S_2 and Case 2- S_1 . This phenomenon is probably due to the preferential development of mounds/buildups (F6) near the shelf-margin promontories. The assignment of constant/small-spread

- velocity for this high-impedance lithofacies tend to increase more localized high-impedance anomalies, and thus further adversely influence the seismic reflections to follow this impedance trend (as analyzed in He et al., 2016).
- Option 2: Similar to the discussion in the introductory examples from the last section, TCE maps for interpretations against modeled G9 HFS bottom from 23 out of 30 models exhibit an apparent ridge of positive anomalies near the shelf margin, with increasing TCE near the shelf-margin promontories than reentrants (Figure 4.19). This TCE pattern is less significant for the low-frequency seismic models, when the interpretations tend to be less steep than the model, with negative TCE updip and positive TCE downdip.
 - Option 3: The idea of integrating horizon patch for a combined surface to better represent the clinoformal modeled stratigraphy of G9 HFS bottom is highly dependent on the complexity of velocity models. This statement is supported by a comparison between structure maps of interpreted horizons against the modeled surface for Case 1 and 2 (Figure 4.18). This interpretation strategy is most applicable to S_1 and S_2 with no or small velocity spread for the Case 1 of mixed successions, whereas extended to S_1 , S_2 and S_3 with up to intermediate velocity spread and continuity. For the cases with large velocity spread (S_4 and S_5), this approach is not very helpful if not entirely invalid.
3. Recommendations: In cases of intermediate to strong intra-facies heterogeneity, interpretation from high-frequency seismic volumes should be sufficient, whereas, for the cases of weak intra-facies heterogeneity, the integration of multi-frequency horizon patches should help most. Moreover, for those with a focus on improving shelf-margin interpretation quality to reflect along-strike topographic variations, a

preferential interpolation near shelf-margin reentrants with well-top-constrained interpolation near the promontories would be beneficial.

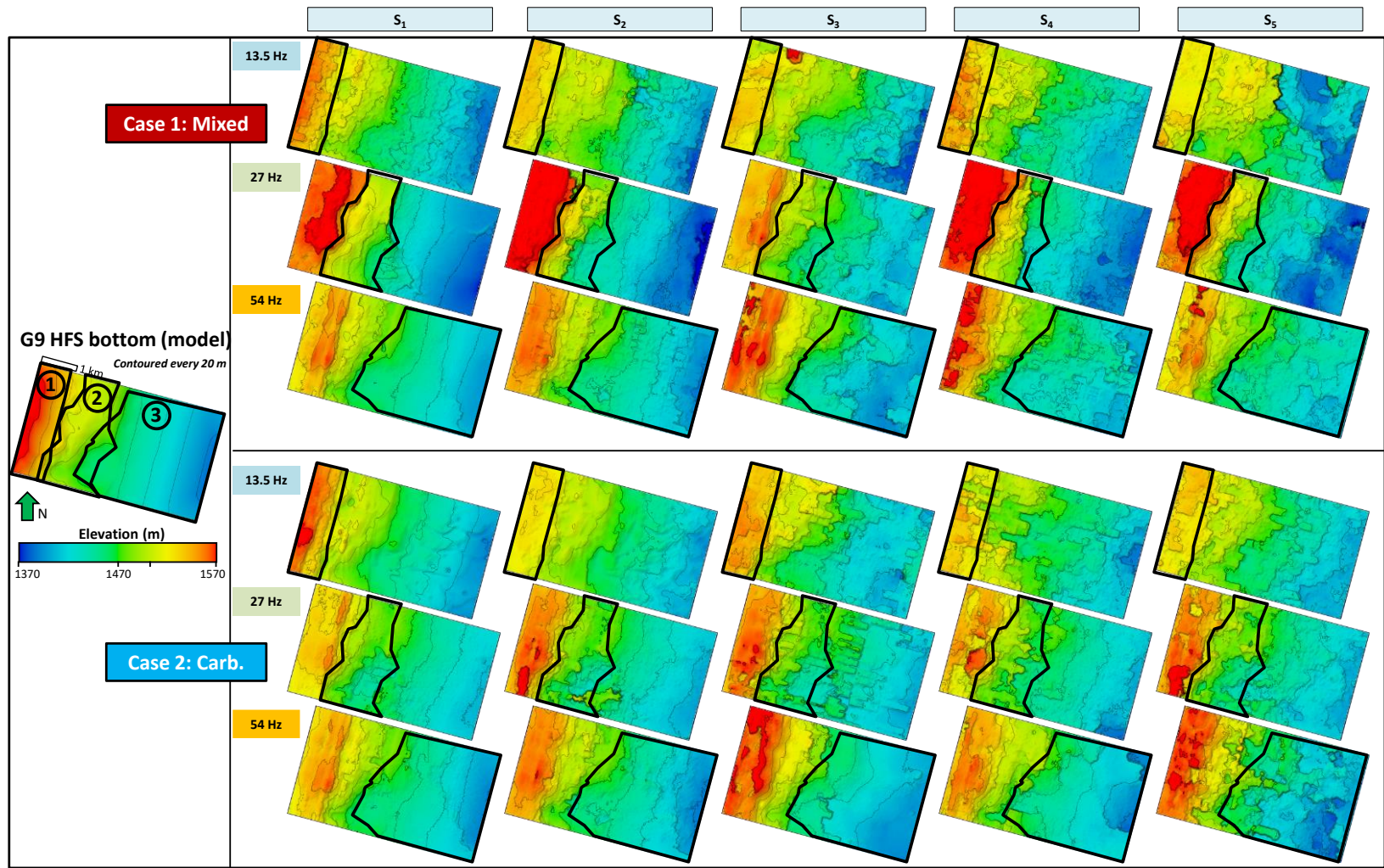


Figure 4.18: Modeled G9 HFS bottom and its interpretations from 30 seismic models.

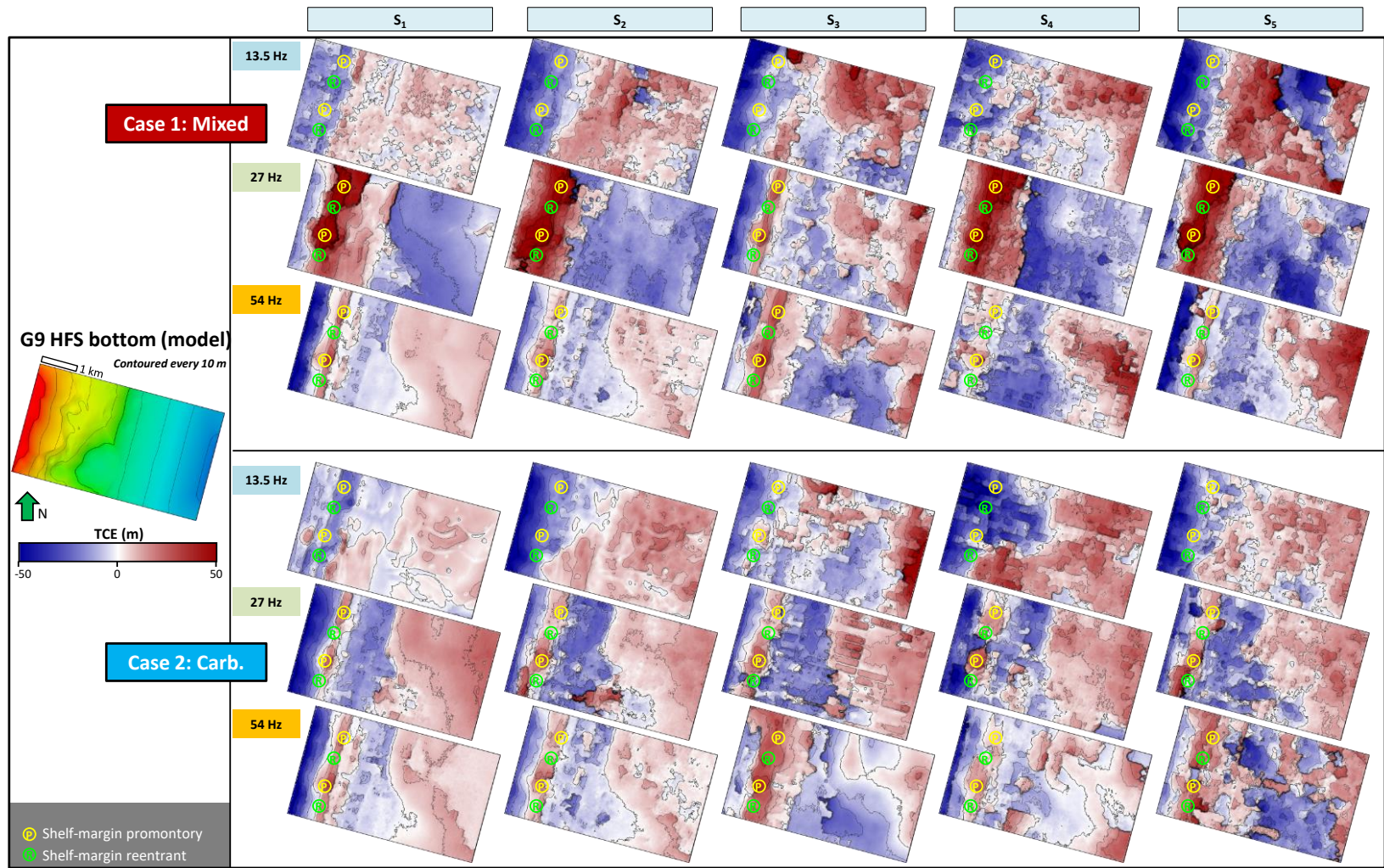


Figure 4.19: Zero-centered TCE maps for G9 HFS bottom from 30 seismic models.

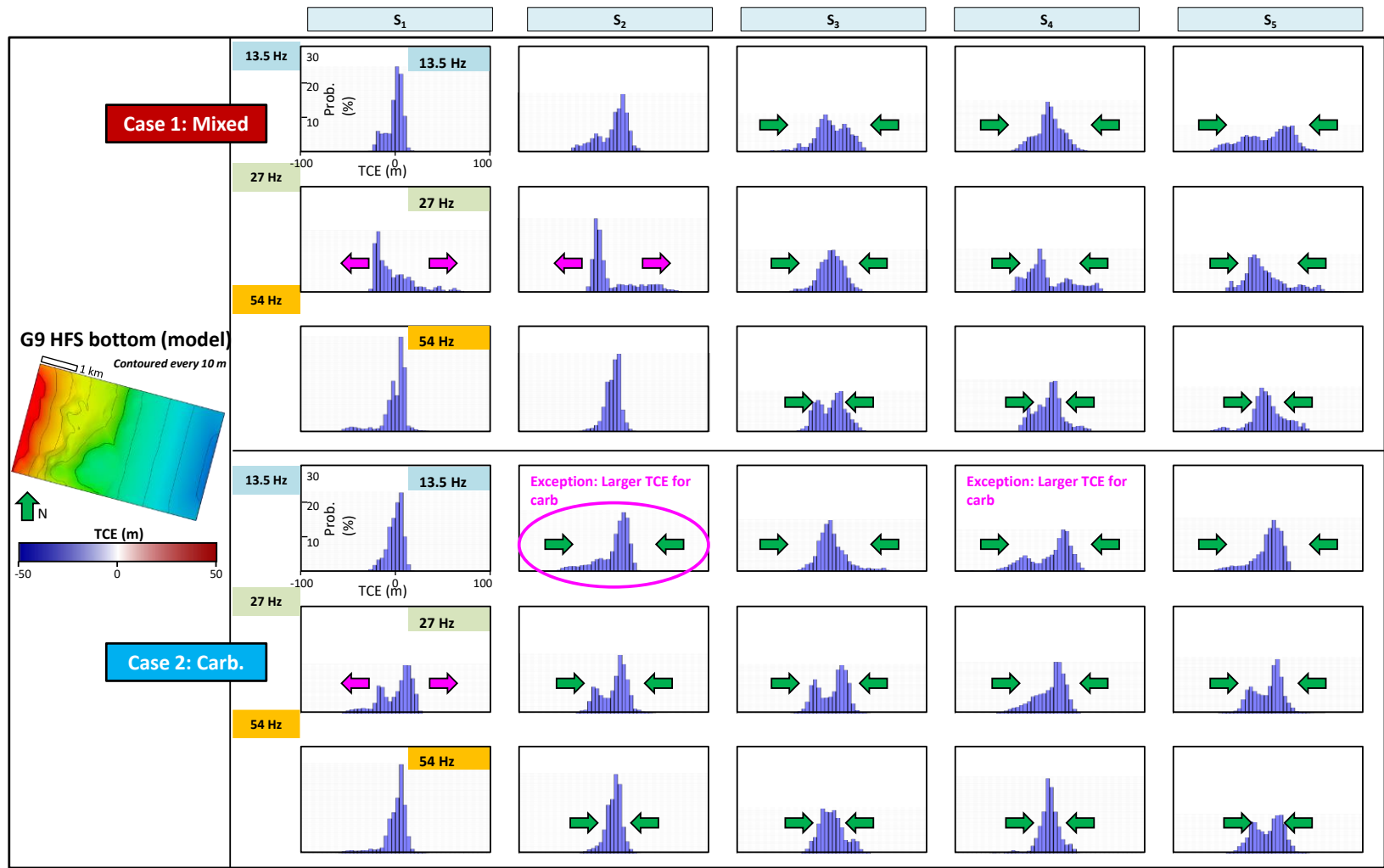


Figure 4.20: Zero-centered TCE histograms for G9 HFS bottom from 30 seismic models.

4.5.3 Evaluation results of diachronous HFC-scale seismic reflections

As during the previous stratigraphic model construction of uSA Formation (Chapter 3), Scott (2006) deformed all HFC tops and flooding surfaces to Hayes sandstone in Lower Grayburg Formation. Therefore, the chronostratigraphic surfaces within uSA Formation should be seaward-dipping. In this example, when evaluating the HFC-scale chronostratigraphic significance of seismic reflections, the author manually picked the most apparent landward-dipping horizon patches as diachronous seismic reflections (Zeng and Kerans, 2003). The author chose S₃ intra-facies heterogeneity, which is reflected as the intermediate spatial velocity variation, and then applied a comparative study on the mixed carbonate/clastic (Case 1) and carbonate (Case 2) shelf margin for an evaluation on the frequency-dependency of HFC-scale diachronous reflections.

This evaluation started with a dip-sectional comparison (IL135, Figure 4.21), with examples of diachronous HFC-scale seismic reflections in the medium-frequency Case 1-S₃ and Case 2-S₃ seismic models. In this example, the author interpreted the G9 HFS top as a seismic +/- zero crossing (yellow dashed lines, Figure Figure 4.21a1, a2, b1, and b2), based on the termination relationships (double-sided arrow, Figure 4.21a1 and a2). Note that, in both cases, the interpreted G9 HFS top is severely diachronous by transecting from G9 HFS-HFC12a bottom to G10 HFS top (compare the yellow dashed line against solid canyon lines of HFC boundaries, Figure 4.21b1 and b2). It better follows the diachronous high-to-low impedance trend (Figure 4.21c1 and c2) mainly caused by landward stepping Lower Grayburg strata (Figure 4.21d1 and d2). Subsequently, the landward-dipping seismic reflectors (pink dashed lines circled with eclipses, Figure 4.21b1 and b2) were located slightly below the interpreted G9 HFS top. In general, these diachronous seismic reflectors tend to follow the low-impedance trend (Figure 4.21c1 and c2) of porous shelf-

margin carbonate reservoirs (Figure 4.21d1 and d2). As shown in the comparison between the Case 1 and Case 2 example, the identified diachronous reflection in the carbonate shelf margin of Case 2 (pink dashed line, Figure 4.21b2) extend wider with a steeper dip than that in Case 1 (pink dashed line, Figure 4.21b1). The former one in Case 2 approximately has a dip of -3.7° and a horizontal extension of 1010 meters, whereas the later one in Case 1 roughly has a dip of -1.5° and a horizontal extension of 380m.

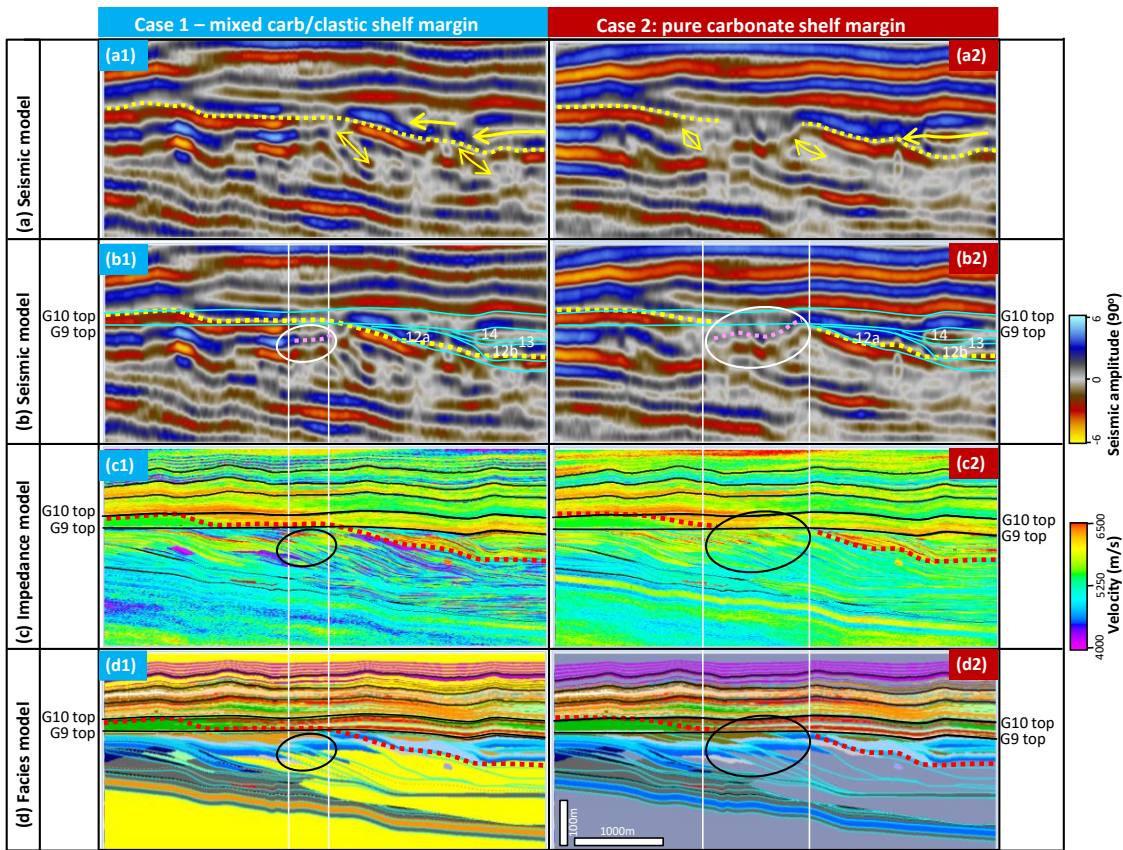


Figure 4.21: A comparison of diachronous internal reflections within G9 HFS in 35Hz seismic models on IL135. (a1) and (b1) are Case 1 seismic models, generated from (d1) a mixed carbonate/clastic lithostratigraphic model, which was assigned with a velocity/ impedance model with S_3 intra-facies heterogeneity. In comparison, (a2)~(d2) are Case-2 equivalent IL135 sections, showing (a2) and (b2) of seismic models, (c2) impedance model, and (d2) lithostratigraphic model. The dashed lines in all subplots are interpreted G9 HFS top following a +/- zero-crossing based on termination relationship (single- and double-sided arrows) interpreted in Figure (a1) and (a2) per case. The eclipses highlights zones with diachronous landward-dipping seismic reflections, whereas the white guiding solid lines aligned the same locations among different models for a convenient comparison.

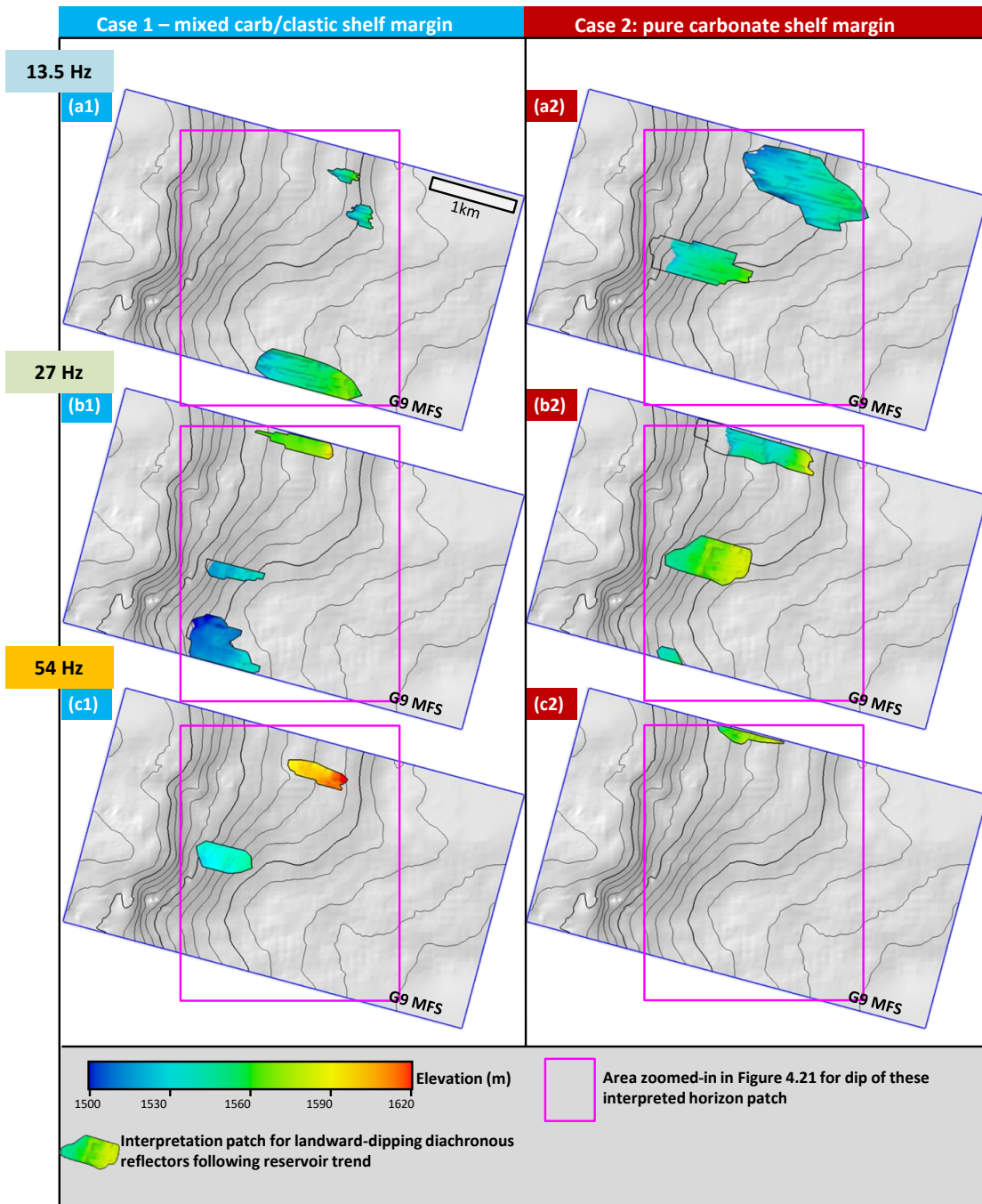


Figure 4.22: Interpretation of diachronous landward-dipping internal HFC-scale reflectors within G9 HFS for the mixed successions at (a1) low-, (b1) medium-, and (c1) high-frequency, and for the carbonate successions at (a2) low-, (b2) medium-, and (c2) high-frequency.

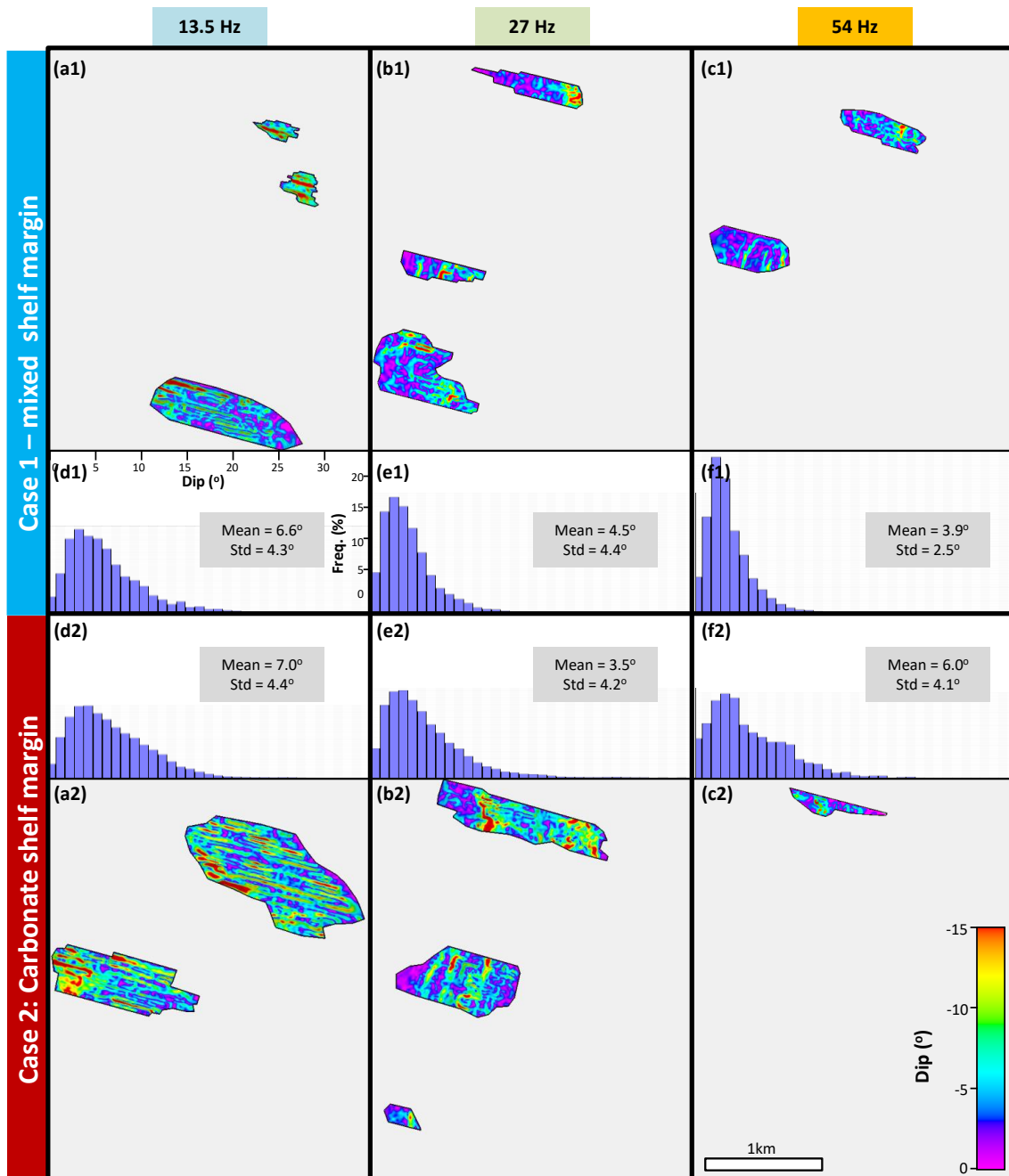


Figure 4.23: A comparison of dip for these diachronous reflectors (magenta boxes in Figure 4.22) following the shelf-margin and upper-slope reservoir trend. (a), (b) and (c) are respectively dip of these horizon patches at low-, medium-, and high-frequency, whereas (d), (e) and (f) are their histograms.

The author preliminarily tested the preferential occurrence of these HFC-scale diachronous reflectors responding to the seismic frequency in mixed versus carbonate shelf margin. First of all, the author extended the above dip-oriented example to 3D for six seismic models at all of three tested frequencies from Case 1- S₃ and Case2- S₃ velocity and density models (Figure 4.22). These horizon patches (colorcoded with elevations, Figure 4.22) were projected on G9 MFS (contoured gray structure maps, Figure 4.22) for a comparison against along-strike shelf-margin promontories and reentrants, given their specific locations oscillate with time. Resultantly, these diachronous patches appear more likely to occur perpendicularly to shelf-margin promontories (Figure 4.22).

Furthermore, the author calculated the dip and dip histograms of these diachronous horizon patches (Figure 4.23). As suggested by a joint analysis of structure (Figure 4.22) and dip (Figure 4.23) of these diachronous horizon patches, increasing seismic frequency helps to mitigate these diachronous HFC-scale reflections following the porous carbonates for both the Case 1-mixed and Case 2-carboante shelf margin. This statement is supported by both a decreasing area of occurrence (Figure 4.22, comparing a1, b1 and c1; also comparing a2, b2, and c2) and gentler dip (Figure 4.23, comparing a1~c1 or d1~f1, also comparing a2~c2 or d2~f2) with an increasing of seismic frequency. Moreover, the author compared these diachronous HFC-scale patches in the mixed (Case 1) versus carbonate (Case 2) shelf margin. This comparison revealed these diachronous reflectors to be more extensive in size (Figure 4.22, comparing a1~c1 with a2~c2) and steeper/more-severely landward-dipping (Figure 4.23, comparing a1~f1 with a2~f2) for the carbonate (Case 2) shelf margin.

At the author's best understanding, the different behavior of diachronous HFC-scale seismic reflectors in mixed versus carbonate shelf margin is probably due to their different impedance trend per cycle (Figure 4.24). The mixed carbonate-siliciclastic cycle has lower-

slope low-impedance sandstone/siltstone jointly creating an HFC-scale low-impedance trend with the shelf-margin and upper-slope porous carbonate (comparing the white eclipse area, Figure 4.24a1~c1). In comparison, in a carbonate HFC cycle, the shelf-margin and upper-slope porous carbonate is bounded by high-impedance outer-ramp and lower-slope facies. Therefore, the low-impedance lithostratigraphic unit relatively stands out to create a contrasting-AI surface which does not follow geologic timeline (comparing the white eclipse area, Figure 4.24a2~c2).

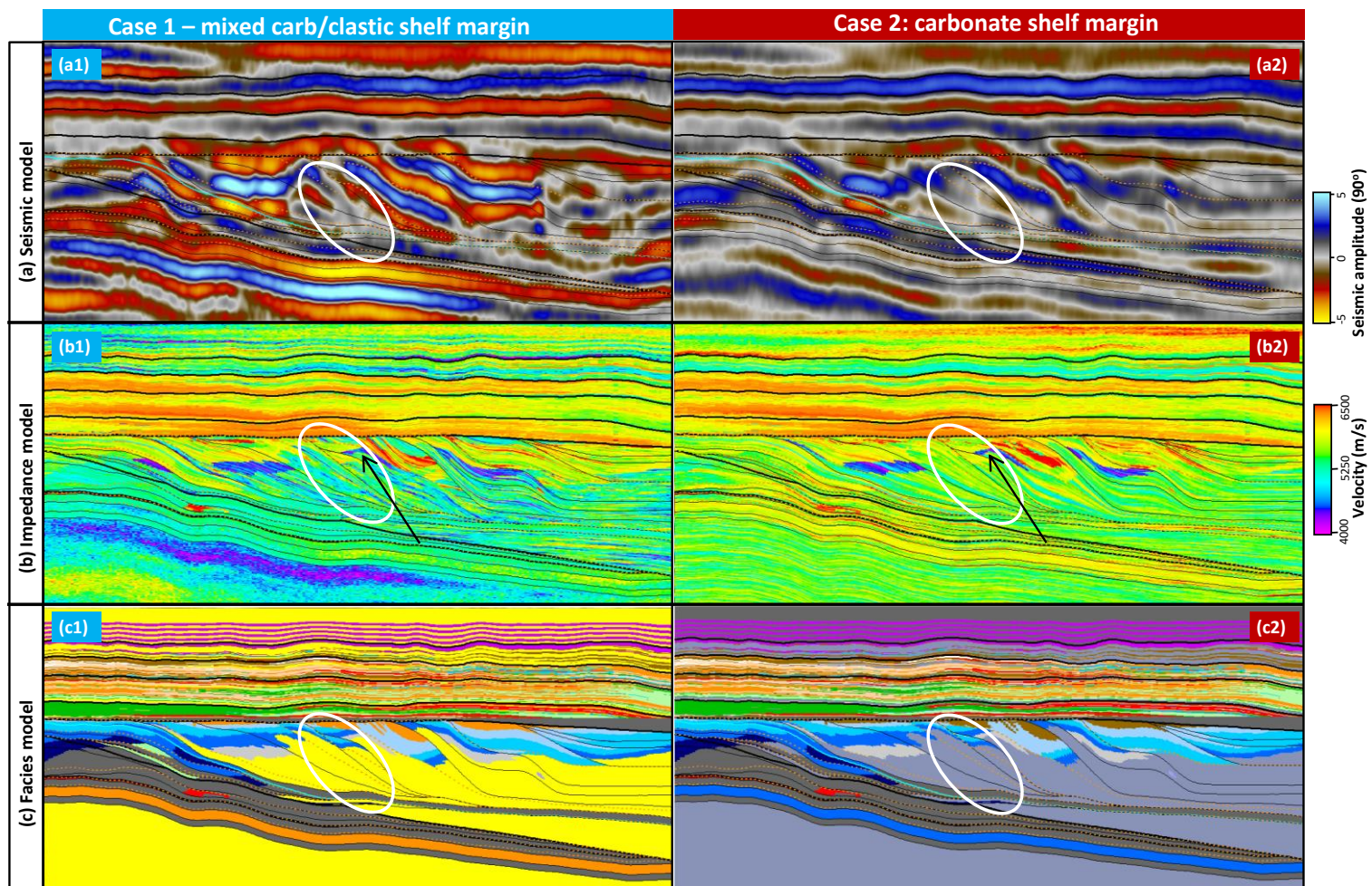


Figure 4.24: A comparison example explaining why diachronous HFC-scale reflector is more extensive and steeper in the carbonate shelf margin in Case 2. (a) dip-oriented seismic sections, (b) impedance models, and (c) facies models.

4.6 DISCUSSIONS ON POTENTIAL FIELD APPLICATIONS

4.6.1 A decision tree based on forward models in Chapter 3 and 4

As for a field seismic volume (Figure 2.25a), selective frequency filtering using continuous wavelet transform/ CWT allows a separation of low-, medium-, and high-frequency components (Figure 2.25b~d). These volumes can further serve as data sources for the decision tree (Figure 2.26) proposed in this study. Upon the forward modeling results in this chapter, the author introduced this decision tree to search proper interpretation strategies/hints (purple boxes, Figure 2.26) in improving seismic chronostratigraphic analysis at the HFS and HFC scale. This decision tree best suits, when the geoscientists can provide critical judgments (green diamonds, Figure 2.26) on the following four aspects:

1. The first-and-foremost question on mixed or pure carbonate lithology facilitates an identification of the error-prone scale that requires special cautions. The author recommend being more cautionary on the HFS-scale interpretation of reservoir-bounding surfaces for a mixed succession, whereas being more alerted on the HFC-scale diachronous seismic reflections following the reservoir-prone lithofacies for a carbonate succession.
2. Subsequently, for an interested horizon of HFS surface, the judgment on its topography further helps the selection of interpretation method. For a flat-lying stratigraphic surface, one can better reply on interpretation from a high-frequency seismic volume. In comparison, the interpretation of a clinoformal surface requires additional information from the 3rd judgment.

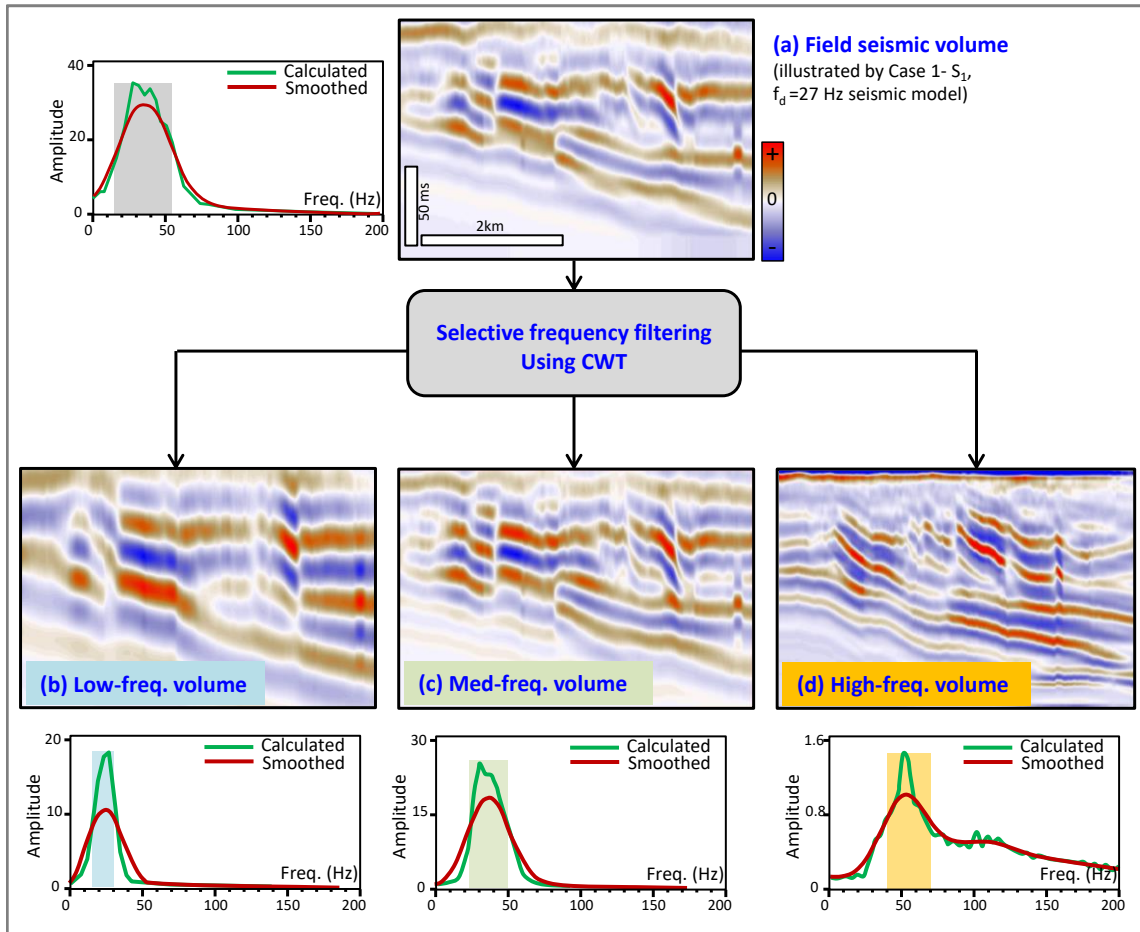


Figure 4.25: Data preparation for different frequency volumes as inputs for the decision tree in Figure 4.26. (a) Input seismic volume. In this case, IL116 from the normal-frequency time-domain seismic model was used for an illustration. (b)~(d) are resultant low-, medium-, and high-frequency sections from selective frequency filtering using CWT.

3. For a clinoformal surface, one can further question its surrounding intra-facies spatial velocity variation/intra-facies heterogeneity. If this heterogeneity is intermediate to fierce, interpretation from a high-frequency volume would help improve the seismic chronostratigraphic correlation. Otherwise, one needs to consider alternative solutions via the 4th judgment.
4. For a clinoformal surface with surrounding strata of gentle intra-facies heterogeneity, one can keep questioning the availability of well controls. In cases with well controls near the error-prone shelf-margin promontories, the author recommend an integration of preferential interpretation from medium/high-frequency seismic volume with well-top-constrained interpolation in the error-prone area (Option 2). In comparison, in areas lacking well constraints, an integration of multi-frequency horizon patches would be most effective, by utilizing the platform patch from low-frequency interpretation, the upper-slope patch from medium-frequency interpretation, and the lower-slope to basin patch from high-frequency interpretation.

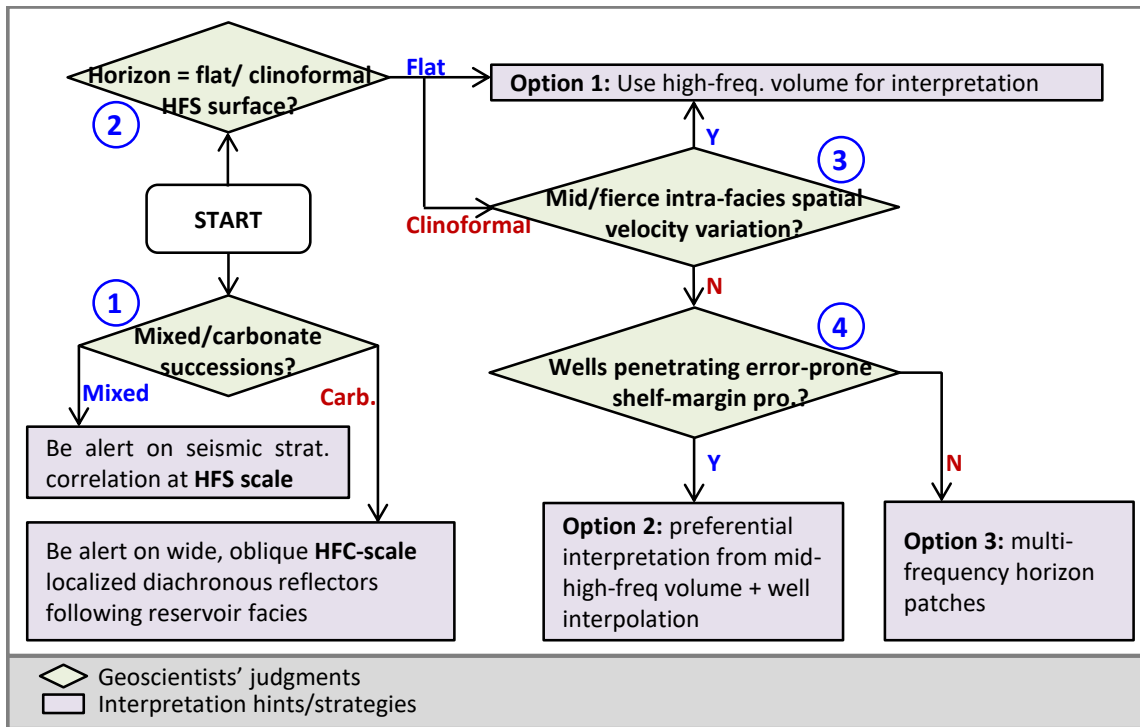


Figure 4.26: A solution tree proposed based on forward modeling results in Chapter 4.

4.6.2 A hybrid volumetric-picking scheme based on Chapter 2

As this decision tree requires basic geoscientists' inputs, the author also considered another scenario when it lacks geoscientists' expert knowledge. An attribute-driven volumetric picking scheme (Figure 4.27) is promising to fill this gap. The author proposed this scheme in Chapter 2 based on ten forward seismic models upon flat-lying siliciclastic reservoir models. Theoretically, to improve seismic chronostratigraphic correlation at the reservoir scale, one can make a judgment on whether reflections in a window follow stratigraphic surfaces. In cases when seismic reflections follow geologic surfaces, automated dip-field based volumetric picking (Lomask, 2006; Fomel, 2010) should be sufficient for dense horizon picking seismic events as chronostratigraphic surfaces. Otherwise, phantom slicing (stratal slicing, proportional slicing, and so on; Zeng, 1994; Posamentier, 1996) can be used to approximate chronostratigraphic surfaces. What worth

to mention, as for the central idea in this attribute-driven volumetric picking scheme, the author advocated using a seismic volume, which has a good correlation with TCE and selected from the forward modeling studies, to replace the human judgments. Regarding algorithm implementation, this selected seismic attribute as a proxy of TCE can be modified as a weighting function in a published 3D volumetric picking algorithm (Equation 4.1) to drive the selection of volumetric picking following dip field or phantom slicing.

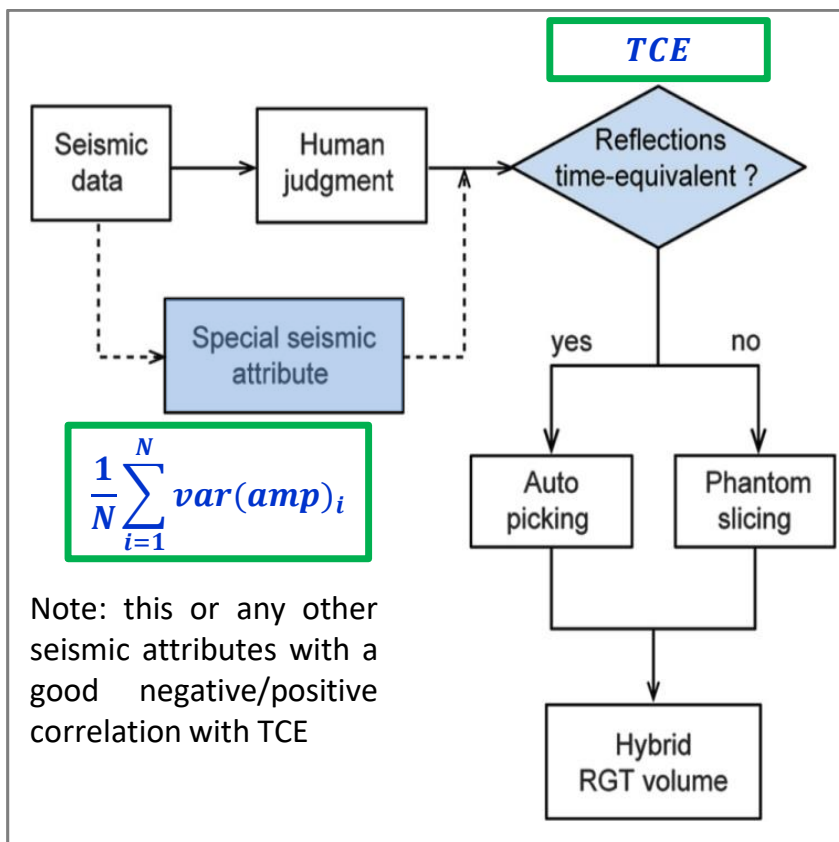


Figure 4.27: An attribute-driven volumetric picking scheme to tie the chronostratigraphic significance of seismic reflections (quantified as TCE here) with a particular seismic attribute. Chapter 2 proves the mean of amplitude variance to be highly correlated with TCE for flat-lying siliciclastic reservoirs.

$$0 \approx \text{residual} = \mathbf{W} (\nabla \boldsymbol{\tau}(x, y, t) - \mathbf{p}_\epsilon(x, y, \boldsymbol{\tau})) \quad (4.1)$$

where

∇ : gradient operator

$\tau(x, y, t)$: time-shift field

p_ϵ : estimated dip

W : weighting function

The published volumetric picking equation (4.1) cited here comes from Lomask (2006, Equation 2.24), where the regression originated from Fomel (2002).

4.7 CONCLUSIONS AND FUTURE WORK

In this study, the author tested the fundamental assumption of seismic stratigraphy as applied to interpret HFS surfaces, and to interpret HFC-scale reflections from its initial recommended scale when the basic interpretive unit is a depositional sequence (Mitchum et al., 1977b). For the sake of accommodating as many realistic scenarios as possible, the author tested upon both mixed carbonate/clastic (Case 1) and carbonate system (Case 2). For each case, the author modeled five scenarios of intra-facies heterogeneity ($S_1 \sim S_5$) reflected as different spatial velocity variations and then simulated the seismic responses at low-, medium-, and high-frequencies.

The forward modeling studies have illustrated

- A few general conclusions on the validity of 'chronostratigraphic significance of seismic reflections', when it is applied to interpret HFS surfaces. Table 4.2 summarized the generalized results. In this table, the symbol '>' represents a better validity to using the 'chronostratigraphic significance of seismic reflections' in seismic chronostratigraphic correlation.

Influencing factors	General conclusions
1. Stratal geometry	Flat > clinoformal
2. Lateral lithofacies variation	Gentle > faster
3. Mixed vs. pure system	Carbonate > Mixed carb/clastic
4. Intra-facies heterogeneity	Gentle > fierce
5. Seismic frequency	High frequency

Table 4.2: General conclusions for influencing factors on the ‘chronostratigraphic significance of seismic reflections at the HFS scale.

- a comparative result on the existence of HFC-scale diachronous reflectors following the porous reservoir-prone lithofacies: this phenomenon preferentially occur near the shelf-margin promontories, and is more severe for the carbonate than the mixed carbonate/clastic shelf margin, thus requires more cautions. Fortunately, increasing seismic frequency, in general, helps mitigate these diachronous HFC-scale localized reflectors.

Upon the forward modeling results, a decision tree was proposed to assist geoscientist’s selection from three alternative approaches to improve seismic chronostratigraphic correlation at the HFS and HFC scale. Furthermore, to deal with an area with very limited geoscientists’ prior knowledge, the author extended a discussion to the attribute-driven volumetric picking scheme proposed in Chapter 2, by discussing its underlying logic, as well as possible algorithm implementation. Future works are recommended to select a seismic attribute as a proxy of TCE from different scenarios.

Chapter 5: Conclusions and Future Work

5.1 CONCLUSIONS

This dissertation evaluated the validity of the fundamental assumption of seismic stratigraphy, which is also known as the chronostratigraphic significance of seismic reflections, at the reservoir scale (HFS and finer scale). In spite of a broader impact on multiple reservoir-scale application from this study as stated in Chapter 1, the author focused on the evaluation and discussions on improving the interpretation of reservoir-bounding HFS-scale surfaces, which will further enhance the accuracy of static reservoir model construction. The model construction in this study evolves from conceptual to realistic, in order to approximate reservoir geology of (1) shallow-marine siliciclastic reservoirs in Starfak Field, GoM, (2) shallow-water mixed carbonate-siliciclastic Upper San Andres shelf margin – Grayburg platform, Permian Basin, and (3) shallow-water carbonate Abo shelf margin – Clear Fork platform, Permian Basin.

This dissertation has achieved three-fold contributions respectively on modeling hierarchical heterogeneity and resultant seismic responses, on the evaluation of five predefined variables on the chronostratigraphic significance of seismic reflections, and on the recommendations for seismic chronostratigraphic correlation at the reservoir scale. Respectively, the author concludes that

1. The hierarchical heterogeneity, which is intrinsic in facies and property models, can be modeled via an integration of high-resolution sequence stratigraphic framework, published 3D depositional models, outcrop analogs and discrete observations. A selective usage of geostatistical methods and their parameters is critical in 3D geocellular and acoustic property model construction so that the populated models can address questions in 3D reservoir-scale interpretations.

2. Five predefined variables interactively influence the chronostratigraphic significance of seismic reflections at the reservoir scale, and alternative solutions if not picking a seismic event as an HFS surface. In general, one can expect
 - Variable 1 – clinoformal versus flat-lying HFS surface:

Horizon interpretations of both surfaces are safer to apply ‘chronostratigraphic significance of seismic reflections’ within carbonate than mixed carbonate/clastic successions. Increasing seismic frequency, in general, helps improve the accuracy of seismic chronostratigraphic interpretation for a flat-lying HFS surface, especially for stratigraphic intervals with either fast lateral lithofacies variation or severe intra-facies heterogeneity featured by a large velocity spread and poor velocity continuity. In comparison, increasing seismic frequency is less influential in improving the accuracy of seismic chronostratigraphic interpretation, and is valid only when the intra-facies heterogeneity is intermediate to fierce.
 - Variable 2 – lateral lithofacies variation:

For a flat-lying/gently-dipping stratigraphic interval, increasing its lateral lithofacies variation, in general, would lead to degraded seismic chronostratigraphic interpretation/increasing TCE, which can be improved by increasing seismic frequency. Chapter 2 fitted a power function between the lateral impedance variogram range and the mean of amplitude variance. Therefore, the author inferred a positive correlation between this particular seismic attribute and TCE, thus recommend to use it to revise the weighting function in published volumetric picking algorithm to improve the accuracy of computation seismic chronostratigraphy. Besides, for a strongly-progradational stratigraphic interval, its faster lateral lithofacies variation compared with overlying platforms, can result in HFC-scale misinterpretations.

- Variable 3 – mixed carbonate/clastic versus carbonate successions with complex lithofacies-sonic velocity relationship:

The TCE is, in general, smaller for carbonate successions than that for mixed carbonate-siliciclastic successions, when one interprets either flat or clinoformal stratigraphy at HFS scale. This effect is more significant on the flat than the clinoformal stratigraphy. At the HFC scale, the author observed diachronous landward-dipping reflections following the porous shelf-margin reservoir facies, which is more severe for the carbonate than the mixed shelf margin. Fortunately, increasing seismic frequency can mitigate this HFC-scale diachronous phenomenon, by reducing the size and land-ward dipping angle of these diachronous patchy reflectors.

- Variable 4 – intra-facies heterogeneity reflected as spatial sonic velocity/impedance distribution:

In general, an increasing in lateral impedance variation would lead to increasing TCE within flat-lying siliciclastic stratigraphy. For the mixed carbonate/clastic (Case 1) and carbonate successions (Case 2), the author modeled spatial velocity variation as a combination of velocity value spread and spatial velocity continuity via five scenarios (S_1 ~ S_5). It appears that for both cases, the more severe TCE's occurs for S_4 and S_5 when the velocity spread is large. Fortunately, increasing seismic frequency significantly improves the chronostratigraphic correlation for these scenarios.

- Variable 5 – seismic frequency:

As discussed when addressing other variables, interpretation from high-frequency seismic volume does help improve seismic chronostratigraphic interpretation in limited scenarios, such as flat-lying stratigraphy and clinoformal stratigraphy with

- intermediate to fierce intra-facies heterogeneity. Beyond of its applicable conditions, to reconstruct a clinoformal surface with small intra-facies heterogeneity, one can consider applying preferential interpretation with well-interpolation based on TCE map-view distributions gained from the forward modeling studies or integrate horizon patches from interpretations from different frequency components, which were obtained via selective frequency filtering.
3. Based on the forward modeling studies, the proposed decision tree in Chapter 4 for manual interpretation strategies and attribute-driven volumetric picking scheme in Chapter 2 respectively suits scenarios with or without sufficient geoscientists' prior knowledge.

5.2 FUTURE WORK

Entailing the completion of this dissertation, the author and her advisers consider the listed two topics as potential future work, including

- Future work on attribute-driven volumetric picking. This topic would require a further search for a particular seismic attribute with high correlation with TCE from the mixed carbonate/clastic and the carbonate shelf-margin-platform successions built in Chapter 3 and 4. We perceive it as an extension of Chapter 2 which proposed the attribute-driven volumetric picking scheme upon the forward modeling results of flat-lying siliciclastic stratigraphy and thus need further attribute selection for the rest models in this dissertation. The final deliverables would further contribute to computation seismic chronostratigraphy, especially in scenarios with limited geoscientists' prior knowledge.
- Future work on the influence from these improved reservoir-bounding surfaces on reservoir property modeling. Up till this point, this dissertation mainly focused on

improving seismic chronostratigraphic correlation for reservoir-bounding surfaces at HFS scale, with a secondary touch on diachronous HFS-scale seismic reflections following shelf-margin porous reservoir-prone lithostratigraphic surfaces. A further evaluation on how the improved chronostratigraphic reservoir-bounding HFS surface and stratigraphic layering further contributes to reservoir property prediction can be another interesting extension of this study. Kingdom Field dataset, with closely spaced wells and recently collected production data, can be an excellent test ground.

Appendix

In this study, the author constructed the intermediate case of spatial velocity distribution (S_3), using the normalized velocity distribution per facies from Chapter 3, and the best efforts in fitting velocity variograms for selected zones using the available data. This appendix includes details in velocity variogram analysis and modeling.

As for the subsurface-constrained Grayburg-Lower Queen Formation of G10~G13 HFS, the author started with a map-view anisotropy analysis via a standardized variance map (Figure A.1a) on a grid of 200 by 200 meters. As the standardized variance just narrowly approached one in its minor orientation (75°), which roughly aligns with the depositional dip direction, the author estimated an anisotropy ratio of 1.72 from the 0.6 contour. Afterward, the author calculated an experimental variogram per lag along both the major (shown as green dots) and minor orientation (shown as magenta dots, Figure A.1b). The author then applied a least-square fit and then obtained a spherical variogram with a minor range of 3205 m. Furthermore, the author assigned 5515 m as the major range after multiplying the estimated anisotropy ratio. Finally, the author adopted the nugget and sill from this map-view variogram analysis, and then manually fitted the vertical range per HFS (red dots in Figure A.1c) of Grayburg-Lower Queen Formation, referring to their experimental variograms (black dots in Figure A.1.c).

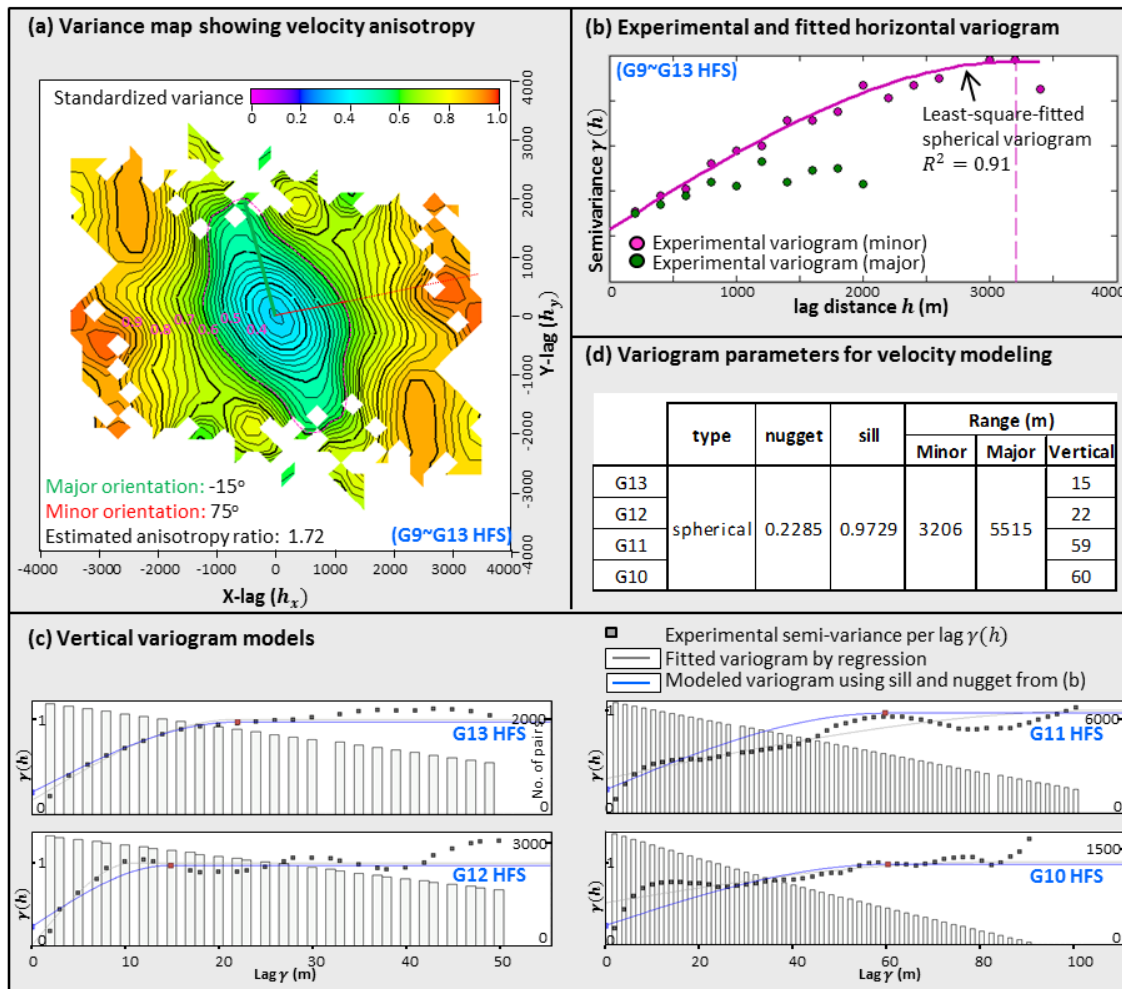


Figure A.1: Velocity variogram analysis per HFS for subsurface constrained G10~G13 HFS of Grayburg and Lower Queen platforms. (a) experimental standardized variance map showing velocity anisotropy. (b) Experimental variogram along major (green dots) and minor orientation (magenta dots), where a spherical variogram was fitted along the minor orientation by least-square regression. (c) Manually-fitted vertical range after fixing the variogram nugget and sill from (b). (d) a table showing resultant velocity variogram parameters.

In comparison, as for the outcrop-constrained Upper San Andres shelf margin, its velocity variogram analysis was implemented upon 63 outcrop plugs from Kenter et al. (2001). These sonic velocity samples were imported as pseudo logs and then upscaled to attach to the 2D stratigraphic grid of HFC 6 (Figure A.2a) with two zones: one is the siliciclastic-rich transgressive/T-hemicycle, whereas the other is the carbonate-dominant regressive hemicycle. Subsequently, the author calculated experimental semi-variance per lag (black squares in Figure A.2b) along vertical and horizontal orientation for both T- and R-hemicycle. Finally, a spherical variogram was fitted per zone using least-square regression, with parameters recorded in Figure A.2c.

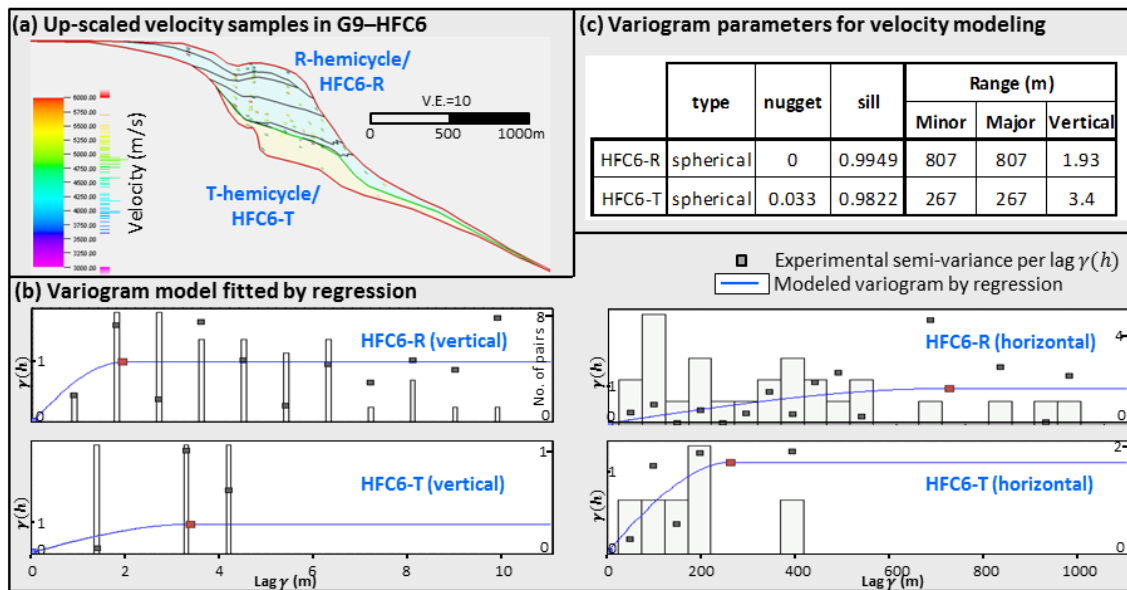


Figure A.2: Velocity variogram analysis for the transgressive/T-hemicycle and regressive/R-hemicycle of Sonnenfeld and Cross (1993)'s HFC6 in G9 HFS. (a) up-scaled velocity samples to the stratigraphic grid of HFC5 in G9 HFS, which contains two zones of T-hemicycle and R-hemicycle, (b) variogram models fitted by least-square regression for two zones, and (c) recorded variogram parameters.

Regarding the comparison and analysis of these fitted variograms for the selected zone, the author first compared the fitted variogram models for Grayburg-Lower Queen platforms (Figure A.1) and the Upper San Andres shelf margin (Figure A.2). This comparison suggested a more continuous spatial velocity distribution for the platforms, with its larger vertical, major and minor range approximately in the magnitude of 4~15 times than the later one. In addition, the larger nugget for the former one at zero lag suggested a chaotic correlation when two points are closely-spaced. Within the Grayburg-Lower Queen platform, the fitted vertical ranges indicated an increasing velocity continuity with the depth from G13 to G10 HFS. This result is probably due to a thicker lithostratigraphic bedding in G10 HFS compared with interbedded sandstone and anhydrite in G13 HFS. Finally, a comparison of the fitted variograms for the T- and R- hemicycle of HFC6 suggested a more continuous velocity distribution for the carbonate-dominant regressive hemicycle than the siliciclastic-rich transgressive hemicycle. This result agrees with the field observations of less homogeneous sandstone in the transgressive hemicycle.

Glossary

The author managed to limit the usage of abbreviations. Table G.1 listed all abbreviations used in this dissertation.

	Abbreviations	Full terms	References
Hierarchical sequence stratigraphic terms	SS	Supersequence/Sloss (1963)'s sequence	Sloss (1963)
	PCS/CS	Permian composite sequence	Kerans and Fitchen (1995)
	HFS	High frequency sequence	
	HFC	High frequency cycle	
Sequence set for a CS	HSS	Highstand sequence set	Mitchum and Wagoner (1991)
	TSS	Transgressive sequence set	
	LSS	Lowstand sequence set	
HFS names	G9 HFS	Guadalupian 9 HFS	Kerans and Fitchen (1995)
	L7 HFS	Leonardian 7 HFS	
Permian Basin Formation names	uSA	Upper San Andres Formation	King (1948) Hayes (1959) Kerans and Nance (1991)
	Grbg	Grayburg Formation	
	Q	Queen Formation	
	BCS	Brushy Canyon Sandstone Tongue	
	CCS	Cherry Canyon Sandstone Tongue	
Permian Basin Provinces and outcrops	HSS	Hayes Sandstone	Galley (1958) Hayes (1959)
	NW shelf	Northwest shelf	
	CBP	Central Basin Platform	
	LCC	Last Chance Canyon	

Table G.1: Abbreviations used in this dissertation.

References

- Adams, E. W., J. P. Grotzinger, W. A. Watters, S. W. Schröder, D. S. McCormick, and H. A. Al-Siyabi, 2005, Digital characterization of thrombolite-stromatolite reef distribution in a carbonate ramp system (terminal Proterozoic, Nama Group, Namibia): *AAPG Bulletin*, 89, 1293–1318, doi: 10.1306/06160505005.
- Aigner, T., M. Doyle, D. Lawrence, M. Epting, and A. van Vliet, 1989, Quantitative modeling of carbonate platforms: Some examples, in P. D. Crevello, J. L. Wilson, J. F. Sarg, and J. F. Read, eds., *Controls on carbonate platform and basin development*: SEPM, Special Publication 44, 27–37.
- Anselmetti, F. S., and G. P. Eberli, 1993, Controls on sonic velocity in carbonate: *Pure and Applied Geophysics*, 141, 287–323, doi: 10.1007/BF00998333.
- Anselmetti, F. S., and G. P. Eberli, 1997, Sonic velocity in carbonate sediments and rocks, in F.J. Marfurt, and A. Palaz, eds., *Carbonate seismology*: SEG, Geophysical Development Series 6, 53–74.
- Anselmetti, F. S., and G. P. Eberli, 2001, Sonic velocity in carbonates — A combined product of depositional lithology and diagenetic alterations, in R. N. Ginsburg, ed., *Prograding carbonate platform margin Great Bahama Bank*: SEPM, Special Publication 70, 173–216.
- Batzle, M. and Z. Wang, 1992, Seismic properties of pore fluids: *Geophysics*, 57, 1396–1408.
- Barnaby, R. J., and W. B. Ward, 2007, Outcrop Analog for Mixed Siliciclastic–Carbonate Ramp Reservoirs—Stratigraphic Hierarchy, Facies Architecture, and Geologic Heterogeneity: Grayburg Formation, Permian Basin, U.S.A: *Journal of Sedimentary Research*, 77, 34–58.
- Barnes, A. E., 2001, Seismic attributes in your facies: *CSEG Recorder*, 26, 41–47.
- Bellian, J. A., C. Kerans, and D. C. Jennette, 2005, Digital outcrop models: Applications of terrestrial scanning lidar technology in stratigraphic modeling: *Journal of Sedimentary Research*, 75, 166–176, doi: 10.2110/jsr.2005.013.
- Baudouy, S., and C. Legorjus, 1991, Sendji field--People's Republic of Congo, Congo Basin, in N. H. Foster ed., *TR: Structural Traps V*: p. 121 –149.
- Behrens, R. A., M. K. MacLeod, T. T. Tran, and A. Alimi, 1998, Incorporating seismic attribute maps in 3D reservoir models: *SPE Reservoir Evaluation & Engineering*, 1, 122–126.
- Bellian, J. A., C. Kerans, and D. C. Jennette, 2005, Digital outcrop models: applications of terrestrial scanning lidar technology in stratigraphic modeling: *Journal of sedimentary research*, 75, 166–176.

- Bellian, J. A., C. Kerans, and J. Repetski, 2012, Digital outcrop model of stratigraphy and breccias of the southern Franklin Mountains, El Paso, Texas, in R. Derby, R. D. Fritz, S. A. Longacre, W. A. Morgan, and C. A. Sternbach, eds., *The great American carbonate bank: The geology and economic resources of the Cambrian-Ordovician Sauk megasequence of Laurentia*: AAPG Memoir 98, 909–939.
- Biddle, K. T., W. Schlager, K. W. Rudolph, and T. L. Bush, 1992, Seismic model of a progradational carbonate platform, Picco di Vallandro, the dolomites, Northern Italy: *AAPG Bulletin*, 76, 14–30.
- Brie, A., D. L. Johnson, and R. D. Nurmi, 1985, Effect of spherical pores on sonic and resistivity measurements: SPWLA 26th Annual Logging Symposium, Society of Petrophysicists and Well-Log Analysts, June 17–20.
- Bruin, G. D., N. Hemstra, and A. Pouwel, 2007, Stratigraphic surfaces in the depositional and chronostratigraphic (Wheeler-transformed) domain: *The Leading Edge*, 26, 883–886, doi: 10.1190/1.2756868.
- Buckley, S.J., J. A. Howell, H. D. Enge, and T. H. Kurz., 2008, Terrestrial laser scanning in geology: data acquisition, processing and accuracy considerations: *Journal of Geological Society*, 165, 625–638.
- Burton, D., D. B. Dunlap, L. J. Wood, and P. P. Flaig, 2011, Lidar intensity as a remote sensor of rock properties: *Journal of Sedimentary Research*, 81, 339–347.
- Broadhead, R. F., Z. Jianhua, and W. D. Raatz, 2004, *Play Analysis of Major Oil Reservoirs in the New Mexico Part of the Permian Basin: Enhanced Production Through Advanced Technologies*, New Mexico Bureau of Geology & Mineral Resources.
- Bryant, I., D. Carr, P. Cirilli, N. Drinkwater, D. McCormick, P. Tilke, and J. Thurmond, 2000, Use of 3D digital analogues as templates in reservoir modelling: *Petroleum Geoscience*, 6, 195–201.
- Catuneanu, O., 2006, *Principles of sequence stratigraphy*: Elsevier Science.
- Chopra, S. and K. J. Marfurt, 2007, *Seismic attributes for prospect identification and reservoir characterization – Issue 11 of Geophysical development series*: Tulsa, Society of Exploration Geophysicists, 464 p.
- Christensen, N. I., and D. L. Szymanski, 1991, Seismic properties and the origin of reflectivity from a classic Paleozoic sedimentary sequence, valley and ridge province, southern Appalachians: *Geological Society of America Bulletin*, 103, 277–289.
- Claerbout, J. F., 1992, *Earth soundings analysis: Processing versus inversion*: Blackwell Scientific Publications.

- Coffin, M., L. Gahagan, L. Lawver, T. Lee, and E. Rosencrantz, 1992, Atlas of Mesozoic/Cenozoic reconstructions (200 Ma to present day), PLATES Progress Report No. 1-0192, University of Texas, Institute for Geophysics.
- Daly, C., S. Quental, and D. Novak, 2010, A faster, more accurate Gaussian simulation: Presented at GeoCanada — Working with the Earth.
- Darton, N., and J. Reeside, 1926, Guadalupe group: Geological Society of America Bulletin, 37, 413–428.
- Deutsch, C.V., and A.G. Journel, 1998, GSLIB geostatistical software library and user's guide (2nd edition): Oxford University Press, New York, 369p.
- de Groot, P., G. de Bruin, and K. McBeath, 2006, OpendTect SSIS—Sequence stratigraphic interpretation system: Drilling and Exploration World, 15, 31–34.
- Dolberg, D. M., J. Helgesen, T. H. Hanssen, I. Magnus, G. Saigal, and B. K. Pedersen, 2000, Porosity prediction from seismic inversion, Lavrans Field, Halten Terrace, Norway: The Leading Edge, 19, 392–399.
- Donovan, D., and E. Jones, 1979, Causes of world-wide changes in sea level: Journal of the Geological Society, 136, 187–192.
- Doyen, P., 2007, Seismic reservoir characterization: An earth modelling perspective, EAGE.
- Dubrule, O., 1998, Geostatistics in petroleum geology: AAPG, Continuing Education Course Note Series 35.
- Dunham, R. J., 1962, Classification of carbonate rocks according to depositional textures: AAPG Memoir 1: Classification of Carbonate Rocks – A symposium, 108 –121.
- Dutton, S. P., E. M. Kim, R. F. Broadhead, C. L. Breton, W. D. Raatz, S. C. Ruppel, and C. Kerans, 2004, Play analysis and digital portfolio of major oil reservoirs in the Permian basin: Application and transfer of advanced geological and engineering technologies for incremental production opportunities, final report prepared for the U.S. Department of Energy, University of Texas at Austin, Bureau of Economic Geology, 408p.
- Eberli, G. P., S. A. Flavio, K. Dick, S. Tokiyuki, and D. W. James, 2002, The chronostratigraphic significance of seismic reflections along the Bahamas transect: Marine Geology, 185, 1–17, doi: 10.1016/S0025-3227(01)00287-0.
- Elrick, M., and J. F. Read, 1991, Cyclic ramp-to-basin carbonate deposits, Lower Mississippian, Wyoming and Montana; a combined field and computer modeling study: Journal of Sedimentary Research, 61, 1194–1224.
- Embry, A. F., and J. E. Klovan, 1971, A late Devonian reef tract on northeastern Banks Island, NWT: Bulletin of Canadian Petroleum Geology, 19, 730–781.

- Enge, H. D., S. J. Buckley, A. Rotevatn, and J. A. Howell, 2007, From outcrop to reservoir simulation model: Workflow and procedures: *Geosphere*, 3, 469–490, 10.1130/GES00099.1.
- Entzminger, D., K. Ferdinand, D. Lawson, B. Loucks, P. Mescher, and K. Patty, 2000, Corrigan-Cowden—Breathing new life into an old waterflood: The Permian basin: Proving ground for tomorrow’s technologies: West Texas Geological Society Publication 00-109, 75.
- Falivene, O., P. Arbus, A. Gardiner, G. Pickup, J. A. Muoz, and L. Cabrera, 2006, Best practice stochastic facies modeling from a channel-fill turbidite sandstone analog (the Quarry outcrop, Eocene Ainsa Basin, Northeast Spain: *AAPG Bulletin*, 90, 1003–1029.
- Fischer, A. G., and M. Sarnthein, 1988, Airborne silts and dune-derived sands in the Permian of the Delaware Basin: *Journal of Sedimentary Research*, 58, 637–643, doi: 10.1306/212F8E0E-2B24-11D7-8648000102C1865D.
- Fisher, W. L., E. Gama, H. A. Ojeda y Ojeda, 1973, Estratigrafia sismica e sistema deposionais da Formacao Piacabucu: XXVII Congresso Brasileiro de Geologia, *Anais*, 123–133.
- Fitchen, W., 1993, Sequence stratigraphic framework of the upper San Andres Formation and equivalent basinal strata in the Brokeoff Mountains, Otero County, New Mexico: 44th Field Conference, Guidebook, Carlsbad Region, New Mexico and West Texas, 185-193.
- Fomel, S., 2007, Shaping regularization in geophysical estimation problems: *Geophysics*, 72, no. 2, R29–R36, 10.1190/1.2433716.
- Fomel, S., 2010, Predictive painting of 3D seismic volumes: *Geophysics*, 75, A25–A30, doi: 10.1190/1.3453847.
- Fournier, F., and J. Borgomano, 2007, Geological significance of seismic reflections and imaging of the reservoir architecture in the Malampaya gas field (Philippines): *AAPG Bulletin*, 91, 235–258, 10.1306/10160606043.
- Galli, A., G. Le Lo ch, F. Geffroy, and R. Eschard, 2006, An application of the truncated pluri-Gaussian method for modeling geology, in T. C. Coburn, J. M. Yarus, and R. L. Chambers, eds., *Stochastic modeling and geostatistics: Principles, methods, and case studies: AAPG, Computer Applications in Geology* 5, 109–122.
- Gardner, G. H.F., L.W. Gardner, A.R. Gregory, 1974, Formation velocity and density – the diagnostic basics for stratigraphic traps: *Geophysics*, 39, 770–780.
- Goovaerts. P., 1997, *Geostatistics for Natural Resources Evaluation*: New York, Oxford, Oxford University Press, 496 p.

- Grammer, G. M., P. M. M. Harris, and G. P. Eberli, 2004, Integration of outcrop and modern analogs in reservoir modeling: Overview with examples from the Bahamas: AAPG Memoir 80: 1–22.
- Grötsch, J., and C. Mercadier, 1999, Integrated 3-D reservoir modeling based on 3-D seismic: the Tertiary Malampaya and Camago buildups, offshore Palawan, Philippines: AAPG bulletin, 83, 1703–1728.
- Hallam, A., 1992, Phanerozoic sea-level changes, Columbia University Press.
- Hampson, D. P., J. S. Schuelke, and J. A. Quirein, 2001, Use of multiattribute transforms to predict log properties from seismic data: Geophysics, 66, 220–236.
- Hardage, B. A., R. L. Remington, and P. E. Murray, 2007, Reflections have a "Tipper Point": AAPG Explorer, Geophysical Corner, 27, 32–35.
- Harms, J. C. and L. C. Pray, 1974, Erosion and deposition along the Mid-Permian intracratonic basin margin, Guadalupe Mountains, Texas: The Society of Economic Paleontologists and Mineralogists Modern and Ancient Geosynclinal Sedimentation (SP19), 37.
- Harrison, S. C., 1966, Depositional mechanics of the Permian Cherry Canyon Sandstone Tongue, Last Chance Canyon, New Mexico, Texas Tech University.
- Hart, B. S., 2013, Whither seismic stratigraphy? Interpretation, 1, SA3–SA20.
- Hayes, P. T., 1959, San Andres limestone and related Permian rocks in Last Chance Canyon and vicinity, southeastern New Mexico: AAPG Bulletin, 43, 2197–2213.
- He, Y. and H. Zeng, 2014a, Chronostratigraphy at seismic scale: rethinking Vail et al.'s basic assumption: GSH Journal, 1, 40, 11–15.
- He, Y., and H. Zeng, 2014b, Experiment on the selection of time-transgression predictive seismic attributes: AAPG Hedberg Research Conference 'Interpretation Visualization in the Petroleum Industry', Houston, Texas, June 1–4.
- He, Y., H. Zeng, C. Kerans, and B. A. Hardage, 2015a, Seismic chronostratigraphy at reservoir scale: Statistical modeling: Interpretation, 3, SN69–SN87, doi: 10.1190/INT-2014-0136.1.
- He, Y., H. Zeng, X. Janson, and C. Kerans, 2015b, Influence of spatial velocity distribution on seismic imaging of mixed carbonate-siliciclastic clinofolds based on outcrop-based synthetic model of the Permian San Andres Formation, Last Chance Canyon, NM, USA: SEG Technical Program Expanded Abstract 2015: 1612–1617, doi: 10.1190/segam2015-5912322.1.
- He, Y., C. Kerans, H. Zeng, X. Janson, and S. Z. Scott, 2016, Reservoir-scale significance of seismic reflections of a strongly prograding shelf margin: 3D outcrop-constrained seismic models: SEG Technical Program Expanded Abstract 2016: 1818–1823, doi: 10.1190/segam2016-13762587.1.

- He, Y., C. Kerans, H. Zeng, X. Janson, S. Scott, 2017a, Seismic characterization of stratigraphic architecture: outcrop- and well-based three-dimensional forward seismic modeling of Permian San Andres-Grayburg strata (abs.): AAPG Search and Discovery Article #90291, 2017 AAPG Annual Convention and Exhibition, Houston, Texas, April 2-5, 2017.
- He, Y., H. Zeng, and C. Kerans, 2017b (in review), Seismic chronostratigraphy of mixed versus pure carbonate shelf margin in Permian Basin: SEG 2017 Annual Meeting, September 24-27, Houston.
- He, Y., C. Kerans, H. Zeng, X. Janson, and S. Z. Scott, 2017c (in preparation), Improving 3D seismic horizon interpretation for reservoir model construction: an example of 3D geocellular and seismic model of Permian San Andres shelf-Grayburg platform mixed clastic-carbonate strata.
- Hentz, T. F., and H. Zeng, 2003, High-frequency Miocene sequence stratigraphy, offshore Louisiana: cycle framework and influence on production distribution in a mature shelf province: AAPG Bulletin, 87, 197–230, doi: 10.1306/09240201054.
- Hiebert, S. F., 2013, High-resolution correlation framework of the Grayburg Formation-Shattuck Escarpment and Plowman Ridge: testing models of shelf-to-basin frameworks: Master Thesis, The University of Texas at Austin, Austin, Texas, 111p.
- Horak, R. L., 1985, Trans-Pecos tectonism and its effect on the Permian basin: Structure and tectonics of trans-Pecos Texas: West Texas Geological Society Field Conference, publication, 85-81.
- Isaaks, E., and R. M. Srivastava, 1989, An introduction to Applied Geostatistics: New York, Oxford University Press, 561 p.
- Janson, X., and S. Fomel, 2011, 3-D Forward seismic model of an outcrop-based geocellular model: SEPM Concepts in Sedimentology and Paleontology, 10, 86–106.
- Janson, X., C. Kerans, J. A. Bellianand, and W. Fitchen, 2007, Three-dimensional geological and synthetic seismic model of Early Permian redeposited basinal carbonate deposits, Victorio Canyon, West Texas: AAPG Bulletin, 91, 1405–1436, 10.1306/05210705188.
- Janson, X., H. Zeng, B. Loucks, Q. Wang, C. Wang, S. Li, T. Yang, Y. Xia and L. Xu, 2010, An ultra-deep paleokarst system in the Ordovician, North-Central Tarim Basin, China: outcrop analog and synthetic seismic models: SEG Technical Program Expanded Abstract 2010, 1531–1534.
- Janson, X., and S. Fomel, 2011, 3-D forward seismic model of an outcrop-based geocellular model: Concepts in Sedimentology and Paleontology 10, 87-106.

- Jennette, D. C., and W. A. Pryor, 1993, Cyclic alternation of proximal and distal storm facies: Kope and Fairview Formations (Upper Ordovician), Ohio and Kentucky: *Journal of Sedimentary Research*, 63, 183-203.
- Kenter, J. A., F. Podladchikov, M. Reinders, S. J. Van der Gaast, B. W. Fouke, and M. D. Sonnenfeld, 1997, Parameters controlling sonic velocities in a mixed carbonate-siliciclastics Permian shelf-margin (upper San Andres formation, Last Chance Canyon, New Mexico): *Geophysics*, 62, 505–520.
- Kenter, J., G. Bracco Gartner, and W. Schlager, 2001, Seismic models of a mixed carbonate-siliciclastic shelf margin: Permian upper San Andres Formation, Last Chance Canyon, New Mexico: *Geophysics*, 66, 1744–1748.
- Kerans, C., and W. M. Fitchen, 1995, Sequence hierarchy and facies architecture of a carbonate-ramp system: San Andres Formation of Algerita Escarpment and western Guadalupe Mountains, West Texas and New Mexico: The University of Texas at Austin, Bureau of Economic Geology Report of Investigations No. 235, 86 p.
- Kerans, C., and K. Kempter, 2002, Hierarchical stratigraphic analysis of a carbonate platform, Permian of the Guadalupe Mountains: The University of Texas at Austin, Bureau of Economic Geology (American Association of Petroleum Geologists/Datapages Discovery Series No. 5), CD-ROM.
- Kerans, C., S. F. Hiebert, and J. A. Parker, 2014, Differential compaction at pre-existing shelf margins as a control on stratigraphic traps in Permian mid- to outer shelf successions: AAPG Datapages/Search and Discovery Article #90190, AAPG Southwest Section Annual Convention, Midland, Texas.
- Kerans, C., and H. Nance, 1991, High-frequency cyclicity and regional depositional patterns of the Grayburg Formation, Guadalupe Mountains, New Mexico: Sequence Stratigraphy, Facies and Reservoir Geometries of the San Andres, Grayburg and Queen Formations, Guadalupe Mountains, New Mexico and Texas: SEPM, Permian Basin Section Publication, 32, 53–96.
- Kerans, C., T. Playton, R. Phelps, and S. Scott, 2013, Ramp to rimmed shelf transition in the Guadalupian (Permian) of the Guadalupe Mountains: Deposits, Architecture, and Controls of Carbonate Margin, Slope, and Basinal Settings: SEPM, Special Publication, 105, 26–49.
- Kerans, C., and J. Sitgreaves, 2015, Integrated sequence stratigraphic reservoir model and seismic characterization - Grayburg Formation, Central Basin Platform, 2015 Extended Abstract Volume RCRL Annual Meeting, Bureau of Economic Geology, The University of Texas at Austin.
- Kerans, C., and S. W. Tinker, 1999, Extrinsic stratigraphic controls on development of the Capitan reef complex: SEPM Special Publication No. 65, 15–36.

- Kerans, Charles, and Tinker, S. W., 1997, Sequence stratigraphy and characterization of carbonate reservoirs: SEPM (Society for Sedimentary Geology), Short Course Notes No. 40, 165 p.
- Kessinger, W., 1992, Extended split-step Fourier migration: 62nd Society of Exploration Geophysicists Meeting, Expanded Abstracts, 917–920.
- King, P. B., 1942, Permian of West Texas and Southeastern New Mexico: PART 1: AAPG Bulletin, 26, 535–763.
- King, P. B., 1948, Geology of the southern Guadalupe Mountains, Texas: Professional Paper 215, U.S. Geological Survey.
- Krige, D., 1951, A statistical approach to some basic mine valuation problems on the Witwatersrand: Journal of the Southern African Institute of Mining and Metallurgy, 52, 119–139.
- Lawrence, D. T., M. Doyle, and T. Aigner, 1990, Stratigraphic simulation of sedimentary basins: concepts and calibration: AAPG Bulletin, 74, 273–295.
- Le Loc'h, G., H. Beucher, A. Galli, and B. Doligez, 1994, Improvement in the truncated Gaussian method: combining several Gaussian functions: ECMOR IV-4th European Conference on the Mathematics of Oil Recovery.
- Lo, T.-W., and W. M. Bashore, 1999, Seismic constrained facies modeling using stochastic seismic inversion and indicator simulation, a North Sea example: 1999 SEG Annual meeting.
- Loewenthal, D., L. Lu, R. Roberson, and J. W. C. Sherwood, 1976, The wave equation applied to migration: Geophysical Prospecting, 24, 380–399.
- Lomask, J., A., S. Guitton, S. Fomel, J. Claerbout, and A. Valenciano, 2006, Flattening without picking: Geophysics, 71, 13–20, doi: 10.1190/1.2210848.
- Lottes, A. L., and D. B. Rowley, 1990, Reconstruction of the Laurasian and Gondwanan segments of Permian Pangaea: Geological Society of London, Memoirs, 12, 383–395.
- Macurda, B. M., Jr., 2012, Seismic reflections: do they have lithostratigraphic or chronostratigraphic properties? Presented at the William Smith Meeting “Strata and time: probing the gaps in our understanding.”
- Matheron, G., H. Beucher, C. De Fouquet, A. Galli, D. Guerillot, and C. Ravenne, 1987, Conditional simulation of the geometry of fluvio-deltaic reservoirs: SPE Annual Technical Conference and Exhibition.
- Marion, D., A. Nur, H., Yin, and D. Han, 1992, Compressional velocity and porosity in sand – clay mixtures: Geophysics, 57, 554–563.
- Mayer, L. A., T. H. Shipley, and E. L. Winterer, 1986, Equatorial Pacific seismic reflectors as indicators of global oceanographic events: Science, 233, 761–764.

- Meissner, F., 1967, Cyclic sedimentation in middle Permian strata of the Permian Basin, west Texas and New Mexico: in *Cyclic sedimentation in the Permian Basin--symposium*, Midland, Texas, West Texas Geol. Soc.
- Meissner, F. F., 1972, Cyclic sedimentation in Middle Permian strata of the Permian basin, west Texas and New Mexico: *Cyclic sedimentation in the Permian Basin*, 203-232.
- McDermott, R. W., 1983, Depositional processes and environments of the Permian sandstone tongue of the Cherry Canyon Formation and the Upper San Andres Formation, Last Chance Canyon, Southeastern New Mexico, University of Texas at Austin.
- Meckel, L. D., Jr., and A. K. Nath, 1977, Geologic considerations for stratigraphic modeling and interpretation: *AAPG Memoir 26*, 417-438.
- Mitchum Jr, R. M., P. R. Vail, and J. B. Sangree, 1977a, Seismic stratigraphy and global changes of sea level: Part 6. Stratigraphic interpretation of seismic reflection patterns in depositional sequences: Section 2. Application of seismic reflection configuration to stratigraphic interpretation, in C.E. Payton ed., *AAPG Memoir 26: Seismic stratigraphy – Applications to Hydrocarbon Exploration*, p. 117-133.
- Mitchum, R. M., P. R. Vail, and S. Thompson III, 1977b, Seismic stratigraphy and global changes of sea level, Part 2: The depositional sequence as a basic unit for stratigraphic analysis, in C. E. Payton, ed., *Seismic stratigraphy—application to hydrocarbon exploration: AAPG Memoir 26*, 53-62.
- Murray, R.C., 1960, Origin of porosity in carbonate rocks: *Journal of Sedimentary Research*, 30, 59-84.
- Neidell, N. S., and E. Poggiagliolmi, 1977, Stratigraphic modeling and interpretation—geophysical principles and techniques: *AAPG memoir 26*, 389-416.
- Osleger, D., and J. F. Read, 1991, Relation of eustasy to stacking patterns of meter-scale carbonate cycles, Late Cambrian, USA: *Journal of Sedimentary Research*, 61, 1225-1252, doi: 10.1306/D426786B-2B26-11D7-8648000102C1865D.
- Pedersen-Tatalovic, R., A. Uldall, N. L. Jacobsen, T. M. Hansen, and K. Mosegaard, 2008, Event-based low-frequency impedance modeling using well logs and seismic attributes: *The Leading Edge*, 27, 592-603.
- Petersen, L. M., and R. S. Jacobs, 2003, Stratigraphic and Lithologic Zonation in the East Cowden Grayburg Unit, Ector County, Texas: Potential for Horizontal redevelopment of a Mature Waterflood?
- Phelps, R. M., 2006, Sequence stratigraphic and architectural characterization of a Permian carbonate ramp, upper San Andres Formation, Last Chance Canyon, New Mexico, PhD dissertation, The University of Texas at Austin, Austin, Texas, 169p.
- Phelps, R. M., and C. Kerans, 2007, Architectural Characterization and Three-Dimensional Modeling of a Carbonate Channel-Levee Complex: Permian San Andres

- Formation, Last Chance Canyon, New Mexico, U.S.A: *Journal of Sedimentary Research*, 77, 939–964.
- Posamentier, H. W., G. A. Dorn, M. J. Cole, C. W. Beierle, and S. P. Ross, 1996, Imaging elements of depositional systems with 3-D seismic data: a case study: Gulf Coast Section SEPM Foundation 17th Annual Research Conference, Extended Abstract, 213–228.
- Posamentier, H. W., and P. R. Vail, 1988, Eustatic controls on clastic deposition II—sequence and system tract models, in C. K. Wilgus, B. S. Hastings, C. G. St. C. Kendall, H. W. Posamentier, C. A. Ross, and J. C. Van Wagoner, eds., *Special Publication of Society of Economic Paleontologists and Mineralogists*, 42, 125–154.
- Pringle, J., A. Westerman, J. Clark, N. Drinkwater, and A. Gardiner, 2004, 3D high-resolution digital models of outcrop analogue study sites to constrain reservoir model uncertainty: an example from Alport Castles, Derbyshire, UK: *Petroleum Geoscience*, 10, 343–352.
- Rafavich, F., C. S. C. Kendall, and T. Todd, 1984, The relationship between acoustic properties and the petrographic character of carbonate rocks: *Geophysics*, 49, 1622–1636.
- Ruppel, S., 2001, Opportunities for recovery of remaining oil in San Andres reservoirs: Example from Fuhrman-Mascho field, University Lands Block 10, Andrews County, Texas: PUBLICATIONS-WEST TEXAS GEOLOGICAL SOCIETY, 105–126.
- Sarg, J., 1999, The second-order cycle, carbonate-platform growth, and reservoir, source, and trap prediction.
- Sarg, J., and P. Lehmann, 1986a, Facies and Stratigraphy of Lower-Upper San Andres Shelf Crest and Outer Shelf and Lower Grayburg Inner Shelf: Proc. San Andres/Grayburg Formations, Guadalupe Mountains, New Mexico. and Texas, Permian Basin Research Conference (PBS-SEPM Pub. No. 86-25), Midland, Texas, 9–36.
- Sarg, J., and P. Lehmann, 1986b, Lower-Middle Guadalupian facies and stratigraphy, San Andres/Grayburg Formations, Permian Basin, Guadalupe Mountains, New Mexico: Lower and Middle Guadalupian Facies, Stratigraphy, and Reservoir Geometries, San Andres/Grayburg Formations, Guadalupe Mountains, New Mexico and Texas: SEPM (Society for Sedimentary Geology) Permian Basin Section, Tulsa, Oklahoma, 1–8.
- Sarnthein, M., and L. Diester-Haass, 1977, Eolian-sand turbidites: *Journal of Sedimentary Research*, 47, 868–890.
- Sarnthein, M., and B. Koopmann, 1980, Late Quaternary deep-sea record on northwest African dust supply and wind circulation: *Palaeoecology of Africa*, 12, 239–253.

- Schramm, M. W., Jr., E. V. Dedman, and J. P. Lindsey, 1977, Practical stratigraphic modeling and interpretation, in C. E. Payton, ed., *Seismic Stratigraphy—application to hydrocarbon exploration: AAPG Memoir 26*, 477–502.
- Scotese, C. R., 2004, A continental drift flipbook: *The Journal of Geology*, 112, 729–741.
- Scott, S. Z., 2007, Application of ground-based LIDAR to constrain topographic strike-variability and facies proportions of progradational San Andres Formation clinofolds, Last Chance Canyon, NM, Master Thesis, The University of Texas at Austin, 110 p.
- Shepherd, M., 2009, Reservoir modeling and geostatistics, in M. Shepherd, ed., *AAPG Bulletin Memoir 91*, p. 157, doi:10.1306/13161203M91337.
- Shi, G., Z. Xu, J. Yarus, R. L. Chambers, R. Guetter, 2013, Systems and methods for creating a surface in a faulted surface: U.S. Patent US 13/816,450, applied in 2013.
- Shrestha, R. K., and M. Boeckmann, 2002, Stochastic seismic inversion for reservoir modeling: *SEG Technical Program Expanded Abstracts 2002*: 902–905.
- Shrestha, R. K., and M. Boeckmann, 2003, Seismic-dependent Facies and Porosity Modeling of the Rotliegend Gas Field: *SEG Technical Program Expanded Abstracts 2003*: 390–393.
- Sheriff, R. E., 1977, Limitations on resolution of seismic reflections and geologic detail derivable from them: Section 1. Fundamentals of Stratigraphic Interpretation of Seismic Data, in C.E. Payton ed., *AAPG Memoir 26: Seismic stratigraphy – Applications to Hydrocarbon Exploration*, 3–13.
- Silver, B. A., and R. G. Todd, 1969, Permian cyclic strata, northern Midland and Delaware basins, west Texas and southeastern New Mexico: *AAPG Bulletin*, 53, 2223–2251.
- Skinner, J. W., 1946, Correlation of Permian of west Texas and southeast New Mexico: *AAPG Bulletin*, 30, 1857–1874.
- Sloss, L., 1963, Sequences in the cratonic interior of North America: *Geological Society of America Bulletin*, 74, 93–114.
- Sonnenfeld, M., 1991a, High-frequency cyclicity within shelf-margin and slope strata of the upper San Andres sequence, Last Chance Canyon: *Sequence Stratigraphy, Facies and Reservoir Geometries of the San Andres, Grayburg, and Queen Formations, Guadalupe Mountains, New Mexico and Texas: SEPM, Permian Basin Section, Special Publication*, 32, 11–51.
- Sonnenfeld, M. D., 1991a, Anatomy of offlap in a shelf-margin depositional sequence: upper San Andres Formation (Permian, Guadalupian), Last Chance Canyon, Guadalupe Mountains, New Mexico, Master's thesis, Colorado School of Mines, Golden, Colorado, 297p.

- Sonnenfeld, M. D., and T. A. Cross, 1993, Volumetric Partitioning and Facies Differentiation within the Permian Upper San Andres Formation of Last Chance Canyon, Guadalupe Mountains, New Mexico: Chapter 17, in R. G. Loucks and J.F. Sarg eds., AAPG Memoir 57: Carbonate Sequence Stratigraphy: Recent Development and Applications, 435 – 474.
- Soreghan, G. S., and M. J. Soreghan, 2013, Tracing clastic delivery to the Permian Delaware basin, USA: implications for paleogeography and circulation in westernmost equatorial Pangea: *Journal of Sedimentary Research*, 83, 786 –802.
- Stafleu, J., and M. D. Sonnenfeld, 1994, Seismic models of a shelf-margin depositional sequence: Upper San Andres Formation of Last Chance Canyon, New Mexico: *Journal of Sedimentary Research*, B64, 481–499.
- Stark, T. J., 2004, Relative geologic time (age) volumes– relating every seismic sample to a geologically reasonable horizon: *The Leading Edge*, 23, 928–932, doi: 10.1190/1.1803505.
- Stark, T. J., H. Zeng, and A. Jackson, 2013, An introduction to this special section: chronostratigraphy: *The Leading Edge*, 32, 132–138, doi: 10.1190/tle32020132.1.
- Stoffa, P. L., J. T. Fokkema, R. M. de Luna Freir, and W. P. Kessinger, 1990, Split-step Fourier migration: *Geophysics*, 55, 410–421, doi: 10.1190/1.1442850.
- Thurmond, J. B., P. A. Drzewiecki, and J. R. Markello, 2001, Three dimensional mapping of Permian mud-mounds, Last Chance Canyon, New Mexico: GSA Annual Meeting, November 5-8, 2001.
- Thurmond, J. B., P. A. Drzewiecki, and X. Xu, 2005, Building simple multiscale visualizations of outcrop geology using virtual reality modeling language (VRML): *Computers & Geosciences*, 31, 913–919.
- Tipper, J. C., 1993, Do seismic reflections necessarily have chronostratigraphic significance? *Geological Magazine*, 130, 47–55.
- Tucker, M. E., 2003, Mixed clastic–carbonate cycles and sequences: Quaternary of Egypt and Carboniferous of England: *Geologia Croatica*, 56, 19–37.
- Vail, P. R., R. M. Mitchum Jr., and S. Thompson III, 1977a, Seismic Stratigraphy and Global Changes of Sea Level, Part 3: Relative changes of sea level from coastal onlap, in C. E., Payton, ed., *Seismic Stratigraphy – Application to Hydrocarbon Exploration: AAPG Memoir 26*, 63–81.
- Vail, P. R., R. M. Mitchum, Jr., and S. Thompson III, 1977b, Seismic Stratigraphy and Global Changes of Sea Level, Part 4: Global Cycles of Relative Changes of Sea Level, in C. E. Payton, ed., *Seismic Stratigraphy – Application to Hydrocarbon Exploration: American Association of Petroleum Geologists Memoir 26*, 83–97.
- Vail, P. R., R. M. Mitchum Jr., and S. Thompson III, 1977c, Seismic stratigraphy and global changes of sea level, Part 5: Chronostratigraphic significance of seismic

- reflections, in C. E., Payton, ed., *Seismic Stratigraphy – Application to Hydrocarbon Exploration: AAPG Memoir 26*, 99–116.
- Van Horn, J., 2001, Sendji Formation reservoir delineation based on 2-D and 3-D inversion, Yombo Field, offshore Congo: *The Leading Edge*, 20, 435–441.
- Van Sicken, D. C., 1958, Depositional topography--examples and theory: *AAPG Bulletin*, 42, 1897–1913.
- Vernik, L., and A. Nur, 1992, Petrophysical classification of siliciclastics for lithology and porosity prediction from seismic velocities: *American Association of Petroleum Geologists Bulletin*, 76, 1295–1309.
- Weber, K. J., and L. C. van Geuns, 1990, Framework for constructing clastic reservoir simulation models: *Journal of Petroleum Technology*, 42, 1248–1297.
- Wonham, J., M. Cyrot, T. Nguyen, J. Louhouamou, and O. Ruau, 2010, Integrated approach to geomodelling and dynamic simulation in a complex mixed siliciclastic–carbonate reservoir, N'Kossa field, Offshore Congo: *Geological Society, London, Special Publications*, 347, 133–163.
- Yao, T., and A. Chopra, 2000, Integration of seismic attribute map into 3D facies modeling: *Journal of Petroleum Science and Engineering*, 27, 69–84.
- Yarus, J. M., R. L. Chambers, and M. Maučec, 2012, Facies Simulation in Practice: Lithotype proportion mapping and Plurigaussian Simulation, a powerful combination: Paper P-014 presented at the 9th International Geostatistics Congress, Oslo, Norway, 11-15.
- Zeng, H., 1994, Facies-guided 3-D seismic modeling and reservoir characterization: The University of Texas at Austin, Ph.D. dissertation, 164 p.
- Zeng, H., and M.M. Backus, 2005a, Interpretive advantages of 90°-phase wavelets: Part 1—modeling: *Geophysics*, 70, no. 3, C7–C15, doi: 10.1190/1.1925740.
- Zeng, H., and M. M. Backus, 2005b, Interpretive advantages of 90°-phase wavelets: Part 2—seismic applications: *Geophysics*, 70, C17–C24, doi: 10.1190/1.1925741.
- Zeng, H., M. M. Backus, K. T. Barrow, and N. Tyler, 1998a, Stratal slicing, part I: Realistic 3-D seismic model: *Geophysics*, 63, 502–513, doi: 10.1190/1.1444351.
- Zeng, H., S. C. Henry, and J. P. Riola, 1998b, Stratal slicing, part II: Real 3-D seismic data: *Geophysics*, 63, 514–522, doi: 10.1190/1.1444352.
- Zeng, H., F. H. Hentz, and L. J. Wood, 2001, Stratal slicing of Miocene – Pliocene sediments in Vermilion Block 50 – Tiger Shoal Area, offshore Louisiana: *The Leading Edge*, 410 –419.
- Zeng, H., and Kerans, C., 2003, Seismic frequency control on carbonate seismic stratigraphy: a case study of the Kingdom Abo sequence, West Texas: *AAPG Bulletin*, 87, 273–293, doi: 10.1306/08270201023.

Vita

Yawen He was born on September 25th, 1990 in Hefei, Anhui, China, to Fangbo He and Yingchuan Li. She entered China University of Petroleum (East China) in Qingdao, Shandong, China in 2007, and received a B.E. in Prospecting Technology and Engineering (Exploration Geophysics track) and a B.A. in English Language and Literature in July 2011. Starting from the fall of 2011, she entered The University of Texas at Austin for her Ph.D. study in Jackson School of Geosciences. Upon receiving her degree, she will join PGS this June in Houston as a geophysicist.

Permanent email: yawenhe@utexas.edu

This dissertation was typed by Yawen He.